

**Estimation of Effective Scatterer Size and Number Density
in Near-Infrared Tomography**

A Thesis

Submitted to the Faculty

in partial fulfillment of the requirements for the

degree of

Doctor of Philosophy

in

Department of Physics and Astronomy

by

Xin Wang

DARTMOUTH COLLEGE

Hanover, New Hampshire

(February 2007)

Examining Committee:

(Chair) Brian W. Pogue, Ph.D.

Keith D. Paulsen, Ph.D.

James W. LaBelle, Ph.D.

Miles P. Blencowe, Ph.D.

Adam Wax, Ph.D.

Wendy A. Wells, MD

Charles K. Barlowe, Ph.D.
Dean of Graduate Studies

Abstract

Light scattering from tissue originates from the fluctuations in intra-cellular and extra-cellular components, so it is possible that macroscopic scattering spectroscopy could be used to quantify sub-microscopic structures.

Both electron microscopy (EM) and optical phase contrast microscopy were used to study the origin of scattering from tissue. EM studies indicate that lipid-bound particle sizes appear to be distributed as a monotonic exponential function, with sub-micron structures dominating the distribution. Given assumptions about the index of refraction change, the shape of the scattering spectrum in the near infrared as measured through bulk tissue is consistent with what would be predicted by Mie theory with these particle size histograms.

The relative scattering intensity of breast tissue sections (including 10 normal & 23 abnormal) were studied by phase contrast microscopy. Results show that stroma has higher scattering than epithelium tissue, and fat has the lowest values; tumor epithelium has lower scattering than the normal epithelium; stroma associated with tumor has lower scattering than the normal stroma.

Mie theory estimation scattering spectra, was used to estimate effective particle size values, and this was applied retrospectively to normal whole breast spectra accumulated in ongoing clinical exams. The effective sizes ranged between 20 and 1400 nm, which are consistent with subcellular organelles and collagen matrix fibrils discussed previously. This estimation method was also applied to images from cancer regions, with results indicating that the effective scatterer sizes of region of interest (ROI) are pretty close to that of the background for both the cancer patients and benign patients; for the

effective number density, there is a big difference between the ROI and background for the cancer patients, while for the benign patients, the value of ROI are relatively close to that of the background. Ongoing MRI-guided NIR studies indicated that the fibroglandular tissue had smaller effective scatterer size and larger effective number density than the adipose tissue.

The studies in this thesis provide an interpretive approach to estimate average morphological scatter parameters of bulk tissue, through interpretation of diffuse scattering as coming from effective Mie scatterers.

ACKNOWLEDGEMENTS

There are lots of people I would like to thank for a huge variety of reasons.

First of all, I would like to give my great thanks to my Supervisor, Dr. Brian W. Pogue. I could not have imagined having a better advisor and mentor for my PhD. He gave me great support and encouragement over the last four years and played a key role in my research. He impressed deeply me with his kindness and his endless patience for students. Without his common-sense, knowledge, perceptiveness and patience I would never have finished.

I would like to thank Dr. Keith D. Paulsen, Dr. James W. LaBelle, Dr. Miles P. Blencowe, and Dr. Adam Wax for their thoughtful suggestions on my proposal and for being on my committee in spite of a busy schedule.

I am very grateful to Dr. Wendy A. Wells for her great help in tissue collection and analysis. Her willingness to help and enthusiasm in research contributed a lot to this thesis.

Although not a committee member herself, Dr. Shudong Jiang deserves my sincere thanks. She gave me lots of kind help and good suggestions in my research, especially in experimental study and patient study. I appreciate for her input on the tomography system and all the clinical studies, which provide us highly valuable clinical data to analyze.

Many thanks to Dr. Steven Poplack and Christine Kogel for their clinical collaboration and help.

My sincere thanks to all my group members Dr. Hamid Dehghani, Dr. Roger Springett, Dr. Bin Chen, Dr. Andrew L. Darling, Dr. Subhadra Srinivasan, Dr. Ben Brooksby and Dr. Xiaomei, Dr. Heng Xu, Dr. Chao Sheng, Dr. Xiaodong Zhou, Scott Davis, Summer Gibbs, Phaneendra Yalavarthy, Colin M. Carpenter, Dax S. Kepshire, Jia Wang and Zhiqiu Li for their patience, useful discussion, and all around good times.

Finally, I would like to thank other assorted friends and family members for keeping tabs on me. Special thanks to my parents, Qinghua Wang and Yuzhi Zhai, and my sister, Lei Wang, for their endless love and support.

This research has been funded by grants PO1CA80139 and U54CA105480.

Table of Contents

<u>Abstract</u>	ii
<u>Acknowledgements</u>	iv
<u>Table of Contents</u>	vi
<u>List of Tables</u>	xii
<u>List of Figures</u>	xiv
<u>Chapter 1: Overview</u>	1
<u>1.1. Introduction</u>	1
<u>1.2. Background of NIR tomography</u>	2
1.2.A. Background of current breast cancer imaging methods.....	2
1.2.B. Background of NIR breast cancer imaging.....	4
<u>1.3. NIR tomography imaging at Dartmouth College</u>	7
1.3.A NIR tomography imaging system.....	7
1.3.B Optical properties image reconstruction.....	8
1.3.C Functional image formation	10
1.3.D Power Law	11
<u>1.4. Scatterer size and number density estimation from NIR tomography</u>	13
1.4.A. Significance of scatter relative to tissue disease.....	13
1.4.B. Previous studies in scatter interpretation	15
<u>1.5. Angular scattering distribution study of breast tissue</u>	17
<u>1.6 Microscopic study of the breast tissue section</u>	18
1.6.A. Electron microscopy study of breast tissues.....	18
1.6.B. Phase contrast microscopic study of breast tissues.....	19

<u>Chapter 2: Mie Scattering Theory Interpretation</u>	<u>21</u>
<u>2.1. Introduction.....</u>	<u>21</u>
<u>2.2. Scattering in Electronic Magnetic field.....</u>	<u>23</u>
<u>2.3. Mie Theory - Scattering from a Sphere.....</u>	<u>25</u>
<u>2.4. Scattering Phase Function.....</u>	<u>30</u>
<u>2.5. Scattering Spectra Power Law Fit.....</u>	<u>31</u>
<u>2.6. Dependent Scattering.....</u>	<u>31</u>
<u>Chapter 3: Approximation of Mie scattering parameters (Effective scatterer size</u>	
<u>and number density) in near-infrared tomography.....</u>	<u>33</u>
<u>3.1. Introduction.....</u>	<u>34</u>
<u>3.2. Methods.....</u>	<u>35</u>
3.2.A. Mie Theory Interpretation.....	35
3.2.B. Scattering Spectra Power Law Fit.....	37
3.2.C. Scattering from Tissue Spectra.....	37
3.2.D. Image Reconstruction of Absorption and Scattering Coefficients.....	38
3.2.E. Simulation Studies.....	39
3.2.F. Phantom Studies.....	40
3.2.G. Clinical Studies.....	41
<u>3.3 Results.....</u>	<u>41</u>
3.3.A. Influence of Particle Size Distribution.....	41
<u>3.3.B. Simulation Results of the Optimal Estimated Values for Particle</u>	
<u>Size and number Density.....</u>	<u>44</u>

3.3.C. Estimated Values of Particle Size and Number Density of Intralipid Phantoms.....	46
3.3.D. Estimated Values of Particle Size and Number Density of Normal Subjects with Different Radiographic Density Categories .	46
3.4. Discussion	49

Chapter 4: Image Reconstruction of Effective Mie Scattering Parameters of Breast Tissue in Vivo with Near-Infrared Tomography.....54

4.1. Introduction.....55

4.2. Method.....55

4.2.A. Image Reconstruction of Absorption and Scattering Coefficients.55

4.2.B. Effective Scatterer Size and Number Density Estimation Method 56

4.2.C. Effective Scatterer Size and Number Density Image Reconstruction Method57

4.3 Effective Scatterer Size and Number Density Image Reconstruction

Studies..... 58

4.3.A. Phantom Study.....59

4.3.B. Image Reconstruction of $\langle a \rangle$ and N for Human Breast Tissue...60

4.3.C. Study of Subject Images from the MRI-NIR System.....60

4.4. Results.....62

4.4.A. Empirical Equations for Estimation of $\langle a \rangle$ and N.....62

4.4.B. Phantom Study Results.....64

4.4.C. Patient Imaging Study Results.....66

4.4.D. MRI-NIR Subject Study Results.....	72
<u>4.5. Discussion</u>	<u>75</u>
<u>4.6. Conclusions.....</u>	<u>79</u>
<u>Chapter 5: Breast Tissue Mie Scattering Parameter Estimation through Angle-Resolved Scattering Measurements</u>	<u>80</u>
<u>5.1 Introduction.....</u>	<u>80</u>
<u>5.2 Method.....</u>	<u>81</u>
5.2.A Mie Theory.....	81
5.2.B Simulation Study.....	83
5.2.B.1 The Forward Simulation Study	83
5.2.B.1.1 The effect of effective scatterer size and distribution upon angular scattering	84
5.2.B.1.2 The comparison between different laser polarizations.....	85
5.2.B.2 The Simulation Studies for Effective Scatterer Size Estimation.....	86
5.2.B.2.1 Effective Scatterer Size Estimation Method..	86
5.2.B.2.2 Effective Scatterer Size Estimation Results..	87
5.2.C Experimental Study.....	89
5.2.C.1 Experimental Apparatus.....	90
5.2.C.2 Experimental Samples.....	91
<u>5.3. Results.....</u>	<u>93</u>
5.3.A Results for Phantoms with the Cylindrical cuvette.....	93

5.3.B Results for Phantoms in Thin Cuvette.....	94
5.3.C Results for Breast Tissue.....	95
<u>5.4. Effective Scatterer Size Estimation Results.....</u>	<u>96</u>
5.4.A Effective Scatterer Size Estimation Results for Phantom	96
5.4.B Effective Scatterer Size Estimation Results for Breast Tissue....	99
<u>5.5. Discussion.....</u>	<u>102</u>

Chapter 6: Estimation of Sub-Cellular Particle Size Histograms with Electron Microscopy.....103

<u>6.1. Introduction.....</u>	<u>103</u>
<u>6.2. Samples and Methods.....</u>	<u>107</u>
6.2.A Quantitative pathology analysis.....	107
6.2.B. Electron microscopy.....	108
6.2.C. Image Processing.....	109
6.2.D. Mie Theory calculation for reduced scattering spectra.....	110
<u>6.3 Results.....</u>	<u>111</u>
6.3.A Typical EM images.....	111
6.3.B EM images Analysis.....	115
6.3.C Reduced scattering spectra calculation.....	120
<u>6.4. Discussion.....</u>	<u>122</u>
<u>6.5 Conclusions.....</u>	<u>125</u>

Chapter 7: Breast Tissue Phase Contrast Measurements to Assess Relative Microscopic Scattering126

<u>7.1. Introduction.....</u>	<u>126</u>
7.1.A. Phase Contrast Microscope.....	126
7.1.B. Interpreting Microscopic Tissue Slices stained with H&E (Hematoxylin and Eosion)	131
<u>7.2 Methods and Materials.....</u>	<u>132</u>
7.2.A. Tissue acquisition	132
7.2.B. Apparatus.....	132
7.2.C. Image Acquisition.....	133
7.2.D. Image Analysis.....	134
7.2.E. Samples.....	135
<u>7.3. Results.....</u>	<u>135</u>
7.3.A Case Studies.....	135
7.3.A.1 Normal tissues.....	135
7.3.A.2 Ductal carcinoma.....	137
7.3.A.3 Lobular Tumor.....	143
7.3.A.4 Fibroadenoma (Benign Tumor)	148
7.3.B. Statistical analysis.....	150
7.3.B.1 Statistical analysis based on case	150
7.3.B.2 Statistical analysis based on ROI.....	154
<u>7.4 Conclusion.....</u>	<u>158</u>
<u>Chapter 8 : Concluding remarks.....</u>	<u>159</u>
<u>References.....</u>	<u>162</u>

List of Tables

Table 3.1. Effective Particle Size and Number Density estimated from mean scattering spectrum data acquired in vivo from normal breasts. The scattering coefficients were taken as the whole breast effective obtained for each subject. ED = Extremely Dense, HD = Heterogeneously Dense, S = Scattered fibroglandular densities, F= Almost entirely fat.

.....49

Table 4.1. Power function estimates for effective scatterer size $\langle a \rangle$ and normalized number density $\log_{10}(N_0)$, given the index of refraction values specified for outside (n_1) and inside (n_2) the spheres. For $\langle a \rangle$ the power series was taken out to 7 orders, whereas for $\log_{10}(N_0)$, only 3 orders were required.59

Table 4.2 The variance parameters for the Box and whisker plot of (a) average effective scatterer sizes and (b) average effective number density for groups of subjects in terms of cancer and benign lesions.71

Table 4.3 The p-values to determine if the values are significantly different from each tissue type, using a Student's t-test on all (a) average effective scatterer sizes and (b) average effective number density for groups of subjects in terms of cancer and benign lesions.71

Table 6.1 The tissue samples used in this study were analyzed with quantitative pathology estimates from immunohistochemical specimen slides to calculate the epithelial to stromal ratio (E:S), fat to stromal and epithelial ratio (F:S/E), complete tissue type ratios, microvascular density (MVD), microvascular area (MVA).108

Table 6.2 Fitting parameter results for a double exponential decay model for the particle size histogram data shown in Figure 6.7.	119
Table 6.3 Scattering power got from fitting the $\mu_s'(\lambda)$ in figure 6.6.using power law...	121
Table 7.1 The variance parameters for Box and whisker plot of the phase contrast gray scale values of all cases for each tissue classification.	151
Table 7.2 The p-values to determine if the values are significantly different from each tissue type, using a Student's t-test on the phase contrast values of all cases.	153
Table 7.3 The variance parameters for Box and whisker plot of the phase contrast gray scale values of all ROIs for each tissue classification.	155
Table 7.4 The p-values to determine if the values are significantly different from each tissue type, using a Student's t-test on phase contrast values of all ROIs.	157

List of Figures

Figure 1.1. Plot of NIR absorption spectra for water, lipids, Hb-O₂ and Hb-R [1-4] values for absorption coefficient are displayed for anatomically relevant concentrations for breast tissue. 5

Figure 1.2. Photograph of the NIR tomography system used for breast imaging, with light generation electronics below on a rotary table. The fiber optics for contact with the tissue are located above on 16 linear translation stages.[5] 8

Figure 1.3. In (a), an anatomically coronal T1-weighted MRI displays adipose (outer) and glandular (inner) tissue types. In (b), MRI data guides a two-region parameter fitting algorithm. [6] The absorption coefficient is at left and the reduced scattering coefficient is at right, and the units of each color bar are in mm⁻¹.10

Fig 1.4 Reduced scattering coefficients at six wavelengths are shown, measured from a patient, along with the model function fit to the data [7].12

Fig 1.5 One MRI-NIR patient data set is used, with (a) showing the MRI image, and (b) the MRI-guided reconstructions of chromophore and scattering images [8].13

Figure 2.1. The incident field (E_1, H_1) gives rise to a field (E_i, H_i) inside the particle and scattered field (E_2, H_2) in the medium surrounding the particle.21

Figure 2.2. The incident field (E_1, H_1) gives rise to a field (E_i, H_i) inside the particle, and scattered field (E_2, H_2) in the medium surrounding the particle.25

Figure 3.1. (a) Comparison of Gaussian, uniform and exponential particle size distributions with the same effective particle size $\langle a \rangle = 1000\text{nm}$. (b) Calculated reduced scattering spectra for these three particle size distributions with the same refractive index

change ($n_1=1.311$ and $n_2=1.451$). (c) Comparison of reduced scattering spectra for three different refractive indexes for the same size distribution with effective particle size $\langle a \rangle=1000\text{nm}$. Inset plot is the comparison of these three spectra after normalized at 800nm . (d) Comparison of reduced scattering spectra for four different effective particle sizes with the same exponential size distribution and refractive index ($n_1=1.36$, $n_2=1.4$).

.....43

Figure 3.2. (a) Error function for estimating effective particle size using simulated test data with a true effective particle size of $\langle a \rangle=100\text{nm}$. The minimum of the function presents the optimal estimation of particle size. (b) Same for number density assuming an effective particle size $\langle a \rangle=100\text{nm}$ and number density $N=1 \times 10^{19} \text{ m}^{-3}$. (c) Estimates of effective particle size based on test data with true values of $\langle a \rangle=50, 100, 200, 500$ and 1000nm , with $N=1 \times 10^{19} \text{ m}^{-3}$. (d) Corresponding estimates of number density indicating that number density does not change significantly with changes in particle size.45

Figure 3.3. (a) Error function for estimating effective scatterer size using phantom data with an Intralipid concentration of $C=1.045\%$. The minimum of the function presents the optimal estimation of particle size $\langle a \rangle=110\text{nm}$. (b) Same for number density using the estimated effective scatterer size $\langle a \rangle=110\text{nm}$ and the optimal estimation of number density is $N=2.3 \times 10^{19} \text{ m}^{-3}$. (c) Estimate of effective scatterer size for Intralipid phantoms with varying concentration. (d) Same for Number Density.47

Figure 3.4. (a) Error function for estimating effective scatterer size using the data from a patient with fatty breast type. The minimum of the function presents the optimal estimation of particle size $\langle a \rangle=300\text{nm}$. (b) Same for number density using the estimated effective scatterer size $\langle a \rangle=300\text{nm}$ and the optimal estimation of number density is

$N=7.5 \times 10^{17} \text{ m}^{-3}$. (c) Effective Scatterer sizes from individual normal subject exams, grouped by radiographic density. (d) Same for Number Density.....48

Figure 4.1. The relationship between scatter power, b , and effective scatterer size, $\langle a \rangle$, is shown in (a) for simulated data (points) and the best fit polynomial curve (coefficients in Table 1). The relationship between effective normalized number density (the effective number density when $A=1$) and scatter power is shown in (b) for the same parameters, with the fitted polynomial curve shown (coefficients in Table 4.1).63

Figure 4.2. In (a) a diagram of the phantom geometry is shown, and in (b) a set of reconstructed images of the phantom with 1.0% Intralipid concentration is shown. The background medium was a solid resin phantom used in many previous studies [9].65

Figure 4.3. The results are shown for different intralipid concentrations of (a) average effective scatterer size, $\langle a \rangle$, and (b) average effective number density, N , using bulk values from within the inclusion region, as shown in the previous figure.66

Figure 4.4. In (a) reconstructed NIR images are shown for a cancer patient, showing the plane of the tumor in the breast, sliced in a cranocaudal view. The panel of images shows total hemoglobin concentration (Hb_T), oxygen saturation (Oxy), water fraction (Wat), scatter power (Scatt. Power) and amplitude (Scatt. Ampl.), as well as effective scatterer size (Effec. Size) and number density (Num. Density) images. In (b) the reconstructed NIR images for a patient with a benign tumor in the breast are shown.69

Figure 4.5. The Box and whisker plot of (a) average effective scatterer sizes and (b) average effective number density for groups of subjects in terms of cancer and benign lesions. ‘o’ indicate all the data point, while ‘o’ with ‘x’ inside is the mean value for each group of data.70

Figure 4.6. Reconstructed images for two of the MRI-NIR subjects (a & b) are shown, with the MRI image in (Region), and hemoglobin (Hb_T), oxygen saturation (Oxy), water fraction (Wat), scatter power (Scatt Power), scatter amplitude (Scatt Ampl.). Estimates of $\langle a \rangle$ and N are shown in (Effec. Size) and (Num. Dens.), as calculated from (Scatt Power) and (Scatt Ampl.). Image (b) is predominantly fatty tissue (grey in MR Image), whereas (a) is predominantly fibroglandular tissue (darker in MR Image).73

Figure 4.7. The average tissue values are shown pooled for all MRI-NIR subject images, for effective scatterer size (a), and number density (b), for adipose and fibroglandular tissues.....74

Figure 5.1: The phase function was calculated using Mie theory for mono-sized scattering media with sizes: $a=100\text{nm}$, 200nm , 500nm and $1\mu\text{m}$, using $m=1.2$, for both (a) 0° (b) 90° laser polarization;84

Figure 5.2: Phase functions were calculated using Mie theory for multi-sized media with exponential size distribution functions and $\langle a \rangle = 100\text{nm}$, 200nm , 500nm and $1\mu\text{m}$, $m=1.1$ using (a) 0° (b) 90° laser polarization.85

Figure 5.3 Angular scattering from Mie theory for (a) mono-sized medium with $a=100\text{nm}$, $m=1.2$; (b) mono-sized medium with $a=1\mu\text{m}$, $m=1.2$; (c) multi-sized medium with exponential size distribution function and $\langle a \rangle = 100\text{nm}$, $m=1.1$. Blue solid line for 0° polarization, red dashed line for 90° polarization.86

Figure 5.4 Effective scatterer size estimation results for mono-size scattering medium with true size $a=100\text{nm}$ using different normalization angles and different laser polarizations with different noises added. The y-axis shows the least-square difference

between the simulated data and the value for each possible size of scatterer. The minimum value is precisely near 100 ± 10 nm as would be expected.88

Figure 5.5 Effective scatterer size estimation results are shown for mono-size scattering medium with true size $a=500$ nm using different normalization angles and different laser polarizations with different noises added. The y-axis shows the least-square difference between the simulated data and the value for each possible size of scatterer. The minimum value is precisely near 500 ± 5 nm as would be expected.89

Figure 5.6: The diagram of the experimental setup is shown for angle resolved light scattering measurement. The set up used was a HeNe laser with collimated output beam at 633 nm wavelength, and a silicon photodiode detector with automated gain control, from Newport Inc.90

Figure 5.7: (a) Cylindrical specimens were used for particle or cells in solution. (b)Thin cuts of tissue were used for ex vivo sample.91

Figure 5.8 Angular scattering measurement for the following phantoms held in cylindrical cuvette, including (a) polystyrene microspheres in suspension with $a=100$ nm; (b) polystyrene microspheres suspension with $a=1\mu$ m; and (c) diluted Intralipid. The data shows blue ‘*’ points for 0° polarization, and magenta ‘o’ points for 90° polarization....94

Figure 5.9 Angular scattering measurement for the following phantoms held in thin cuvette (a) polystyrene microspheres suspension with $a=100$ nm; (b) polystyrene microspheres suspension with $a=1\mu$ m; (c) Intralipid. The data shows blue ‘*’ points for 0° polarization, and magenta ‘o’ points for 90° polarization.....95

Figure 5.10 Angular scattering measurements are shown for the following breast tissue sections held in a thin cuvette, for (a) fat tissue and (b) fibroglandular tissue, using

thickness of 120um. The data shows blue ‘*’ points for 0° polarization, and magenta ‘o’ points for 90° polarization.	96
Figure 5.11 The fitting result for the polystyrene microspheres suspension with a=100nm using different normalization angles of (a) 60° and (b) 130°.	97
Figure 5.12 The fitting result for the polystyrene microspheres suspension with a=1um using different normalization angles of (a) 60° and (b) 130°.	97
Figure 5.13 The fitting result for the Intralipid suspension using different normalization angles of (a) 30° and (b) 60°.....	98
Figure 5.14 Angular scattering measurements for fat and fibroglandular breast tissue with thickness 120um. The polarization of the laser is 90°.	100
Figure 5.15 The fitting result for the fibrous tissue section using different normalization angles of (a) 60° and (b) 130°.	100
Figure 5.16 The fitting result for the fat tissue section using different normalization angles of (a) 60° and (b) 130°.	101
Figure 6.1 Electron microscopy images of normal adipose tissue example images are shown in (a) and (b), at 4000X and 29,000X respectively.	112
Figure 6.2 Electron microscopy images of normal fibroglandular tissues (a) and (b) at magnifications of 4000X and 15000X respectively.	113
Figure 6.3 Electron microscopy images of low grade infiltrating ductal carcinoma tissue (a) and (b) at magnifications of 4000X and 15000X respectively.	114
Figure 6.4 Electron microscopy images of higher grade infiltrating ductal carcinomas tissues (a) and (b) at magnifications of 2550X and 9900X respectively.	115

Figure 6.5 (a) shows the thresholded image of the original EM image for one particular threshold value, where the parts that were marked in red will be analyzed to get size information, while the left parts will not be analyzed. (b) shows the outline of the red-marked parts in (a). In (c) the red-marked parts in (a) were represented as ellipses of the approximate size. The result of this analysis is presented as a histogram of particle sizes in (d).....116

Figure 6.6 (a) shows the thresholded image of the original EM image for one particular threshold value, where the parts that were marked in red will be analyzed to get size information, while the left parts will not be analyzed. (b) shows the outline of the red-marked parts in (a). In (c) the red-marked parts in (a) were represented as ellipses of the approximate size. The result of this analysis is presented as a histogram of particle sizes in (d).117

Figure 6.7 Particle size distributions obtained by combining results from Image Processing as described in this paper (a) Normal adipose histogram; (b) Normal fibroglandular tissue histogram; (c) Low grade ductal carcinoma tissue; (d) High grade ductal carcinoma tissue.118

Figure 6.8 The reduced scattering coefficient spectrum, $\mu_s'(\lambda)$, is shown as calculated by (a) the solid spherical Mie theory calculation and (b) for the shell simulation of Mie theory, using the particle distribution histograms in figure 6.7.120

Figure 7.1.  is phase retarding material. (a) is positive phase plate, and (b) is negative phase plate. [9].127

Figure 7.2. This figure shows how a negative phase plate works. In the figure (1) is the specimen, (2) is the negative phase plate.128

Figure 7.3. This figure shows how a positive phase plate works. (1) is the specimen, (2) is the positive phase plate.129

Figure 7.4. (a) shows 3 different parts in the tissue. (b) shows the different scattering intensity of these three parts. If we use a negative phase plate, then we can get a phase contrast image as shown in (c), and if we use a positive phase plate, then we can get a phase contrast image as shown in (d).130

Figure 7.5. An H&E stained breast tissue sample. Stromal collagen is pink-orange, the epithelial nuclei are blue-purple (near the bottom). Fat tissue dissolves in the fixation process, and is therefore observed as open white areas surrounded by pink stroma.131

Figure 7.6. the (a) phase contrast image and (b) H&E staining image from the same location on a normal breast tissue section136

Figure 7.7. the (a) phase contrast image and (b) H&E stained image of the entire montage image section of normal breast tissue, which is the same as in Figure 7.6.137

Figure 7.8. the (a) phase contrast image and (b) H&E staining image over the whole section of a Ductal Carcinoma breast tissue.139

Figure 7.9. the co-localized phase contrast image and H&E staining image from separate areas: (a) invasive ductal carcinoma (b) Ductal carcinoma In Situ and (c) normal tissue of the same Ductal carcinoma section as shown in Figure 7.8.140

Figure 7.10. the (a) H&E image and (b) phase contrast image over the whole section of a Ductal carcinoma.....141

Figure 7.11. the (a) H&E staining image and (b) phase contrast image over the whole section of a Ductal Carcinoma In Situ breast tissue section.142

Figure 7.12. the (a) H&E staining image and (b) phase contrast image over the whole section of a Invasive Lobular Carcinoma breast tissue section.144

Figure 7.13. the (a) H&E image and (b) phase contrast image over the whole section of a Lobular carcinoma (with Invasive Lobular Carcinoma and Lobular Carcinoma In Situ), illustrating the lower scatter in the epithelium.145

Figure 7.14. the co-localized (a) phase contrast and (b) H&E image from the LCIS, at higher power than shown in Figure 7.13. Again, stroma is higher in scatter and epithelium is lower.146

Figure 7.15. the (a) H&E image and (b) phase contrast image over the whole section of a Invasive Lobular Carcinoma section.147

Figure 7.16. the (a) H&E image and (b) phase contrast image over the whole section of a Fibroadenoma section.148

Figure 7.17. the co-localized (a) H&E image and (b) phase contrast image from the a Fibroadenoma section at higher power.149

Figure 7.18. the (a) H&E image and (b) phase contrast image over the whole section of a Fibroadenoma breast tissue section.149

Figure 7.19. The Box and whisker plot of the gray scale values of all cases on the phase contrast images. (a) and (b) are using different grouping.152

Figure 7.20. The Box and whisker plot of the gray scale values of all kinds of tissue on the phase contrast images. (a) and (b) are using different grouping.156

Chapter 1: Overview

1.1. Introduction

This thesis describes the study of how light scatters in different breast tissues, and eventually how an ‘effective’ size and number density can be estimated from non-invasive measurements of light transmitted through breast tissue. The approach examines multi-spectral frequency domain Near Infrared (NIR) tomography data, as well as ex vivo data from breast tissues. The estimation method is described, along with image reconstruction techniques which take advantage of the measurement of a scattering spectrum which is derived by diffuse imaging but can be matched to single scattering spectra from Mie scatter theory. The estimation method and image reconstruction method of the effective scatterer size and number density were tested using computer simulations, tissue-simulating ‘phantoms’, and patient volunteers.

In addition, angular resolved scattering light distribution measurements were examined as a second method to extract scatterer size distribution information. This was completed on optically thin tissue sections and dilute suspensions.

The culminating part of this work involved imaging breast tissue sections with the electronic microscope (EM), a phase contrast microscope and a regular optical microscope with H&E stained tissue sections. The goal of this last study was to have a clear concept of the tissue’s morphology and composition, relative to the contribution to bulk tissue scatter, with a particular focus on the change in morphology from diseased to normal breast tissues.

This thesis is organized into eight chapters:

Chapter 1: Overview

Chapter 2: Mie theory Review

Chapter 3: Effective scatterer size and number density estimation

Chapter 4: Effective scatterer size and number density image reconstruction

Chapter 5: Angular scattering distribution study of breast tissue

Chapter 6: Electronic microscopic study of the breast tissue section

Chapter 7: Phase contrast and H&E staining microscopic study of tissue sections

Chapter 8: Concluding remarks

The work presented in this thesis builds on clinical trials research in NIR breast imaging conducted at Dartmouth College and other institutions. In order to give a better understanding of the motivation of the research described herein, a brief history of NIR imaging is provided in this overview chapter.

1.2. Background of NIR tomography

1.2.A. Background of current breast cancer imaging methods

X-ray mammography is the most currently widely accepted and practiced method for breast cancer screening. It is estimated that 48 million mammograms are performed each year in the United States. Mammography is optimized as a low dose x-ray methodology; using high contrast, high-resolution film and an x-ray system designed specifically for imaging thin body tissues. Successful treatment of breast cancer depends on early diagnosis, and as such mammography plays a major role in early detection of these cancers. X-ray mammography has high resolution and when used in an annual screening approach, it is very good at detecting breast abnormalities in older woman [1].

The US Food and Drug Administration (FDA) reports that mammography can find 85 to 90 percent of breast cancers in women over 50 and can discover a lump up to two years before it can be felt. The benefits of mammography far outweigh the risks and inconvenience. However, X-ray mammography has a low positive predictive value [2, 3], requiring the need for additional imaging tests. About 80% of biopsies are performed on benign tumors. Also, it has lower sensitivity for dense breast tissues and are therefore not recommended in a screening approach for women younger than 49 [1].

Breast ultrasound is frequently used to evaluate breast abnormalities that are found with screening or diagnostic mammography or during a physician performed clinical breast exam. Ultrasound is excellent at imaging cysts: round, fluid-filled, pockets inside the breast, and it can often quickly determine if a suspicious area is in fact a cyst (always non-cancerous) or an increased density of solid tissue (dense mass) which may require a biopsy to determine if it is malignant (cancerous). Though breast ultrasound has excellent contrast-resolution, it lacks the small spatial-resolution of conventional mammography, and therefore, ultrasound is not used as a screening tool for breast cancer. Rather, ultrasound is used to investigate an abnormality detected by mammography or during a physician performed breast exam.

Currently, there is no non-invasive imaging modality used for distinguishing benign and malignant tumors. So alternative breast cancer imaging methods could have the potential to decrease the number of unnecessary biopsies, as well as improve detection and diagnosis in younger women. One alternative imaging modality which has the potential to achieve these goals is near infrared diffuse imaging.

1.2.B. Background of NIR breast cancer imaging

Over the past decade there has been increasing research dedicated to the field of biomedical optics, and the medical utility of light. One goal in this field is to develop diagnostic imaging modalities based upon near infrared (NIR) spectroscopy. NIR imaging and spectroscopy research has focused on a variety of potential clinical applications with a major focus on tissue hemoglobin and oxygen saturation imaging [4-11]. This is made possible by a spectral window that exists within tissues in the 700-900nm region as shown in Figure 1.1, in which photon transport is dominated by scattering rather than absorption, and allows for measurements through many centimeters of tissue. Biological tissue acts a turbid optical medium in this wavelength range, in which light transport is dominated by elastic scattering [12-14], resulting from refractive index fluctuations at a microscopic level of cellular organelles. When imaging through bulk tissues the diffusion approximation has been the most useful approach for modeling. The image reconstruction task in a tomography mode involves solving an inverse problem using this diffusion model of photon transport, which has been extensively studied [15].

Optical methods could potentially offer several advantages over existing radiological techniques. First, the optical method is non-ionizing, thus high doses and repeated imaging procedures can be employed without any harm to the patient. Second, optical methods offer the potential to differentiate between soft tissues due to their different absorption or scattering properties at these wavelengths. Thirdly, optical spectroscopy can be built into existing clinical imaging systems, as is shown later in this thesis. NIR absorption in tissue is dominated by oxy-hemoglobin, deoxy-hemoglobin,

water, and lipid. Scattering is generated by microscopic fluctuations in refractive index, and is related to the structure of the tissue resulting from membrane bound sub-cellular organelles [16-21]. So perhaps the most dominant advantage of optical imaging is the ability to measure functional information either from molecular signatures or tissue ultra-structural information [22, 23] by the specific absorption by intrinsic chromophores and scattering-structure relationship. However, this functional information cannot be readily obtained using other current clinical modalities.

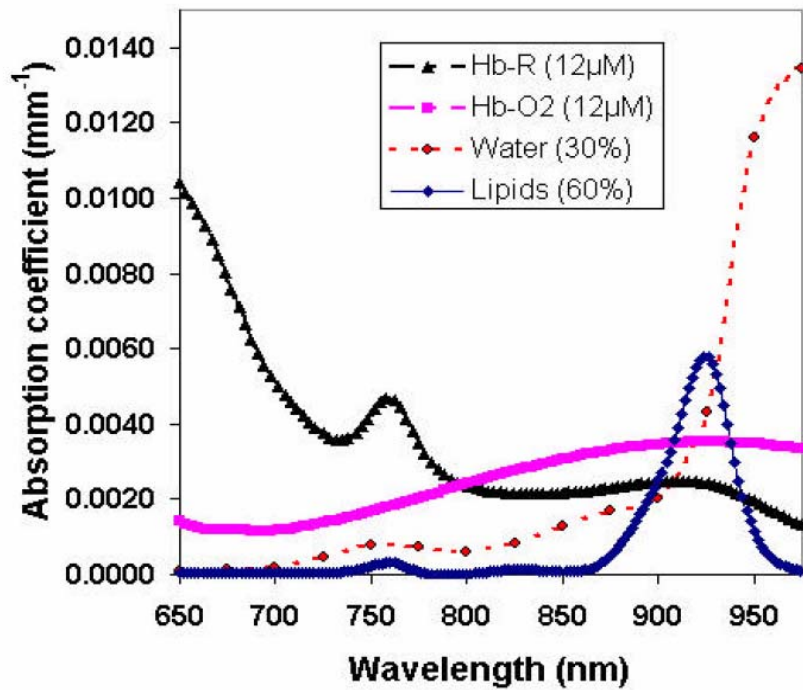


Figure 1.1. Plot of NIR absorption spectra for water, lipids, Hb-O2 and Hb-R [2, 24-26] values for absorption coefficient are displayed for anatomically relevant concentrations for breast tissue.

NIR measurement systems can be used to detect diffuse reflectance [17], transmittance [6], or a combination of the two when detection points surround the tissue under investigation [27, 28]. The latter arrangement represents a tomography system, which is the most capable of resolving subtle heterogeneity contrasts deep within tissue.

The system may be revised to provide measurements of the full NIR wavelength spectrum [29], or measurements of several discrete wavelengths, which are either pulsed [30] or modulated [24], in order to separate effects of absorption from scattering. Over the past decade, there has been considerable interest in developing NIR tomography as a breast imaging modality to characterize abnormalities non-invasively [3, 31-35].

By definition, a cancerous tumor is growing rapidly, which leads to angiogenesis and hence a localized increased concentration of blood [35-37]. As a result hemoglobin concentration is a strong indicator of breast malignancy, and a 4:1 hemoglobin contrast has been observed at the edge of breast cancer tumors relative to the normal tissue [38]. Also these rapidly growing tumors tend to outstrip the oxygen supply, and a 1.4 to 4.4 times lower oxygen pressure has been observed in breast cancer tumors [39]. De-oxygenated and oxygenated blood (specifically hemoglobin), water, and lipids have different absorption spectra in the visible and near-infrared, allowing separation of these components by measurements at multiple wavelengths. NIR imaging can detect localized increase in hemoglobin (blood) concentration and decrease in blood oxygen saturation, so it can potentially detect and distinguish benign and malignant breast cancer tumors. A two to four fold increase in hemoglobin concentration within breast cancers relative to healthy tissue [40, 41] has been estimated by NIR imaging.

Recent studies have shown that scattering contrast between malignant and benign processes appears to be significant [42]. The morphologic changes from normal to diseased breast tissue are seen by light microscopy in the cellular epithelial component and the surrounding support stroma. Generally, the hallmark of an epithelial malignancy is an increase in the overall epithelial cell density with increased nuclear and nucleolar

size. Microscopic sub-cellular alterations exist that may not be apparent in standard pathological analysis. Hence, variations in the scattering spectral features, which can be measured tomographically, may encode morphologic and pathophysiologic changes in tissue at the microscopic level.

1.3. NIR tomography imaging at Dartmouth College

1.3.A. NIR tomography imaging system

The current NIR tomography system [28] at Dartmouth is shown in Figure 1.2. It consists of 48 source and detector optical fibers, positioned in a circular array, with three planes of 16 fibers each. The fibers are attached to a radial positioning system which allow for variable diameter fiber movement. A collection of laser diode light sources (661, 761, 785, 808, 826 and 849nm) are amplitude modulated at 100 MHz. For each wavelength, measurements are taken sequentially in each plane. The light is delivered to the breast through one of the 16 in-plane fibers. The diffusely transmitted light is detected by the remaining 15 in-plane fibers that are aligned to output to each of 15 photomultiplier tube (PMT) detectors that sample the signal in parallel. Typical of frequency domain systems, modulated sources are used in order to extract amplitude and phase of the light transmitted through the breast. These two data types allow for the separation of absorption and scattering properties in the reconstruction process.

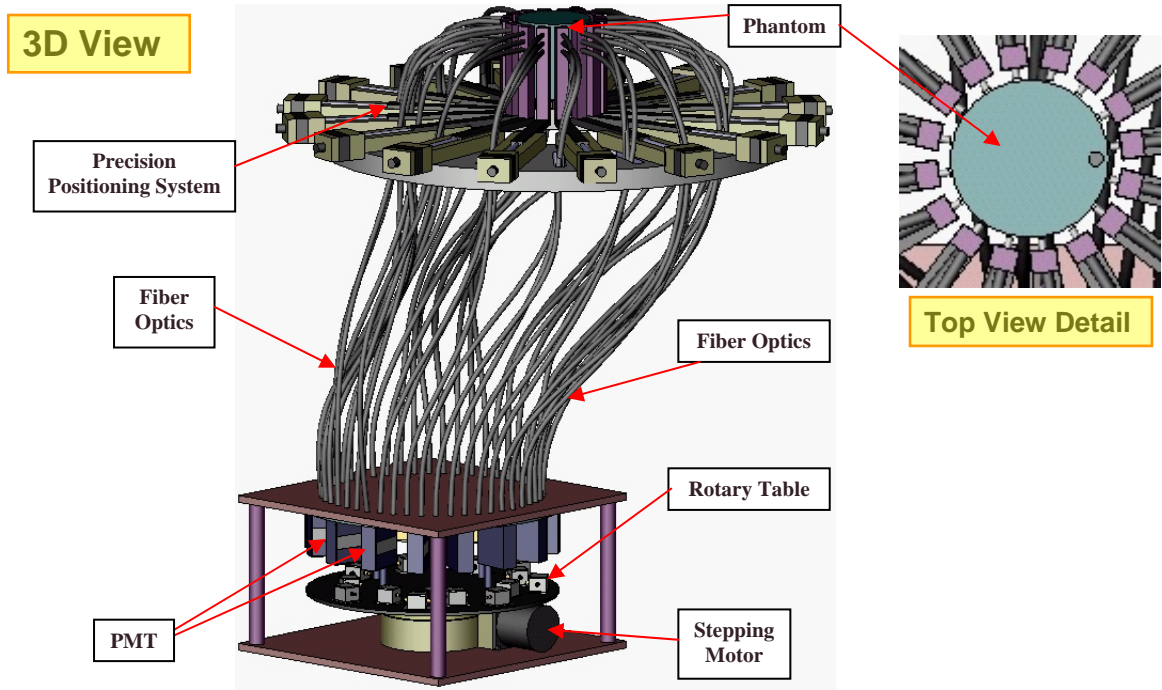


Figure 1.2. Photograph of the NIR tomography system used for breast imaging, with light generation electronics below on a rotary table. The fiber optics for contact with the tissue are located above on 16 linear translation stages.[43]

1.3.B. Optical properties image reconstruction

As discussed in 1.2.B, within a highly scattering medium [4, 44], the light propagation is reasonably well approximated by the diffusion equation (1.1):

$$-\nabla \cdot D(\mathbf{r})\nabla \Phi(\mathbf{r}, \omega) + \left(\mu_a(r) + \frac{i\omega}{c} \right) \Phi(\mathbf{r}, \omega) = S(r, \omega), \quad (1.1)$$

where
$$D = \frac{1}{3(\mu_a + \mu_s')} \quad (1.2)$$

and $S(r, \omega)$ is an isotropic light source at position r , $\Phi(r, \omega)$ is the light fluence rate (W/mm^2) at r , c is the speed of light in tissue, ω is the frequency of light modulation, μ_a is the absorption coefficient (mm^{-1}), D is the diffusion coefficient (mm), and μ_s' is the

reduced scattering coefficient (mm^{-1}). For a given μ_a and μ_s' distribution, the diffusion equation is used to predict the optical flux at the detector sites for each source excitation.

The diffusion equation (1.1) can be solved using the finite element method (FEM) given the optical properties of the medium, the source and boundary conditions. In the image reconstruction, the goal is to recover the optical properties at each FEM node location, based on measurements of optical flux at the detector sites on the tissue surface. For this purpose, an initial estimated value of the optical properties is needed, which is usually determined based on a homogeneous estimation of the tissue volume [45]. And then the final image reconstruction is achieved iteratively numerically by minimizing the difference between the calculated data Φ^C , and measured data Φ^M , for all source/detector combinations (NM).

$$\chi^2 = \sum_{i=1}^{NM} (\Phi_i^C - \Phi_i^M)^2 \quad (1.3)$$

A modified Newton's method is employed to iteratively update the optical properties:

$$\Delta\mu = (J^T J + \lambda I)^{-1} J^T (\Phi^C - \Phi^M)^T \quad (1.4)$$

defining the optical property updates, $\Delta\mu = [\delta D_j, \delta\mu_{aj}]$ at each reconstructed node j .

Here, λ is a regularization factor to stabilize matrix inversion and J is the Jacobian matrix for our model.

Typical images of μ_a and μ_s' properties from one of our MRI-guided breast tissue imaging [46] are shown in Figure 1.3. Figure 1.3(a) is the anatomically coronal T1-weighted MRI displaying adipose (outer) and glandular (inner) tissue types. Figure 1.3 (b) is the MRI data guided reconstructed μ_a and μ_s' properties.

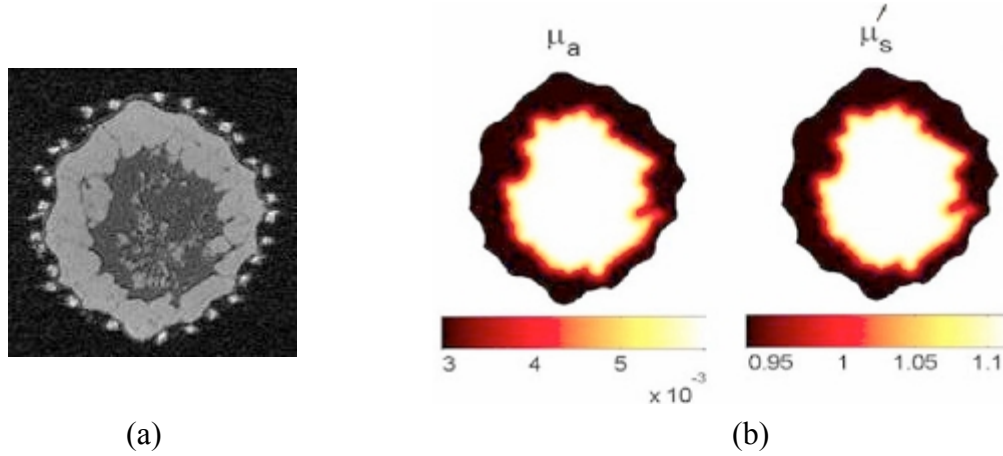


Figure 1.3. In (a), an anatomically coronal T1-weighted MRI displays adipose (outer) and glandular (inner) tissue types. In (b), MRI data guides a two-region parameter fitting algorithm. [46] The absorption coefficient is at left and the reduced scattering coefficient is at right, and the units of each color bar are in mm^{-1} .

1.3.C. Functional image formation

Absorption at any wavelength (λ) is assumed to be a linear combination of the absorption due to all relevant chromophores in a sample:

$$\mu_a(\lambda) = \sum_{i=1}^N \varepsilon(i, \lambda) C_i \quad (1.5)$$

where ε is the molar absorption coefficient for wavelength λ , and C is the concentration of each chromophore [18]. For breast tissue, we usually assume a combination due to oxygenated hemoglobin (Hb-O_2), deoxygenated hemoglobin (Hb-R), and water. Figure 1.1 shows a plot of absorption spectra for Hb-O_2 , Hb-R , water, and lipids for anatomically relevant concentrations in breast tissue over the entire NIR wavelength range. Hence, given μ_a at the k^{th} pixel for multiple wavelengths, a linear inversion of equation (1.4) determines the array of C values representing the concentrations of the three chromophores:

$$C_{\vec{k}} = E^{-1} \mu_{a,\vec{k}} \quad (1.6)$$

The matrix E contains the molar absorption coefficients, having elements $\varepsilon(i, \lambda)$ for the i^{th} chromophore at the different wavelengths used.

1.3.D. Power Law

The scattering spectrum of tissue (i.e. reduced scattering coefficients reconstructed at different wavelengths) provides information about the nature of the scattering particles and hence the composition of tissue. Rather than applying Mie scattering theory directly, a more empirical approach was first proposed by van Staveren et al [47], who fit the scattering spectrum of Intralipid. A number of groups have adopted the approach to characterize the spectrum of the reduced scattering coefficient observed in tissues [16, 41, 48, 49]. In these studies, the scattering spectra are considered to satisfy a power law relationship. Empirically, when there is a broad range of scattering particle sizes, this spectrum is described by a power law curve of the type:

$$\mu_s'(\lambda) = A \lambda^{-b} \quad (1.7)$$

where A and b are model parameters for scattering amplitude and scattering power, respectively. Here λ is wavelength in μm , and μ_s' has unit mm^{-1} .

In Figure 1.4 a typical spectral data set is shown for the reduced scattering coefficient from a near-infrared tomography breast exam along with a fit to the power law in equation (1.7) [42]. Equation (1.7) describes a smooth function with no oscillations in the spectrum, and conveniently restricts the fitting process to only two

parameters. The curve is quasi-linear in the NIR region, and appears to fit data from a large number of wavelengths reasonably well [50].

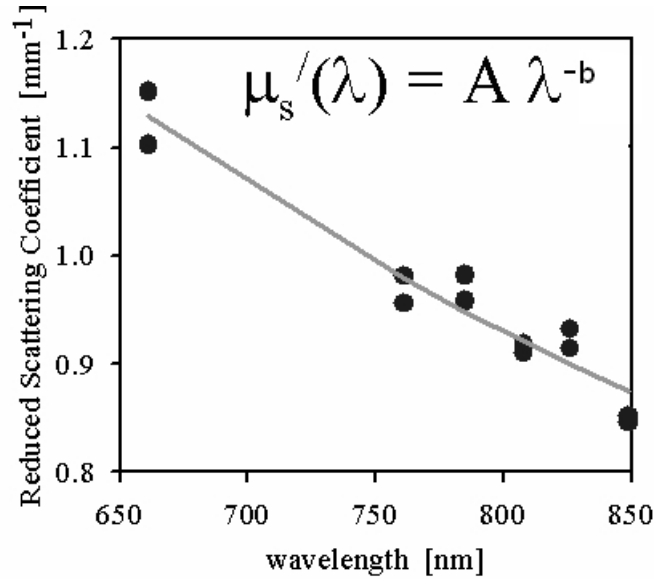


Fig 1.4 Reduced scattering coefficients at six wavelengths are shown, measured from a patient, along with the model function fit to the data [42].

Figure 1.4 shows a power law function fit to two representative scattering spectra for breast tissue measured in vivo at six wavelengths. Together, these two parameters may reflect variations in breast structural composition due to different sub-cellular organelle and extra-cellular structural sizes/densities for fatty and glandular tissue.

The reconstructed chromophore and scattering images for the same breast tissue as in Figure 1.3 are shown in Figure 1.5. Figure 1.5(a) is the anatomically coronal T1-weighted MRI displaying adipose (outer) and glandular (inner) tissue types. Figure 1.5 (b) is the reconstructed chromophore and scattering images.

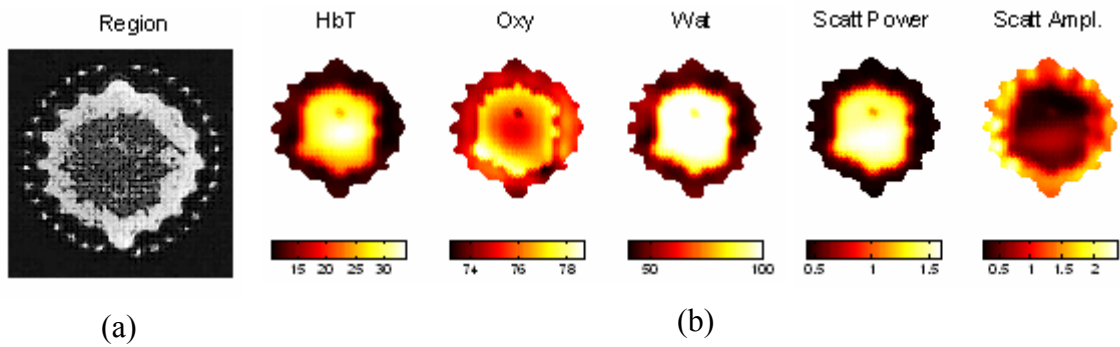


Fig 1.5 One MRI-NIR patient data set is used, with (a) showing the MRI image, and (b) the MRI-guided reconstructions of chromophore and scattering images [51].

1.4 Scatterer size and number density image reconstruction from NIR tomography

In 1.3.D, it was mentioned that the reduced scattering spectrum can be reasonably well characterized by a power law [47, 52]. Parameters associated with this fit are the scattering amplitude (A) and the scattering power (b), which can be obtained by fitting the reduced scattering spectra with the power law. Instead of getting A and b, it would be ideal to get information about the physical traits of the tissue, such as scatterer size and volume density. As a forward problem, it is known that morphological changes in the tissue matrix affect the optical properties and thus the light distribution [53]. The hypothesis being examined here is to solve the inverse problem, to obtain the morphological ultra-structure estimates from the scattered light spectrum.

1.4.A Significance of scatter relative to tissue disease

It is important to clarify what is known, and not known, about how light scatters in tissues, paying attention to the observable changes between normal and diseased tissues. The morphologic changes from normal to diseased breast tissue are seen by light

microscopy in the cellular epithelial components as well as the surrounding support stroma. Generally, the hallmark of an epithelial malignancy is an increase in the overall epithelial cell density with increased nuclear and nucleolar size. In order to facilitate invasion into the surrounding stroma, sub-cellular compositional changes in that matrix structure also occur. Microscopic sub-cellular alterations exist that may not be apparent in standard pathological analysis. Macroscopic scattering of light from tissue is thought to originate from the multiple microscopic fluctuations in refraction index between intracellular organelles and extracellular structures, typically bounded by bi-lipid membranes [19-21]. The origin of the transport scattering coefficient, which can be measured tomographically, is likely to result from these differences in the index of refraction between the extracellular or cytoplasmic fractions of tissue and the lipid composition of the membranes bounding each cell and cellular organelle. Hence, variations in the scattering spectral features, which can be measured tomographically, may encode morphologic and pathophysiologic changes in tissue at the microscopic level. While it is possible to postulate causes of scattering in tissue, it is considerably more difficult to design objective experiments which prove a given hypothesis.

Several studies have demonstrated that light transport in tissue is dominated by elastic scattering. Modeling the light scattering particles as spheres is one of the few tractable ways to proceed in using the scattering information. Much of the scatterer in tissue is thought to be subcellular organelles such as mitochondria, lysosomes, Golgi bodies, vesicles, etc, all of which have sizes in the range of 50-500nm or less [48, 54]. Additionally scattering from well organized cells in culture have been studied extensively with a focus on estimating the scattering from the nucleus. Studies by Wax, Mourant and

Backman have all indicated that scattering from larger structures such as the nucleus could be present, but are a small signal superimposed upon the dominant scattering from smaller particles, which are significantly less than 1 micron in size (Wax et al, 2002; Mourant et al, 2001). While these are almost never spherical, individual photons events with the membranes would clearly interact with a radius of curvature which might be considered spherical at the local level. So although Mie theory applies only for spheres in a homogenous background [47, 55, 56], it has been used successfully in the interpretation of many natural scattering phenomena and is a reasonable first order approximation [57].

1.4.B Previous studies in scatter interpretation

Previous studies of particle size determination from scattering spectra have been focused on mucosal diseases or dilute cell suspensions where the scattering by cell nuclei has been a primary emphasis [54, 58-62] and in general an increased nuclear scatterer size has been found in the diseased tissue. In these studies, subtle oscillations in the reduced scattering spectrum or in the angular scattering distribution were used to estimate nuclear size through fits to Mie theory calculations. In other investigations, more focus has been paid to the scattering of small particles in tissue. However, the extent to which small and large particle size scatterers can be simultaneously fit with sparse data is not yet clear, although with full angular or spectral reflectance, it is evident that reasonable estimation of both can be achieved [44, 63-65]. Mie scattering interpretation serves as a reasonable starting point to analyze elastic transport scattering spectra, and with sparse wavelength data, it appears likely that only information about smaller scattering particles can be effectively estimated.

In all prior attempts to estimate particle size, some assumptions have been made about the histogram of particle sizes in tissue, which then allows the estimation problem to be reduced to only two parameters, namely the mean particle size and number density. For larger particles, like cell nuclei, the histogram shape has been assumed to be Gaussian [27, 58, 64, 66, 67]. However, smaller particles, like mitochondria, golgi bodies, lysosomes etc, have often been assumed to be arranged in a log-normal distribution [54]. There is also a strong rationale for using a simple exponential function for the distribution of smaller particles in tissue, as the density of smaller organelle structures clearly continues to decrease well below our ability to image these structures with optical microscopy. In tissue phantom studies, Intralipid provides a distribution of sizes where the histogram has been determined by electron microscopy to be exponentially distributed [47] with a mean particle size of 97 nanometers.

Although the larger structures, such as cell nuclei, typically 5-15 μ m in diameter can also scatter light, the primary scattering centers are thought to be the collagen fiber network of the extracellular matrix, the mitochondria, and other intracellular substructures, all with dimension smaller than optical wavelengths [14, 58]. Beauvoit et al. [68] used time-resolved spectroscopy to compare the scattering from isolated mitochondria with the isolated hepatocyte and whole liver. The results indicated that the mitochondrial compartment is the primary factor for the light scattering in hepatic tissue, and the light scattering in normal rat tissues and tumors is roughly proportional to the mitochondria content. Dunn et al. [69] used finite-difference time-domain (FDTD) method to calculate the scattering from a combination of organelles within a cell and got the conclusion that at near infrared wavelengths, small organelles play a more important

role than the nucleus in scattering from a cell. The studies here focuses on these smaller particles, and shows a good fit to data when smaller particle estimates are considered the dominant method of interaction, contributing to the scatter spectrum in the near infrared.

1.5 Angular scattering distribution study of breast tissue

Like the scattering spectrum, the angular scattering phase distribution is also related to the scatterer size distribution. There have been several studies devoted to developing a better understanding of the relationship between the angular distribution of the scattering and the size of the scatterer. Pyhtila et al [70] used low-coherence interferometry to get the angular distribution of backscattered light, and determined the size of subsurface epithelial cell nuclei by comparing the data with Mie theory. Drezek et al. [20] used an automated goniometer to measure the scattering properties of dilute cell suspensions, and compared the measurements with FDTD predictions. And their FDTD and experimental results indicated that scattering properties are strongly influenced by cellular biochemical and morphological structure. Mourant et al.[64] took measurements from three separate pairs of suspensions of M1 cells, nuclei and mitochondria, and measurements of isolated organelles indicated that the scattering from the nuclei most closely resembles that from the cells, and the mitochondria and other similarly sized organelles are responsible for scattering at large angles, whereas nuclei are responsible for small-angle scattering. Wilson et al. [71] used angularly resolved light scattering measurements on suspensions of EMT6 cells and on mitochondria isolated from rabbit liver and found an oxidative-stress-induced mitochondrial swelling.

In this thesis, angular resolved scattering light distribution measurements provide a second method for extracting particle size distribution information. This is completed on optically thin tissue sections or dilute suspensions, by comparing experimentally measured phase functions with those calculated by Mie theory. This method could be used to compensate for the smaller size range in particle size estimation, caused by limited wavelengths available in NIR tomography.

1.6 Microscopic study of the breast tissue section

In the final section of this thesis, breast tissue was studied with several types of microscopy: the electron microscope (EM), the phase contrast microscope and finally the optical microscope with H&E stained tissue section. The goal of this work was to have a clearer physical concept of the tissue's morphology and how each type relates to the sub-microscopic morphology which cause scatter, and how this changes from normal to diseased breast tissue. This will help to understand the status of the tissue by estimation of the morphology (the average particle size and number density) information which should correlate with the non-invasive estimation method used on tomography data.

1.6.A Electron microscopy study of breast tissues

Although recently there has been considerable research devoted to particle sizing through comparing the scattering spectra or angular scattering distribution with Mie scattering theory [54, 58, 60-62, 72-76], in order to compare with our estimation result and improve the estimation method, a direct way to quantify the size distribution of particles is needed. The light microscope is limited in resolution to near 0.2 micrometers

due to light diffraction limits. Electron microscopy (EM) has considerably better resolution (0.1nm for TEM, 1nm for SEM), and can be used to see the fine details of the interior structures of organic cells (nucleus, mitochondria...etc.).

Benz et al [77] used TEM to determine the size distribution of intracellular polyethylene particles. Wilson et al. [71] used EM on suspensions of EMT6 cells and on mitochondria isolated from rabbit liver to analyze the particle size information for comparison with the estimates from angularly resolved light scattering measurements. Van Staveren et al [47] used EM to quantify the size distribution of Intralipid, a well known and well characterized scattering solution of emulsified lipids in water. Van Staveren showed that the particle size distribution is an exponentially decaying function, with larger numbers of small particle sizes and significantly fewer at large sizes.

In the inverse problem, it is possible to compare the estimated scatterer size distribution with the result obtained from EM; in the forward problem, the scattering spectra was used with the size distribution from EM, and compared with the results from NIR tomography.

1.6.B Phase contrast microscopic study of breast tissues

While EM images can provide basic morphology information about tissue, but it is still unknown which kind of tissue in the breast has the most dominant contribution to overall observed scattering, which includes the biochemical properties of breast tissue, such as refractive index. However, the phase contrast and H&E staining microscopic study of breast tissue sections can provide this information on a more microscopic to mesoscopic scale.

The phase contrast microscope is a vital instrument in biological and medical research. When dealing with transparent and colorless components in a cell, histology stains are an alternative but at the same time the fixation process significantly alters the chemical processes in it. Phase contrast enhances visibility of transparent and colorless objects by using two distinct paths through the microscope out of phase, thereby allowing interference when there are adjacent changes in index of refraction in the sample. In the phase contrast microscopy images, the brightness in the image depends on the scattering intensity of the object. So it can provide relative information about the relative scattering intensity on the tissue section.

H & E staining is the most common staining to show cellular components. Hematoxylin, as a basic dye, has an affinity for the nucleic acids of the cell nucleus and stains the nucleus in blue; while eosin is an acidic dye with an affinity for intracellular or extracellular materials and stains them in pink. Areas of malignancy with high epithelial content are often strongly blue or purple stained, such that the H&E stained image is routinely used to determine the tissue type by pathologist assessment. So if both phase contrast and H&E stained images are used from the same section, the relative scattering values can be categorized for each tissue type. This information is essential to correlate which tissue types lead to which scattering properties in breast tissue.

Chapter2. Mie Scattering Theory Interpretation

2.1 Introduction

Scattering can be one of the most important optical properties of an object when the particle is similar to or smaller than the wavelength of the interacting radiation. Light is an electromagnetic wave which can be scattered, and this phenomena can be explained using formal electromagnetic wave theory and solved using Maxwell equations.

If an object is illuminated by an incident electromagnetic wave $((E_i, H_i)$ in Figure 1), under the force of the incoming electric and magnetic fields, the bound discrete electric charges (electrons (e) and protons (p)) that compose this object are set into oscillation [55, 56]. Accelerated electric charges (e and p in Figure 2.1) can radiate electromagnetic energy $((E_s, H_s)$ in Figure 2.1) in all directions dependent upon the incident wave and the geometry and dielectric properties of the particle. This secondary radiation is the scattered wave, which has a vector field dominated by the properties of the object.

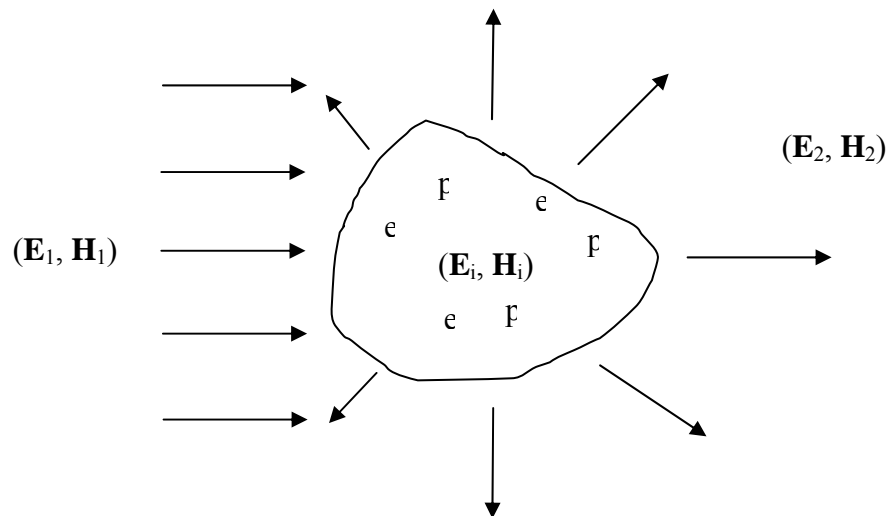


Figure 2.1. The incident field $(\mathbf{E}_1, \mathbf{H}_1)$ gives rise to a field $(\mathbf{E}_i, \mathbf{H}_i)$ inside the particle and scattered field $(\mathbf{E}_2, \mathbf{H}_2)$ in the medium surrounding the particle.

Our interest in studying scattering stems from two kinds of problems. First is the direct problem, in which the distribution of scattered radiation is determined based on the characteristics of the scatterer. The second is the inverse problem, in which the characteristics of an object (its shape, size, etc.) are determined from the measured scattering data. Usually several different types of scattering centers may give rise to the same pattern of scattered radiation, so the solution to the inverse problem is not unique. Some pre-assumptions are needed in the inverse problem, in order to get specific characteristics of the scatterers uniquely. In this thesis, light scattering techniques were used to determine the size of the scatterers in the breast tissue by assuming the shape and composition of the scatterers first.

The scattering system could be a single particle or a collection of particles in a system. The fundamental problem is to quantitatively model the scattering by a single particle. In this chapter, Maxwell's equations are used to solve for the scattering by a single particle with arbitrary shape function, and then this general solution is used to further derive the exact analytical solution for scattering by a single spherical particle. However, macroscopic scattering samples always consist of many particles, so at the end of this chapter, the scattering from a collection of many particles is also discussed, which turns out to be a simple summation of the solution for a single particle.

In this study the treatment is restricted to elastic scattering, in which the frequency of the scattered light is the same as that of the incident light. Major theoretical approaches to describing elastic light scattering are Rayleigh scattering and Mie scattering. In order for Rayleigh's model to apply, the scatterer must be much smaller than the wavelength (λ) of the scattered wave, in which the shape of the scatterer does not matter; while Mie

theory is applied to spherical particles with size comparable to the wavelength (λ) of the scattered wave, and it reduces to Rayleigh approximation when the scatterer is much smaller than the wavelength (λ) of the scattered. The inelastic scattering effects include Brillouin scattering, Raman scattering, and Compton scattering, in which the frequency of the scattered light is different from that of the incident light.

2.2 Scattering in Electromagnetic field

Scattering of the electromagnetic field can be solved with Maxwell equations, following the derivation outlined most comprehensively by Bohren and Huffman [56]. The approach assumes the incident wave is plane harmonic wave, which is not a significant restriction because an arbitrary field can be decomposed to its spatial Fourier component plane waves.

As shown in Figure 2.1, using $(\mathbf{E}_i, \mathbf{H}_i)$ for the field inside the particle, while $(\mathbf{E}_o, \mathbf{H}_o)$ is used for the field outside the particle, then they are related by the following expression:

$$\vec{E}_o = \vec{E}_1 + \vec{E}_2, \vec{H}_o = \vec{H}_1 + \vec{H}_2$$

The time harmonic scattering field in elastic scattering can be obtained by solving Maxwell's equations (2.1-2.4) with boundary conditions in Equations (2.5-2.6) [56]:

$$\nabla \cdot \vec{E} = 0 \quad (2.1)$$

$$\nabla \cdot \vec{H} = 0 \quad (2.2)$$

$$\nabla \times \vec{E} = i\omega\mu\vec{H} \quad (2.3)$$

$$\nabla \times \vec{H} = -i\omega\epsilon \vec{E} \quad (2.4)$$

$$(\vec{E}_o - \vec{E}_i) \times \vec{n} = 0 \quad (2.5)$$

$$(\vec{H}_o - \vec{H}_i) \times \vec{n} = 0 \quad (2.6)$$

where \mathbf{n} is the outward directed normal to the surface of the particle.

Equations (2.1-2.4) can be combined to obtain \mathbf{E} and \mathbf{H} to satisfy the vector wave equation:

$$\begin{aligned} \nabla^2 \vec{E} + k^2 \vec{E} &= 0, \nabla^2 \vec{H} + k^2 \vec{H} = 0 \\ k^2 &= \omega^2 \mu\epsilon \end{aligned}$$

Constructing a general vector function, which is simply defined as the curl of a scalar times a unit vector, $\vec{M} = \nabla \times (\vec{r}\psi)$. This field then satisfies $\nabla \cdot \vec{M} = 0$ by definition, and it also satisfies the vector wave equation $\nabla^2 \vec{M} + k^2 \vec{M} = 0$ if ψ is then also a solution to the scalar wave function equation (2.7):

$$\nabla^2 \psi + k^2 \psi = 0 \quad (2.7)$$

Another vector function $\vec{N} = \frac{\nabla \times \vec{M}}{k}$ also satisfies $\nabla^2 \vec{N} + k^2 \vec{N} = 0$. So solving equation (2.7) is what is needed to obtain a solution for the scattered field.

The most important exact solution to the problem of scattering by a small particle is that for a sphere of an arbitrary radius and refractive index, which is called Mie scattering theory. When modeling scattering where the scattering center is an irregularly shaped particle, there are numerical methods that must be used along with a numerical

model of the shape of the particle [20]. The most common approach used in this situation is finite-difference time-domain (FDTD) method [69].

2.3 Mie Theory - Scattering from a Sphere

Mie theory is a complete analytical solution of Maxwell equations for the scattering of electromagnetic radiation by spherical particles (also called Mie scattering). It assumes a homogeneous, isotropic and optically linear material irradiated by an infinitely extending plane wave.

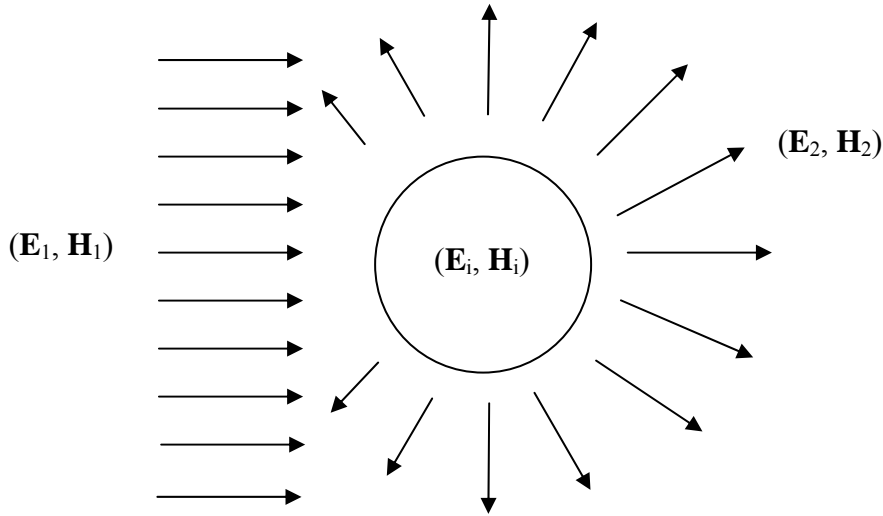


Figure 2.2. The incident field $(\mathbf{E}_1, \mathbf{H}_1)$ gives rise to a field $(\mathbf{E}_i, \mathbf{H}_i)$ inside the particle, and scattered field $(\mathbf{E}_2, \mathbf{H}_2)$ in the medium surrounding the particle.

If the scattering particle is spherical, the exact solution of ψ could be obtained by solving equation (2.7) in spherical polar coordinates [56],

$$\psi_{emn} = \cos m\phi P_n^m(\cos\theta) z_n(kr)$$

$$\psi_{omn} = \sin m\phi P_n^m(\cos\theta) z_n(kr)$$

$$\text{So, } \vec{M}_{emn} = \nabla \times (\vec{r}\psi_{emn}), \quad \vec{M}_{omn} = \nabla \times (\vec{r}\psi_{omn}),$$

$$\vec{N}_{emn} = \frac{\nabla \times \vec{M}_{emn}}{k}, \quad \vec{N}_{omn} = \frac{\nabla \times \vec{M}_{omn}}{k},$$

Then the electric fields can be expanded in these vector spherical harmonics as,

$$\vec{E}_1 = E_0 \sum_{n=1}^{\infty} i^n \frac{2n+1}{n(n+1)} (\vec{M}_{o1n}^{(1)} - i\vec{N}_{e1n}^{(1)})$$

$$\vec{E}_i = \sum_{n=1}^{\infty} E_n (c_n \vec{M}_{o1n}^{(1)} - id_n \vec{N}_{e1n}^{(1)})$$

$$\vec{E}_2 = \sum_{n=1}^{\infty} E_n (ia_n \vec{M}_{o1n}^{(3)} - b_n \vec{N}_{e1n}^{(3)})$$

Similar treatment is required in the magnetic fields. The coefficients a_n and b_n could be obtained using the boundary conditions (2.5-2.6), and after considerable algebra the following values for the coefficients can be obtained,

$$a_n = \frac{m\psi_n(mx)\psi'_n(x) - \psi_n(x)\psi'_n(mx)}{m\psi_n(mx)\xi'_n(x) - \xi_n(x)\psi'_n(mx)}$$

$$b_n = \frac{\psi_n(mx)\psi'_n(x) - m\psi_n(x)\psi'_n(mx)}{\psi_n(mx)\xi'_n(x) - m\xi_n(x)\psi'_n(mx)}$$

At last the scattering cross section can be obtained as

$$C_{sca} = \frac{W_s}{I_i} = \frac{2\pi}{k^2} \sum_{n=1}^{\infty} E_n (2n+1) (|a_n|^2 + |b_n|^2) \quad (2.8)$$

$$W_s = \int_A \vec{S}_s \cdot \vec{ndA} = \int_A (\vec{E}_2 + \vec{H}_2) \cdot \vec{ndA}$$

Where I_i is the incident irradiance, W_s is the rate at which energy is scattered across the surface of the scattering particle, \mathbf{S}_s is the Poynting vector associated with the scattering wave.

Almost all scattering systems consist of an ensemble of many particles. If the number of particles are sufficiently small and their separation is sufficiently large, then in the neighborhood of any particle the total field scattered by all the other particles is small compared with the external field. With this assumption (of single scattering in the near field) the total scattered field is simply the sum of the fields scattered by the individual particles, each of which is acted on only by the external field in isolation from the other particles. Additionally, if the separations of the particles are random, which implies incoherent scattering, then there is no systematic relation among the phases of the waves scattered by the particles, and so the scattering by the system is just the sum of the irradiances scattered by the individual particles [56]. This kind of scattering by a system is called independent incoherent scattering, and in Mie theory, the independent scattering assumption is the central hypothesis used to allow application of it to real situations.

Mie theory provides an exact solution for the scattering and the anisotropy coefficients of perfect dielectric spheres of arbitrary size in a uniform background medium [47, 55, 56]. In Mie theory, the reduced scattering spectra of bulk homogeneous samples can be approximately expressed as:

$$\mu_s'(a, \lambda) = N C_{sca}(m, a, \lambda) [1 - g(m, a, \lambda)] \quad (2.9)$$

$$g = \langle \cos(\theta) \rangle = \int_{4\pi} P(\theta) \cos(\theta) d\Omega \quad (2.10)$$

$$P(\theta) = \frac{1}{C_{sca}} \frac{dC_{sca}}{d\Omega} \quad (2.11)$$

where λ is the wavelength, a is the particle size (the radius of the particle), N is the number density, m is the refractive index ratio from inside to outside the particles ($m=n_2/n_1$, where n_1 and n_2 are the refractive index outside and inside the particles respectively), $g(m,a,\lambda)$ is the anisotropy coefficient from one particle with size a , $C_{scat}(m,a,\lambda)$ is the total scattering cross section [56], $P(\theta)$ is the scattering phase function. This expression is used to estimate the refraction and reflection from a spherical particle. The framework can be extended to approximate a multi-sized scattering particle medium by summing the scattering contributions over all particle sizes and adding an approximate normalized size distribution factor, $f(a)$, which describes the histogram of particle number density per unit particle size, to compensate for the number of particles at each given size.

$$\mu_s'(\lambda) = \sum_{i=1}^p N f(a_i) \mu_s'(a_i, \lambda)$$

$$\sum_i f(a_i) = 1$$

So, in a multi-sized medium, the reduced scattering spectra can be approximately expressed as the summation weighted by the distribution factor:

$$\mu_s'(\lambda) = N \sum_{i=1}^p f(a_i) C_{sca}(m, a_i, \lambda) [1 - g(m, a_i, \lambda)] \quad (2.12)$$

The average scatterer size could be expressed as:

$$\langle a \rangle = \sum_i a_i f(a_i) \quad (2.13)$$

Equation (2.12) has implicit assumptions that the particle index changes are all the same, which is a limitation that should be recalled when it is applied in various problems. However, it is possible that m only influences the amplitude of μ_s' , rather than the shape of the spectral in the NIR regime. Thus, while the assumption of constant m is unfortunate, it still does allow an estimation of the particle size, given some a priori information about the $f(a_i)$ function.

In equation (2.12), the particle number density only influences the amplitude of the scattering coefficients, but not the shape of the scattering spectra in the NIR range. So there are only two parameters to determine the shape of the scattering spectra including:

- (i) distribution function, and
- (ii) relative refractive index, m .

The distribution function could be separated as two parts:

- (i) histogram shape $f(a_i)$, and
- (ii) average particle size.

So we only need to consider the three parameters, including:

- (i) histogram shape $f(a_i)$, and
- (ii) average scatterer size, $\langle a \rangle$, and
- (iii) relative refractive index, m .

when evaluating the shape of the scattering spectra. By setting two of the parameters to be the same, we can observe the influence of the third parameter on the scattering spectra. These relationships are examined in detail with theoretical and experimental studies in the next chapter.

If the type of the distribution function and relative refractive index can be set by some known information, then there are only two parameters left to estimate in equation (2.12): average scatterer size and number density [22], which are called the effective scatterer size and number density.

Strictly speaking, Mie theory can only be applied to optical scattering from spherical particles, but it does provide a first-order approximation for the scattering from a particle of arbitrary shape with size that comparable to the wavelength of the incident electromagnetic wave. Beside, when the size of the scattering particle is pretty small compared with the wavelength of the incident electromagnetic wave, Mie theory does give a good description for the scattering effects since in this case the shape of the scattering particle is not so much important as its size is much smaller than the wavelength of the incident electromagnetic wave.

2.4 Scattering Phase Function

The phase function specifies the angular distribution of the scattered light. It is defined as the differential scattering cross section divided by the total scattering cross section, as shown in equation (2.11).

In a multi-sized medium, the phase function (the volume-averaged angular-scattering function) of the tissue slice is the sum of the angular-scattering functions of the individual particles weighted by their respective scattering coefficients. In Mie theory, at a given wavelength, the phase function for a multi-sized distribution of particles in a medium is expressed as the following equation.

$$P(\theta) = \frac{\sum_i f(a_i) \mu_s(a_i) P_i(\theta)}{\sum_i f(a_i) \mu_s(a_i)} \quad (2.13)$$

Where $\mu_s(a_i)$ and $P_i(\theta)$ is the scattering coefficient and scattering phase function for a sphere with radius a_i .

From equation (2.13) we can see there are two parameters to determine the phase function: the shape of the size distribution function, and the average particle size. If we make some assumption about the shape of the size distribution function, then there is only the average particle size left for estimation. Once we get the angularly resolved scattering data for the experiment, we can get the average particle size information by comparing it with the Mie theory model.

2.5 Scattering Spectra Power Law Fit

As stated in 1.3.D, Rather than applying Mie scattering theory directly, a more empirical approach (equation 1.7) was first proposed by van Staveren et al [47], who fit the scattering spectrum of Intralipid.

2.6 Dependent Scattering

As discussed above, in Mie theory the independent scattering assumption is made, in which the scattering properties of the isolated particles are used, while the effects of the closely neighbored particles are neglected. Actually the interaction of light with particles is composed of multiple internal reflections and redirections of the incident light. The relative position of these particles should be taken into account for the redirections of incident light. Scattering is termed dependent if the scattering

characteristics of the participating particles depend on the separation of these particles between each other [78].

Effects from dependent scattering were first mentioned by Tinsley and Bowman [79] in 1949. In 1971 Hottel et al [80] empirically found a correlation between the change in scattering efficiency Q_s^{dep}/Q_s^{ind} and interparticle clearance l in units of the radiation wavelength λ for monodisperse, non-absorbing polystyrene spheres suspended in water:

$$\log_{10} \log_{10} \left(\frac{Q_s^{dep}}{Q_s^{ind}} \right) = 0.25 - 5.1 \frac{l}{\lambda} \quad (2.15)$$

Commonly, the larger the distance between particles, the less the dependent scattering.

Chapter 3: Approximation of Mie scattering parameters (Effective scatterer size and number density) in near-infrared tomography

A method for estimating Mie theory scattering parameters from diffuse light tomography measurements in breast tissue is discussed in this chapter. This approach provides an estimate of the effective scatterer size and number density given assumptions about the index of refraction change expected in lipid membrane-bound scatterers. When using a sparse number of wavelengths in the reduced scattering spectra, the parameter extraction technique is limited to representing a continuous distribution of scatterer sizes that appears to be dominated by an exponential decrease with increasing particle size. This fitting method was tested on simulated data and then on Intralipid-based tissue-phantom data giving an effective particle size of $93 \pm 17 \text{ nm}$ which is in excellent agreement with expectations. It was also applied retrospectively to breast tissue spectra acquired from normal healthy volunteers where the effective particle size and number density were found to be in the range of 20 to 1400nm. Grouping of the data based upon radiographic breast density, as a surrogate measure of tissue composition yielded values of 20-65nm, 25-200nm, 140-1200nm and 150-1400nm, respectively, for the four BI-RADS density classifications of extremely dense, heterogeneously dense, scattered and fatty. These results are consistent with the microscopic characteristics of each breast type given the expected progression from predominantly collagenous connective tissue (extremely dense category) to increasing proportions of glandular epithelium and fat (intermediate density categories) to predominantly fat (fatty category).

3.1 Introduction

Relationship between the optical and biological properties of tissue is necessary for the optical techniques in tissue diagnostics. Currently great interest exists in exploiting the scattering spectrum of tissue to characterize its microscopic properties which may provide fundamental insight into the morphological features that are observed in the macroscopic diffuse light signal [54, 58-62, 81]. There have been important advances in particle sizing through Mie scattering theory [54, 58, 60-62, 72-76]. This is the inverse problem, in which the characteristics of the scatterer (its shape, size, etc.) are determined from the measured scattering data. In this chapter, a method is presented to analyze bulk tissue reduced scattering spectra in terms of their approximate Mie scatterer parameters.

As stated in chapter 2, several different types of scattering centers may give rise to the same pattern of scattered radiation, so the solution to the inverse problem is usually not unique. Some pre-assumptions are needed to make in the inverse problem in order to get some specific characteristics of the scatterers, hopefully uniquely. The purpose of this thesis is to determine the effective size and number density of the scatterers in breast tissue using light scattering techniques.

One of the goals of NIR tomography research has been to provide clinicians with new information about the underlying properties of benign and malignant breast disease [5, 26, 40, 41, 82]. However, there is emerging data indicating that NIR scattering spectra are correlated to the normal composition of breast tissue, and that changes in breast physiology can be detected by variations in scattering spectra [49, 83]. In mammography, there are four classifications of breast density which are designated in the BI-RADS

(American College of Radiology Breast Imaging Reporting and Data System) lexicon: almost entirely fat (fatty), scattered fibroglandular (scattered), heterogeneously dense (HD), and extremely dense (ED) [84]. In the work proposed here, these classifications are used as a basis for categorizing normal breast tissues into groups, where prior results have indicated a good correlation between scattering and the increase in radiographic density category when a group of women with mammographically normal breast were imaged [18].

In this chapter, a method for extracting the effective particle size and number density from the reduced scattering coefficient spectrum is proposed. The scattering spectrum is sampled at 6 wavelengths (661, 761, 785, 808, 826 and 849nm) measured for transmission through normal breast tissue using a clinical breast tomography system. The assumptions and limitations of the fitting process are discussed to put the study in perspective with prior work, and the method utilized is analyzed through simulated and tissue-phantom data to establish its accuracy.

3.2. Methods

3.2.A. Mie Theory Interpretation

As stated in chapter 2, Mie theory provides an exact solution for the scattering and the anisotropy coefficients of perfect dielectric spheres of arbitrary size in a uniform background medium [47, 55, 56]. Using this theoretical framework, the reduced scattering spectra of multi-sized scattering particle medium can be approximately expressed as equation (2.12).

$$\mu_s'(\lambda) = N_o \sum_{i=1}^p f(a_i)(\pi a_i^2) Q_{scat}(m, a_i, \lambda)[1 - g(m, a_i, \lambda)] \quad (2.12)$$

where λ is the wavelength, a is the particle size (the diameter of the particle), m is the refractive index ratio from inside to outside the particles ($m=n_2/n_1$, where n_1 and n_2 are the refractive index outside and inside the particles respectively) and $Q_{\text{scat}}(m,a,\lambda)$ is a dimensionless scattering efficiency factor that is calculated from an analytic series expansion which is the solution to the scattered wave intensity from the sphere [56]. The normalized size distribution factor $f(a)$ compensates for the number of particles at each given size. This expression is used to estimate the refraction and reflection from a spherical particle.

Equation (2.12) has implicit assumptions that the particle index changes are all the same, which is a limitation that should be recalled when it is applied in various problems. However, it is possible that index changes typically result only in changes of amplitude in μ_s' , rather than changes in the spectral features in the NIR regime. Thus, while the assumption of constant n is unfortunate, it still does allow an estimation of the particle size, given some a priori information about the $f(a_i)$ function, which describes the histogram of particle number density per unit particle size.

And as discussed in Chapter 2, if the type of the distribution function and relative refractive index can be set by some known information, then there are only two parameters left to estimate in equation (2.12): average scatterer size and number density [22, 23], which are called the effective scatterer size and number density.

Since the reduced scattering spectra $\mu_s'(\lambda)$ depends on the histogram of particle number density per unit particle size $f(a_i)$, it is important to carefully analyze how these particular functions might impact the results of the study. Three histogram shapes have been examined, including 1) a step function, 2) a normalized Gaussian function and 3) an

exponentially decaying function. Each is used with the same average particle size and same total number density to determine differences in μ_s' , caused by different histogram shape assumptions.

3.2.B. Scattering Spectra Power Law Fit

As stated in chapter 1.3.D, rather than applying Mie scattering theory directly, the empirical power law (equation (1.7)) proposed by van Staveren et al [47], was used.

3.2.C. Scattering from Tissue Spectra

Reduced scattering coefficients at 6 wavelengths have been obtained with an experimental clinical imaging system (described in detail elsewhere [85]). The limited number of wavelengths is not sufficient for identifying oscillations in the scattering spectra of the type that might be observed from larger Mie scattering particles, as observed in Figure 3.1 (d) for the 10 micron sized particles. Nonetheless, if it is assumed that the dominant particle sizes are smaller and thus the large particle oscillations are small, the data may be used to compare with Mie theory calculations in the wavelength range 660nm-850nm. To estimate particle size and number density, the 6 experimental reduced scattering coefficients are fit to predictions of the power law expression in Eq.(1.7), first to get the scattering amplitude and scattering power, and then to generate the reduced scattering coefficients at 15 wavelengths (650, 675, 700, 725, 750, 775, 800, 825, 850, 875, 900, 925, 950, 975 and 1000nm). To extract the effective particle size, we normalized these 15 reduced scattering coefficients at one wavelength (800nm was used). By normalizing the scattering coefficients, the influence of number density was

eliminated, so there is only one parameter (effective particle size) needed in the first fitting. Comparing these 15 data with Mie theory results from equation (2.12) (also normalized at 800nm) using a least-squares minimization, the effective particle size can be effectively estimated. With the effective particle size established, the number density can then be estimated by comparing the original 15 data (no normalization) with Mie theory (equation (2.12)) using a second least-squares minimization method. In the least-squares minimization method, the deviation of the experimental data from the Mie prediction is expressed as the error function:

$$\chi = \left(\frac{1}{n} \sum_{i=1}^n ((\mu_s^i \text{exp} - \mu_s^i \text{o}) / \mu_s^i \text{o})^2 \right)^{\frac{1}{2}} \quad (3.1)$$

where χ is the error norm, calculated as the squares difference between the experimental data and the Mie theory. Here, n is the total number of wavelengths at which we have the reduced scattering coefficient data, $\mu_s^i \text{exp}$ is the experimental reduced scattering coefficient at the i th wavelength, $\mu_s^i \text{o}$ is the reduced scattering coefficient at the i th wavelength calculated from Mie theory. In this study, no attempt was made to perform non-linear fit, but rather a complete search was done through all parameter values, and the minimum value of χ was used to determine the best estimate.

3.2.D. Image Reconstruction of Absorption and Scattering Coefficients

Reduced scattering spectra was obtained with the clinical imaging system at Dartmouth [85]. Briefly, the system measures diffusely transmitted amplitude and phase shift at 100 MHz through up to 12 cm of tissue, and is designed for breast imaging for characterization of tumors non-invasively. The measurements are taken at six wavelengths (661, 761, 785, 808, 826 and 849 nm) and the data is calibrated by a

homogeneous phantom, and then fit to a finite element diffusion theory prediction of the data. The finite element model is iteratively fit to the measurements through a Newton minimization method, and images of absorption and reduced scattering coefficient are recovered at all wavelengths. In recent years, a direct reconstruction approach has been implemented which uses the known spectrum of the absorbing species in the tissue (hemoglobin, oxyhemoglobin, water) and the assumed model of scattering shown in equation (1.7). This inversion algorithm is described in detail in previous papers and is believed to provide more accurate prediction of the scattering parameters A and b from equation (1.7) [86].

3.2.E. Simulation Studies

Intralipid is a fat emulsion that is used clinically as an intravenously administered nutrient and provides a convenient scattering component in a tissue phantom to investigate propagation of light in tissue [47]. For Intralipid, there is considerable evidence to suggest its particle distribution is exponential, especially considering the dominant fraction of Rayleigh scattered light which occurs in the blue region of the spectrum [87]. In the van Stanveren paper [47], the size distribution of the scattering particles in Intralipid-10% was determined by transmission electron microscopy to be exponential and the effective particle size was reported to be 97(±3)nm. If the functional form of $f(a_i)$ is a normalized exponential function with respect to a_i :

$$f(a_i) = \frac{e^{-a_i / \langle a \rangle}}{\langle a \rangle} \quad (3.2)$$

then the effective particle size $\langle a \rangle$ can be estimated by an iterative fit between the data and this model.

To validate the method, simulated data was used to test the fitting process. The effective particle size in the simulation study was selected in the smaller size range (<1000nm), which is the size range of collagen fiber networks in the extracellular matrix, mitochondria, and other intracellular vesicles [88], but not include the larger size, such as that of cell nuclei, typically 5-15 μ m in diameter. The first 5 groups of simulated data included the following effective size and number densities: 1) $\langle a \rangle = 50\text{nm}$, $N = 1 \times 10^{19} \text{m}^{-3}$; 2) $\langle a \rangle = 100\text{nm}$, $N = 1 \times 10^{19} \text{m}^{-3}$; 3) $\langle a \rangle = 200\text{nm}$, $N = 1 \times 10^{19} \text{m}^{-3}$; 4) $\langle a \rangle = 500\text{nm}$, $N = 1 \times 10^{19} \text{m}^{-3}$; 5) $\langle a \rangle = 1000\text{nm}$, $N = 1 \times 10^{19} \text{m}^{-3}$. These data were generated computationally using the expression in Eq. (2.12) for the 6 wavelengths that are available in our tomography system. These data were used as synthetic scattering spectra in order to determine how accurately the fitting process can be completed.

3.2.F. Phantom Studies

The tomography system was used to validate the particle size fitting approach with data from tissue-simulating phantoms. Liquid phantoms were used, composed of Intralipid at 11 different concentrations, to obtain a reduced scattering coefficient spectrum at 6 wavelengths. The data at each concentration was analyzed with the method described above for estimating the effective particle size and number density. By varying the concentration, each spectrum should result in the same particle size (97(\pm 3)nm according to van Staveren's paper [47]) as only the number density in the liquid is altered when the concentration varies. Thus the ratio of number density over concentration should be constant for these test solutions.

3.2.G. Clinical Studies

In a final step the fitting method was applied to normal breast tissue data. The study was approved by the institutional committee for the protection of human subjects. Near-infrared imaging studies were performed on asymptomatic women recruited into the study following a negative mammogram. Informed consent was provided prior to the NIR imaging exam. Normal subjects were stratified by age (i.e. 10 year intervals) and by one of four radiographic density categories (fatty, scattered, heterogeneously dense, and extremely dense). Data from 31 normal subjects were used; right and left breasts were analyzed separately. Scattering coefficient spectra at the six wavelengths were estimated for the entire slice tissue, and these were fit with the algorithm. Effective particle size and number density were determined from the spectra, and the resulting data were grouped according to the radiographic density of the subjects.

3.3 Results

3.3.A. Influence of Particle Size Distribution

The influence of parameter selections on the resulting reduced scattering spectra is shown for a specific case in Figure 3.1, where the effects of 1) size distribution function, 2) effective particle size and 3) index of refraction change are illustrated. Figure 3.1(a) indicates the relative shape of the three distribution functions (i.e. histogram shapes) considered, a Gaussian function ($f(a) = e^{\frac{-(a-1000)^2}{2 \times 10^2}} / 25$), a step function (if $0 < a < 2000$, $f(a) = 1/2000$; otherwise, $f(a) = 0$) and an exponential decreasing function ($f(a) = 9.5 \times 10^{-4} e^{-9.5 \times 10^{-4} a}$). They are normalized and have the same effective particle size ($\langle a \rangle = 1000 \text{nm}$). For the Gaussian distribution with a small variance, most particles

are clustered around 1000nm. For the step function, the particles are distributed evenly between zero to 2000nm, for the exponential function, more particles exist in the smaller size range. A comparison of scattering spectra among these three different histogram shapes with the same effective particle size and same refractive index $n_1=1.311$, $n_2=1.451$ is shown in Figure 3.1(b). In this graph, the exponential distribution has the largest scattering coefficient while the Gaussian distribution has the smallest one. Based on this result and the distribution characteristics of these three functions it is evident that the particles with smaller size have more impact upon the magnitude of the scattering spectrum in the wavelength range 650-1000nm. This figure also shows the characteristic oscillatory components in the scattering spectrum associated with the Gaussian distribution that have been observed in other epithelial studies of elastic scattering.

The comparison of reduced scattering coefficients among three different sets of refractive indexes is shown in Fig.3.1(c). These results were calculated with the same exponential size distribution, and effective particle size, but with refractive index values of $n_1=1.33$, $n_2=1.45$ ($m=1.09$); $n_1=1.33$, $n_2=1.40$ ($m=1.05$) and the smallest set $n_1=1.33$, $n_2=1.35$ ($m=1.02$). The figure indicates that as the difference between two refractive indexes increases, the scattering intensity increases. The scattering spectra have also been normalized at 800nm (inset graph in Fig.3.1(c)) in order to observe whether differences in spectral shape are caused by changes in relative refractive index $m = n_2/n_1$. It is clear that in the spectral shape changes are nominal; hence, the assumption in equation (2.12) that refractive indexes are same for all particle sizes appears reasonable.

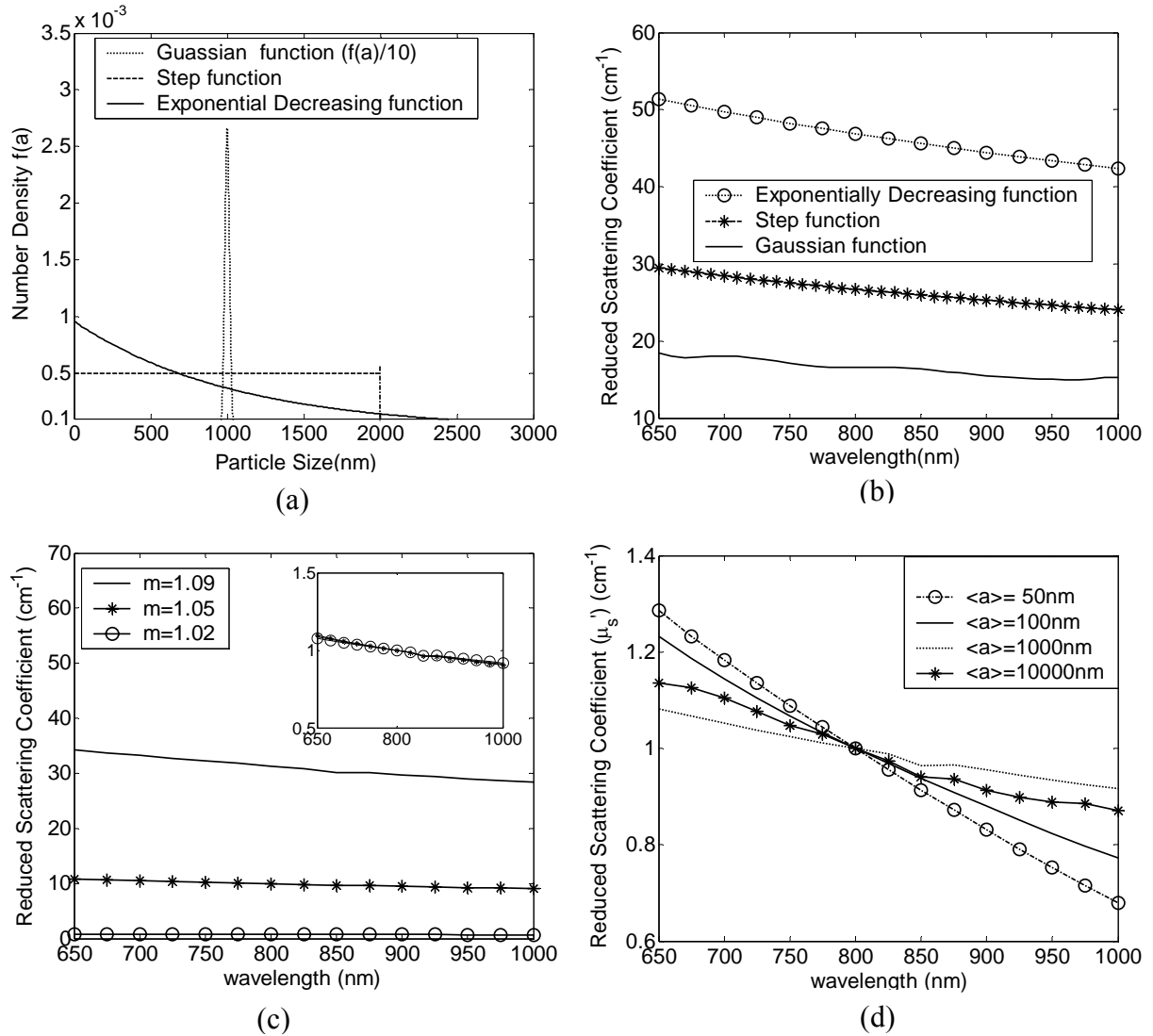


Figure 3.1. (a) Comparison of Gaussian, uniform and exponential particle size distributions with the same effective particle size $\langle a \rangle = 1000\text{nm}$. (b) Calculated reduced scattering spectra for these three particle size distributions with the same refractive index change ($n_1 = 1.311$ and $n_2 = 1.451$). (c) Comparison of reduced scattering spectra for three different refractive indexes for the same size distribution with effective particle size $\langle a \rangle = 1000\text{nm}$. Inset plot is the comparison of these three spectra after normalized at 800nm. (d) Comparison of reduced scattering spectra for four different effective particle sizes with the same exponential size distribution and refractive index ($n_1 = 1.36$, $n_2 = 1.4$).

The reduced scattering coefficients obtained from four different effective particle sizes, $\langle a \rangle = 50, 100, 1000$ and $10,000$ nm for the exponential particle size distribution and same refractive indexes ($n_1 = 1.36, n_2 = 1.40$) are presented in Figure 3.1(d). The scattering spectra were normalized at 800nm in order to investigate potential shape changes caused by the effective particle size. Here, increasing the effective particle size in the range of 50-1000nm generates a reduced scattering coefficient spectrum that has a smaller overall slope but more oscillatory components. This result is consistent with the prior findings of Mourant et al. [48]. By normalizing the scattering spectra at one wavelength and then comparing it to Mie theory we are able to extract the effective particle size by least-square minimization [70].

3.3.B. Simulation Results of the Optimal Estimated Values for Particle Size and number Density

The least-square minimization method described in equation (3.1) was used to estimate the optimal values for particle size and number density. For simulated test data with a true effective particle size of $\langle a \rangle = 100$ nm and $N = 1 \times 10^{19} \text{ m}^{-3}$, the estimated particle size and number density were 110nm and $0.75 \times 10^{19} \text{ m}^{-3}$. These results are shown in Figures 3.2, which indicates that a unique fitted solution is available through the optimization process. The estimates of effective particle size for simulated data with true values of effective particle sizes of $\langle a \rangle = 50, 100, 200, 500$ and 1000 nm, and number densities of $N = 1 \times 10^{19} \text{ m}^{-3}$, were 80, 110, 150, 550 and 1100nm, respectively, for effective size and $2 \times 10^{18}, 7.5 \times 10^{18}, 2 \times 10^{19}, 8 \times 10^{18}$ and $8 \times 10^{18} \text{ m}^{-3}$, respectively, for

number density. The results are also shown in graphical form in Figure 3.2 and indicate that the extraction method is reasonably robust and accurate when fitting simulated data.

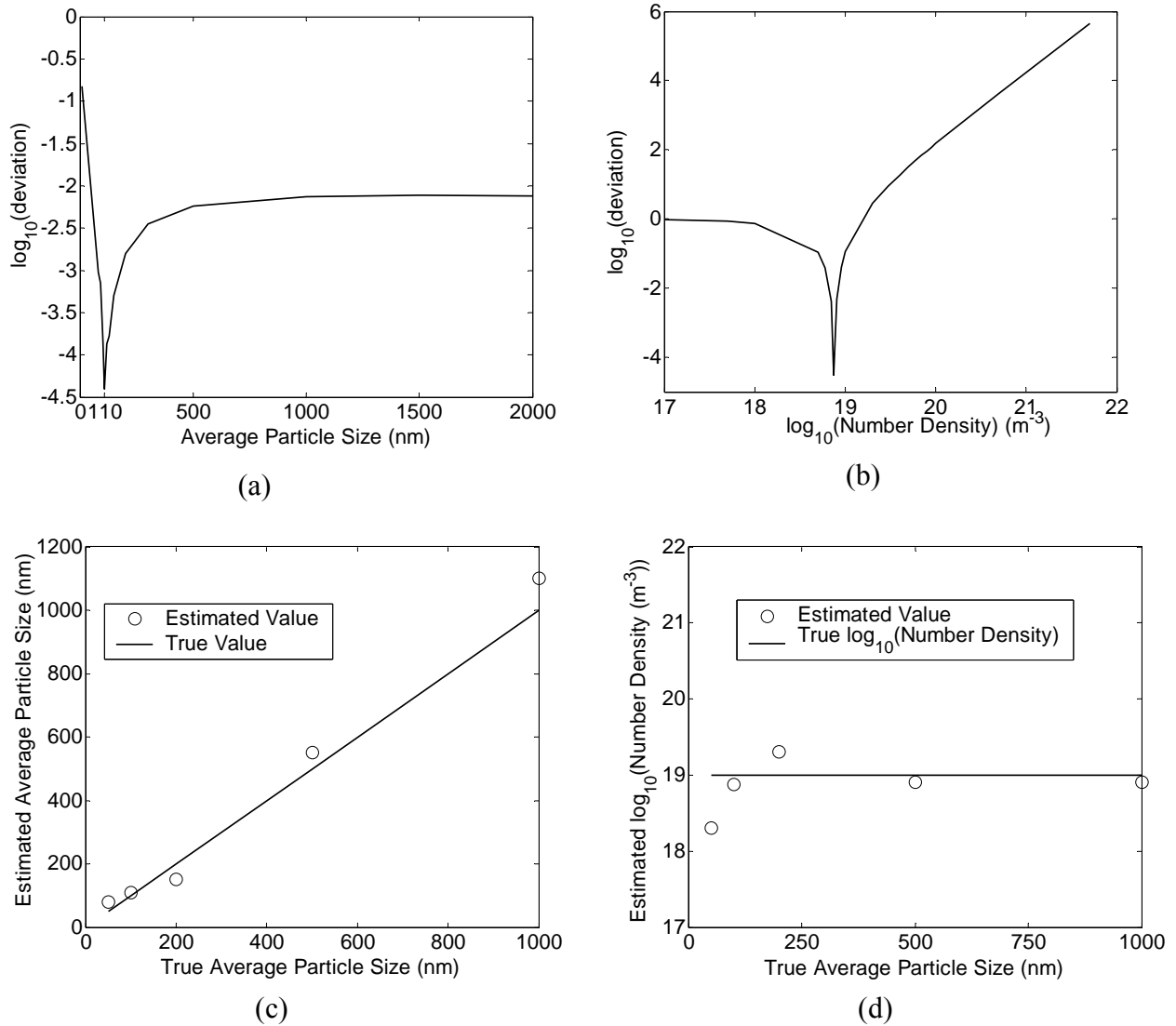


Figure 3.2. (a) Error function for estimating effective particle size using simulated test data with a true effective particle size of $\langle a \rangle = 100 \text{ nm}$. The minimum of the function presents the optimal estimation of particle size. (b) Same for number density assuming an effective particle size $\langle a \rangle = 100 \text{ nm}$ and number density $N = 1 \times 10^{19} \text{ m}^{-3}$. (c) Estimates of effective particle size based on test data with true values of $\langle a \rangle = 50, 100, 200, 500$ and 1000 nm , with $N = 1 \times 10^{19} \text{ m}^{-3}$. (d) Corresponding estimates of number density indicating that number density does not change significantly with changes in particle size.

3.3.C. Estimated Values of Particle Size and Number Density of Intralipid Phantoms

Estimation of effective scatterer size and number density were obtained for the phantoms with 11 different concentrations of Intralipid, and are presented in Figure 3.3. As shown in Figure 3.3 (a) and (b), for the phantom with Intralipid concentration 1.045%, the estimated effective scatterer size and number density by using least square method were 110nm and $2.3 \times 10^{19} \text{ m}^{-3}$. The summary estimated data for all these 11 Intralipid phantoms are shown in Figure 3.3 (c) and (d). The effective scatterer size results ranged from 75nm to 130nm. Over the 11 concentrations used here, the mean effective particle size was 93nm, with a standard deviation of 19nm. This value is close to the Intralipid particle size estimated from electron microscopy reported ($97\text{nm} \pm 3\text{nm}$) in the paper by van Staveren et al [47]. The estimated number density ranged from $1.1 \times 10^{19} \text{ m}^{-3}$ to $3.3 \times 10^{19} \text{ m}^{-3}$, which when divided by Intralipid concentration spanned $2.19 \times 10^{19} \text{ m}^{-3}$ to $2.35 \times 10^{19} \text{ m}^{-3}$. Overall these 11 concentrations, the mean value of number density divided by concentration was $2.26 \times 10^{19} \text{ m}^{-3}$, with standard deviation $0.06 \times 10^{19} \text{ m}^{-3}$. The ratio of the number density over concentration is essentially constant for the 11 concentrations as expected. It appears that in Figure 3.3(a) there is a systematic underestimation of the size below 1% Intralipid, and an overestimation above, but these are comparatively small.

3.3.D. Estimated Values of Particle Size and Number Density of Normal Subjects with Different Radiographic Density Categories

Estimation of effective scatterer size and number density were obtained for the normal patients and are presented in Figure 3.4. All these normal breasts were grouped into one of four radiographic density categories (Fatty, Scattered, HD, ED). As shown in Figure

3.4 (a) and (b), for a patient with fatty breast, the estimated effective scatterer size and number density obtained by using least square method were 300nm and $7.5 \times 10^{17} \text{m}^{-3}$. A clear difference in the mean effective scatterer size and number density for these four compositions of breast tissue was found and shown in Figure 3.4 (c) and (d).

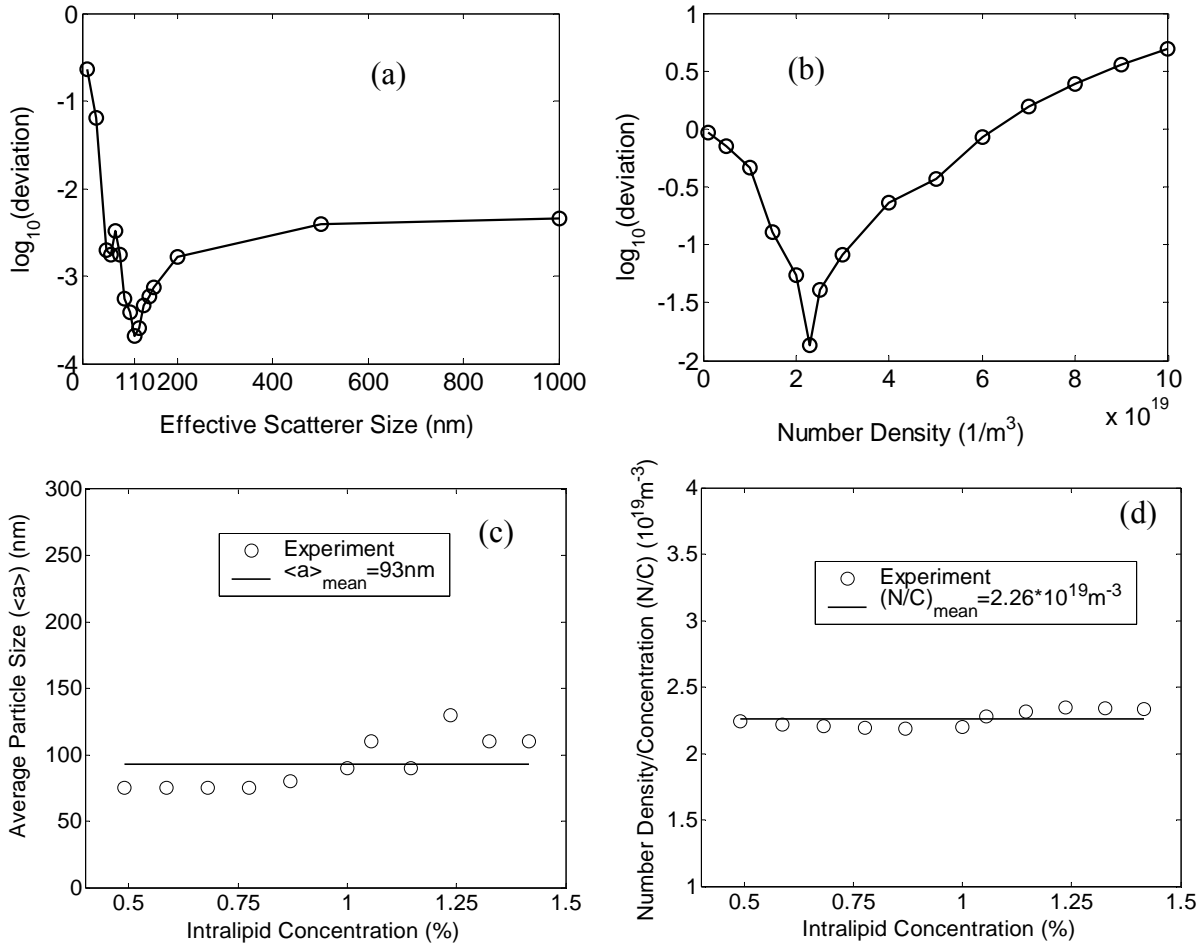


Figure 3.3. (a) Error function for estimating effective scatterer size using phantom data with an Intralipid concentration of $C=1.045\%$. The minimum of the function presents the optimal estimation of particle size $\langle a \rangle = 110 \text{nm}$. (b) Same for number density using the estimated effective scatterer size $\langle a \rangle = 110 \text{nm}$ and the optimal estimation of number density is $N = 2.3 \times 10^{19} \text{m}^{-3}$. (c) Estimate of effective scatterer size for Intralipid phantoms with varying concentration. (d) Same for Number Density.

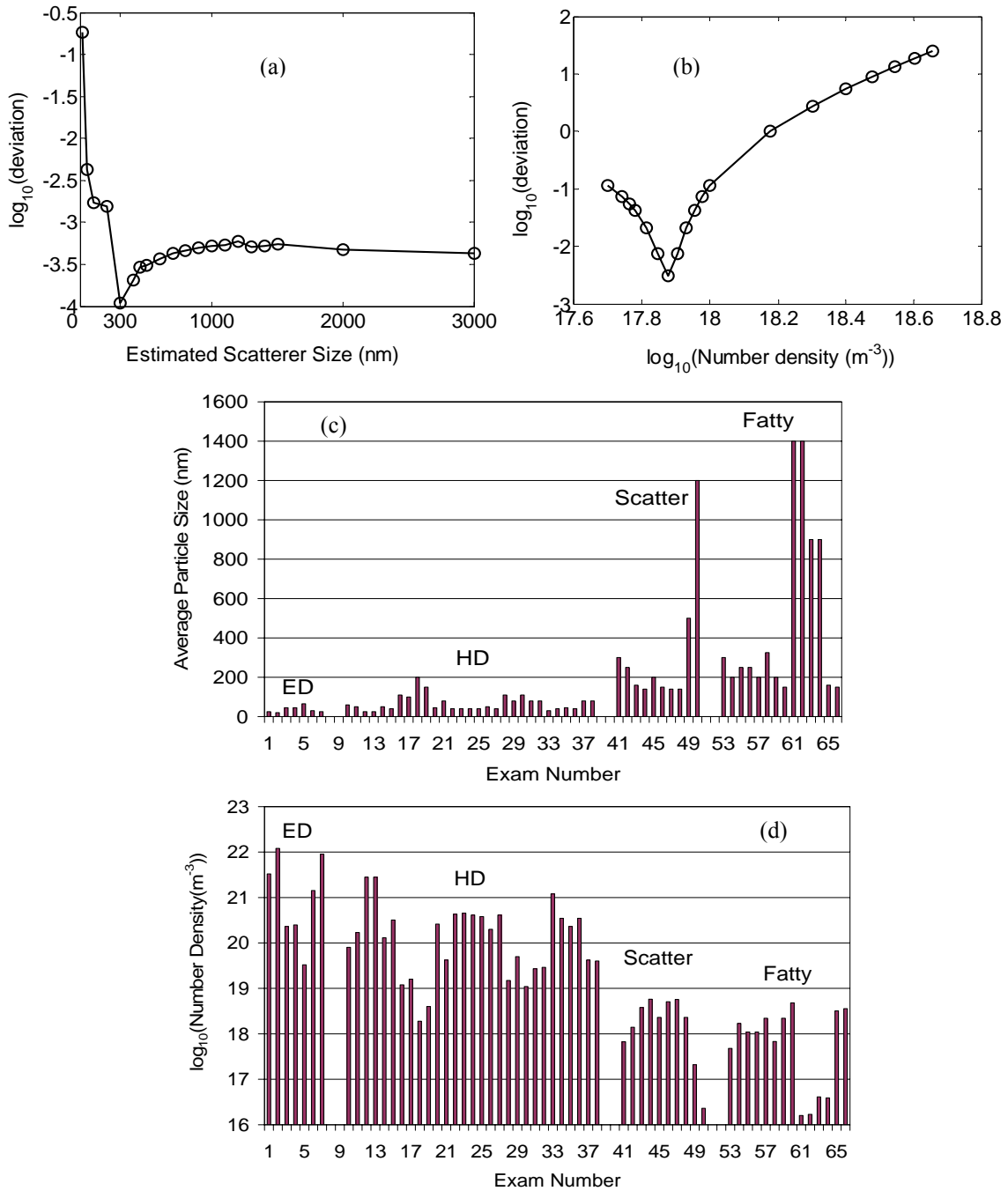


Figure 3.4. (a) Error function for estimating effective scatterer size using the data from a patient with fatty breast type. The minimum of the function presents the optimal estimation of particle size $\langle a \rangle = 300 \text{ nm}$. (b) Same for number density using the estimated effective scatterer size $\langle a \rangle = 300 \text{ nm}$ and the optimal estimation of number density is $N = 7.5 \times 10^{17} \text{ m}^{-3}$. (c) Effective Scatterer sizes from individual normal subject exams, grouped by radiographic density. (d) Same for Number Density.

For the extremely dense (ED) breast type, the effective particle size ranged from of 20 to 65nm, with a mean of 36(\pm 16)nm. For the heterogeneously dense (HD) breast type, the effective particle sizes spanned 25 to 200nm, with a mean of 68(\pm 40)nm. For the scattered type breast, the effective particle sizes covered 140 to 1200nm, with a mean of 318(\pm 330)nm. Finally, for the fatty type breast, effective particle sizes from 150 to 1400nm were found, with a mean of 485(\pm 461)nm. The composite data is summarized in Table 3.1. Over the sequence of increasing effective particle size with breast tissue type (ED, HD, Scattered and Fatty), there is a concordant decrease of the number density.

Breast Type (n = # of subjects)	Mean Effective Size(nm) \pm SD	Size Range (nm) Min-Max	Log₁₀(N/(m³)) \pm SD	Log₁₀(N/(m³)) Range Min-Max
ED (n=4)	36 \pm 16	20-65	21.00 \pm 0.94	19.52-22.08
HD (n=15)	68 \pm 40	25-200	20.03 \pm 0.79	18.28-21.45
S (n=5)	318 \pm 330	140-1200	18.12 \pm 0.77	16.36-18.76
F (n=7)	485 \pm 461	150-1400	17.71 \pm 0.90	16.20-18.68

Table 3.1. Effective Particle Size and Number Density estimated from mean scattering spectrum data acquired in vivo from normal breasts. The scattering coefficients were taken as the whole breast effective obtained for each subject. ED = Extremely Dense, HD = Heterogeneously Dense, S = Scattered fibroglandular densities, F= Almost entirely fat.

3.4. Discussion

Overall, the results indicate that by defining the particle size distribution function, and assuming values of refractive index ratio, based upon the water to lipid membrane

change, Mie theory can be used to estimate an effective scatterer size and number density of breast tissue. The estimates have been derived from bulk transport scattering measurements at six discrete wavelengths, 661, 761, 785, 808, 826 and 849nm, assuming that the reduced scattering spectrum is smooth in shape across the wavelength range. As shown in Figure 3.1, smaller particle sizes lead to similar reduced transport scattering spectra with little oscillation, whereas particles above 1 micron in effective size generate visible oscillations in the reduced scattering spectra as a function of wavelength. Thus, any smoothness assumption in scattering spectrum inherently limits the results to estimating smaller effective particle sizes. The scattering spectra currently reported for bulk breast tissue do not show significant presence of oscillations as a function of wavelength [16, 89]. While this observation could be an artifact of the data processing, it is also reasonable to assume that the dominant scattering particle sizes are less than 1 micron. Although larger structures, such as cell nuclei, typically 5-15 μ in diameter, are known to scatter light, it is certainly true that the largest number of membrane bound structures in tissue are considerably smaller than the nucleus. When imaging cells with phase contrast microscopy, the total backscatter due to the cytoplasm is typically much more significant than the nucleus, indicating that intracellular structures other than the nucleus are important determinants of the scattering spectra. The primary small scattering centers in tissue are thought to be the collagen fiber network of the extracellular matrix, the mitochondria, and other intracellular entities with dimensions smaller than the optical wavelengths [88]. Nonetheless, this assumption is an unsatisfactory compromise, but one that is routinely employed in elastic scattering spectroscopy, and should be further

studied. Yet given the difficulties in extracting sub-wavelength information from samples, it is likely a problem without an easy solution at this time in point.

Given these assumptions and limitations, a fitting procedure is possible where the normalized scattering spectra are used to estimate effective particle size first, and then number density can be readily determined. In making assumptions about the exponential shape of the histogram of particle sizes, and in restricting the data to a sparse number of wavelengths, there is inherent neglect of any oscillatory spectral components that may be present. A third assumption in the procedure used $m=1.09$, as the refractive index ratio between intra and extra cellular cytoplasm and fluid and the bi-lipid membrane. As seen in Figure 3.1 (c) changes in this parameter only appear to affect the overall magnitude of the scattering spectra, without altering its slope. Thus, even if this parameter were in error, it appears likely that it would lead to an error in number density, rather than effective particle size. Figure 3.1 suggests that the strongest effect on the scattering spectra shape was effective particle size; thus, even given the significant assumptions invoked here, that the fitting process is expected to be reasonably accurate in bulk tissue spectroscopy. Estimating Intralipid solutions in this manner worked quite well, and the extension to bulk tissue data appears reasonably good. Hence, the absolute values for effective particle size are likely more reliable than their number density counterparts. Nonetheless, relative changes in both parameters are likely to be quite reliable between samples and between tissue types.

The results show that there are significant changes in the effective particle size and the number density estimation from tomographic imaging between different breast tissue types. Taking into account the limited number of normal volunteers examined, the

grouping of the data in terms of the four density classifications does not seem so well defined, but the overall trend is obvious and the overall trend is what is important. This analysis was applied retrospectively to normal whole breast spectra accumulated in our ongoing clinical exam accruals to examine how particle size and number density vary with physiological differences [2, 26, 49]. Effective particle sizes of 20 to 1400 nm were observed, which are consistent with subcellular organelles and collagen matrix fibrils. Further study of this type of analysis could lead towards a better understanding of how microscopic variations could be detected from bulk tissue measurements, and potentially how these may vary with pathological change.

There are several ways potentially to improve the accuracy and precision of the effective particle size estimates reported here. The accuracy is likely to be increased by increasing the number of wavelengths (15 instead of 6) used to recover the reduced scattering coefficient spectrum and/or their wider distribution in the spectrum. Simulation results indicate that the fitting algorithm improves with increased number of wavelengths; however, our current tomography system is limited to 6 wavelengths, although more could be added in the future. Another approach to improving the estimate is to measure the particle size histogram specifically, as was done explicitly for Intralipid in the paper by van Staveren et al [47]. This may be challenging because it is not evident that electron microscopy shows the same contrast as optical scattering, so the relation between the two may not be direct; however, other approaches such as studying the angular scattering dependence of thin samples may lead to similar information [60, 61]. The method provided in this paper gives out a good estimation for effective particle size and number density for the exponential distributed particles in smaller size range. While

work in these areas in ongoing, the current study indicates that scattering particle size varies with radiographic density, as might be expected from the variety of tissue constituents within these different compositional types of breast tissue, and that Mie theory can be used as a first order approximation of these parameters

Chapter 4: Image Reconstruction of Effective Mie Scattering Parameters of Breast Tissue in Vivo with Near-Infrared Tomography

A method for image reconstruction of the effective size and number density of scattering particles is discussed in this chapter within the context of interpreting Near-infrared (NIR) tomography images of breast tissue. In Chapter 3, an approach to use Mie theory to estimate the effective scattering parameters is examined and applied, given some assumptions about the index of refraction change expected in lipid membrane-bound scatterers. When using a limited number of NIR wavelengths in the reduced scattering spectra, the parameter extraction technique is limited to representing a continuous distribution of scatterer sizes, which is dominated by an exponential decrease in fraction with increasing particle size. In this chapter, image formation of effective scatterer size and number density is presented based on the estimation method in chapter 3. The method was evaluated with Intralipid phantom studies to demonstrate particle size estimation to within 9% of the expected value. Secondly the method was used in NIR patient images, and indicates that for a cancer tumor the effective scatterer size may be different than the background breast values. For benign tumor patients there is not a significant difference in effective scatterer size or number density between tumor and normal tissues. The method was used to interpret MRI-coupled NIR images of adipose and fibroglandular tissues, and indicated that the fibroglandular tissue has smaller effective scatterer size and larger effective number density than the adipose tissue.

4.1. Introduction

In chapter 3 [22], the method for extracting effective scatterer size and number density from the reduced scattering coefficient spectrum was proposed. The scattering spectrum was sampled at 6 wavelengths using the clinical breast tomography system. In this chapter, image reconstruction method for the effective Mie theory scattering parameters is proposed based on the estimation method in chapter 3. The assumptions and limitations of this image reconstruction process are discussed to put the study in perspective with prior work, and the method utilized is analyzed through simulated and tissue-phantom data to establish its accuracy. The value of image reconstruction for effective scatterer size and number density from tomography data could be quite significant; hence, methods to further test and implement the approach are discussed. Acceptance of the relevance of particle size and number density could be easier than the more abstract quantities of scattering amplitude and power, thus this work could have important benefits in the field of medical use of diffuse tomography.

4.2. Methods

4.2.A. Image Reconstruction of Absorption and Scattering Coefficients

Reduced scattering coefficients were obtained with the clinical imaging system in use at Dartmouth [85]. Briefly, the system measures diffusely transmitted amplitude and phase shift at 100 MHz through up to 12 cm of tissue, and is designed for breast imaging for characterization of tumors non-invasively. The measurements were taken at six wavelengths and the data was calibrated by a homogeneous phantom, and then fit to a finite element diffusion theory prediction of the data. The finite element model is iteratively fit to the measurements through a Newton minimization method, and images

of absorption and reduced scattering coefficient are recovered at all wavelengths. The inversion algorithm is described in detail in previous papers and is believed to provide more accurate prediction of the scattering parameters A and b from equation (1.7) [86, 90]. However, related to the fitting for particle size and density, it must be clearly understood that a sparse number of wavelengths cannot be used to accurately fit a highly detailed scattering spectrum. Thus the limited number of wavelengths is not sufficient for identifying oscillations in the scattering spectra that might be observed from larger Mie scattering particles and these have not been observed with any certainty in diffuse spectra. However as indicated in chapter 3, oscillation in the diffuse spectra can be omitted if the dominant scattering particle sizes are thought to be smaller than 1000 nm [22].

4.2.B. Effective Scatterer Size and Number Density Estimation Method

The details of this estimation method is described in chapter 3 [22]. A brief summary of this method is presented here.

To estimate effective scatterer size and number density, with the limited number of wavelengths available, any oscillation in the spectra must be omitted because the dominant scatterer sizes expected are small. The 6 experimental reduced scattering coefficients are fit to predictions of the power law expression in Eq.(1.7), first to get the scattering amplitude and scattering power, and then to generate a function of reduced scattering coefficient as a function of wavelength from 650 to 1000nm. To extract the effective particle size, this reduced scattering coefficient function is normalized at one wavelength (800nm). This normalization eliminates the influence of number density, so that only effective particle size needs to be fit in the first stage. Using a least-squares

minimization, the effective particle size can be effectively estimated. Then the number density can then be estimated by comparing the original un-normalized data with Mie theory (equation (2.12)) using a second least-squares minimization method. In this fitting the following error function is used:

$$\chi = \left(\frac{1}{n} \sum_{i=1}^n ((\mu_s^{i \text{ exp}} - \mu_s^{i \text{ o}}) / \mu_s^{i \text{ o}})^2 \right)^{\frac{1}{2}} \quad (3.1)$$

where χ is the error norm, n is the total number of wavelengths used in the fitting process, $\mu_s^{i \text{ exp}}$ is the experimental reduced scattering coefficient at the i th wavelength, $\mu_s^{i \text{ o}}$ is the reduced scattering coefficient at the i th wavelength calculated from Mie theory.

4.2.C. Effective Scatterer Size and Number Density Image Reconstruction Method

From the estimation method briefly presented above, the effective scatterer size, $\langle a \rangle$, and number density, N , images are estimated from experimental measurements of the scattering power b and amplitude A . As stated in chapter 3, out of $\langle a \rangle$ and N , it is only $\langle a \rangle$ that influences the shape of the scattering spectra in the NIR region. While in equation (1.7), out of parameters A and b , only b influences the shape of the scattering spectra. Therefore in the NIR region effective scatterer size $\langle a \rangle$ can be directly derived from the experimental value of b by comparing the shape of the scattering spectra got from our measurement with that from Mie theory using least square method.

Now normalize the scattering amplitude to $A=1$ at one wavelength (800nm is used here), and then in equation (1.7), μ_s' is only determined by b :

$$\mu_s' = \lambda^{-b} \quad (4.1)$$

While we already derived $\langle a \rangle$ from b , so we can get the number density N by comparing the Mie theory with known $\langle a \rangle$ with equation (4.1) using least square method. We call the number density when $A=1$ as N_0 . So N_0 can also be derived only from the scattering power b . Then for arbitrary A , the effective number density can then be estimated by

$$N = A \times N_0$$

By now, given A and b , both $\langle a \rangle$ and N can be derived with this sequential process.

By simulating a series of b values to get the results for $\langle a \rangle$ and N_0 , an empirical polynomial power function was found for $\langle a \rangle$ as a function of b , and for $\log_{10}(N_0)$ as a function of b . In all these studies, the size distribution function was assumed to be an exponentially decreasing function, and their corresponding relative refractive indexes were used. The equations for $\langle a \rangle$ and $\log_{10}(N_0)$ are represented as polynomial expressions, listed in Table 4.1. Here we selected three typical kinds of relative refractive indexes which are related to the scattering media in the study to analyze. $n_1 = 1.33$, $n_2 = 1.47$ [47] was used for the Intralipid phantom study, while $n_1 = 1.36$, $n_2 = 1.4$ was used [20] for the breast tissue study. For the MRI-NIR patient studies, where the tissues could be uniquely segmented between adipose and fibroglandular tissues, $n_1 = 1.36$ and $n_2 = 1.4$ were used for the fibroglandular tissue, with the latter value being taken for bi-lipid membranes [20], while for the adipose tissues, $n_1 = 1.36$ and $n_2 = 1.49$ were used with the latter value being the measured value for lipid [91]. The corresponding empirical equations for these three sets of refractive indexes were estimated and the coefficients are shown in Table 1. The fit to the data for $\langle a \rangle$ was found to be optimal with a 7th order polynomial, whereas the fit to the data for $\log_{10}(N_0)$ required only a 3rd order polynomial.

power order	BiLipid Membrane		Adipose tissue		Intralipid phantom	
	$n_1=1.36, n_2=1.4$		$n_1=1.36, n_2=1.49$		$n_1=1.33, n_2=1.47$	
	$\langle a \rangle$ (nm)	$\log_{10}(N_0)$ (m^{-3})	$\langle a \rangle$ (nm)	$\log_{10}(N_0)$ (m^{-3})	$\langle a \rangle$ (nm)	$\log_{10}(N_0)$ (m^{-3})
0	2.93e+3	14.7	3.1e+3	14.0	6.67e+3	13.5
1	- 9.57e+3	3.76	- 1.09e+4	2.87	- 2.67e+4	3.41
2	1.35e+4	- 2.71	1.67e+4	- 2.18	4.43e+4	- 2.42
3	- 1.03e+4	0.403	- 1.38e+4	0.316	3.89e+4	0.35
4	4.52e+3		6.58e+3		1.94e+4	
5	- 1.15e+3		- 1.81e+3		- 5.55e+3	
6	1.58e+2		2.68e+2		8.45e+2	
7	- 8.96		- 16.4		- 53.1	

Table 4.1. Power function estimates for effective scatterer size $\langle a \rangle$ and normalized number density $\log_{10}(N_0)$, given the index of refraction values specified for outside (n_1) and inside (n_2) the spheres. For $\langle a \rangle$ the power series was taken out to 7 orders, whereas for $\log_{10}(N_0)$, only 3 orders were required.

4.3 Effective Scatterer Size and Number Density Image Reconstruction Studies

4.3.A. Phantom Study

Data from the tomography system was used to validate this estimation approach with initially using tissue-simulating phantoms with well characterize particle size and density. Heterogeneous gelatin phantoms were used, containing Intralipid inclusions at 5 different concentrations, ranging from 0.75% to 1.75% in steps of 0.25%. This range of inclusion concentrations provided a reduced scattering coefficient spectrum with the same effective particle size but linearly increasing number density. The data at each concentration was analyzed with the method described above with image reconstruction for the effective scatterer size and number density. By varying the concentration, each spectrum is expected to result in the same effective particle size, with a theoretical value near $97(\pm 3)$ nm, as measured by van Staveren et al [47]. This experiment provided an effective way to examine imaging inclusions within an otherwise homogeneous domain.

4.3.B. Image Reconstruction of $\langle a \rangle$ and N for Human Breast Tissue

In the second step the image reconstruction method was applied to cancer breast tissue images. The study was approved by the institutional committee for the protection of human subjects. Near-infrared imaging studies were performed on symptomatic women recruited into the study following an abnormal mammogram, and at the time of referral to biopsy. Informed consent was provided prior to the NIR imaging exam. Data from 12 patients were used in the analysis presented here, including 3 cancer patients and 9 benign tumor patients. For the diseased breast, both the cancer tissue and the background normal tissue were studied, with the region of the tumor was delineated manually based upon a Radiologists prediction of the location of the lesion from the x-ray mammograms. The regional average value was calculated for both the tumor and the normal tissue values. The contralateral breast was also analyzed separately as a whole value. Reconstruction of images for all patients was done with a direct estimate of the scattering parameters based upon an algorithm which incorporates all six wavelength data sets simultaneously and constrains the fitted images to recover hemoglobin, oxygen saturation, water fraction and scattering spectra, fitted to A and b parameters.

4.3.C. Study of Subject Images from the MRI-NIR System

In a final stage in the testing the parameter estimation approach, the data processing method was applied to images from a MRI-coupled NIR system for breast tissue imaging. Despite evidence of high contrast, optical imaging suffers from poor spatial resolution due to the diffuse nature of light propagation in tissue and the

complicated path that photons travel from source to detector. In NIR image reconstruction, knowledge of tissue structure got from MRI can be used to constrain/guide the iterative process, and improve the spatial resolution and quantitative accuracy of recovered physiological parameters. A clinical prototype hybrid imaging system, which combines NIR spectral tomography and magnetic resonance imaging (MRI), was used to determine tissue structure with improved spatial resolution [46, 51, 91-93]. Combining these two methodologies into a platform for simultaneous data acquisition allowed for excellent co-registration and data synergy. NIR reconstructions that use appropriate spatial constraints from a priori structural information about the boundary between adipose and fibroglandular tissue, lead to images with millimeter resolution and better represent the physiological differences between these two types of tissue. Thus, these images were used with the algorithm to predict effective scatterer size and number density, to examine the typical values for adipose and fibroglandular tissue.

The imaging system used, described in detail by Brooksby et al [46], records measurements of NIR light transmission through a pendant breast in a planar, tomographic geometry. A portable cart houses the light generation and detection hardware subsystems. Six laser diodes (660-850 nm) are amplitude modulated at 100 MHz. The bank of laser tubes is mounted on a linear translation stage, which sequentially couples the activated source into 16 bifurcated optical fiber bundles. The central seven fibers deliver the source light while the remaining fibers collect transmitted light and are coupled to photomultiplier tube (PMT) detectors located in the base of the cart. For each source, measurements of the amplitude and phase shift of the 100 MHz signal are acquired from 15 locations around the breast. The optical fiber bundles extend 13 meters

into a 1.5 T whole body MRI (GE Medical Systems) and the two data types (i.e. NIR and MRI) are acquired simultaneously. The patient lies on an open architecture breast array coil (MRI Devices) which also houses the MR-compatible fiber positioning system. The plane of fibers spanning the circumference of a pendant breast can be positioned manually from nipple to chest wall if multiple planes of NIR data are desired.

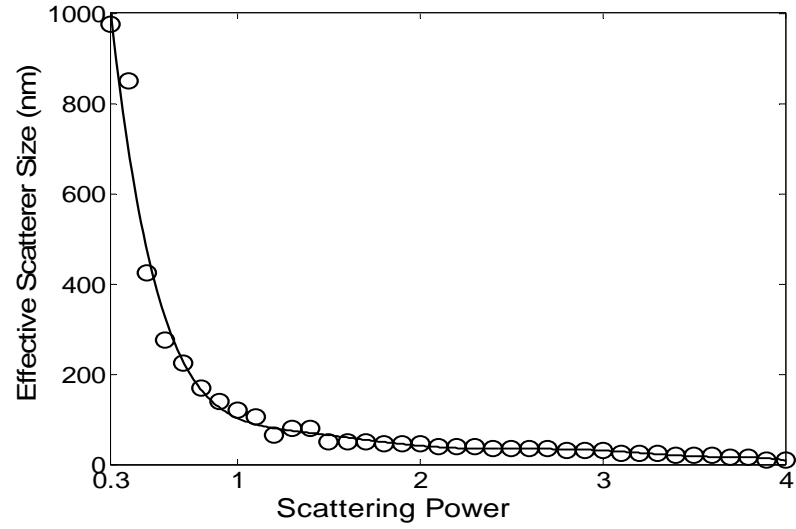
Experience has shown that significant improvement in the stability and accuracy of the reconstruction process can be obtained by incorporating prior anatomical information as an input in the NIR parameter estimation problem [94-100]. MRI priors are implemented through the incorporation of a regularization matrix which has a Laplacian filter shape within the same tissue type, and effectively relaxes these smoothness constraints at the interface between different tissues, in directions normal to their common boundary [91]. This approach provides an inherent smoothing of a given tissue type, such as adipose or glandular tissues, but allows the two tissue types to be significantly different from one another. Based upon a series of phantom studies, this approach, combined with direct spectral reconstruction, has been shown to be the best estimate of the chromophore concentrations and scattering parameters of these normal breast tissues. The values of A and b in these images were then used to generate images of effective scatterer size and number density.

4.4. Results

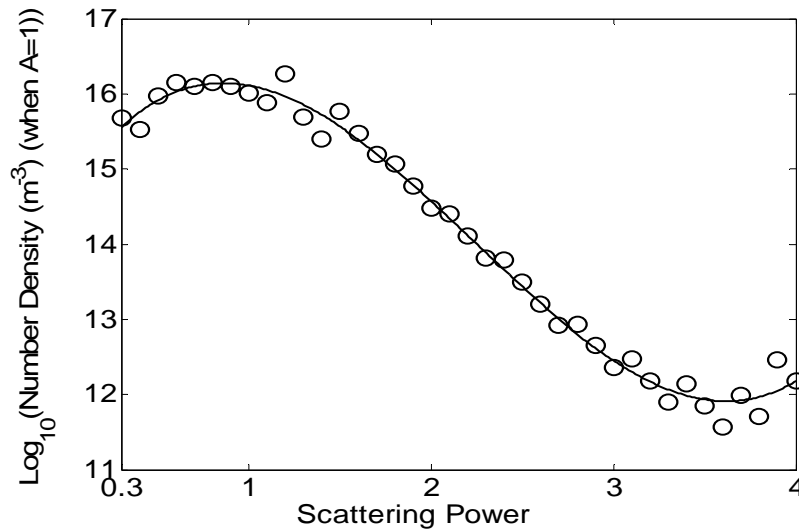
4.4.A. Empirical Equations for Estimation of $\langle a \rangle$ and N

In the imaging problem, the use of the empirical power functions listed in Table 4.1 were ideal to map the reconstructed images of scattering parameters onto the effective scatterer

size and number density images. In all these studies, the size distribution function was assumed to be an exponentially decreasing function, and their corresponding relative refractive indexes were used. For the phantom study, $n_1 = 1.33$, $n_2 = 1.47$ were used [47], and for the cancer patient study, $n_1 = 1.36$, $n_2 = 1.4$ was used [20].



(a)



(b)

Figure 4.1. The relationship between scatter power, b , and effective scatterer size, $\langle a \rangle$, is shown in (a) for simulated data (points) and the best fit polynomial curve (coefficients in Table 1). The relationship between effective normalized number density (the effective number density when $A=1$) and scatter power is shown in (b) for the same parameters, with the fitted polynomial curve shown (coefficients in Table 4.1).

For the MRI-NIR patient studies, where the tissues could be uniquely segmented between adipose and fibroglandular tissues, $n_1 = 1.36$ and $n_2 = 1.4$ were used for the fibroglandular tissue, with the latter value being taken for bi-lipid membranes [20], while for the adipose tissues, $n_1 = 1.36$ and $n_2 = 1.49$ were used with the latter value being the measured value for lipid [91]. The corresponding empirical equations for these three sets of refractive indexes were estimated and the coefficients are shown in Table 1. The fitting figures for the $n_1 = 1.36$, $n_2 = 1.4$ set are shown in Figure 4.1.

4.4.B. Phantom Study Results

In Figure 4.2, (a) shows the diagram of the phantom, and (b) shows the reconstructed images for b (Scatt Power) and A (Scatt Ampl.), from the phantom with an inclusion of Intralipid at concentration of 1.0%. From these two images and using the empirical equations, the reconstructed images of effective scatterer size (Effec. Size) and number density (Num. Density) were obtained as, shown in (b).

The physical region of interest (ROI) was taken as the size of the hole, and the average value over the ROI was estimated. For example, for the phantom with an Intralipid concentration of 1.0% in the inclusion, the effective scatterer size and number density average values in the ROI were 111nm and $2.64 \times 10^{14} \text{ m}^{-3}$.

The summary values for each of the five phantom concentrations of Intralipid are shown in Figure 4.3, with (a) showing the effective scatterer size. The circles indicate the results for of the phantom data. The estimation results for the phantoms with different intralipid concentrations were almost all the same, with an average value of 106nm, which is shown by the solid line in Figure 4.3(a), and standard deviation was 4nm. This

result agrees to within 9% of the expected value of $97\pm 3\text{nm}$ from van Staveren et al, as determined by electron microscopy studies in their paper [47].

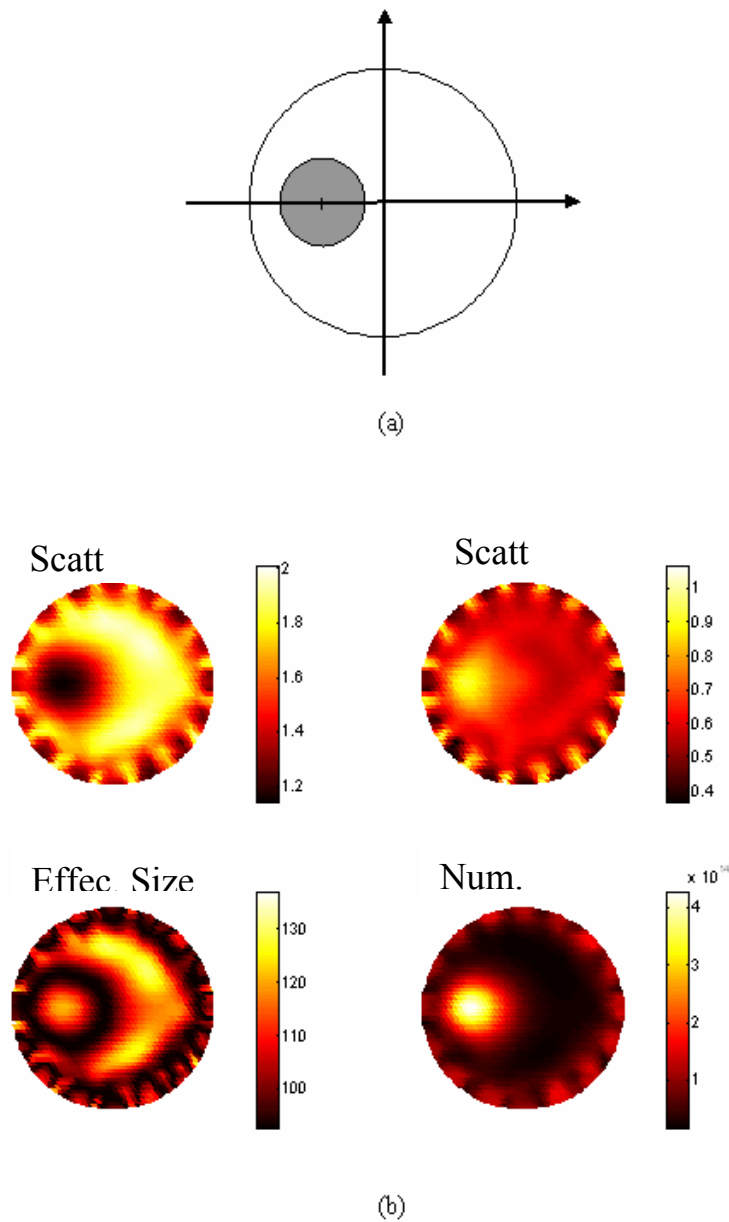


Figure 4.2. In (a) a diagram of the phantom geometry is shown, and in (b) a set of reconstructed images of the phantom with 1.0% Intralipid concentration is shown. The background medium was a solid resin phantom used in many previous studies [92].

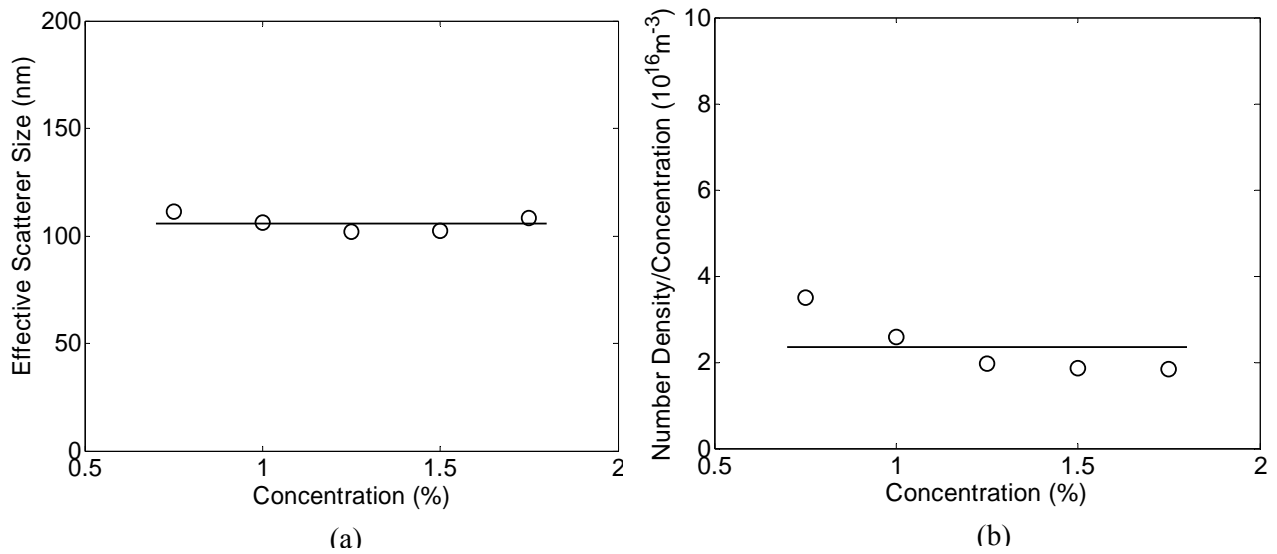


Figure 4.3. The results are shown for different intralipid concentrations of (a) average effective scatterer size, $\langle a \rangle$, and (b) average effective number density, N , using bulk values from within the inclusion region, as shown in the previous figure.

Figure 4.3 (b) shows the result for the ratio of effective number density to concentration, for varying concentrations of the Intralipid inclusion. The circles indicate the results, with the ratio of N over concentration being nearly constant for these phantoms, having average and standard deviation values of $2.4 \times 10^{16} \text{ m}^{-3} \pm 0.7 \times 10^{16} \text{ m}^{-3}$, which are shown by the solid line in Figure 4.3 (b). Since these phantom results were consistent with what was expected, the approach was utilized on human data, in the next section.

4.4.C. Patient Imaging Study Results

Figure 4.4(a) is a representative image example from a patient with an invasive ductal carcinoma tumor in the breast, showing an *en face* or cranocaudal slice of the

breast as viewed toward the patient. From our reconstruction, the hemoglobin (Hb_T), oxygen saturation (Oxy), water fraction (Wat), scattering power (Scatt. Power) and scattering amplitude (Scatt. Ampl.) images were recovered, and these are all shown in Figure 4.4 (a), in the plane of the tumor. Using the two empirical equations for $n_1=1.36$, $n_2=1.4$, the effective scatterer size and number density values were recovered at each pixel in the image, using the images of the scattering power and scattering amplitude. The resulting images are also shown in Figure 4.4(a). These images indicate that the cancer tissue has smaller effective scatterer size and larger effective number density than the background in this case. Figure 4.4 (b) is a representative image example from a patient with a benign tumor in the breast.

The region of interest (ROI) value is the average over the tumor area. The average value over the remaining breast tissue excluded the tumor ROI. The average value for the contralateral breast ROI was estimated at the same mirror location as in the symptomatic breast. Studies have shown that breast tissue is highly symmetric between breasts, such that comparisons between ROI values taken from mirror locations in the symptomatic and normal breasts are a good way to see differences from the normal condition.

Figure 4.5 shows the summary data of (a) average effective scatterer size and (b) number density values for the region of interest (ROI) and the background over all the cancer patients ($n=11$) as well as the benign tumor patients ($n=17$) included in this study in Box and whisker plot. In Figure 4.5, 'o' indicate all the data point, while 'O' with 'x' inside is the mean value for each group of data. Table 4.2 shows the variance parameters for the Box and whisker plot of (a) average effective scatterer sizes and (b) average effective number density for groups of subjects in terms of cancer and benign lesions.

Figure 4.5 (a) indicates that in the patient study, for both the cancer patients and benign patients, the effective scatterer sizes of ROI are pretty close to that of the background. Figure 4.5 (b) indicates that for the cancer patients, the effective number density is much bigger than that of the background, while for the benign patients, the effective number density are relatively close to that of the background. More patients will be studied in the future to get a generic conclusion.

In table 4.3 p-values are given to determine if the values are significantly different from each tissue type, using a Student's t-test on all (a) average effective scatterer sizes and (b) average effective number density for groups of subjects in terms of cancer and benign lesions. For the average effective scatterer size, the p values between ROI and background for cancer patients and for benign patients are 0.036 and 0.008 respectively. This indicates that for average effective scatterer size, there's a significant difference in between ROI and background for both cancer patients and benign patients. For the average effective number density, the p values between ROI and background for cancer patients and for benign patients are 0.03 and 0.06 respectively. This shows for the average effective number density, there's a significant difference between ROI and background for cancer patients, but not a significant difference between ROI and background for benign patients.

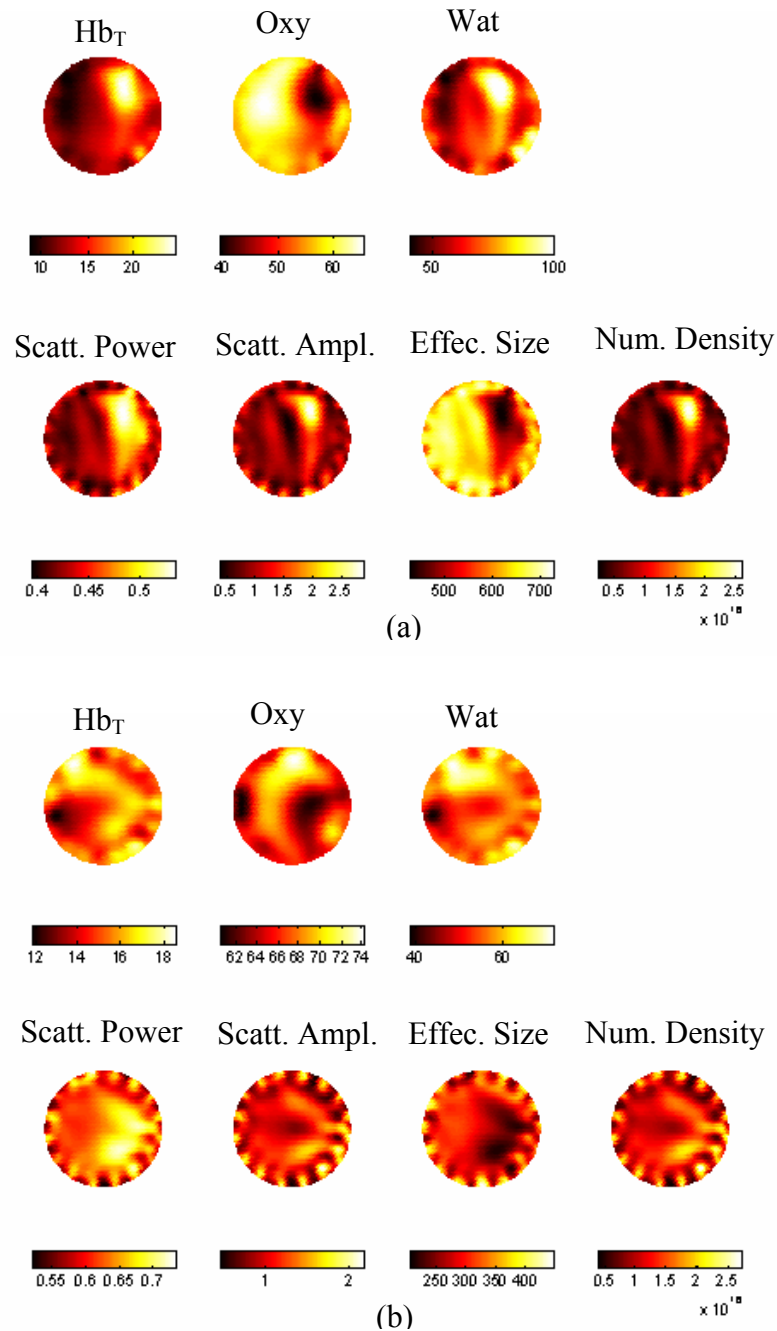
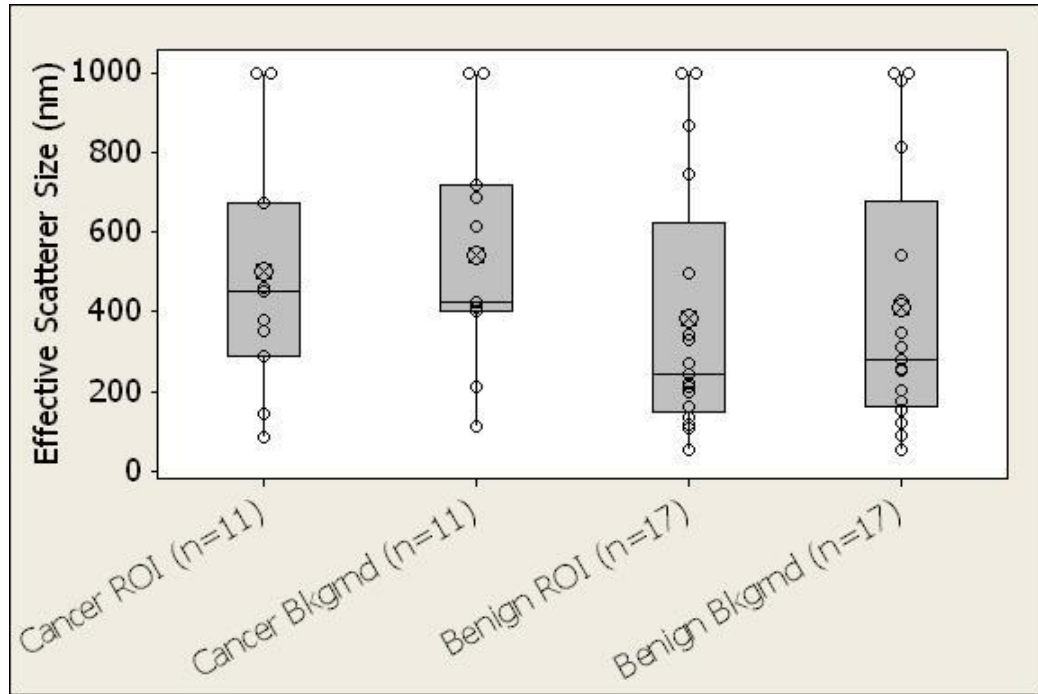
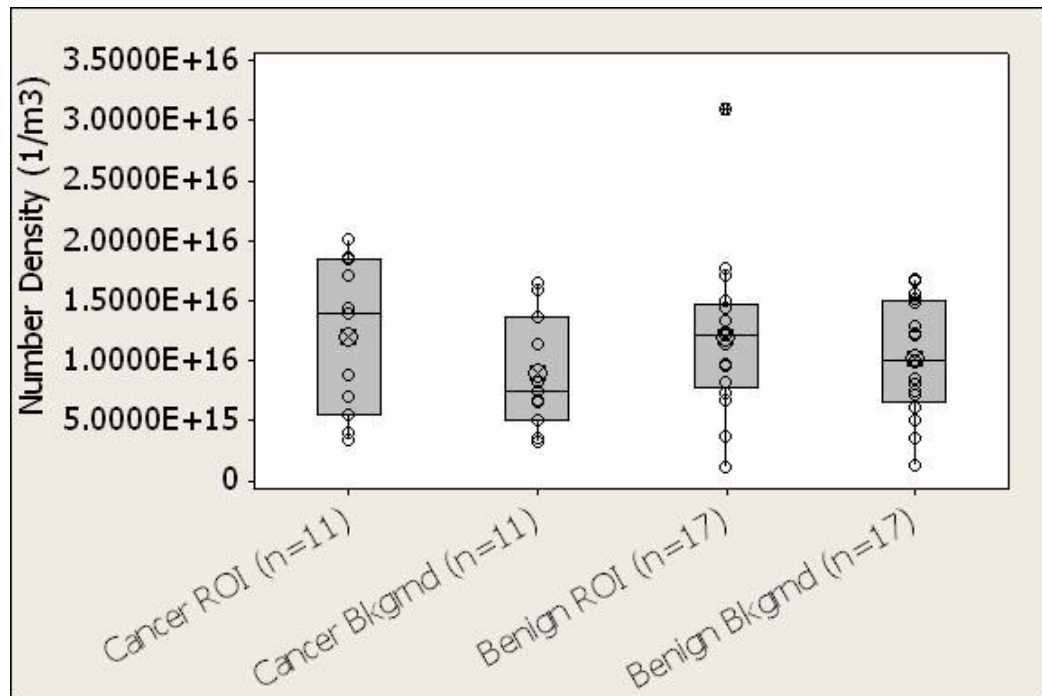


Figure 4.4. In (a) reconstructed NIR images are shown for a cancer patient, showing the plane of the tumor in the breast, sliced in a cranocaudal view. The panel of images shows total hemoglobin concentration (Hb_T), oxygen saturation (Oxy), water fraction (Wat), scatter power (Scatt. Power) and amplitude (Scatt. Ampl.), as well as effective scatterer size (Effec. Size) and number density (Num. Density) images. In (b) the reconstructed NIR images for a patient with a benign tumor in the breast are shown.



(a)



(b)

Figure 4.5. The Box and whisker plot of (a) average effective scatterer sizes and (b) average effective number density for groups of subjects in terms of cancer and benign lesions. ‘o’ indicate all the data point, while ‘o’ with ‘x’ inside is the mean value for each group of data.

Scatterer Size (nm)	cancer ROI (n=11)	cancer Bkgrnd (n=11)	Benign ROI (n=17)	Benign Bkgrnd (n=17)
median	452	422	245	280
q1	290	400	146	163
min	84	111	52	53
max	1000	1000	1000	1000
q3	673	720	621	676
mean	501	544	382	412

(a)

Number density ($10^{16}/m^3$)	cancer ROI (n=11)	cancer Bkgrnd (n=11)	Benign ROI (n=17)	Benign Bkgrnd (n=17)
median	1.39	0.74	1.22	1.01
q1	0.55	0.51	0.70	0.56
min	0.049	0.048	0.11	0.10
max	2.01	1.65	3.09	1.68
q3	1.85	1.37	1.47	1.51
mean	1.08	0.76	1.1	1.0

(b)

Table 4.2 The variance parameters for the Box and whisker plot of (a) average effective scatterer sizes and (b) average effective number density for groups of subjects in terms of cancer and benign lesions.

p-values (<a>)	cancer ROI (n=11)	cancer Bkgrnd (n=11)	Benign ROI (n=17)	Benign Bkgrnd (n=17)
cancer ROI	~	~	~	~
cancer Bkgrnd	0.036	~	~	~
Benign ROI	0.34	0.18	~	~
Benign Bkgrnd	0.48	0.28	0.008	~

(a)

p-values (N)	cancer ROI (n=11)	cancer Bkgrnd (n=11)	Benign ROI (n=17)	Benign Bkgrnd (n=17)
cancer ROI	~	~	~	~
cancer Bkgrnd	0.03	~	~	~
Benign ROI	0.96	0.16	~	~
Benign Bkgrnd	0.44	0.5	0.06	~

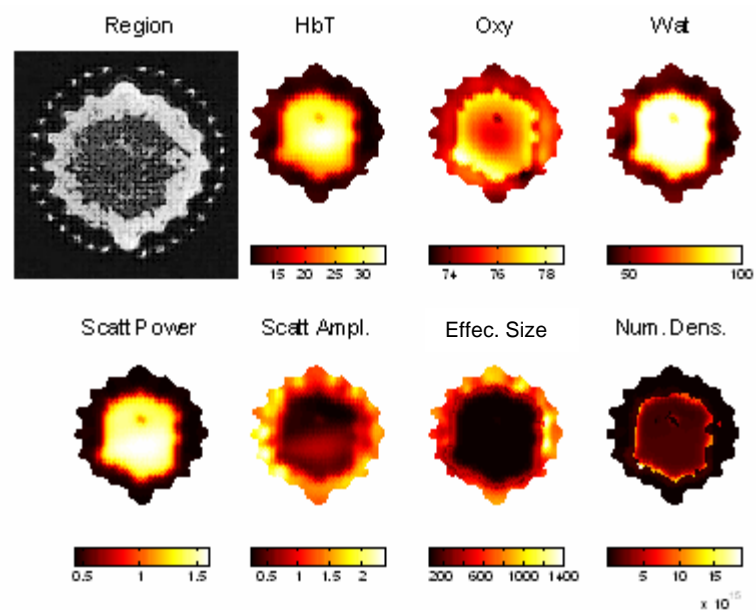
(b)

Table 4.3 The p-values to determine if the values are significantly different from each tissue type, using a Student's t-test on all (a) average effective scatterer sizes and (b) average effective number density for groups of subjects in terms of cancer and benign lesions.

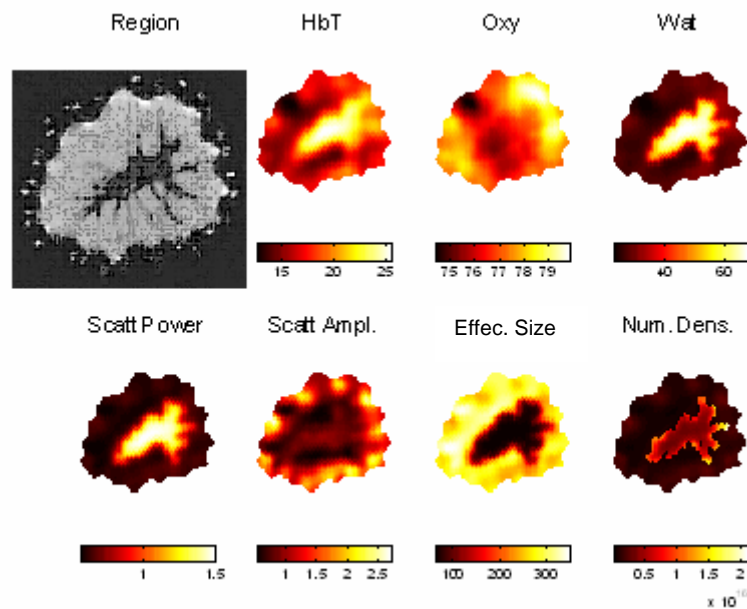
4.4.D. MRI-NIR Subject Study Results

In the final stage of examining the predictions for effective scatterer size and number density values, the images reconstructed with combined MRI-NIR were used. The results for two MRI-NIR patients are shown in Figure 4.6 (a) and (b). Figure 4.6 (a) (Region) is the MRI image for the first patient. The inner part of the breast (darker in the image) is the fibroglandular tissue, and the outer part (gray in color) is the adipose or fatty tissue. The hemoglobin (Hb_T), oxygen saturation (Oxy), water fraction (Wat) and scattering power (Scatt. Power) and amplitude (Scatt. Ampl.) images are shown in Figure 4.6 (a). In the estimation of $\langle a \rangle$ and N images, separate values for n_2 were used for each of the two tissue types, as discussed in the Methods section, and images of the breast interior were recovered. The estimated images for $\langle a \rangle$ (Effec. Size) and N (Num. Density) are also shown in Figure 4.6 (a). These images indicate that the fibroglandular tissue has smaller effective scatterer size and larger effective number density than the fatty tissue. For the second patient, the same conclusion is obtained from these results.

In total, 10 sets of images from the MRI-NIR subjects were used in this evaluation and the summary result for these is shown in Figure 4.7. The summary results show that the fibroglandular tissue has smaller effective scatterer size and larger effective number density than the adipose tissue. For the average effective scatterer size, the t-test between of the fibroglandular and adipose tissue showed a significant difference with a p-value of 0.048. For the number density, the t-test showed a significant difference between the fibroglandular and adipose tissue with a smaller p-value of 0.004. Thus NIR tomography appears to be able to delineate fibroglandular tissue from fatty tissue more by the number density than by the effective size.

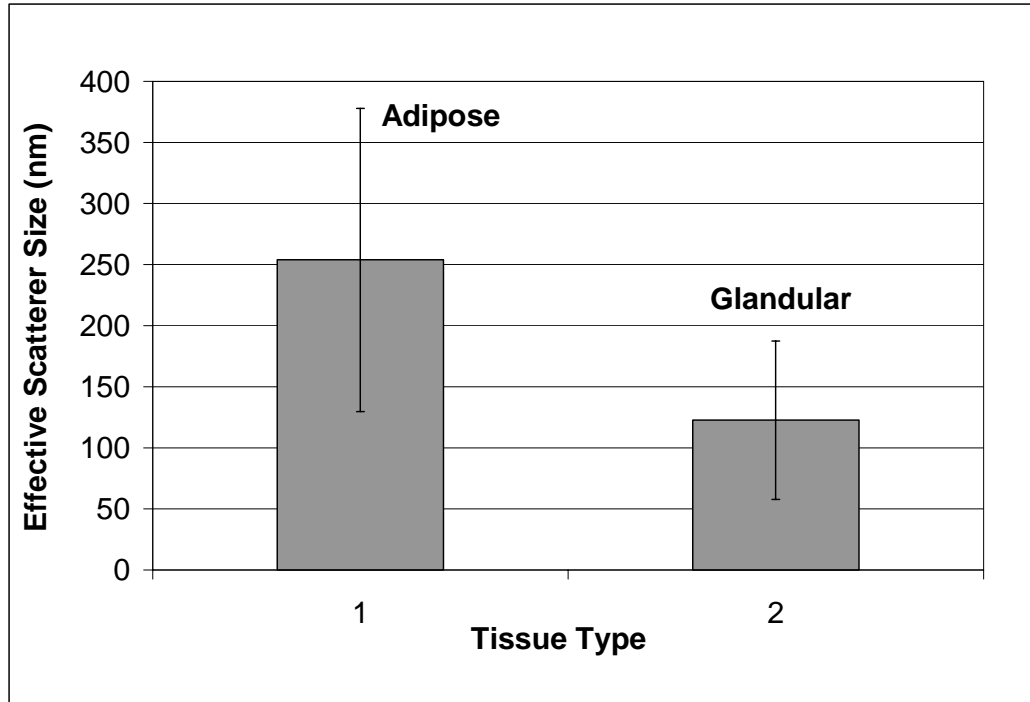


(a)

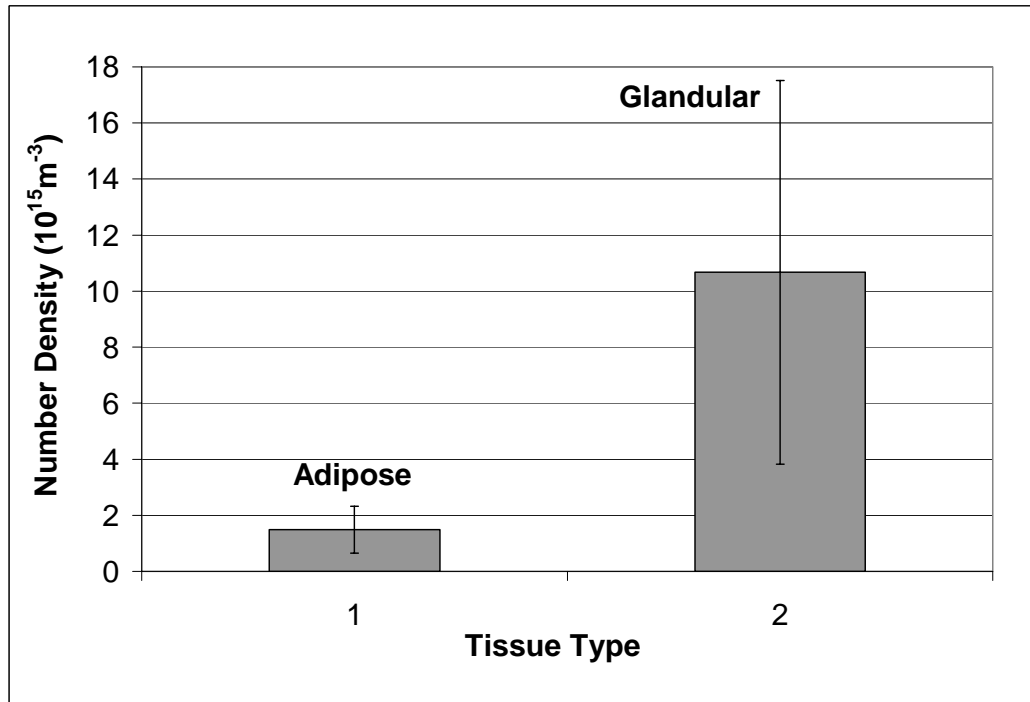


(b)

Figure 4.6. Reconstructed images for two of the MRI-NIR subjects (a & b) are shown, with the MRI image in (Region), and hemoglobin (Hb_T), oxygen saturation (Oxy), water fraction (Wat), scatter power (Scatt Power), scatter amplitude (Scatt Ampl.). Estimates of $\langle a \rangle$ and N are shown in (Effec. Size) and (Num. Dens.), as calculated from (Scatt Power) and (Scatt Ampl.). Image (b) is predominantly fatty tissue (grey in MR Image), whereas (a) is predominantly fibroglandular tissue (darker in MR Image).



(a)



(b)

Figure 4.7. The average tissue values are shown pooled for all MRI-NIR subject images, for effective scatterer size (a), and number density (b), for adipose and fibroglandular tissues.

4.5. Discussion

Overall, results in this chapter indicate that by defining the scattering particle size distribution functions, and assuming values of refractive indexes, Mie theory could be used to estimate images of bulk effective scatterer size and number density. The estimates have been derived from bulk transport scattering measurements at six discrete wavelengths, 661, 761, 785, 808, 826 and 849nm, assuming the reduced scattering spectrum is smooth in shape across the wavelength range. The inherent assumptions in this approach are that the scattering particle size histogram of values is exponentially weighted to smaller size particles, and that the index of refraction can be expressed as a single pair of values inside and outside of the particles. As shown in chapter 3 [22], smaller particle sizes lead to similar reduced transport scattering spectra with little oscillation, whereas particles above 1 micron in size generate visible oscillations in the reduced scattering spectra as a function of wavelength. Thus, any smoothness assumption in scattering spectrum inherently limits the results to estimating smaller scatterer sizes. The scattering spectra currently reported for bulk breast tissue do not show a significant presence of oscillations as a function of wavelength [16, 50, 88]. While this observation could be an artifact of the data processing, it is also reasonable to assume that the dominant scattering particle sizes are less than 1 micron. When imaging cells with phase contrast microscopy, the total backscatter due to the cytoplasm is typically much more significant than the nucleus, indicating that intracellular structures other than the nucleus are important determinants of the scattering spectra, leading to larger fractional oscillations in the spectrum recovered.

In this work, it was assumed that the distribution of scattering particle sizes is exponentially weighted to smaller values. The rationale for this comes from the observation that the largest number of membrane bound structures in tissue are considerably smaller than the nucleus. So although larger structures, such as cell nuclei, typically 5-15 μm in diameter, are known to scatter light, the primary small scattering centers in tissue are thought to be the collagen fiber network of the extracellular matrix, the mitochondria, and other intracellular entities with dimensions smaller than the optical wavelengths [47]. Nonetheless, this assumption is an unsatisfactory compromise, but one that is routinely employed in elastic scattering spectroscopy, and should be further studied. Yet given the difficulties in extracting sub-wavelength information from samples, it is likely a problem without an easy solution at this time in point.

Given these assumptions and limitations, a fitting procedure is possible where the normalized scattering spectra are used to estimate effective scatterer size first, and then effective number density can be readily determined. In making assumptions about the exponential shape of the histogram of scattering particle sizes, and in restricting the data to a sparse number of wavelengths, there is inherent neglect of any oscillatory spectral components that may be present. In addition, a further assumption was made that $n_1 = 1.36$ and $n_2 = 1.4$, for the refractive indexes with material 1 being cellular cytoplasm and fluid and material 2 being the bi-lipid membrane.

The Intralipid phantom study provided a reasonable way for image reconstruction of the effective scatterer size and number density, with a mean size value of 106nm and standard deviation of 4nm (as seen in Figure 4.3). This result agrees to within 9% of the expected value of $97 \pm 3\text{nm}$, suggesting that this method is accurate in this case.

In the patient study, for both the cancer patients and benign patients, the effective scatterer sizes of ROI are pretty close to that of the background. For the cancer patients, the effective number density is much bigger than that of the background, while for the benign patients, the effective number density are relatively close to that of the background. More patients will be studied in the future to get a generic conclusion. For the average effective scatterer size, the p values between ROI and background for cancer patients and for benign patients are 0.036 and 0.008 respectively. This indicates that for average effective scatterer size, there's a significant difference in between ROI and background for both cancer patients and benign patients. For the average effective number density, the p values between ROI and background for cancer patients and for benign patients are 0.03 and 0.06 respectively. This shows for the average effective number density, there's a significant difference between ROI and background for cancer patients, but not a significant difference between ROI and background for benign patients.

For the MRI-NIR subject study, the estimated effective scatterer sizes for adipose and fibroglandular tissues were 254nm and 123nm, respectively. The estimated effective number density for adipose tissue and fibroglandular tissues were $1.5 \times 10^{15} \text{m}^{-3}$ and $10.7 \times 10^{15} \text{m}^{-3}$ separately. This result indicated that the fibroglandular tissue had smaller effective scatterer size and larger effective number density than the adipose tissue, which agrees with the physiologically understood structure of adipose being larger lipid particles and fibroglandular being compound of smaller intracellular and extracellular structures.

One of the larger differences in this study which is different from earlier Mie scattering estimation studies is the estimate that the distribution of the scattering particle

sizes in breast tissue are exponentially weighted. This is not a common assumption in other papers, yet our preliminary work in electron microscopy verifies that this is indeed the case. This is also in agreement with the Intralipid results by van Staveren et al paper [47]. Several other papers use a likelihood function [54] rather than a pure exponential, which has the problem of requiring more free parameters for the shape of the function, making the calculations even more problematic. Yet, the sizes of particles nearest zero have the least impact upon the scattering spectrum, so the difference between a likelihood function and a pure exponential may be insignificant. Clearly further analysis of this assumption should be undertaken, and electron microscopy studies to verify this have been completed and will be reported soon.

There are several ways potentially to improve the accuracy and precision of the effective scatterer size estimates reported here. The accuracy is likely to be increased by using a reduced scattering coefficient spectrum over a wider range in the spectrum and with more wavelengths. Simulation results indicate that the fitting algorithm improves with increased number of wavelengths; however, our current tomography system is limited to only 6, although more will be added in the near future. Another approach to improve the estimate is to measure the scattering particle size histogram specifically by electronic microscopy, as was done explicitly for Intralipid in the paper by van Staveren et al [47], and given particle size histograms could be applied to different tissues individually if the system is used in MRI-guided mode. Other approaches such as studying the angular scattering dependence of thin samples may lead to similar information about the effective scatterer size [60, 61]. A more accurate measurement of the range of changes observed in the refractive index could be used to improve the

estimation, as the refractive index change is clearly not just a single value, but is likely an entire range of values which may or may not be correlated with the range of particle sizes.

4.6. Conclusions

In summary, the patient results indicated that for a cancer tissue, there could be differences in average effective scatterer size and number density between the cancer and normal tissue, but larger numbers of subjects and better quality data is required to assess this. In benign tumor tissue there is no apparent difference from the background tissue. The MRI-NIR subject study indicated that the fibroglandular tissue has smaller effective scatterer size and larger effective number density than the adipose tissue.

The method outlined in this chapter provides a reasonable estimation of effective particle size and density for diffuse tomography applications where there are limited numbers of wavelengths, and when there is an exponential distribution to the scattering particles in the smaller size ranges, and that Mie theory can be used as a first order approximation of these parameters. Medical acceptance of images of particle size and number density may be easier than scattering amplitude and power, due to the inherently clearer physical meaning of the words.

Chapter 5: Breast Tissue Mie Scattering Parameter Estimation through Angle-Resolved Scattering Measurements

In the last two chapters, it was shown that the Mie-type scattering parameters (average/effective scatterer size and number density) can be estimated from the scattering spectra obtained from the NIR tomography system. In this chapter, the average/effective scatterer size is shown to be estimated from the angular-scattering measurements taken in a goniometer system. Polystyrene microsphere suspensions with average particle size of 100nm and 1 μ m were tested, along with Intralipid, and then breast tissue samples. Each was characterized in this manner, to estimate effective scatterer size and to estimate the accuracy of being able to determine these.

5.1. Introduction

Scattering is caused by microscopic fluctuations in the refractive index between intracellular organelles, extracellular structures and their surrounding media. The scattering spectrum of bulk breast tissue has not been extensively investigated, although some early work was done on samples by Peters et al [101]. It is clear that the causes of scattering have their origins in the microscopic composition of the tissue, and that the scattering spectra may have subtle changes between normal and diseased tissues. This early work showed little difference, yet the spectral and spatial scattering of breast tissue samples has not been investigated. Hence, examination of these spectral and spatial features may provide fundamental insight into these pathophysiologic changes, especially since these are known to be linked to the size and density of the scatterers.

In last two chapters, it was shown that by comparing the scattering spectra from the NIR tomography [18, 102] with Mie theory, it was possible to extract information about the average size and number density of scattering centers in vivo [22]. In order to provide an independent measure of these scatterer sizes, an angular scattering measurement [20, 64, 71] is another way to obtain similar size-related information. The scattering phase function specifies the angular distribution of the scattered light, and is defined as the differential scattering cross section divided by the total scattering cross section

As stated in Chapter 2, there is also a relationship between the angular distribution of the scattering amplitude and the size of the scattering particle. So it may be possible to deduce the size information for the angular-resolved scattering measurements.

Like the scattering spectrum, the angular scattering phase distribution is also related to the scatterer size distribution. There have been several studies devoted to developing a better understanding of the relationship between the angular distribution of the scattering and the size of the scatter, which has already been fairly well studied in dilute cells or thin tissue sections [20, 64, 70, 71]. In this thesis, angular resolved scattering light distribution measurements provide a second method for extracting particle size distribution information. This is completed on optically thin tissue sections or dilute suspensions, by comparing the experimentally phase function with that got from Mie theory. This method could be used to compensate for our smaller size range in particle size estimation caused by the limited wavelengths we have and could also be used as a comparison to our estimation method. It is the first time that this angular scattering

measurement was used to estimate effective scatterer size analysis for excised breast tissues.

5.2. Methods

5.2.A Mie Theory

As stated in Chapter 2, in Mie theory, at a given wavelength, the phase function for a multi-sized medium is expressed as:

$$P(\theta) = \frac{\sum_i f(a_i) \mu_s(a_i) P_i(\theta)}{\sum_i f(a_i) \mu_s(a_i)} \quad (2.13)$$

where λ is the wavelength, a is the radius of the particle, m is the refractive index ratio from inside to outside the particles, $m=n_2/n_1$, where n_1 and n_2 are the refractive index outside and inside the particles respectively. $C_{\text{scat}}(m,a,\lambda)$ is the total scattering cross section. $\mu_s(a_i)$ and $P_i(\theta)$ is the scattering coefficient and scattering phase function for a sphere with radius a_i , $f(a_i)$ is a normalized size distribution function

From the equation (2.13) we can see the size distribution function $f(a_i)$ determines the phase function. While the size distribution function could be separated as two parts: the shape of the distribution function and the average size. This average size was named as effective scatterer size. So there are two parameters to determine the phase function: the shape of the size distribution function, and the effective scatterer size. If we make some assumption about the shape of the size distribution function, then there is only the effective scatterer size left for estimation. Once we get the angularly resolved scattering data from the experiment, we can estimate the effective scatterer size information by

comparing it with the Mie theory model using least-square minimization method shown as equation (5.1):

$$\chi = ((P_{\text{exp}} - P_o) / P_o)^2)^{\frac{1}{2}} \quad (5.1)$$

where χ is the error norm, calculated as the squared difference between the experimental data and the Mie theory prediction. Here, P_{exp} is the experimental phase function, P_o is the phase function calculated from Mie theory. In this study, no attempt was made to perform non-linear fit, but rather all possible values of effective size were calculated, and the minimum value of χ was used to determine the best estimate. This approach was taken due to the fact that there appeared to be many local minima in this solution space, and yet through exhaustive sequential estimation, the true global minima were able to be found in most cases.

5.2.B Simulation Study

5.2.B.1 The Forward Simulation Study

In this simulation study the phase function was calculated for different kinds of scattering media using Mie theory. Eight different sets of scattering media were used. It includes:

- (a) mono-sized medium with size $a=100\text{nm}$, 200nm , 500nm and $1\mu\text{m}$, and $m=1.2$;
- (b) multi-sized medium with exponential size distribution function and effective size $\langle a \rangle = 100\text{nm}$, 200nm , 500nm and $1\mu\text{m}$, and $m=1.1$.

The wavelength of the incident light used here was $\lambda=632.8\text{nm}$, and the polarization of the incident light was set to both 0° (P1) and 90° (P2) in order to maximize the data set for fitting.

5.2.B.1.1 The effect of effective scatterer size and distribution upon angular scattering

First was a study of how the effective scatterer size affects the angular scattering. The result is shown in Figure.5.1 and 5.2. It shows that under the same conditions, as the particle size become larger, there are more oscillatory components in the phase function, and more light is scattered in the forward direction. This result is consistent with results in the literature [20]. The second observation that comes from comparing Figures 5.1 and 5.2 is that when the distribution of sizes in the sample becomes broader or distributed in an exponential manner, then the oscillatory components in the angular spectrum are diminished. Thus, it should be expected that in real tissue that these oscillatory components will be considerably smaller than observed in mono-sized samples.

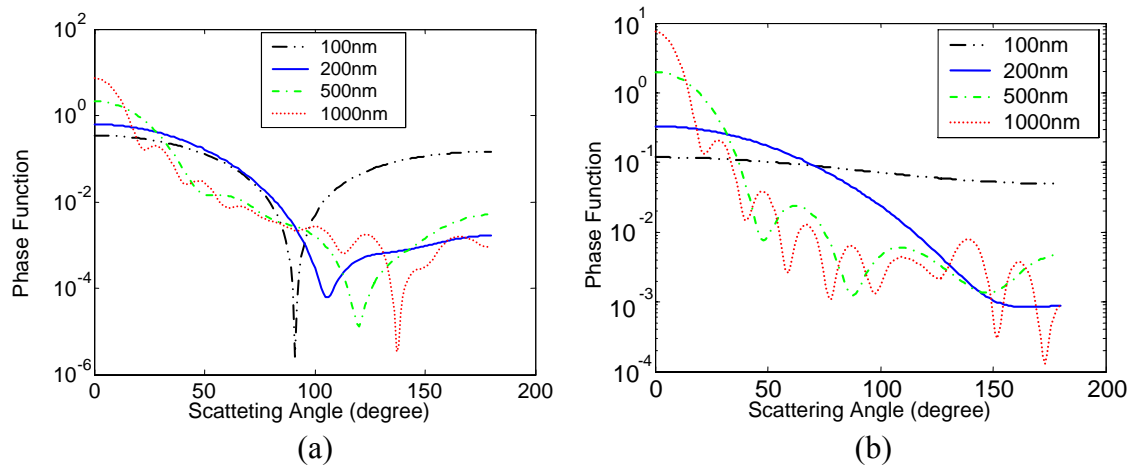


Figure 5.1: The phase function was calculated using Mie theory for mono-sized scattering media with sizes: $a=100\text{nm}$, 200nm , 500nm and $1\mu\text{m}$, using $m=1.2$, for both (a) 0° (b) 90° laser polarization;

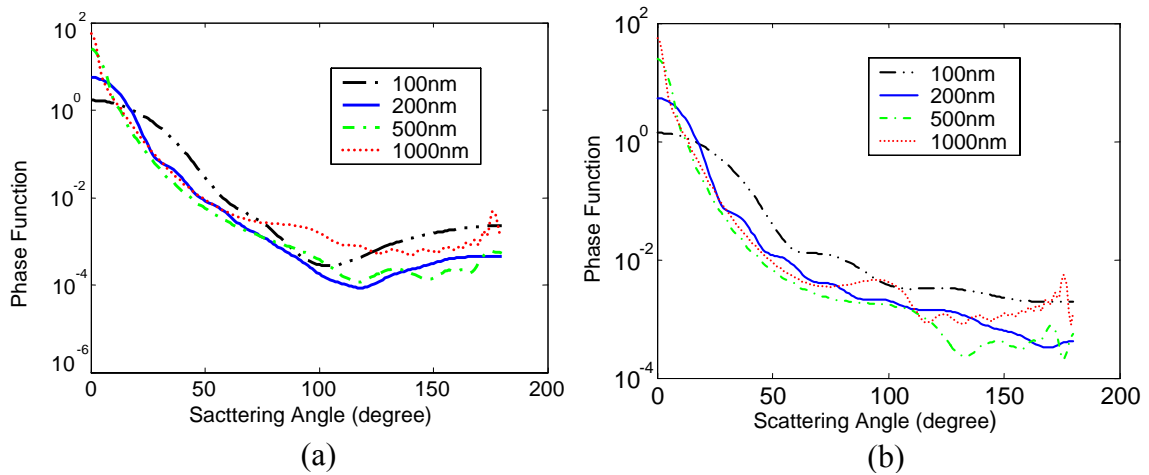


Figure 5.2: Phase functions were calculated using Mie theory for multi-sized media with exponential size distribution functions and $\langle a \rangle = 100\text{nm}$, 200nm , 500nm and $1\mu\text{m}$, $m=1.1$ using (a) 0° (b) 90° laser polarization.

5.2.B.1.2 The comparison between different laser polarizations

In this section, a direct comparison of how the laser polarization affects the angular scattering was studied, for the following three kinds of scattering media:

- (a) mono-sized medium with size $a=100\text{nm}$, and $m=1.2$; and
- (b) mono-sized medium with size $a=1\mu\text{m}$, and $m=1.2$; and
- (c) a distribution of sizes in a medium with exponentially shaped distribution function and mean effective size $\langle a \rangle = 100\text{nm}$, and $m=1.1$.

The result is shown in Figure.5.3. It indicates that at the same conditions, the laser polarization has an obvious effect on the angular scattering.

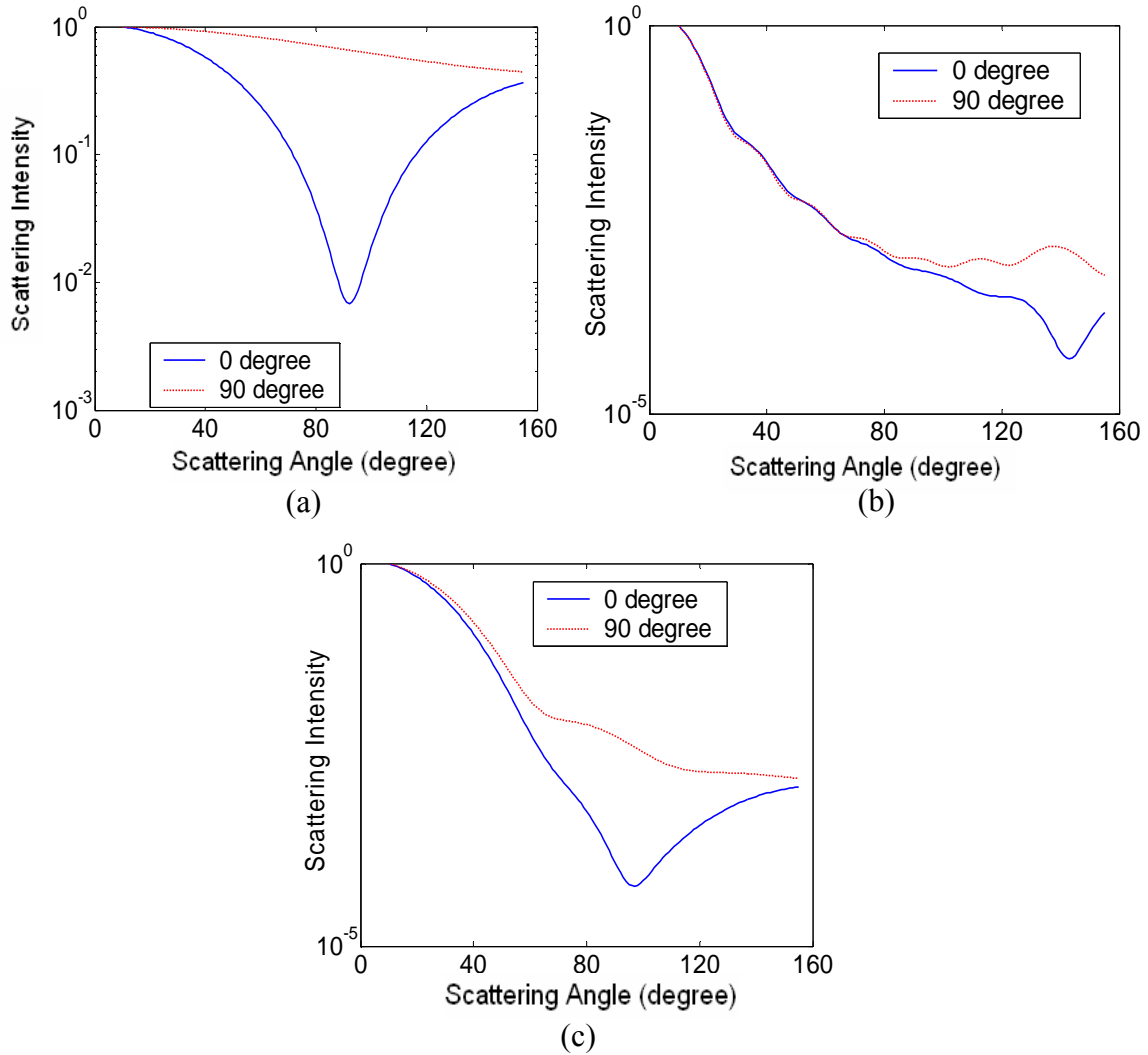


Figure 5.3 Angular scattering from Mie theory for (a) mono-sized medium with $a=100\text{nm}$, $m=1.2$; (b) mono-sized medium with $a=1\mu\text{m}$, $m=1.2$; (c) multi-sized medium with exponential size distribution function and $\langle a \rangle=100\text{nm}$, $m=1.1$. Blue solid line is for 0° polarization, red dashed line for 90° polarization.

5.2.B.2 The Simulation Studies for Effective Scatterer Size Estimation

5.2.B.2.1 Effective Scatterer Size Estimation Method

As stated in 5.2.A, once we obtained the angle-resolved scattering data from the experiment, the effective scatterer size information was estimated by comparison with the Mie theory model using least-square minimization methods, equation (5.1).

The estimation method was tested initially with simulated data following this procedure:

- (1) generate angular scattering phase function data from Mie theory
- (2) add Gaussian-distributed random noise to the simulated data
- (3) normalize these data at a certain angle
- (4) take the logarithm of these data
- (5) calculate the error relative to Mie theory prediction for all effective sizes possible.

As stated in 5.2.B.1.2, there is an obvious difference in angular scattering when using different laser polarizations. So estimation of the effective scatterer size was tried size using data sets from both polarizations, P1 and P2, as well as the ratio between these two data sets.

5.2.B.2.2 Effective Scatterer Size Estimation Results

Data from mono-sized scattering media with true size $a=100\text{nm}$ and 500nm were evaluated, and the results are shown in Figure 5.4 and Figure 5.5 respectively.

In each one, different noises were added, and different normalization angles and different laser polarizations were used. The estimation results are shown in each figure. For example, Figure 5.4(a) indicates, for the mono-sized scattering media with true size $a=100\text{nm}$, if we add 5% noise to the forward data obtained from Mie Theory, and used 50° as the normalization angle, then the estimated sizes were 95nm , 100nm and 90nm , respectively for the three data sets from 0° polarization, 90° polarization, or the ratio between them.

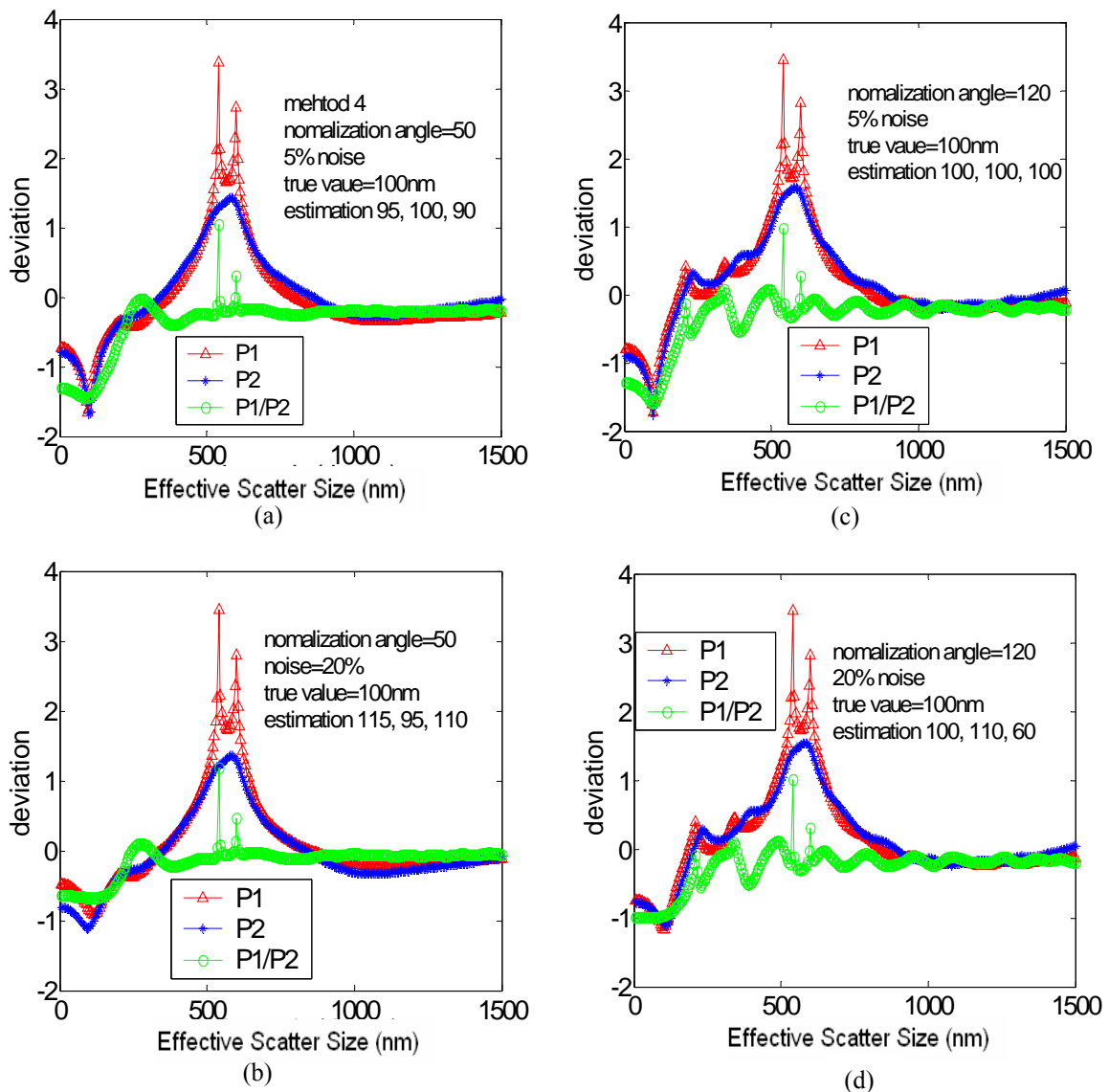


Figure 5.4 Effective scatterer size estimation results for mono-size scattering medium with true size $a=100\text{nm}$ using different normalization angles and different laser polarizations with different noises added. The y-axis shows the least-square difference between the simulated data and the value for each possible size of scatterer. The minimum value is precisely near $100 \pm 10 \text{ nm}$ as would be expected.

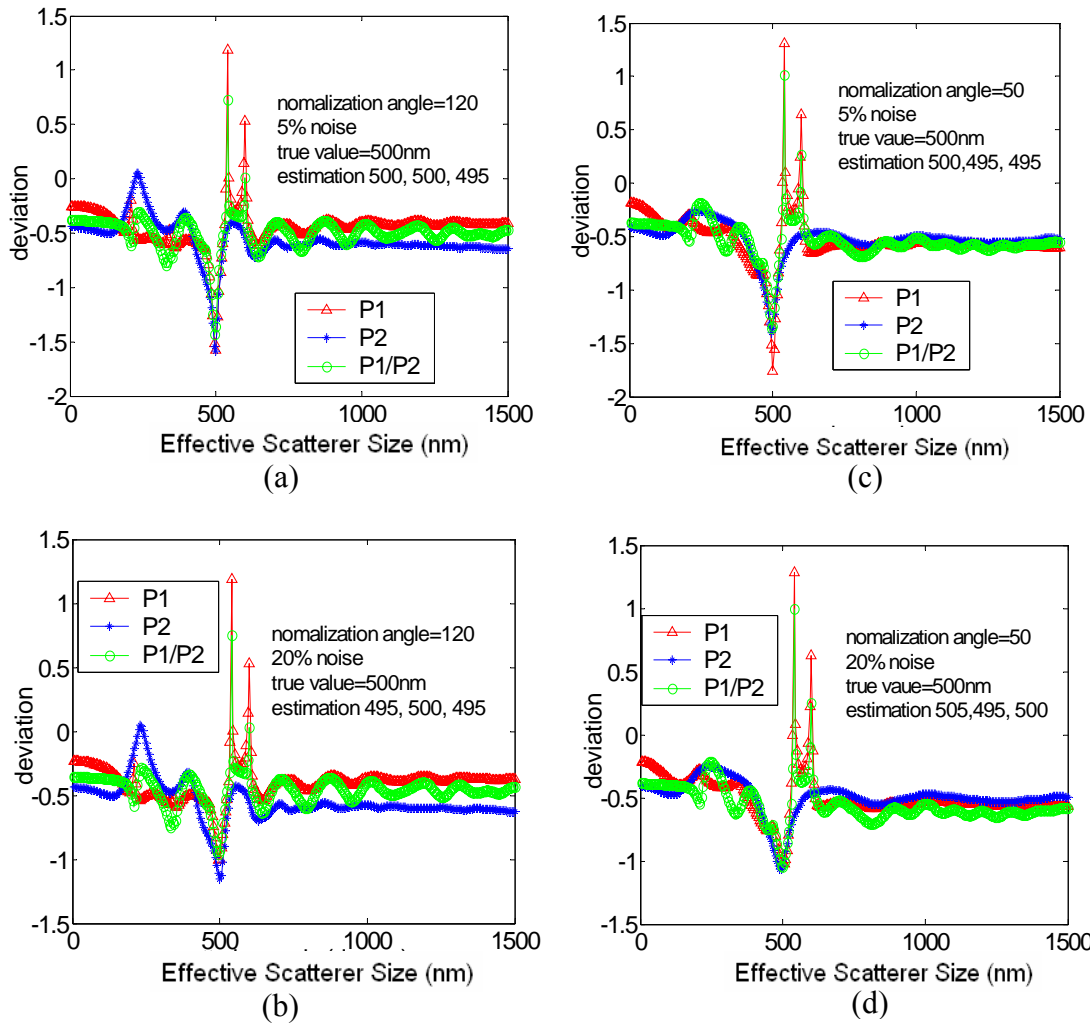


Figure 5.5 Effective scatterer size estimation results are shown for mono-size scattering medium with true size $a=500\text{nm}$ using different normalization angles and different laser polarizations with different noises added. The y-axis shows the least-square difference between the simulated data and the value for each possible size of scatterer. The minimum value is precisely near $500 \pm 5 \text{ nm}$ as would be expected.

The simulation results indicated that reasonable estimation of the size could be achieved with this approach. The only problem is that there were many local minima when we use the least minimization method, and so development of a fast automated fitting procedure appears difficult with these data sets.

5.2.C Experimental Study

5.2.C.1 Experimental Apparatus

A goniometer was used to experimentally measure the phase function of an optically thin tissue section or dilute suspension. A block diagram of the experimental setup is shown in Figure.5.6:

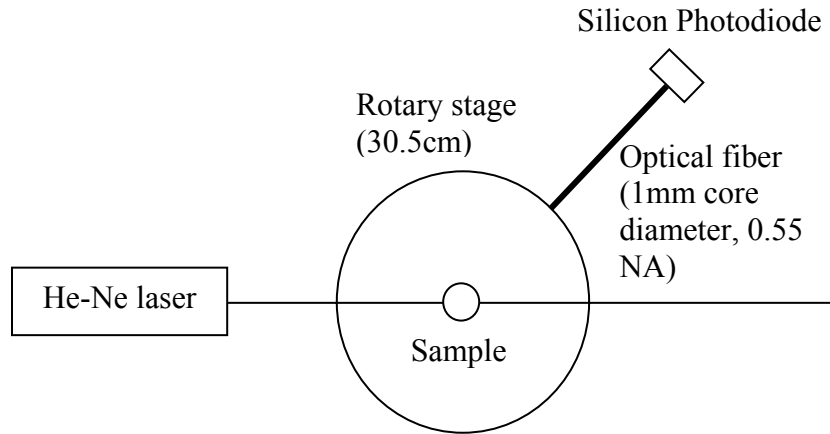


Figure 5.6: The diagram of the experimental setup is shown for angle resolved light scattering measurement. The set up used was a HeNe laser with collimated output beam at 633 nm wavelength, and a silicon photodiode detector with automated gain control, from Newport Inc.

The dilute suspension scattering sample was placed in a cylindrical cuvette (Model 540.115, Helma, Plainview, NY). Thin tissue sections for scattering samples are held between two glass slides with a fixed thickness and waxed edges to create a water tight thin cuvette. These cuvettes were positioned above the center of a 30.5 cm diameter rotary stage (RT-12, Arrick Robotics, Tyler, TX). Red light ($\lambda=632.8$ nm) from a 20 mW helium-neon laser was directed through the cuvette, or directed vertically through the thin tissue section sample. In all of these measurements, the laser was linearly polarized perpendicular or parallel to the surface of the rotary stage. Light scattered from the sample was collected by an optical fiber (1mm core diameter, 0.55 NA) that was mounted

at the edge. Light exiting the fiber was measured by a silicon photodiode (Newport Power Meter) and digitized by a 16-bit DAQ Board (National Instruments Inc.). A PC-controlled stepper motor rotated the stage continuously from approximately 20-150 degrees with respect to the forward direction of the laser at an angular resolution of 0.2 degrees. For a thin tissue section scattering sample, the data between the angular range of 70-110 degrees was taken out from the result, as it was corrupted by diffraction in the glass cuvette walls. The angular position was read out from an optical encoder, and the stage position and photodiode voltage were simultaneously recorded. The data acquisition was automated and controlled by a Labview program. Each scan of the full angular range took approximately 2 minutes.

5.2.C.2 Experimental Samples

The two geometries for sample holders used in this experiment are shown in figure 5.7. The cylindrical geometry in (a), viewed end on, was most useful, but not practical for tissue samples, so the thin slab geometry is more appropriate for tissue samples. The artifacts of this thin slab geometry are many, but most accentuated near 90° and 270° , such that these data are eliminated from the analysis.

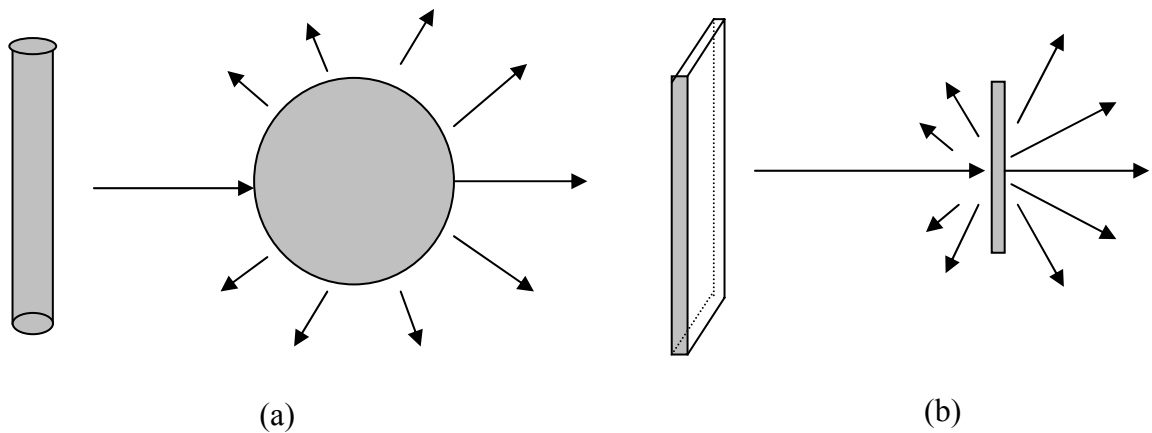


Figure 5.7: (a) Cylindrical specimens were used for particle or cells in solution. (b) Thin cuts of tissue were used for ex vivo sample.

(1) Cylindrical cuvette: for particle or cells in solution. The scattering angle for measurement could cover 20-150 degrees;

(2) Thin cuvette: The scattering angle for measurement could cover 20-70 degrees and 110-150 degrees. Thin slices of tissue or liquid can be used in this sample, held in between two glass slides with a fixed thickness and with waxed edges to create a water tight thin cuvette.

For experimental measurement of the phase function of the dilute suspension, first we need to make the suspension dilute enough to satisfy the condition in which the photons we measured only undergo a single scattering event. Secondly, a background intensity measurement is taken with the suspending solution in the absence of the scattering sample. The sample is then added to the solution and mixed well to be homogeneous. Then the scattering data from the sample suspension itself is obtained by subtracting the background data from the total data.

This study was done with three types of phantoms and two human breast tissue thin sections, including:

(1) Phantoms: (thin slab and cylindrical)

(i) 100nm polystyrene spheres: single-sized ($m=1.6/1.33$).

(ii) 1um polystyrene spheres: single-sized ($m=1.6/1.33$).

(iii) Intralipid: Exponentially decreasing distribution function,

(EM results: $\langle a \rangle = 97 \pm 3 \text{ nm}^{[1]}$, $m=1.47/1.33$).

(2) Breast tissue: (thin slab sections)

(i) Fat tissue section (thickness is 120um) ($m=1.49/1.36$).

(ii) Fibrous tissue section (thickness is 120um) ($m=1.4/1.36$).

5.3. Results

5.3.A Results for Phantoms with the Cylindrical cuvette

The angular scattering measurements for these three phantoms in cylindrical cuvette were obtained from our goniometer system and are shown in Figure.5.8. The results look similar to their corresponding simulation study that is shown in Figure 5.3. There are some differences in terms of the order of magnitude of the curves, yet the shapes of the curves are quite similar to the theoretical estimates. The inability to measure scatter near an angle of zero limits the ability to do a quantitative match, yet normalized and relative data fitting is still possible with these types of measurements.

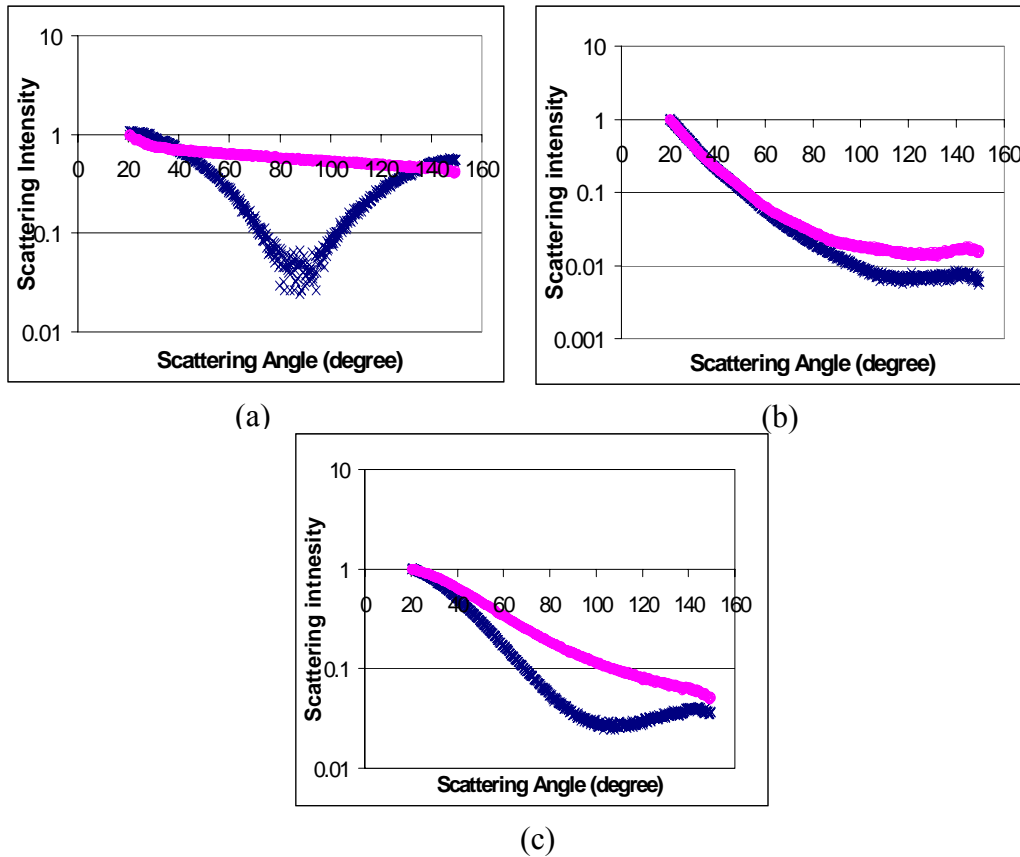


Figure 5.8 Angular scattering measurement for the following phantoms held in cylindrical cuvette, including (a) polystyrene microspheres in suspension with $a=100\text{nm}$; (b) polystyrene microspheres suspension with $a=1\mu\text{m}$; and (c) diluted Intralipid. The data shows blue ‘*’ points for 0° polarization, and magenta ‘o’ points for 90° polarization.

5.3.B Results for Phantoms in Thin Cuvette

The angular scattering measurement for these three phantoms held in thin cuvette (which is formed by two glass slides with a fixed thickness and waxed edges to make it water tight) are shown in Figure.5.9. The results look to their corresponding simulation studies that are shown in Figure 5.3. It indicates that the thin cuvette sample holder worked well for this experiment, so it could be used for the breast tissue section study.

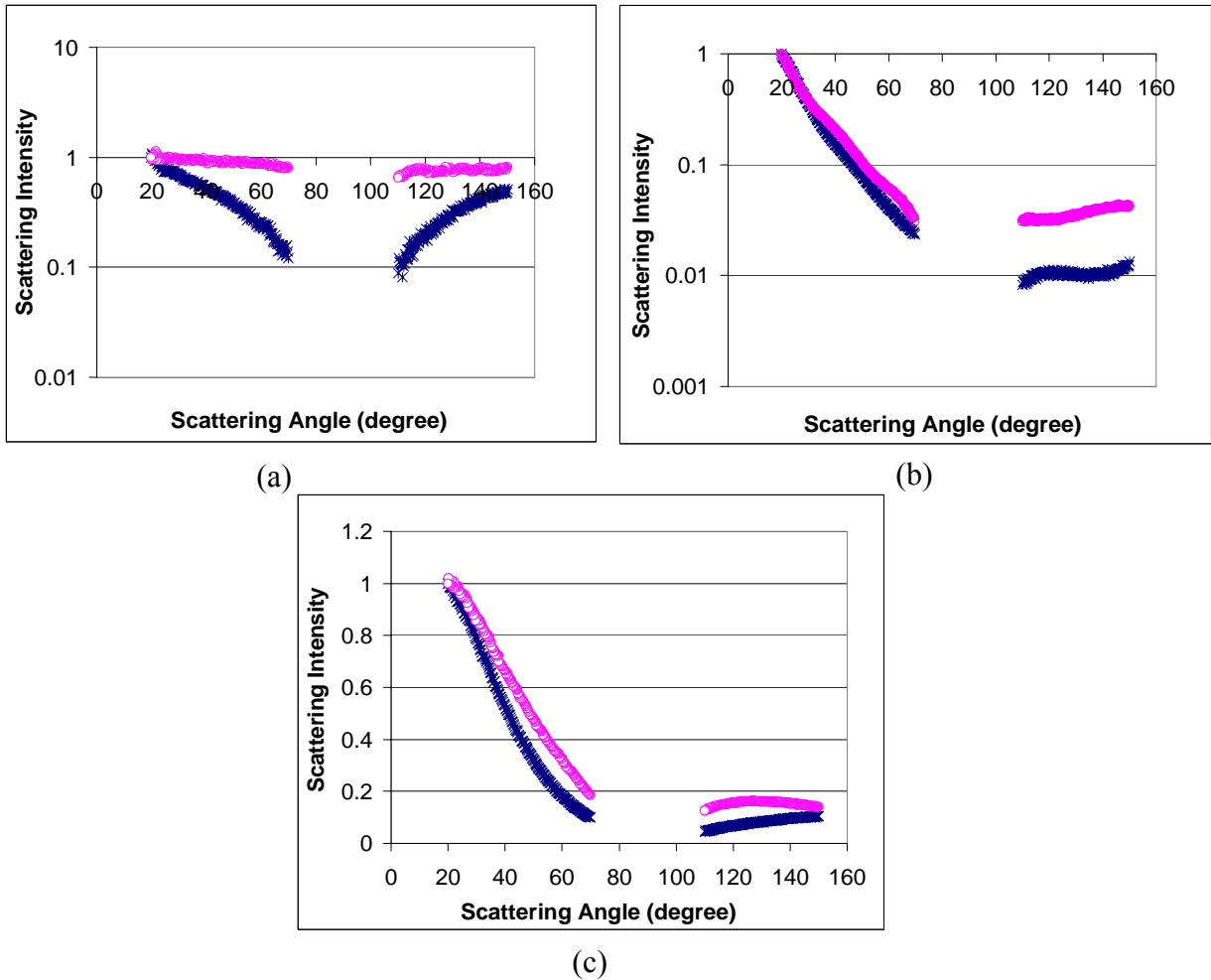


Figure 5.9 Angular scattering measurement for the following phantoms held in thin cuvette (a) polystyrene microspheres suspension with $a=100\text{nm}$; (b) polystyrene microspheres suspension with $a=1\mu\text{m}$; (c) Intralipid. The data shows blue ‘*’ points for 0° polarization, and magenta ‘o’ points for 90° polarization.

5.3.C Results for Breast Tissue

The measured scattered data for breast tissue samples is shown in the figure 5.10. While the features are not as distinct as the sample solutions, it is clear that there are angular shape changes which are distinct between the two samples, especially between 110 and 150 degrees.

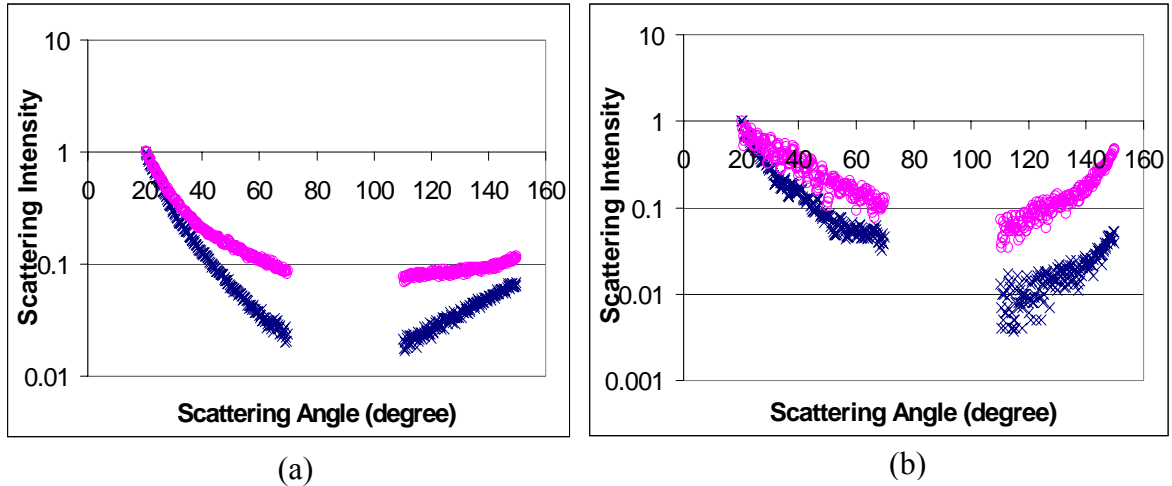


Figure 5.10 Angular scattering measurements are shown for the following breast tissue sections held in a thin cuvette, for (a) fat tissue and (b) fibroglandular tissue, using thickness of 120 μ m. The data shows blue ‘*’ points for 0° polarization, and magenta ‘o’ points for 90° polarization.

5.4. Effective Scatterer Size Estimation Results

5.4.A Effective Scatterer Size Estimation Results for Phantom

Fitting for the effective particle size was completed using the methods described above in section 5.2. For the 100nm polystyrene spheres, the least square error for all possible sizes of particles assuming a mono-disperse size distribution is shown below in Figure 5.11. Different normalization angles and different laser polarizations were used in the fitting. Figure 5.11(a) indicates if we use 60° as the normalization angle, the estimated sizes were 5nm, 70m and 245nm, respectively for the three data sets from 0° polarization, 90° polarization, or the ratio between them. Figure 5.11(b) indicates if we use 130° as the normalization angle, the estimated sizes were 1085nm, 70m and 255nm, respectively for the three data sets from 0° polarization, 90° polarization, or the ratio between them,

indicating that the variety of local minima with different data sets was quite extreme. However the 90 degree polarization data set appeared to be most accurate.

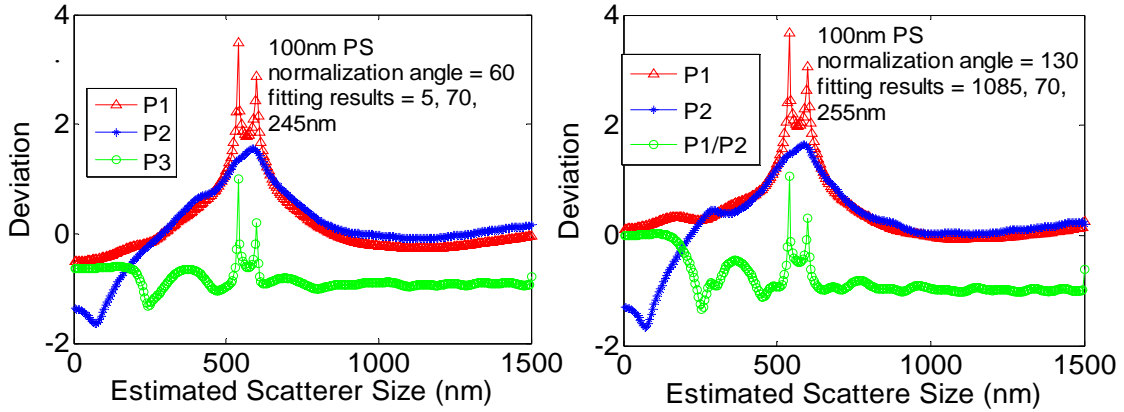


Figure 5.11 The fitting result for the polystyrene microspheres suspension with $a=100\text{nm}$ using different normalization angles of (a) 60° and (b) 130° .

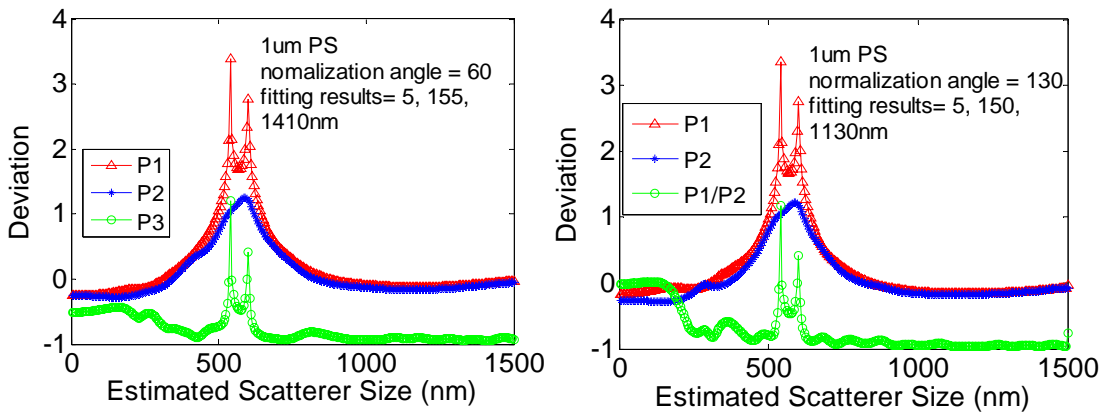


Figure 5.12 The fitting result for the polystyrene microspheres suspension with $a=1\mu\text{m}$ using different normalization angles of (a) 60° and (b) 130° .

For the $1\mu\text{m}$ polystyrene spheres, the least square error for all possible sizes of particles assuming a mono-disperse size distribution is shown below in Figure 5.12. Different normalization angles and different laser polarizations were used in the fitting. Figure

5.12(a) indicates if we use 60° as the normalization angle, the estimated sizes were 5nm, 15m and 1410nm, respectively for the three data sets from 0° polarization, 90° polarization, or the ratio between them. Figure 5.12(b) indicates if we used 130° as the normalization angle, the estimated sizes were 5nm, 150m and 1130nm, respectively for the three data sets from 0° polarization, 90° polarization, or the ratio between them, again showing that the objective function minimization was not ideal for several of these data sets.

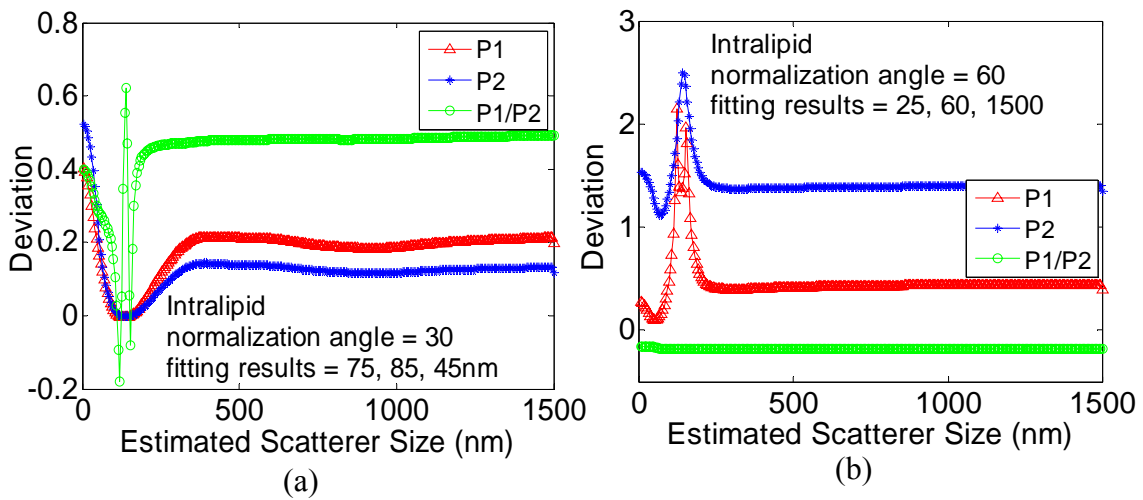


Figure 5.13 The fitting result for the Intralipid suspension using different normalization angles of (a) 30° and (b) 60° .

For the Intralipid, the least square error for all possible sizes of particles assuming an exponential size distribution is shown below in Figure 5.13. Different normalization angles and different laser polarizations were used in the fitting. Figure 5.13(a) indicates if we use 30° as the normalization angle, the estimated sizes were 75nm, 85nm and 45nm, respectively for the three data sets from 0° polarization, 90° polarization, or the ratio

between them. Figure 5.13(b) indicates if we use 60° as the normalization angle, the estimated sizes were 25nm, 60m and 1500nm, respectively for the three data sets from 0° polarization, 90° polarization, or the ratio between them, indicating that the 90 degree polarization wave likely the best data set, and the other two were likely unreliable..

Interestingly, with experimental data the fitting process is not as clear as with simulated noisy data, and the minimal values occur at different sizes based upon the type of data used for fitting. In these cases though, for the smaller-sized scatterer (the 100nm polystyrene spheres and the Intralipid) the 90 degree polarization data appears to provide the best fit to the true particle size; while for the larger-sized scatterer (the 1um polystyrene spheres) the between the two polarization data appears to provide the best fit to the true particle size. This may result from the fact that for the smaller-sized scatterers, 90 degree polarization creates the largest slope change in the data as a function of angle, thereby providing the strongest measure of size; while for the larger-sized scatterers, neither 0 degree polarization or 90 degree polarization create a large slope change in the data as a function of angle. Since the most important scatterers in tissue are thought to be subcellular organelles that has smaller size, such as mitochondria, lysosomes, Golgi bodies, vesicles, and so forth, all of which have sizes in the range of 50 to 500 nm or less [48, 54], we will take the 90 degree polarization when using goniometer to study the breast tissue section.

5.4.B Effective Scatterer Size Estimation Results for Breast Tissue

The angular scattering measurement for tissue sections with laser in P2 polarization are shown in Figure.5.14. It indicates that there are more large angle

scattering, and that indicates a smaller average particle size in the fibroglandular tissue than the fat tissue.

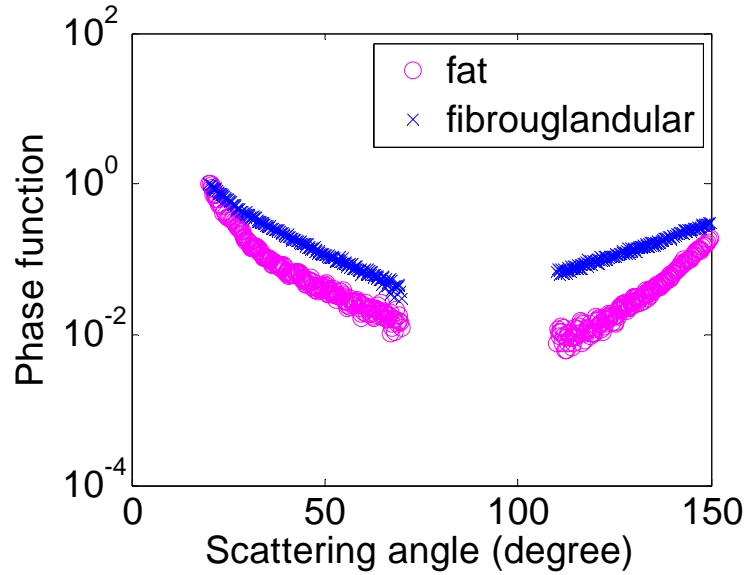


Figure 5.14 Angular scattering measurements for fat (blue ‘x’) and fibroglandular (magenta ‘o’) breast tissue with thickness 120 μ m. The polarization of the laser is 90 $^\circ$.

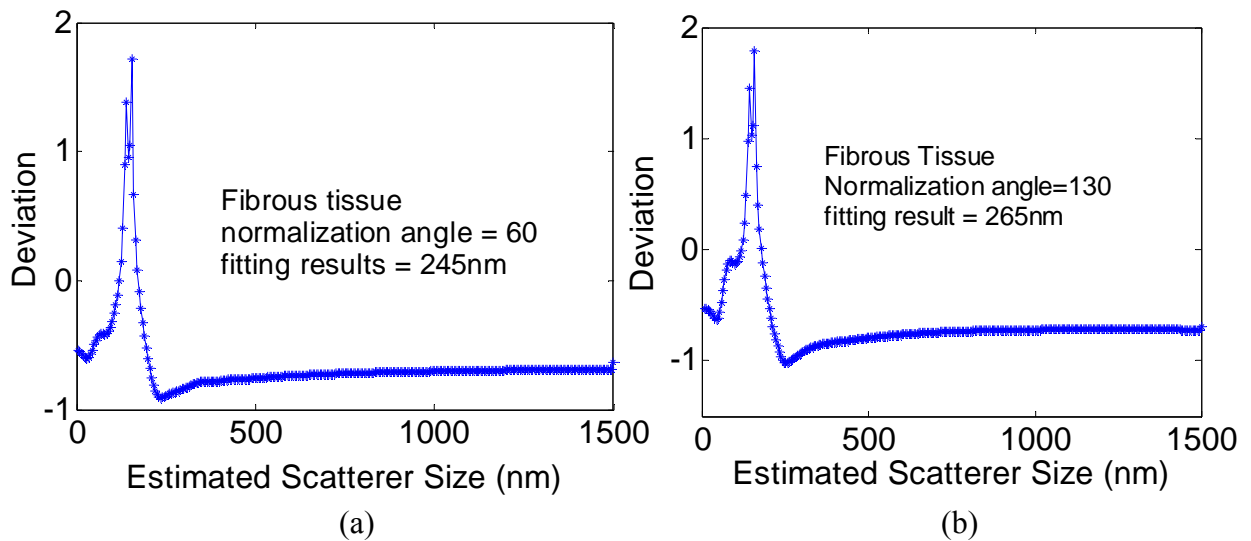


Figure 5.15 The fitting result for the fibrous tissue section using different normalization angles of (a) 60 $^\circ$ and (b) 130 $^\circ$.

For the fibrous tissue, the least square error for all possible sizes of particles assuming an exponential size distribution is shown below in Figure 5.15. Different normalization angles and 90° laser polarizations were used in the fitting. Figure 5.15(a) indicates if we use 60° as the normalization angle, the estimated sizes were 245nm. Figure 5.15(b) indicates if we use 130° as the normalization angle, the estimated sizes were 265nm.

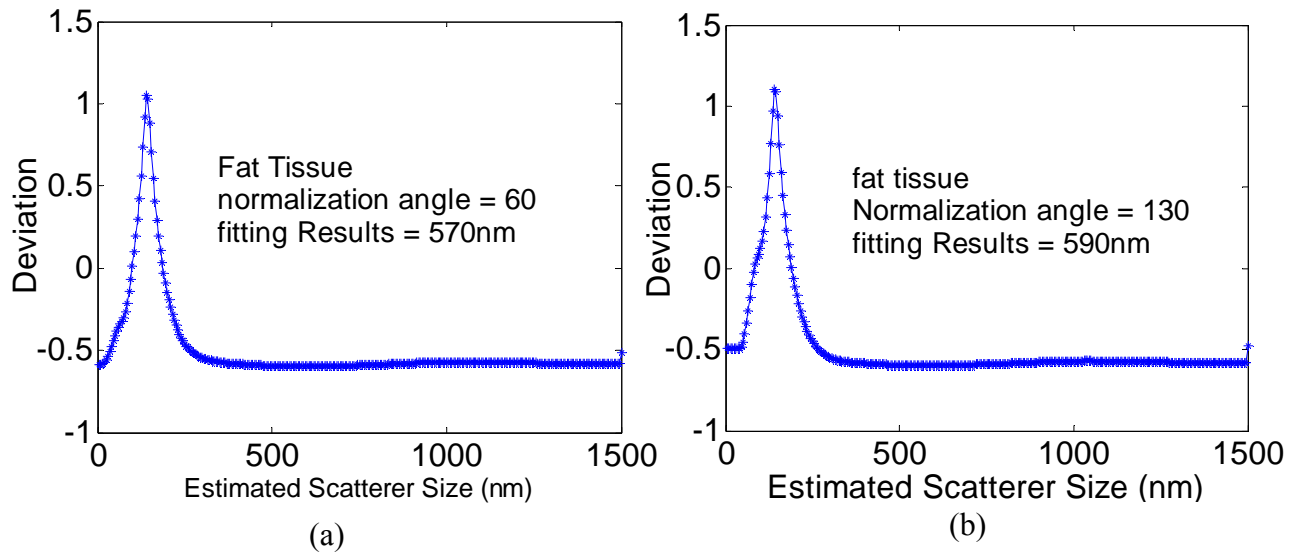


Figure 5.16 The fitting result for the fat tissue section using different normalization angles of (a) 60° and (b) 130° .

For the fat tissue, the least square error for all possible sizes of particles assuming an exponential size distribution is shown below in Figure 5.16. Different normalization angles and 90° laser polarizations were used in the fitting. Figure 5.16(a) indicates if we use 60° as the normalization angle, the estimated sizes were 570nm. Figure 5.16(b) indicates if we use 130° as the normalization angle, the estimated sizes were 590nm.

5.5. Discussion

So by defining the particle size distribution form first, it is possible to use Mie theory to solve for the effective scatterer size from these types of angular scattering measurements. The simulation results and phantom studies indicate that the estimation process appears to have significant problems in finding a global minimum. The major problem experienced was that there appeared to be many local minima in the least squared fitting space, for certain data sets. The particle sizes fit for Intralipid and the 100 micron polystyrene spheres were close when the data set from the 90 degree polarization were used, yet when using 1 micron polystyrene spheres this was not the case. Fitting to data from tissue samples with a small angle for normalization, showed a fit to 255 ± 10 nm size for fibrous tissues and 580 ± 10 nm for fatty tissues. While these numbers are consistent with the general ranges of what would be expected, the accuracy of this approach was felt to be less than satisfactory, and so we did not use it in the rest of the thesis, while the following chapters show some microscopy analysis which was completed as a more direct analysis of the particle sizes.

Chapter 6. Estimation of Sub-Cellular Particle Size Histograms with Electron Microscopy

Scattering originates from the sub-microscopic features of the tissues, yet the existing tools to measure this information and predict which features contribute to the scattering spectrum are limited by the lack of direct method to quantify the particle sizes. Breast tissue was examined here with transmission electron microscopy and analysis showed that the distributions of particle sizes appear well described by a double exponential function for most tissues. The average particle size histograms of high grade infiltrating ductal carcinoma, low grade infiltrating ductal carcinoma, fibroglandular tissue and adipose tissue were examined, and the particle histograms were progressively decreasing in magnitude for these tissue types, and the average size of the particles increased, for these four tissues respectively. Typical particle sizes in the range of 10 to 500 nm for these tissue types, with bi-exponential fitting, gave two particle distributions; one near 20-25 nm for the smaller size and one at 110 to 230 nm for the larger distributions. Mie scatter theory was used to take these particle distributions and calculate scattering spectra. Similar results were obtained to the spectra observed in diffuse tomography, which provides supportive evidence that bulk imaging of scatter may be mapped over to predict factors related to the tissue ultrastructure

6.1 Introduction

As stated in 1.3.C, in NIR tomography the chromophore concentration can be obtained with inversion of the known molar absorption spectra as prior information. In contrast, the scattering of tissue comes from a less predictable origin, such as differences

in the index of refraction between the extracellular or cytoplasmic fractions of tissue, the lipid composition of the membranes bounding each cell and cellular organelle, and the structure of tissue resulting from membrane bound sub-cellular organelles¹⁻⁶. Due to this large complexity, there has not been a direct method to quantify the structure of the tissue from the scattering properties recovered from NIR tomography. Nonetheless, many recent studies have shown that scattering parameters measured from tissue can be uniquely correlated to tissue pathology for epithelial diseases where immediate backscattering was measured [58, 60, 61, 71, 103]. One important feature of NIR tomography in imaging tissues is its potential to characterize the structural changes which occur at the sub-microscopic level, perhaps related to the size and density of sub-cellular features or extracellular features. While much research has focused on extracting cellular and sub-cellular sizes and density values from scattering, there are significant assumptions and simplifications that must be made in this process, mostly related to the application of Mie scattering theory. One important assumption is in the distribution of particle sizes present in tissue. In this study, both normal and diseased breast tissues were examined with electron microscopy to quantify the particle size histogram. These histograms are central to being able to estimate particle size and density from diffuse scattering tomography [22, 23, 91, 92, 104], as well as better understand how light interaction with tissue in general can be used to interpret microscopic features of the tissue.

The most important subcellular organelles that have sizes which would contribute to scattering are mitochondria, lysosomes, Golgi bodies, vesicles, and so forth, all of which have sizes in the range of 50 to 500 nm or less [48, 54]. This size scale is thought

to be in the same range as the wavelength of light, but possibly extending well above and well below this size scale. Thus the light microscope can not provide enough resolution for imaging these scatterers due to the diffraction limitation of light. So, electron microscopy provides a one way to solve this, by being able to image structures with significantly superior resolution. van Staveren et al [47] used electron microscopy to quantify the size distribution of intralipid, a well known and well characterized scattering solution of emulsified lipids in water. They showed that the particle sizes were distributed as an exponentially decaying function with larger numbers of small particle sizes and significantly fewer at large sizes. They showed that estimation of this distribution provided an excellent way to estimate the bulk scattering coefficient spectrum of the solution. Electron microscopy distinguishes electron dense versus non-electron dense features of the tissue, and so membranes and areas of high density protein and lipid content appear darker than areas of interstitial fluid or cytoplasm. To enhance the contrast, tissues are stained with uranyl and lead, so the uranyl binds to phosphates and lead acts as an enhancer to the signal. Phosphates are contained in large amounts in nucleic acids but are also present in membranes. There is considerable support for the belief that intracellular membranes are a major contributor to scattering, yet essentially all the data about this is correlative, and there is not an independent measure of the size available. Thus, this part of the study remains a hypothesis, but will be examined in light of the resulting data.

From chapter 3-5 we know the histogram information is central to being able to estimate particle size and density from diffuse scattering tomography [22, 23]. In chapter 3-5, in breast tissue study, we used the exponentially decaying function as the distribution

shape got by Van Staveren et al [47] from Intralipid using electron microscopy. By this E&M study on breast tissue it might be possible to determine whether this exponentially decaying function assumption is suitable for breast tissue.

A secondary goal of this study was to use the histograms obtained from the EM images to predict the reduced scattering coefficient, and compare them with that observed in diffuse tomography. When the transmission data of diffuse tomography are taken, it is fit to diffusion theory to obtain the reduced scattering spectrum. The same spectrum could then be estimated from Mie theory, and so the goal here was to examine the shape and magnitude of these spectra to see if they are similar. If similar spectra can be obtained, then it makes sense that diffusion theory derived spectra could be used to estimate effective particle size and number density values and images. This has already been shown in previous studies [22, 23], however the justification for using the assumed exponential distribution of particle sizes was not validated prior to this present study.

As stated in 1.4.A, although Mie theory strictly applies only for spheres in a homogenous background [47, 55, 56], yet it has used successfully in the interpretation of natural scattering phenomenon, and is a reasonable first order approximation [57]. However, it is also possible to consider that the scattering from subcellular organelles be viewed as a scattering from coated sphere (shell), where the membrane is a thin layer over another medium. Wilson et al [71] have shown that this gives a good estimate based upon angle resolved reflectance from cell suspensions undergoing apoptosis. Mie theory estimation of the scattering from shells has also been well developed and is also examined in the present study as a possible way to model the scattering, given estimation of the particle distribution histogram. In this chapter, both of these two models are

examined using particle histogram data got from the EM analysis, with the goal to determine which model fits the data more optimally.

6.2 Samples and Methods

6.2. A quantitative pathology analysis

Immediately after excision, 3 cases of normal breast (reduction mammoplasty specimens) and 3 infiltrating ductal carcinomas of breast were evaluated in the Department of Pathology, sampled according to standard diagnostic protocols and processed routinely (formalin-fixation, alcohol dehydration, paraffin-embedding). Each tissue specimen was taken from a different subject. A diagnosis was rendered on 4 micron-thick, routinely stained (hematoxylin and eosin) tissue sections. The histologic details are given in Table 1 [105].

Representative tissue sections from each case were also immunohistochemically stained using the pan-cytokeratin marker 5D3 (which highlights the epithelial component in the tissue) and the pan-endothelial marker CD31 (which highlights the endothelial-lined vascular channels). Tissue type ratios (E:S, Epithelium compared to fat and stromal fibrosis (E:S), fat compared to epithelium and stromal fibrosis (F:S/E), mean vessel density (MVD) and mean vessel area (MVA) in each case were assessed quantitatively using image processing techniques as described in a previous paper [106]. Using optimized color images from each slide, an automated macro in *ImageJ* was used to count vessel density and area based upon the grayscale thresholded outline of the vessels. Unbiased estimates of volume density for each tissue type (fat, stromal fibrosis and epithelium) in the tissue were obtained using point-counting stereology techniques.

Tissue diagnosis	E:S	F:S/E	Fibrosis/Fat/Epithelium	MVD	MVA
Normal breast	0.003	0.471	80 / 36 / 4	0.25	151
Normal breast	0.009	0.460	56 / 40 / 4	0.17	78
Normal breast	0.030	0.104	84 / 11 / 5	0.23	87
Infiltrating ductal carcinoma, low grade	0.166	0.040	6 / 3 / 91	1.02	75
Infiltrating ductal carcinoma, intermediate grade	0.214	0.011	0 / 0 / 100	0.85	74
Infiltrating ductal carcinoma, high grade	0.049	0.044	79 / 8 / 13	0.72	113

Table 6.1 The tissue samples used in this study were analyzed with quantitative pathology estimates from immunohistochemical specimen slides to calculate the epithelial to stromal ratio (E:S), fat to stromal and epithelial ratio (F:S/E), complete tissue type ratios, microvascular density (MVD), microvascular area (MVA).

6.2.B. Electron microscopy

For each of the 6 cases, 2 mm³ portions of fresh breast tissue were fixed in 5 cc 4% buffered glutaraldehyde for at least two hours at 4°C, then placed in 0.1M sodium cacodylate buffer at 4°C for at least 15 min. up to a week. From each of the 3 normal breast specimens, separate areas of fat and fibroglandular tissue were sampled. From each of the 3 breast tumor specimens, representative tumor was sampled. The tissue was then placed in 2% osmium tetroxide with 0.1M sodium cacodylate buffer for one hour at 4°C, followed by graded ethanol (50%, 70%, 90%, 100%) and then L.R. White (50%, 75%, 100%) washes. The tissue was embedded in L. R. White in covered gelatin capsules and allow to stand overnight at room temperature in a hood before being placed in a 60°C oven for 22 to 26 hours. The 0.5 micron thick sections were cut and stained with 1% Toluidine Blue, and selected areas were sectioned at 120 nm thickness, placed on 3.0 mm copper grids, and then stained with uranyl acetate and lead citrate. These samples were examined with a F.E.I.Tecnai F20 FEG Electron Microscope. To capture the relevant

features of each sample appropriately, a series of magnifications, 2550X, 4000X, 5000X, 7000X, 9900X, 15000X, 19500X, 29000X, 43000X, were used when took images for different tissues.

6.2.C. Image Processing

Using the electron microscopy images, the intra and extra cellular particles were quantified based upon the contrast in the EM images. Information about the magnification of the image, the thickness of the section, and then size in pixels of the digital EM picture contributed to converting raw counts into particle density values. The following calculation was used to achieve number density of particles (1/mm³).

$$N = Count \times \left(\frac{\pi 66nm^2}{10 pixels} \right) \times \left(\frac{4000X}{M} \right)^2 \times A \times t \times 10^{-18} \quad (6.1)$$

where *Count* is the number of particles we get from the EM image, *A* is the area in pixels of the image, *t* is the thickness of the section which was set at 100 nm, and *M* was the magnification of the image, here used in the ranges of 2500X up to 43,000X, with a range of sizes for each tissue type. In order to increase the dynamic range over which the sizes could be reliably quantified, it was important to include multiple magnifications of images. In the normal fibroglandular tissue, 6 separate images were analyzed, and in the ductal carcinoma tissue 4 images were quantified, and in the adipose tissue 3 images were quantified, each on different ranges of magnification.

Take one EM picture as an example. It was first thresholded in *ImageJ* based upon a certain threshold. Then a morphological operator *Analyze Particles* in the software package *ImageJ* was used to approximate the image as a conglomeration of

ellipses and then measure the radii of each, thus establishing a particle size distribution. Varying thresholds were examined over the entire range of possible values, and all images were analyzed at 5 different threshold values. In this study it was determined that the threshold value varied the numbers of particles counted, but did not have a major effect upon the shape of the particle size histogram. The same series of procedures were carried out on all images. In order to avoid bias related to the choice of threshold, an equi-spaced range of threshold values were used for each image, and the resulting values were all pooled together for each image to create a composite of values for all thresholds. It is worth to mention that this *Analyze Particles* feature of *ImageJ* works on binary images only, after thresholding, and counts particles that are dark and can be completely separated from other particles. Thus overlapping regions will be lumped together in this type of analysis, yet by varying the threshold value it is possible to limit the effect of overlapping regions. The minimum and maximum allowable particle size was specified in units of pixels to be between 10 and 2500 pixels in size with 250 possible distinct sizes. Thus using images of differing magnification was important to expand the usable dynamic range.

6.2.D. Mie Theory calculation for reduced scattering spectra

In Chapters 3-5, the Mie scattering code for scattering sphere was adapted from a program developed by Dave Barnett, Loughborough University, (<http://www.lboro.ac.uk/departments/el/research/photonics/matmie/mfiles.html>). In this chapter, for a direct comparison between shell and spherical treatment, the Scattering codes for both sphere and shell were adapted from the programs developed by Christian Matzler, Institute for Applied Physics, University of Bern (<http://www.t-matrix.de/>).

Mie.m and Miecoated.m are used separately to calculate the scatter efficiency from sphere and shell. Each code has the output [Q_{ext} , Q_{sca} , Q_{abs} , Q_{backscat} , g , Q_{ratio}]. The input for Mie.m is (m, x) , where $m=n_2/n_1$ is the complex refractive index with n_1 and n_2 being the refractive index of the medium and sphere respectively, and $x = 2\pi a/\lambda$ is the wave number in the medium with a being the particle radius; the input for Miecoated.m is (m_1, m_2, x, y) , where m_1 and m_2 are inner and outer refractive index separately, and $x=2\pi a/\lambda$ and $y=2\pi b/\lambda$ are wave numbers with a and b being the inner and outer radius respectively. Suppose n_1, n_2, n_3 are the indexes of the medium, the shell and the core respectively, then $m_1= n_3/ n_1, m_2= n_2/ n_1$.

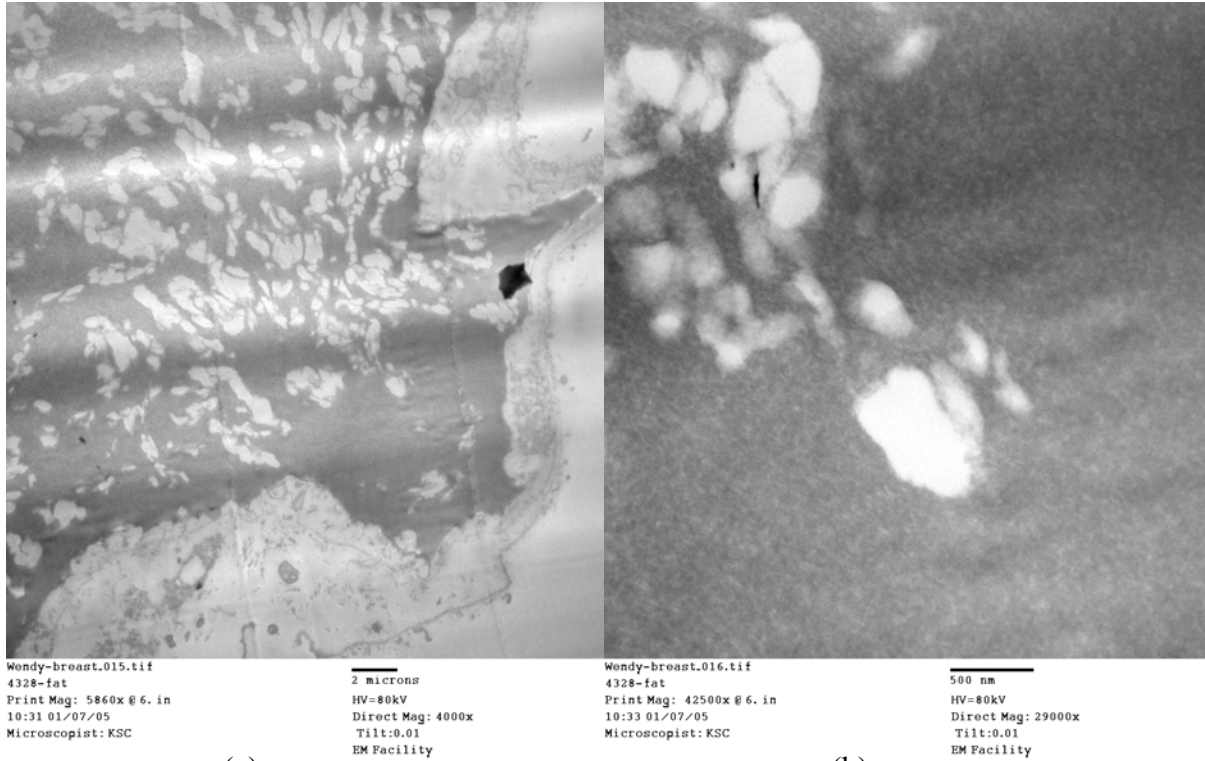
For the sphere model, set $n_1 = 1.35$ and $n_2 = 1.40$, so $m=1.04$. These values correspond with experimental evidence of the indices of the cytoplasm and of the extracellular material [107]. For the shell model, set $n_1 = 1.35$ and $n_2 = 1.46$ and $n_3 = 1.35$. So $m_1=1$ and $m_2=1.0815$. The thickness of the shell was taken to be 9 nm, corresponding to the estimated thickness and index of the bilipid membrane in cells and organelles [108].

The reduced scattering spectra could be obtained using equation (2.12) with the calculated Q_{sca} , g and the histogram obtained from the EM image.

6.3 Results

6.3.A Typical EM images

Structures that can be viewed in electron microscopy are shown Figures 6.1-6.4 for typical adipose tissue, fibroglandular tissue, low grade infiltrating ductal carcinoma tissue and high grade infiltrating ductal carcinoma tissue separately.



(a) (b)
Figure 6.1 Electron microscopy images of normal adipose tissue example images are shown in (a) and (b), at 4000X and 29,000X respectively.

From all these images, we could tell that adipose tissue is distinctly different from other tissues, with well circumscribed fatty regions distributed across the image in Figure 6.1(a). Close up view of some of these are shown in Figure 6.1(b). Cutting Adipose sections is known to be difficult, due to the fact that the tissue does not solidify well and tends to smear during the cutting process. Thus, obtaining clear adipose sections for EM microscopy is challenging.

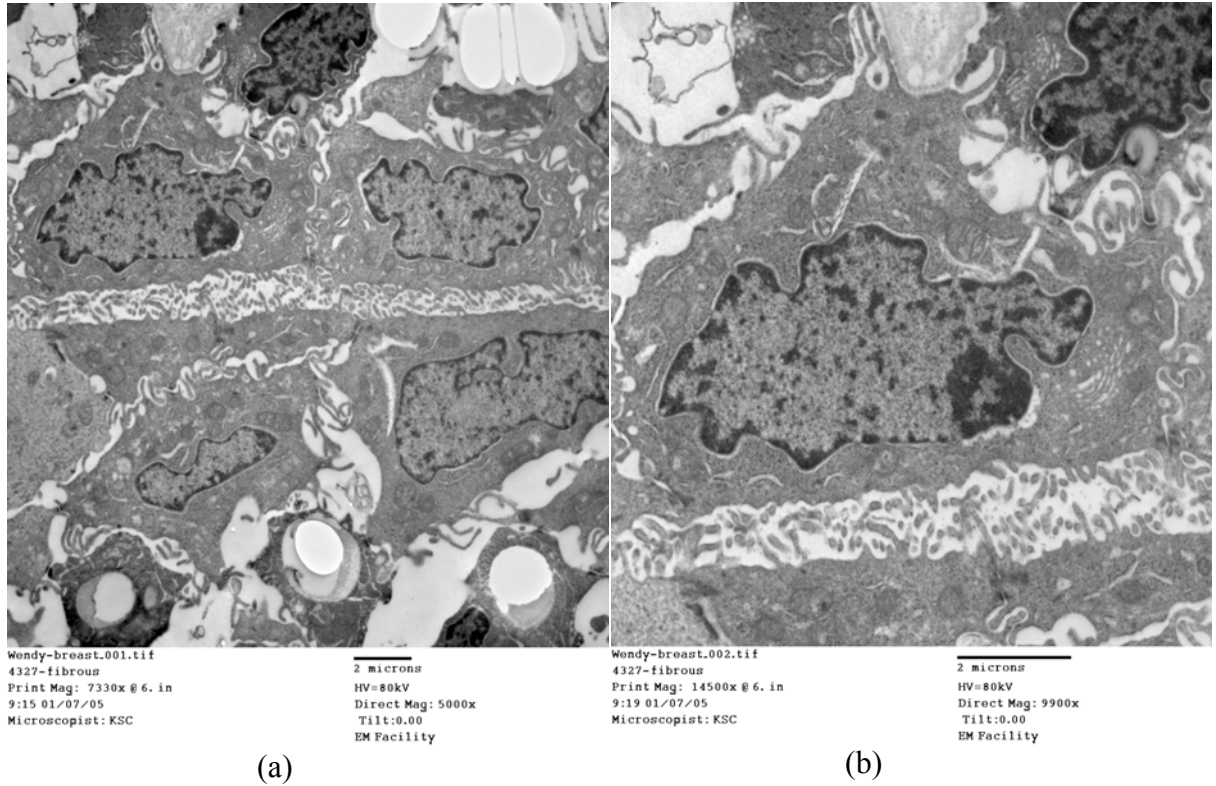


Figure 6.2 Electron microscopy images of normal fibroglandular tissues (a) and (b) at magnifications of 4000X and 15000X respectively.

Fibroglandular tissues are dominated by epithelial cells and structural matrix components of collagen. In Figure 6.2(a), there are several epithelial cells which can be found by their darker nuclear regions, which are distended in these cells and scattered in their interior. Around these nuclear regions, there are many mitochondria and other subcellular constituents. Basically the majority of the cellular interior is composed of a bi-lipid layer bound organelles, as can be seen more clearly in Figure 6.2(b).

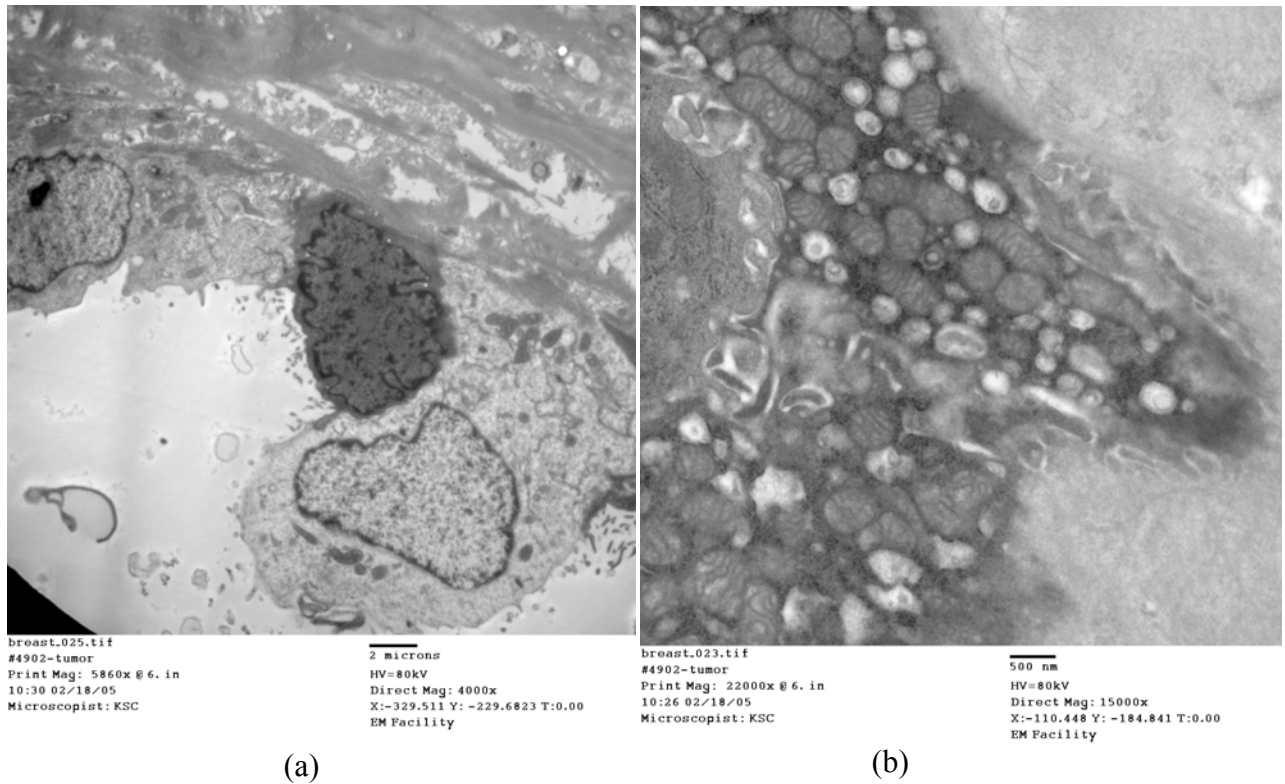


Figure 6.3 Electron microscopy images of low grade infiltrating ductal carcinoma tissue (a) and (b) at magnifications of 4000X and 15000X respectively.

In carcinoma tissues, as shown in Figure 6.3 for a low grade infiltrating ductal carcinoma tissue and Figure 6.4 for a high grade infiltrating ductal carcinoma tissue, the epithelial cells are more infiltrating and generally have larger nuclei and higher numbers of mitochondria. The overall pattern is highly variable and thus it is difficult to come up with standardized descriptions. Both low magnification images (Figure 6.3 (a) and Figure 6.4 (a)) and high magnification images (Figure 6.4 (a) and Figure 6.4 (a)) are presented here for a better view.

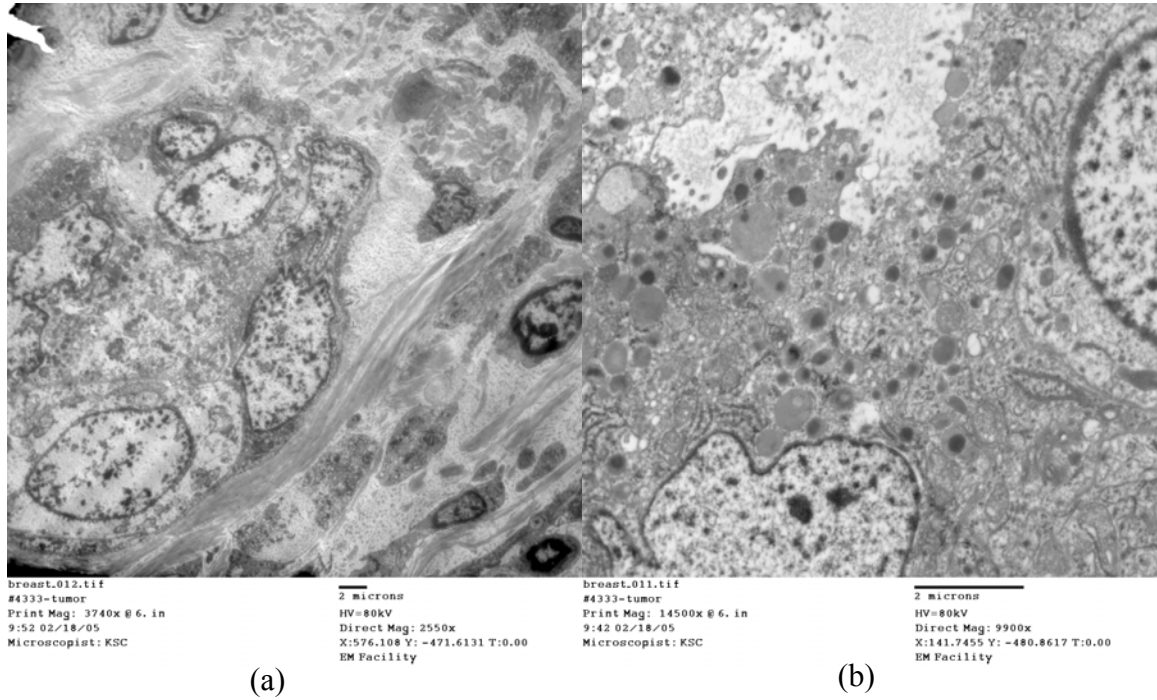


Figure 6.4 Electron microscopy images of higher grade infiltrating ductal carcinomas tissues (a) and (b) at magnifications of 2550X and 9900X respectively.

6.3.B EM images Analysis

The process for particle size analysis of the EM image Figure 6.2 (a) is shown in Figure 6.5. (a) shows the thresholded image of the original EM image for one particular threshold value, where the parts that were marked in red were analyzed to get size information, while the remaining parts were not analyzed. Here (b) shows the outline of the red-marked parts in (a). In (c) the red-marked parts in (a) were represented as ellipses of their approximate size. The resulting distribution from this analysis is presented as a histogram of particle sizes in (d).

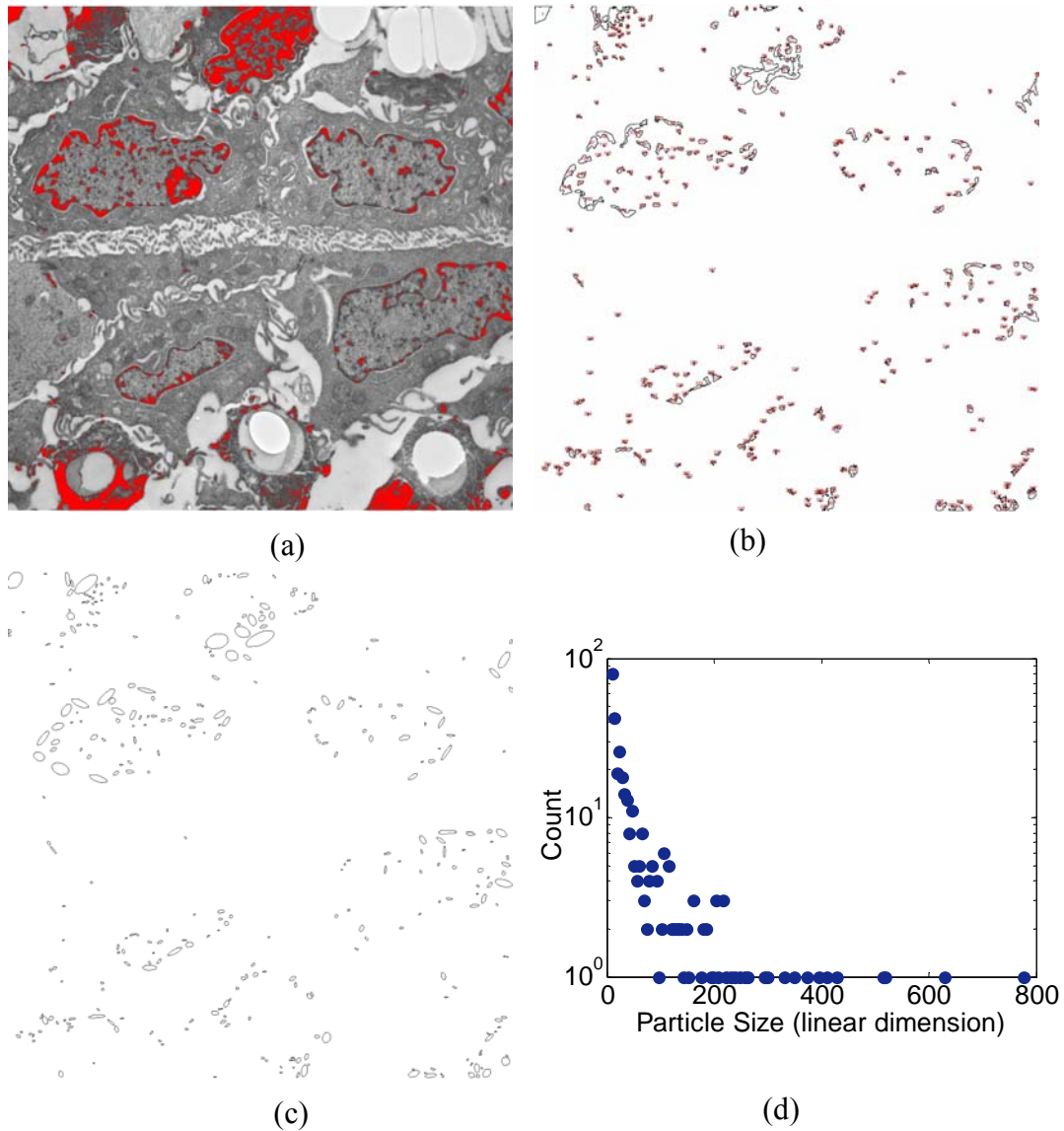


Figure 6.5 (a) shows the thresholded image of the original EM image for one particular threshold value, where the parts that were marked in red will be analyzed to get size information, while the left parts will not be analyzed. (b) shows the outline of the red-marked parts in (a). In (c) the red-marked parts in (a) were represented as ellipses of the approximate size. The result of this analysis is presented as a histogram of particle sizes in (d).

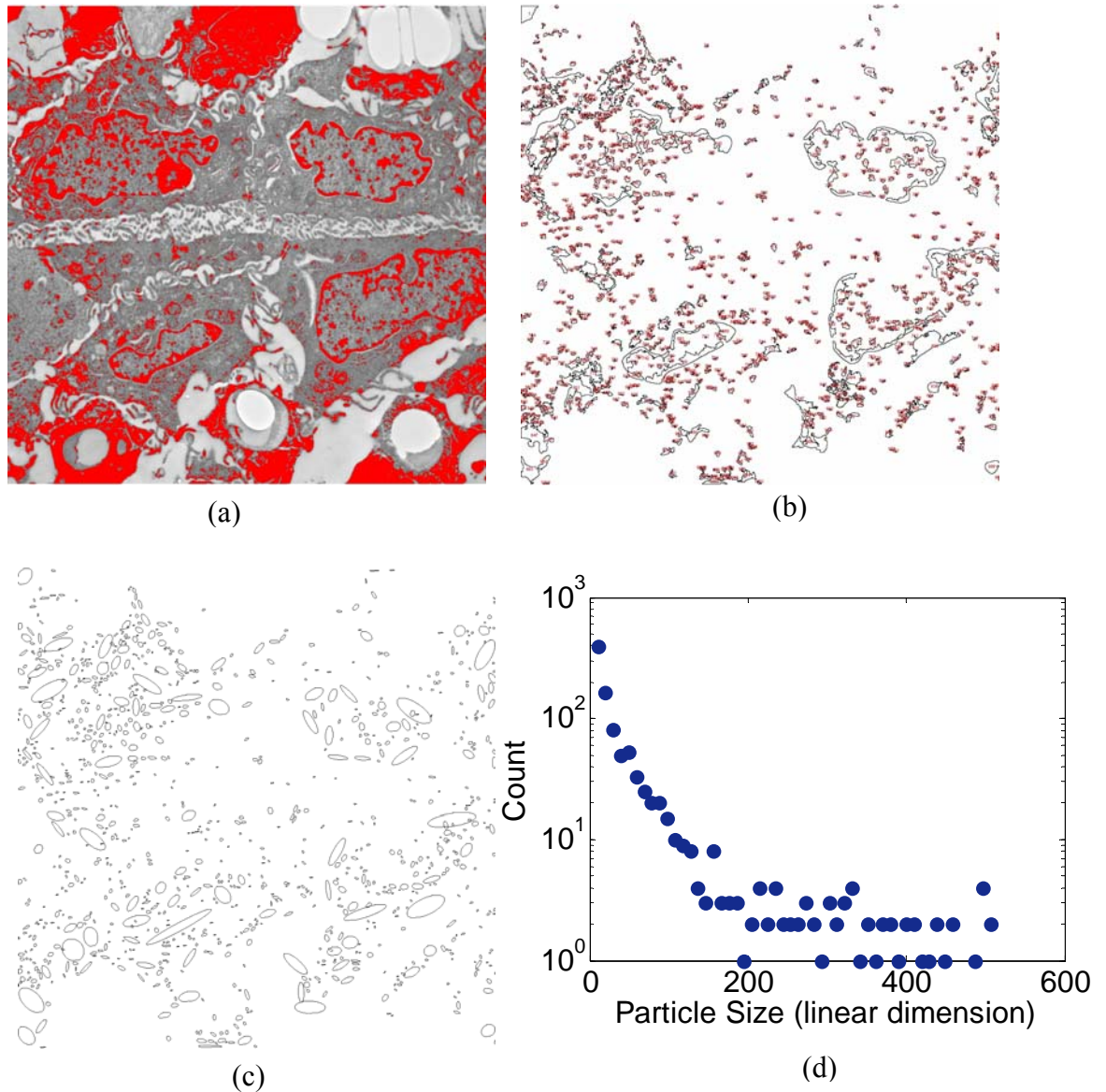


Figure 6.6 (a) shows the thresholded image of the original EM image for one particular threshold value, where the parts that were marked in red will be analyzed to get size information, while the left parts will not be analyzed. (b) shows the outline of the red-marked parts in (a). In (c) the red-marked parts in (a) were represented as ellipses of the approximate size. The result of this analysis is presented as a histogram of particle sizes in (d).

Figure 6.6 also shows a particle size analysis process for the EM image Figure 6.2(a) using a different threshold value from that used in Figure 6.5. Comparison between Figure 6.5(d) and Figure 6.6(d) indicates that threshold value varied the numbers of

particles counted, but did not have a major effect upon the shape of the particle size histogram. They also show that as the particle size increased, the histogram of data points displayed higher and higher variance, typical of poor statistics. Typically there were many small counts such as 1 or 2 at higher particle sizes, where the accuracy of the method breaks down. The data points toward the end of the particle size range were disregarded when the variance reached 50% of the mean value, as these basically had very poor statistical power because the error in accurately counting large particle numbers on high magnification was unacceptable. The size range was expanded through use of EM images with multiple magnifications. Instead of using these error prone counts at larger particle sizes, lower magnification imaging was used to count the particles with larger size, while higher magnification imaging was used to count the particles with smaller size. In this study, for analyzing the particle size from those four types of breast tissues, EM images with multiple magnifications were used for each type such that three different ranges of particle sizes could be counted and combined.

The particle size distribution of each of these four tissue types was determined using multiple slices and multiple imaging fields for each. The number of images analyzed in each type was between 2 and 4. The result of each of these four tissue types is displayed in Figure 6.7, and the best fitting to these data are also shown, with bi-exponential fitting to the fibroglandular and cancer tissues, and single exponential fitting to the adipose tissue data because the adipose tissue is not as heterogeneous as fibroglandular tissue and has a smaller range of particle sizes. The results of the best fitting to these data are shown in Table 2.

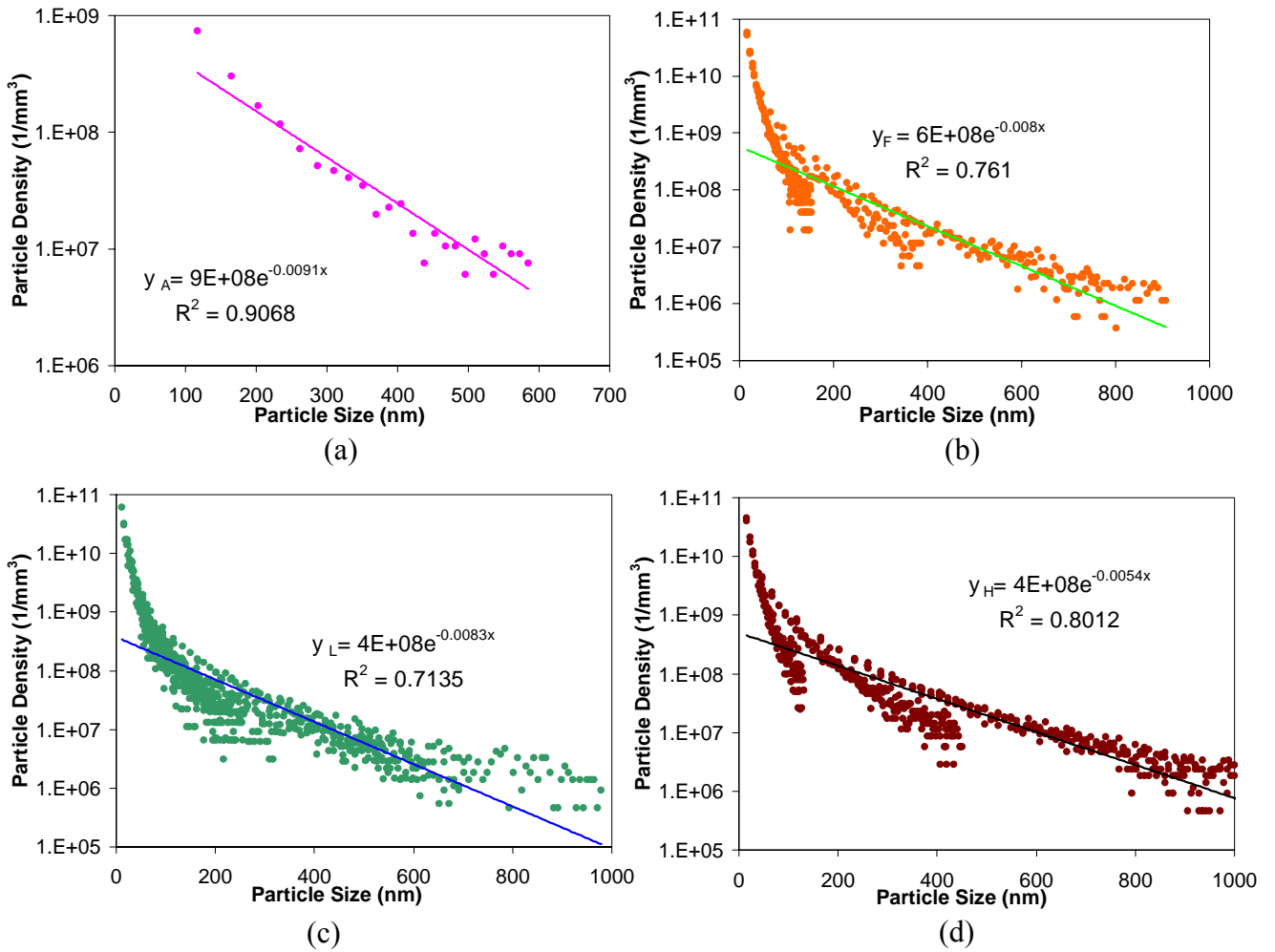


Figure 6.7 Particle size distributions obtained by combining results from Image Processing as described in this paper (a) Normal adipose histogram; (b) Normal fibroglandular tissue histogram; (c) Low grade ductal carcinoma tissue; (d) High grade ductal carcinoma tissue.

Tissue	N_1	$\langle x \rangle_1$ [nm]	N_2	$\langle x \rangle_2$ [nm]
Normal fibroglandular	2×10^{10}	22.8	2×10^8	159
Normal adipose	—	—	9×10^8	110
Low-grade epithelium	9×10^9	27.2	8×10^7	196
High-grade epithelium	1×10^8	25.0	1×10^8	233

Table 6.2 Fitting parameter results for a double exponential decay model for the particle size histogram data shown in Figure 6.7.

6.3.C Reduced scattering spectra calculation

The raw data from each histogram was averaged at each particle size, and used in Mie theory calculations to estimate the reduced scattering spectra. The calculations were done for all 4 tissue types, using both sphere and shell computations. Treatment of the scattering particles as spheres and as shells yielded a similar relationship between $\mu_s'(\lambda)$ and wavelength, λ .

Adipose tissue was consistently characterized by small $\mu_s'(\lambda)$ values and high grade epithelial tissue with large ones. In fact, for both treatments, the order of high grade, low grade, fibroglandular, adipose was preserved. In both cases, $\mu_s'(\lambda)$ values for tumor tissue were clearly separate from those of normal tissue, showing some promise in the ability to use Mie theory based calculations to catalogue the scattering in breast tissue.

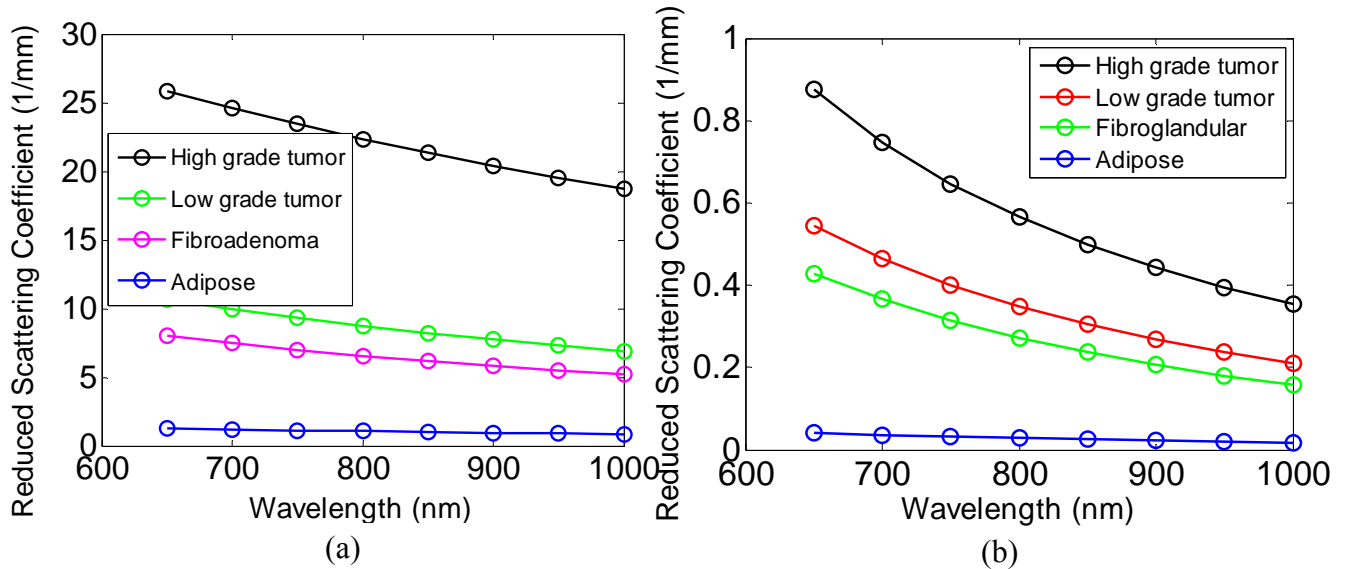


Figure 6.8 The reduced scattering coefficient spectrum, $\mu_s'(\lambda)$, is shown as calculated by (a) the solid spherical Mie theory calculation and (b) for the shell simulation of Mie theory, using the particle distribution histograms in figure 6.7.

In general, $\mu_s'(\lambda)$ values for the spherical treatment exceeded expected value based on clinical data [18, 49, 68, 109]. The shell treatment, however, generated values a little bit lower than this clinical data. At first glance, the shell treatment is better since it generates $\mu_s'(\lambda)$ values closer to the clinical data. However, as analyzed in chapter 3, the magnitude of the reduced scattering spectra could also be influenced by the refractive index, while the shape of the reduced scattering spectra (the slope of the spectra) relates only to the shape and size information of the scatterer. So the shape of the scattering spectra is more important in determining which kind of model is better in simulating the scattering in tissue.

In the power law (equation 1.7), the scattering power was a good indicator for the shape of the scattering spectra. By fitting the scattering spectra in Figure 6.8 to power law (equation 1.7), we get the scattering power for each type of tissue from both the spherical treatment and the shell treatment. The fitting results are shown in Table 6.3. It shows the sphere model generate scattering powers in the range of 0.75 to 1.0, which are pretty close to the expected value based on clinical data [18, 49, 51, 109], while the values got from the shell model exceeded the expected value.

So although the shell treatment provides a better $\mu_s'(\lambda)$ in magnitude, considering that the shape of the reduced scattering spectra (which could be indicated by the scattering power in power law) is more important in determining which kind of model is better in simulating the scattering in tissue, the spherical treatment is more optimally in simulating the scattering in tissue than the shell treatment. It is likely that the magnitude of the predicted scatterer is less important, as this is more affected by the number density

estimate, and the number density estimate is likely less accurate in this analysis than is the particle size distribution.

Tissue Type b	Adipose	Fibroglandular	Infiltrating Ductal Carcinoma, Low Grade	Infiltrating Ductal carcinoma, High Grade
Model				
Sphere	0.85	1.0	1.0	0.75
Shell	2.0	2.3	2.2	2.1

Table 6.3. Scattering power got from fitting the $\mu_s'(\lambda)$ in figure 6.6.using power law.

6.4. Discussion

In general, this EM image study is observational in nature, and the particle size analysis in this study provides supporting evidence for the overall hypothesis that light scatters from membrane bound subcellular and extracellular structures which are have a large range of sizes, weighted exponentially more towards the smallest observable scale. But there are still several problems need to be paid attention to, considering the complication of this work caused by the small scale of the ultrastructure.

A major assumption in the current paper is that structures as observed by EM accurately represent the same structures which cause light scattering in tissue. This is clearly a troubling assumption and yet the tools to objectively evaluate this are arguably lacking at the present time. The type of images shown in Figures 6.1 to 6.4 show membrane-bound structures and areas of electron-dense sub-cellular features, due to the contrast mechanism in electron microscopy which preferentially provides contrast to these. This approach makes some sense, since there is data to support the idea that membrane bound organelles contribute significantly to scattering [68, 110], and this is because of their change in refractive index from the background medium. But it is

possible that certain substructures observed in these images do not have the same change in index of refraction as others, and contribute less to the overall scattered signal. And if this is true, this can potentially contaminate the results of the study. In future studies, possibly near-field microscopy or phase contrast microscopy could help to catalogue maps of correlation between the observed structures in cells and that magnitude of scattering from each.

There can be concern that the tissue handling to prepare for electron microscopy might alter the tissue structure, however the tissue is fixed prior to preparation, and so the only major deformation expected is in the preparation of fatty tissue, which is hard to cut in thin sections. However care was taken to try and obtain samples which were minimally distorted by the preparation and cutting, prior to microscopy.

The choice of method to quantify the particle sizes in an automated way was another possible area of complication in the study, but hand counting of particles was simply not reliable, due to the large sample sizes needed for each tissue type and the large number of particles present per image and significant potential for observer bias in the counting process where multiple size scales are involved. Hand counting of selected slides was done and provided a consistent picture, although it has the complicating problems of observer bias in determining what is and is not a particle. After using grids overlaid on the images to attempt particle counting by hand, it was concluded that this was not clearly a reliable method for counting particles where the size range varied by over an order of magnitude, with potentially overlapping particles present. So the only objective way to proceed was chosen as computer-assisted counting.

The computer-assisted semi-automatic counting approach also has problems, in that there is potential bias in the way that the image was thresholded and the way that the algorithm appeared to link regions which were perhaps independent particles yet appeared to be touching in the thresholded image. Yet in the end when a large range of threshold values were used for any single image, the shape of the histogram resulting was always similar, with simply a change in the vertical offset. The type of data shown in Figure 6.7 is very typical of the retrieved data in most images. The results indicated that the histograms of particle sizes are all effectively double exponential shapes, except for adipose tissue which appeared to have only a single exponential shape. These are consistent with inspection of the images, which certainly shows a much larger number of small features as compared to the larger ones. This observation has very important implications for Mie theory or scatter theory modeling of the distributions, as they then present a simple distributions, where the mean of the distribution (for a single exponential) is equal to the decay parameter. This feature makes modeling of the distribution with a single parameter extremely useful. The overall number density (i.e. the numbers on the y-axis in Figure 6.7), are perhaps more questionable than the shape of the functions because in this study it was determined that the threshold value varied the numbers of particles counted, but did not have a major effect upon the shape of the particle size histogram. Thus, a major conclusion of this paper is that EM image analysis is reasonably good at estimating the average scatterer sizes, but potentially less accurate at estimating the absolute number densities of these particles.

6.5 Conclusions

In summary, this study provides evidence for the fact that the particle sizes are distributed exponentially in sub-cellular structures, and that given assumptions about the index of refraction change, the shape of the scattering spectrum in the near infrared is consistent with what would be predicted by these particle size histograms. The estimation of scattering from Mie-theory shells has a better agreement with the observed reduced scattering coefficient magnitude in bulk breast tissue, but the estimation of scattering from Mie-theory spheres has a better agreement with the observed reduced scattering coefficient shape in bulk breast tissue. Considering that the shape of the reduced scattering spectra is more important in determining which kind of model is better, the sphere model is more optimally than the shell model in modeling the scattering in tissue. It is likely that the most definitive part of this study is the predication of the average particle sizes for the different tissue types, which are all in the range of 110 to 230 nm, with the normal tissues being smaller in average size, and the cancer tissues having larger average size. Adipose tissues seemed to have the most uniform size distribution, with only a single exponential distribution. Collagen and stromal tissues were not studied extensively in this study, however subsequent to this it was observed that collagen-based regions can have the most dominant contribution to scattering, and so future studies should focus on estimating the histograms of these stromal tissues.

Chapter 7. Breast Tissue Phase Contrast Measurements to Assess Relative Microscopic Scattering

7.1 Introduction

In this chapter, the scattering properties of breast tissue were studied by phase contrast microscopy imaging, which indicates the relative scattering intensity of each part in the breast section. Tissues were separated into their individual biological sub-types and the phase contrast observed was quantified using multiple samples for each. This approach provides a microscopic quantification of which tissues types lead to more scattering, and also allows a more direct correlation between the scatter signal and the tissue ultrastructure as studied by electron microscopy.

7.1.A Phase Contrast Microscope

The phase contrast microscope is a vital instrument in biological and medical research. When dealing with transparent and colorless components in a cell, fixation and staining is an alternative but at the same time the fixation stage alters the scattering properties of the tissue and stops all biological processes in it. The phase contrast microscope has made it possible to study living cells, with cell division being an example of a process that has been examined in detail with it. Phase contrast imaging enhances the observed edges of transparent and colorless objects by influencing the optical path of the light. This process is able to show components in a cell or bacteria, which would be very difficult to see in an ordinary light microscope. Fritz Zernike was awarded with the Nobel

Prize in Physics in 1953 for the invention of this microscope, because of its importance both as a new physical tool, as well as an invaluable biological tool.

In microscopy, when light passes through the specimen, some rays are refracted and thus the path of travel is altered. Some pass directly through, but because of the change in index of refraction, the path is delayed by a fraction of a wavelength or so, as compared to the uninfluenced light. This difference in phase is not visible to the human eye. However, the change in phase can cause a difference in brightness by using a phase plate in the microscope.

A phase plate is mounted in or near the objective rear focal plane in order to selectively alter the phase by a quarter of a wavelength. This either affects the light that travels peripheral to the axis of travel (negative phase plate) or the light that travels directly along the axis of travel, undeviated (positive phase plate), after passing through the specimen. Figure 7.1 shows these two kinds of phase plates.



Figure 7.1.  is phase retarding material. (a) is positive phase plate, and (b) is negative phase plate. [9].

Figure 7.2 shows how does a negative phase plate work. The negative phase plate retards the light from an object, so the light from an object passing through the edges of the objective lens is retarded a half wavelength and the light through the center is not retarded at all, and they are out of phase by a half wavelength. They cancel each other when the objective lens brings the image into focus. A reduction in brightness of the

object is observed. The degree of reduction in brightness depends on the internal complexity of the index of refraction at the sub-microscopic level. Generally, the more complex the distribution of phase shifts that are present, then the darker the image will be.

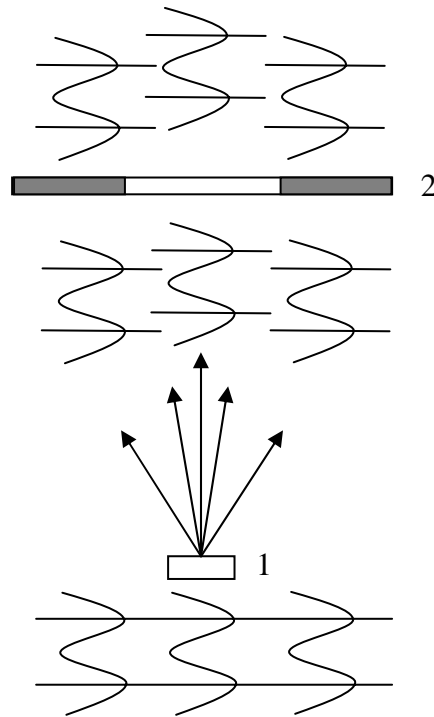


Figure 7.2. This figure shows how a negative phase plate works. In the figure (1) is the specimen, (2) is the negative phase plate.

Figure 7.3 shows how a positive phase plate works. The positive phase plate retards the light from an object at the center of the objective lens by a quarter of wavelength, then the light from an object at the edge of the objective lens is retarded a quarter of wavelength and the light to the center is also retarded a quarter of wavelength. They are in phase and an enhancement in brightness of the object is observed when the objective lens brings the image into focus. . The degree of enhancement in brightness

depends on the scattering intensity of the object. The more complex the distribution of refractive indexes in the sample is, the brighter the image becomes overall, corresponding to a higher scattering intensity.

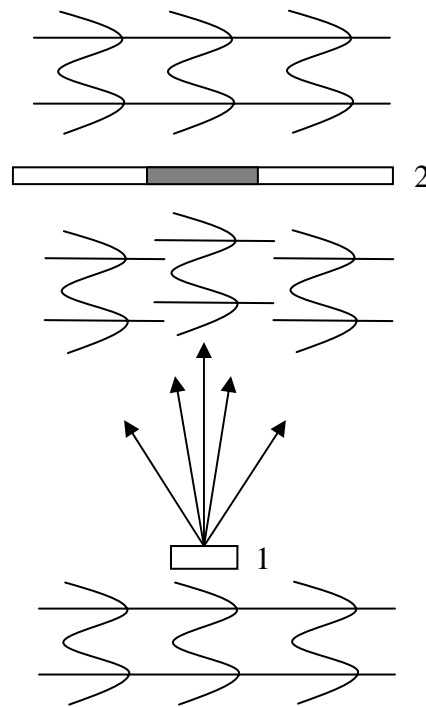


Figure 7.3. This figure shows how a positive phase plate works. (1) is the specimen, (2) is the positive phase plate.

In Figure 7.4 (a), the tissue in part 1 has the strongest scattering intensity, that in part 2 has the moderate scattering intensity, and that in part 3 has the lowest scattering intensity. The stronger the scattering intensity, the more deviated is the light passing through as shown in (b). If we use a negative phase plate, then we can get a phase contrast image as shown in (c), and if we use a positive phase plate, then we can get a phase contrast image as shown in (d).

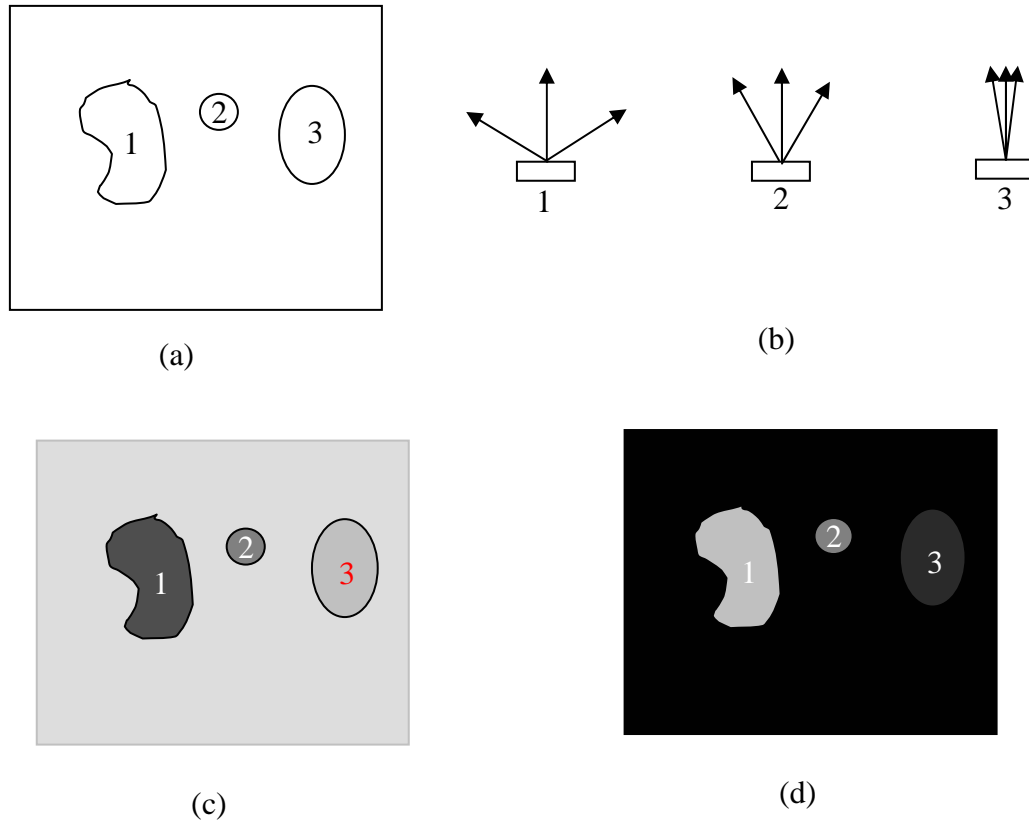


Figure 7.4. (a) shows 3 different parts in the tissue. (b) shows the different scattering intensity of these three parts. If we use a negative phase plate, then we can get a phase contrast image as shown in (c), and if we use a positive phase plate, then we can get a phase contrast image as shown in (d).

So, in positive phase contrast microscopy images, the brightness in the image depends on the scattering intensity of the object, providing information about which part of the tissue takes the most important role in scattering.

7.1.B Interpreting Microscopic Tissue Slices stained with H&E (Hematoxylin and Eosin)

H & E staining is by far the most commonly used stain to show cellular components. Hematoxylin, as a basic dye, has an affinity for the nucleic acids of the cell nucleus and stains the nucleus in blue; eosin is an acidic dye with an affinity for intracellular or extracellular materials and stains them in pink. The cytoplasmic structures of epithelial cells stain pink-orange with eosin, as do collagen and basement membranes. Figure 7.5 shows a low power H&E-stained breast tissue sample. The stromal collagen stains pink-orange and the epithelial nuclei stain blue-purple.

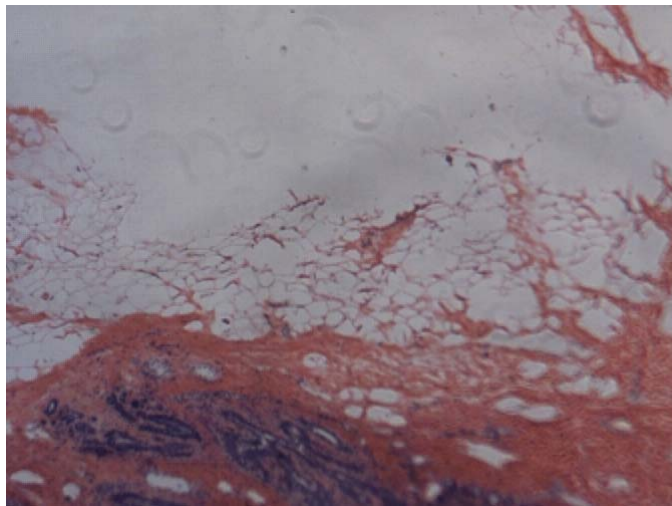


Figure 7.5. An H&E stained breast tissue sample. Stromal collagen is pink-orange, the epithelial nuclei are blue-purple (near the bottom). Fat tissue dissolves in the fixation process, and is therefore observed as open white areas surrounded by pink stroma.

By comparing phase contrast microscope images with the same slides then stained with H&E, it is possible to outline different tissue types in the phase contrast image. This

process was used to delineate tissues and quantify the apparent scatter as observed in phase contrast, for different biological tissue origins.

7.2 Methods and Materials

7.2.A. Tissue acquisition:

The Tissue Bank in the Department of Pathology at the Dartmouth-Hitchcock Medical Center (DHMC) snap freezes fresh tissue from all surgical specimens and stores it at -80oC if there is tissue available over and above that required for a standard-of-care clinical pathologic diagnosis. Currently, some 3000 specimens can be identified in the Tissue Bank, all linked to the pathology diagnostic data in the Laboratory Information System (LIS). We searched the Tissue Bank at DHMC for samples of normal breast, benign tumors and malignant tumors. Sequential frozen sections of each specimen, each at 4 microns thickness, were cut after the frozen tissue had been embedded in OCTTM.

7.2.B Apparatus

In this study a Nikon inverted microscope DIAPHOT-TMD (811829, Japan) was used throughout. It had a positive phase plate (Nikon Phase Contrast-2 ELWD 0.3, 206320, Japan) for phase contrast imaging, and a 16 bit CCD camera [name make and model here]. The light source is a Nikon super high pressure mercury lamp. So the background of each phase contrast image was black, the tissue that had higher scatter intensity appeared brighter, while the tissue that had lower scatter intensity appeared to be darker. In all work, a 4X magnification was used on the microscope in order to keep the images fairly low power such that groups of the same type of tissue were quantified

together as a 'bulk' value, rather than looking at individual sub-cellular components. The Diagnostic instrument system has a 60X magnification. The frozen breast tissue sections were cut at 4 μ m thickness.

7.2.C. Image Acquisition

Phase contrast imaging was performed on one of the unstained frozen tissue sections from each sample after they had been removed from the freezer one at a time and allowed to acclimate to room temperature. A series of images were taken, covering the entire section area, and then all of the images were joined together, to obtain one montage image of the whole section.

Following this, the frozen tissue sections were fixed and H&E stained in the Pathology department to better distinguish the microscopic tissue morphology. A series of images were then taken of these H&E stained sections. The process was the same as with phase contrast sections and another montage image of the whole H&E stained section was obtained.

Two sets of macroscopic images resulted then for each tissue section, one phase contrast and one an H&E image. A detailed analysis of both images was carried out by pairing the locations of the different tissue types in each, under the guidance of a surgical pathologist, Wendy Wells, M.D. Using the H&E-stained montage, the variable histologic subtypes in each section were defined, as described in 7.2.D and the grey scale phase contrast measures were compared with the corresponding morphology.

7.2.D. Image Analysis

In the following analysis, the Pathology terminology used to classify the tissues included the following:

1. Fat

2. Epithelium: a. Benign: normal, fibrocystic disease or tumor (fibroadenoma)

b. Malignant:

i) Invasive (Ductal carcinoma or Lobular carcinoma)

ii) Non-invasive (Ductal carcinoma In Situ, DCIS or Lobular carcinoma in Situ, LCIS)

3. Stroma:

a. Benign-associated stroma: the stroma adjacent to benign epithelium

b. Malignant-associated stroma: the stroma adjacent to malignant epithelium (invasive or non-invasive)

c. Normal stroma: the stroma not associated with any epithelium (collagen, fibrosis)

The process of quantifying different kinds of tissue in terms of the phase contrast values was carried out in grey-scale using the *ImageJ* software package. The grey-scale value indicates the relative scattering intensity of the tissue. Since we are using a positive phase plate, the higher the grey-scale value, corresponded to higher scattered intensity. The background intensity in each image was also quantified to subtract off the background intensity value. This process was important because the actual background intensity values were subject to slight variation from image to image.

7.2.E. Samples

The study included a total of 33 breast tissue sections, with:

1. 10 normal breast tissues;
2. 23 abnormal breast tissues, including the sub-types:
 - (1) 13 Ductal cancer (including Invasive Ductal carcinoma and Ductal carcinoma In Situ),
 - (2) 4 Lobular cancer (including Invasive Lobular carcinoma and Lobular carcinoma in Situ),
 - (3) 6 Fibroadenoma.

7.3. Results

Figures 7.6 through 7.18 show the phase contrast images and corresponding H&E images of a series of breast tissue sections with different tissue types: Normal tissue, Invasive Ductal carcinoma, Ductal carcinoma In Situ, Invasive Lobular carcinoma, Lobular carcinoma in Situ, and Fibroadenoma. Following these case studies, a statistical analysis of a series of images is presented.

7.3.A Case Studies

7.3.A.1 Normal tissue

Figure 7.6 shows a normal breast tissue section, (a) is the phase contrast image and (b) is the corresponding H&E staining image. In (b) the epithelium is dark purple and the stroma is red. We could also recognize some light purple tissue around the dark epithelium, which is the epithelium associated stroma. In the corresponding phase

contrast image, the epithelium appears dark grey, the stroma looks bright, and the epithelium associated stroma looks light grey. This indicates that the stroma has higher scattering intensity than the epithelium, and the epithelium associated stroma is affected by the epithelium and have a scattering intensity between the epithelium and the normal stroma.

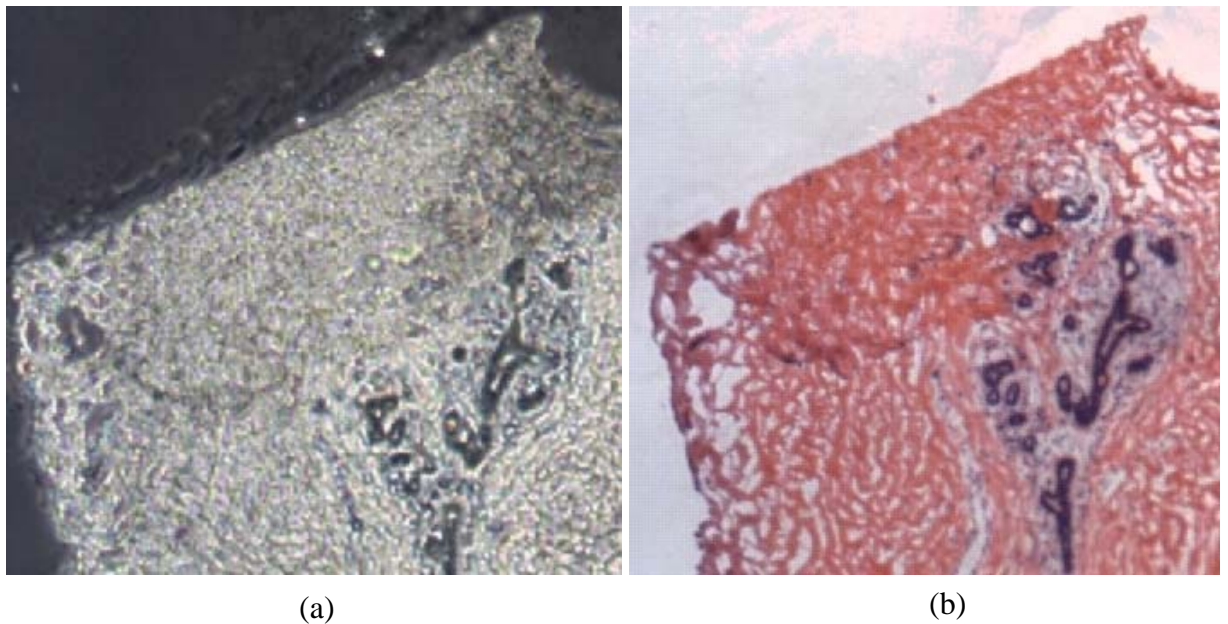
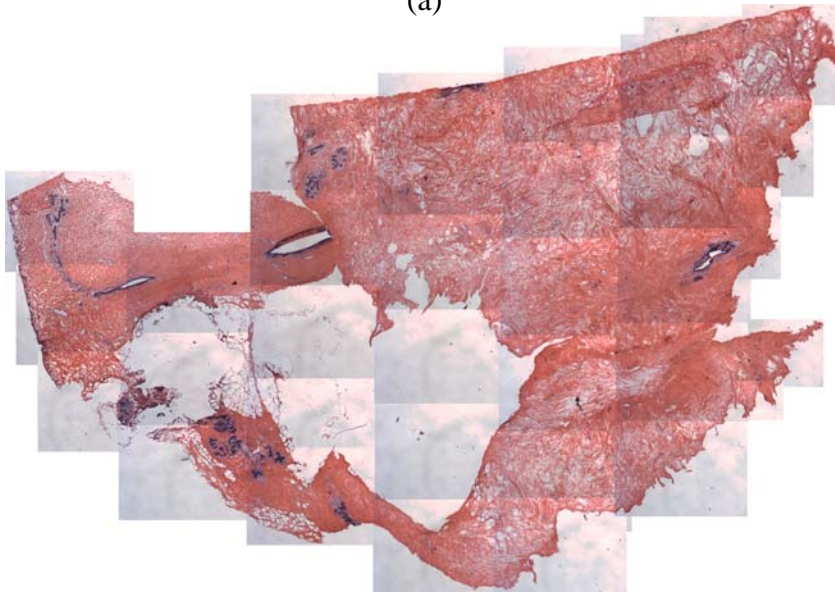


Figure 7.6. the (a) phase contrast image and (b) H&E staining image from the same location on a normal breast tissue section

By montaging the images from all locations together, the phase contrast images and H&E stained images for a whole section breast tissue is obtained, as shown in Figure 7.7. From (b) it is apparent that that there is mostly stroma in the normal section, and little epithelium.



(a)



(b)

Figure 7.7. the (a) phase contrast image and (b) H&E stained image of the entire montage image section of normal breast tissue, which is the same as in Figure 7.6.

7.3.A.2 Ductal carcinoma

Ductal carcinoma is the most common form of breast cancer. It develops in the ducts that carry the milk from the lobules (milk glands) to the nipple. Ductal carcinomas

can be either in situ (non-invasive) or invasive breast cancer. In Ductal Carcinoma in Situ (DCIS), cancer cells stay inside the duct of the breast in which it originated. It can involve a small or large area of the breast, but does not spread outside the duct into the normal surrounding breast tissue, to the lymph nodes, or to other organs. Invasive Ductal Carcinoma (IDC) accounts for nearly 80% of breast cancers. It also begins in a milk duct, but unlike ductal carcinoma in situ, it invades the fatty and fibroglandular tissue of the breast. This invasive carcinoma has the potential to metastasize, or spread to other parts of the body through the bloodstream or lymphatic system.

Case 1:

In this case, there are invasive ductal carcinoma, non-invasive ductal carcinoma In Situ (DCIS) and normal tissue in the breast tissue section. The contrast image and H&E staining image from the whole section of this cancerous breast tissue section is shown in Figure 7.8. From the H&E stained images, it is obvious that there is much more epithelium in comparison to associated stroma in the invasive ductal carcinoma as compared with the non-invasive DCIS and the normal tissue. In the phase contrast image, the epithelium appears to be darker than stroma.

The detailed phase contrast images and H&E stained images of the invasive ductal carcinoma, non-invasive DCIS and normal part of this section are all shown in Figure 7.9 (a)-(c). In (a) are the images from an invasive ductal carcinoma, and (b) are the images from the non-invasive DCIS, and (c) are the images from the normal part.

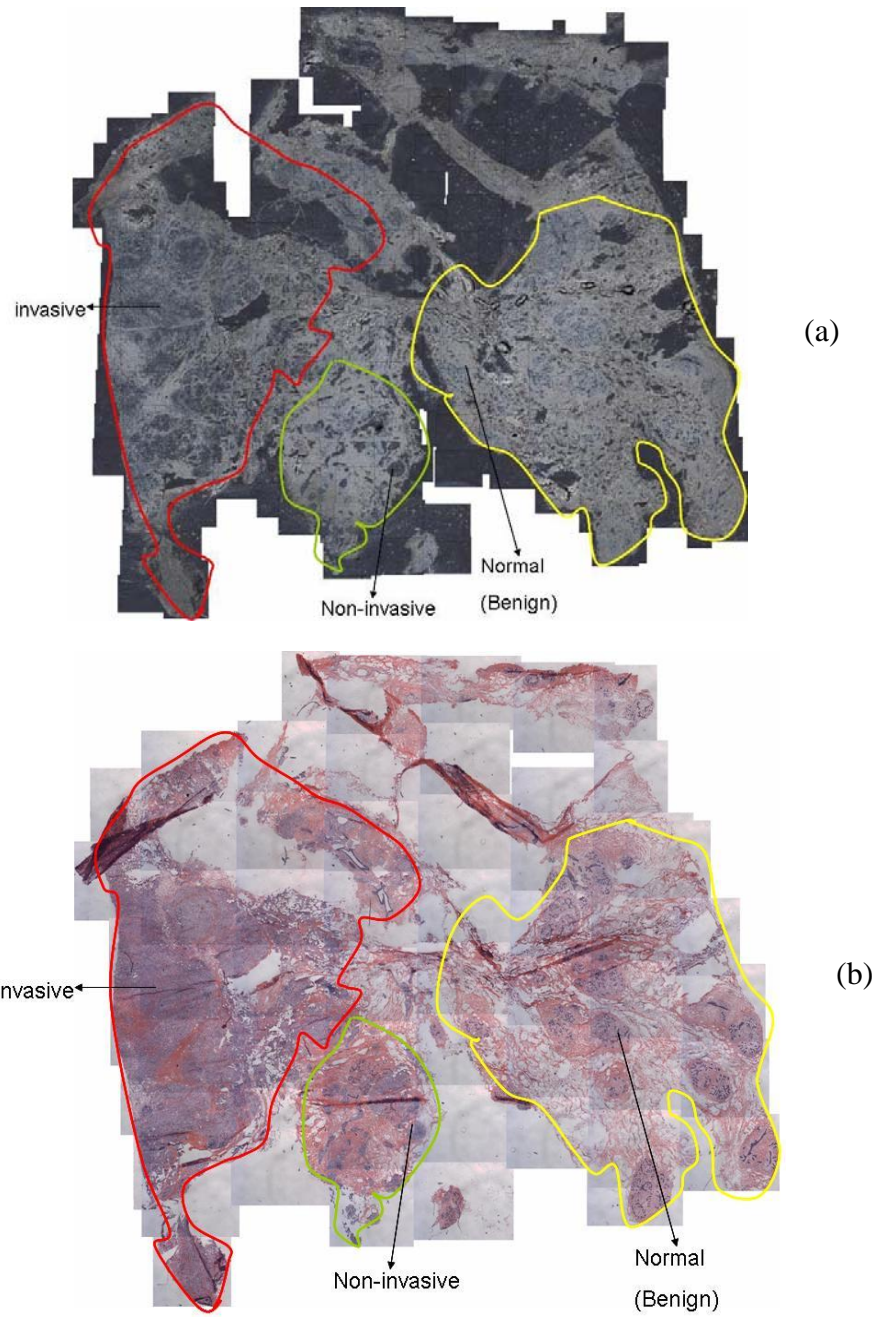
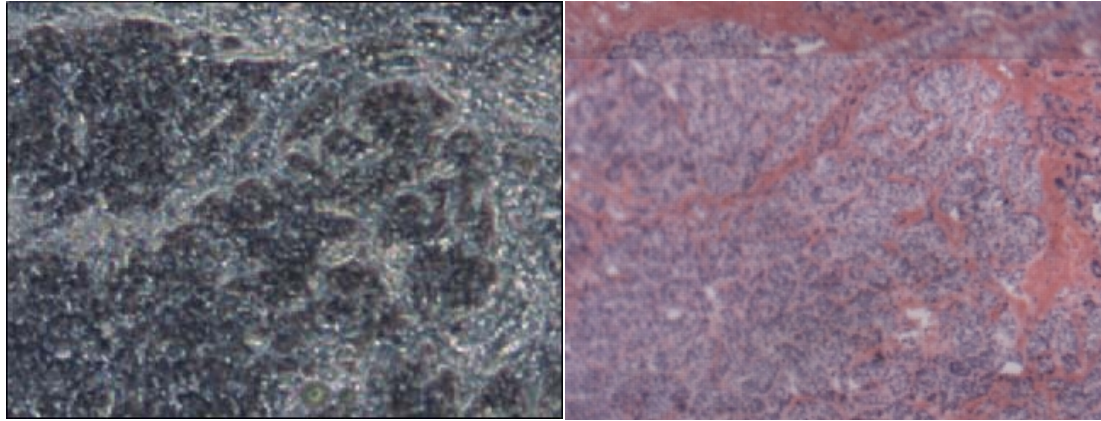
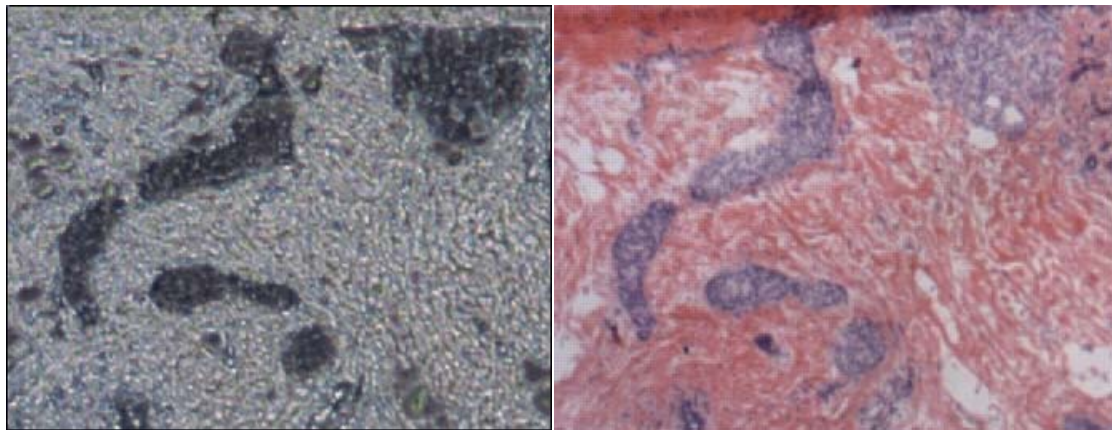


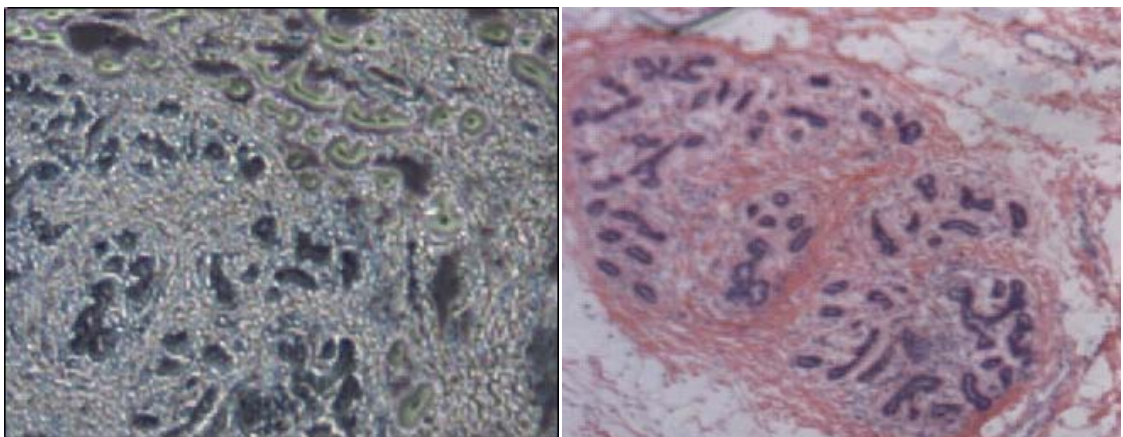
Figure 7.8. the (a) phase contrast image and (b) H&E staining image over the whole section of a Ductal Carcinoma breast tissue.



(a)



(b)



(c)

Figure 7.9. the co-localized phase contrast image and H&E staining image from separate areas: (a) invasive ductal carcinoma (b) Ductal carcinoma In Situ and (c) normal tissue of the same Ductal carcinoma section as shown in Figure 7.8.

Case 2:

Figure 7.10 is another case of Ductal carcinoma, in which there is both invasive malignant tissue and normal tissue. As in Case 1, there is much more epithelium in the area of invasive malignant tissue as compared with the normal tissue.

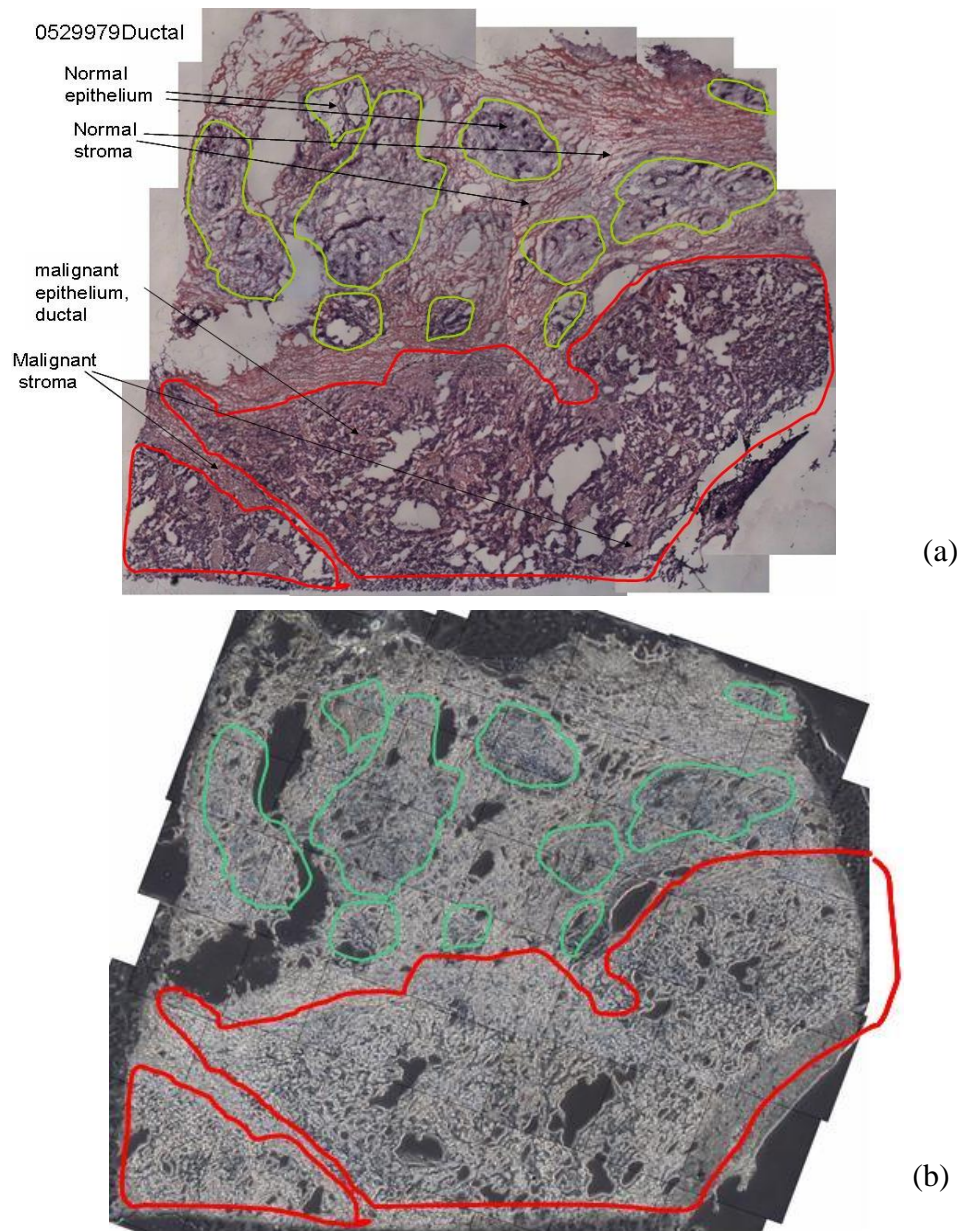


Figure 7.10. the (a) H&E image and (b) phase contrast image over the whole section of a Ductal carcinoma.

Case 3:

Figure 7.11 is a Ductal carcinoma In Situ case.

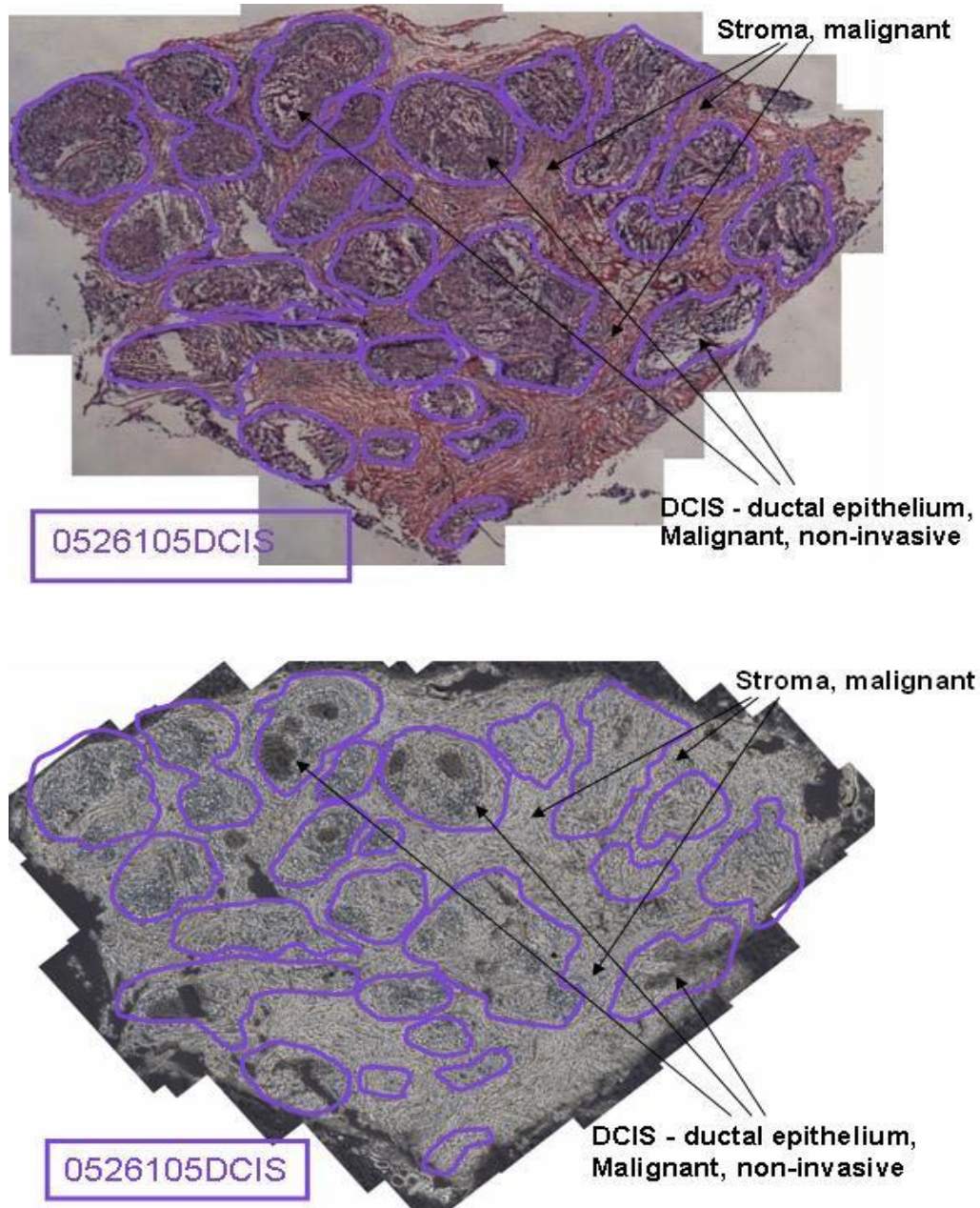


Figure 7.11. the (a) H&E staining image and (b) phase contrast image over the whole section of a Ductal Carcinoma In Situ breast tissue section.

7.3.A.3 Lobular Tumor

Lobular carcinoma is far less common than ductal carcinoma, but it can present itself in both breasts more often than other types of breast cancer. Lobular carcinoma can be either in situ or invasive breast cancer. Lobular carcinoma in situ, a marker of increased risk to develop invasive cancer in the same or both breasts, is defined as the presence of neoplastic cells expanding the acini in a lobular unit. There is no infiltration through the wall of the lobules. Similar to invasive ductal carcinoma (IDC), invasive lobular carcinoma (ILC) has the potential to metastasize and spread to other parts of the body. It extends from the milk-producing glands into the fatty tissue of the breast. About 10% to 15% of breast cancers are invasive lobular carcinomas. Invasive lobular carcinoma also can be more difficult to detect by mammogram than IDC, making it important to have mammograms annually.

Cases 1-3 below are distinct cases of Lobular carcinoma.

Case 1: Invasive Lobular carcinoma

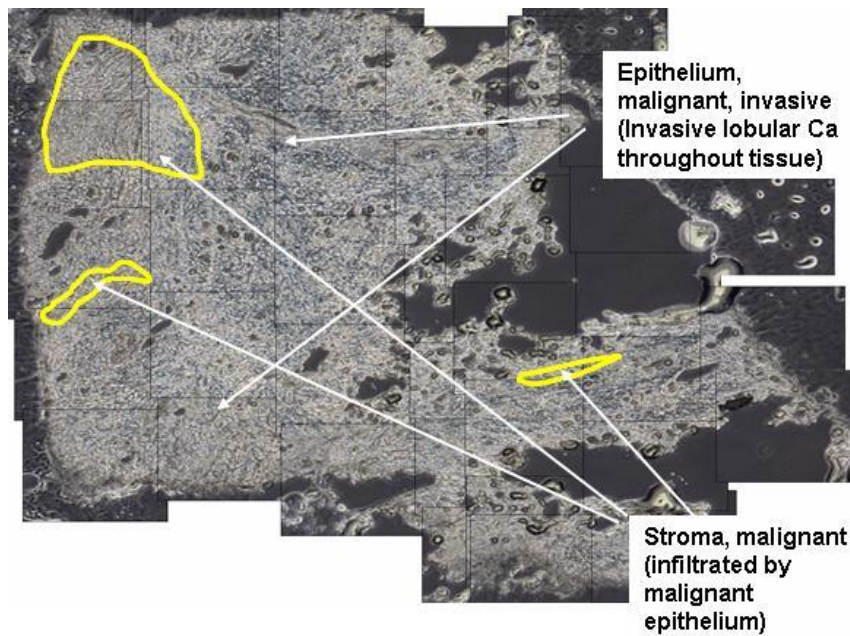
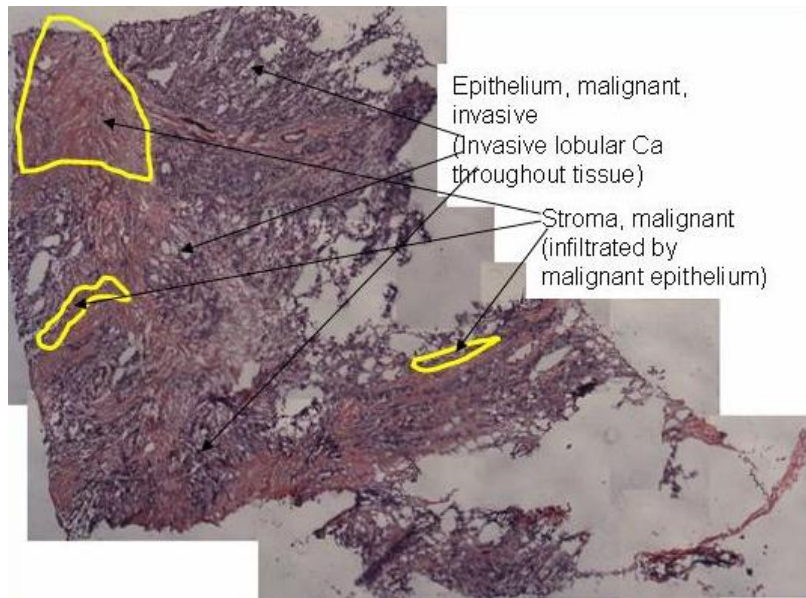


Figure 7.12. the (a) H&E staining image and (b) phase contrast image over the whole section of a Invasive Lobular Carcinoma breast tissue section.

Case 2: Lobular carcinoma (with Invasive Lobular Carcinoma and Lobular Carcinoma In Situ)

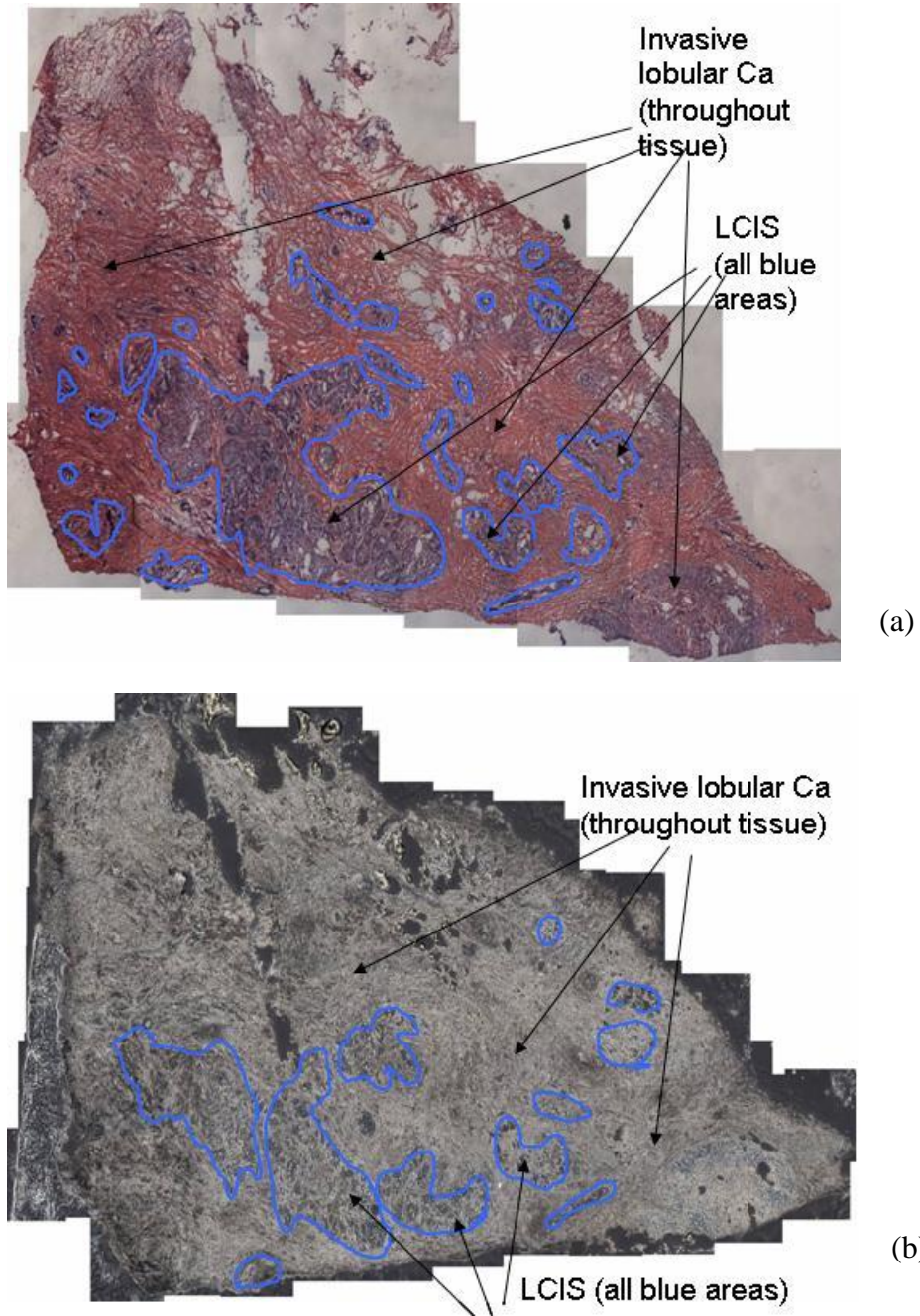


Figure 7.13. the (a) H&E image and (b) phase contrast image over the whole section of a Lobular carcinoma (with Invasive Lobular Carcinoma and Lobular Carcinoma In Situ), illustrating the lower scatter in the epithelium.

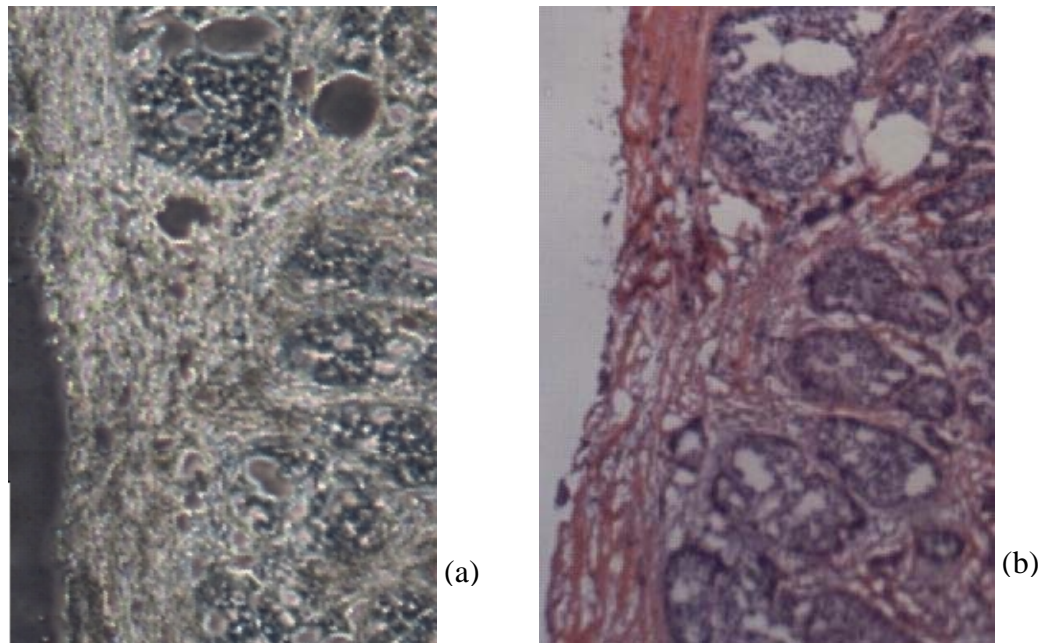
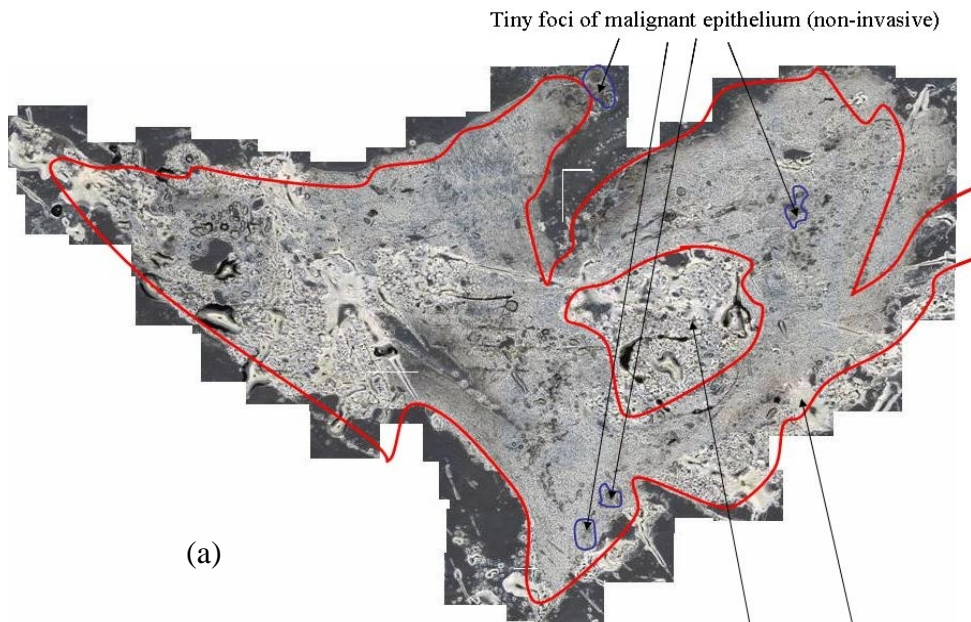


Figure 7.14. the co-localized (a) phase contrast and (b) H&E image from the LCIS, at higher power than shown in Figure 7.13. Again, stroma is higher in scatter and epithelium is lower.

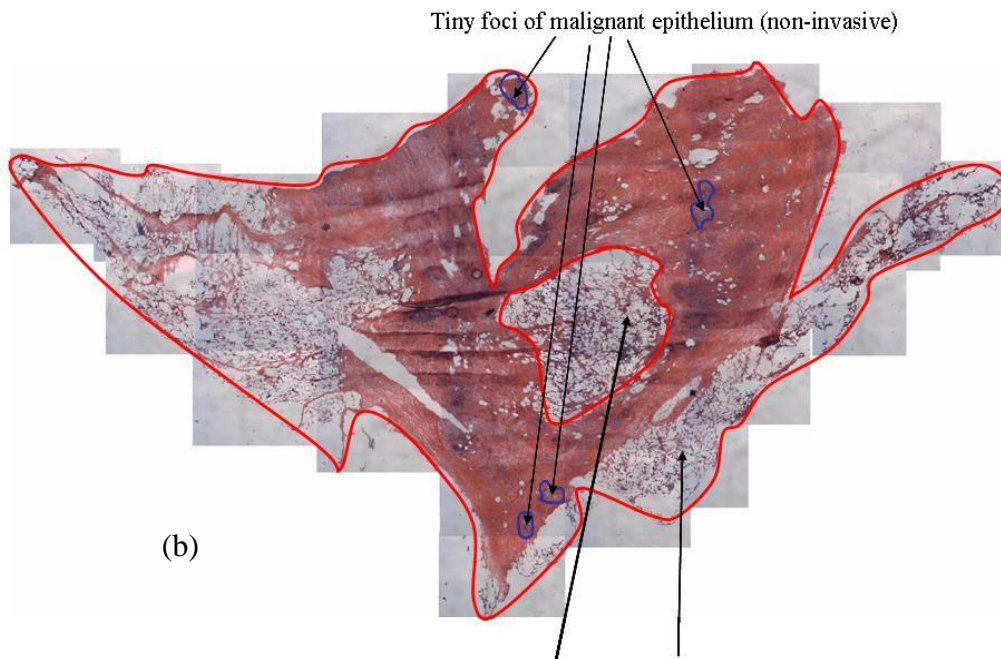
Case 3: Invasive Lobular carcinoma

In this case shown in figure 7.15, the entire tissue is infiltrated by invasive malignant epithelium, including the surrounding fat and the fat in the center of the tissue.



(a)

The entire tissue is infiltrated by malignant epithelium (invasive), including the surrounding fat and the fat in the center of the tissue



(b)

The entire tissue is infiltrated by malignant epithelium (invasive), including the surrounding fat and the fat in the center of the tissue

Figure 7.15. the (a) H&E image and (b) phase contrast image over the whole section of a Invasive Lobular Carcinoma section.

7.3.A.4 Fibroadenoma (Benign Tumor)

Fibroadenoma is a benign tumor characterized by abnormal proliferation of both glandular and fibrous tissues. It is most common in women between the ages of 15 and 30, and is found in 10% of all women.

Figure 7.16 and 7.18 are the phase contrast images and H&E staining images of two Fibroadenoma cases. Figure 7.17 is a detailed phase contrast images and H&E staining image of Fibroadenoma. The stroma associated with the fibroadenoma epithelium is light purple in the H&E staining images, and looks darker in the phase contrast images. This is different from the stroma (normal stroma) that is not associated with the fibroadenoma, which is pink in the H&E staining image and quite bright in the phase contrast image.

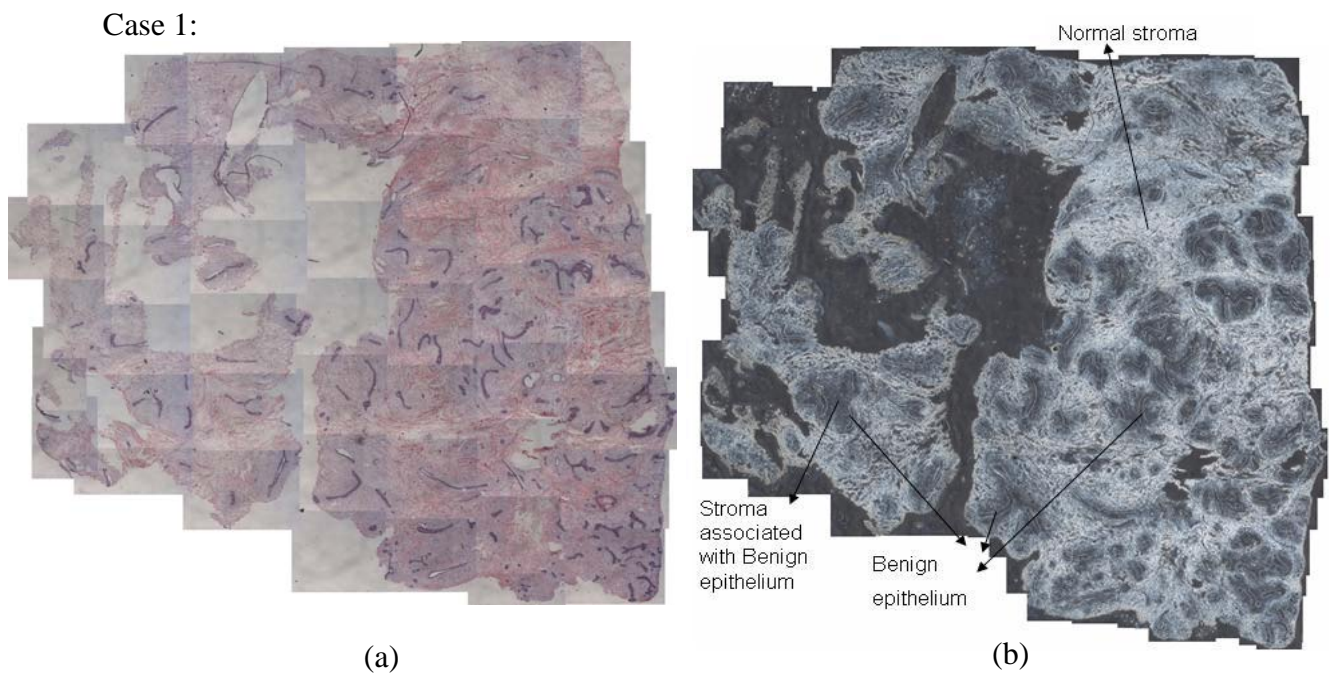


Figure 7.16. the (a) H&E image and (b) phase contrast image over the whole section of a Fibroadenoma section.

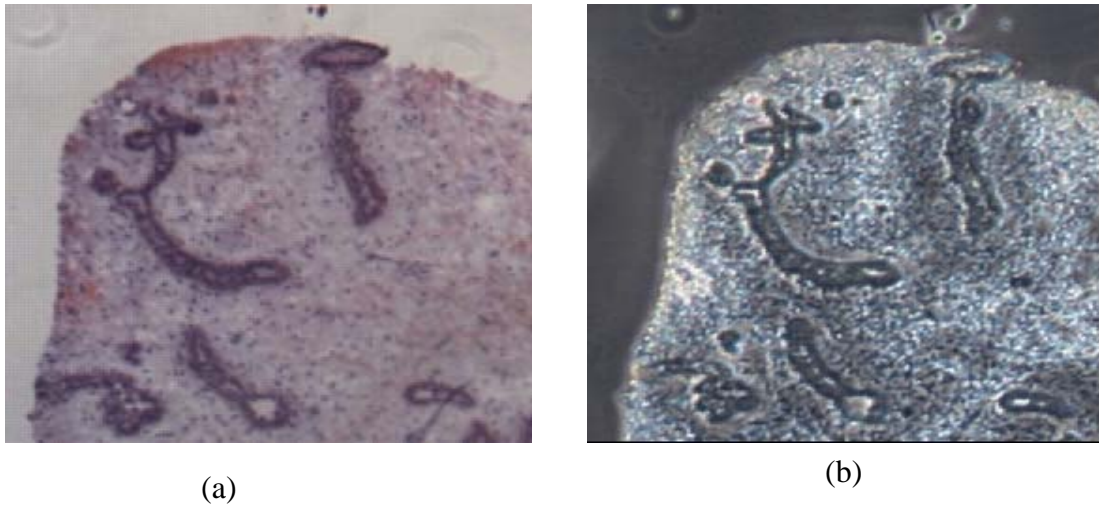


Figure 7.17. the co-localized (a) H&E image and (b) phase contrast image from the a Fibroadenoma section at higher power.

Case 2:

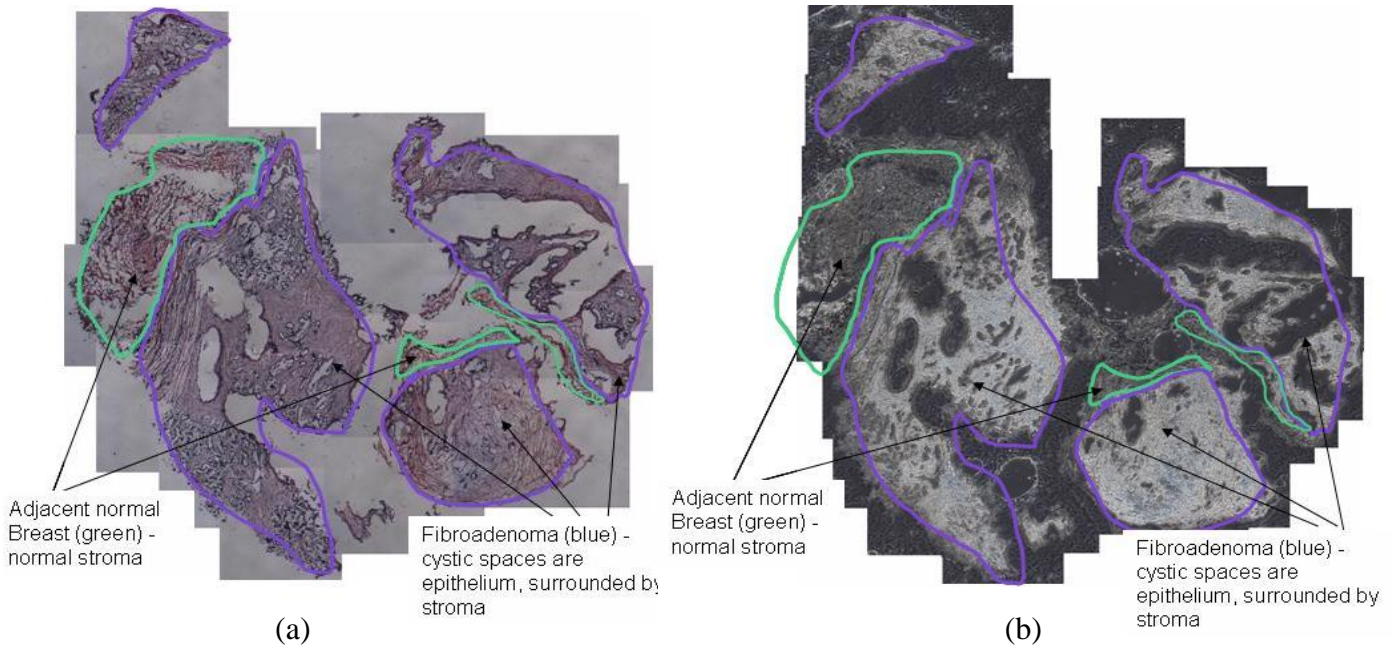


Figure 7.18. the (a) H&E image and (b) phase contrast image over the whole section of a Fibroadenoma breast tissue section.

7.3.B. Statistical analysis

The phase contrast images were quantified in gray scale using software *ImageJ* according to the Pathology terminology stated in Section 7.2.C and grouped together as grey scale intensity values, after background correction.

For each kind of tissue on the phase contrast image of one tissue section, the gray scale values were taken from approximately 10 regions of interest (ROI), which are called ROI values, and then their weighted average was taken to be the gray scale value for that kind of tissue on that section, which are called case values.

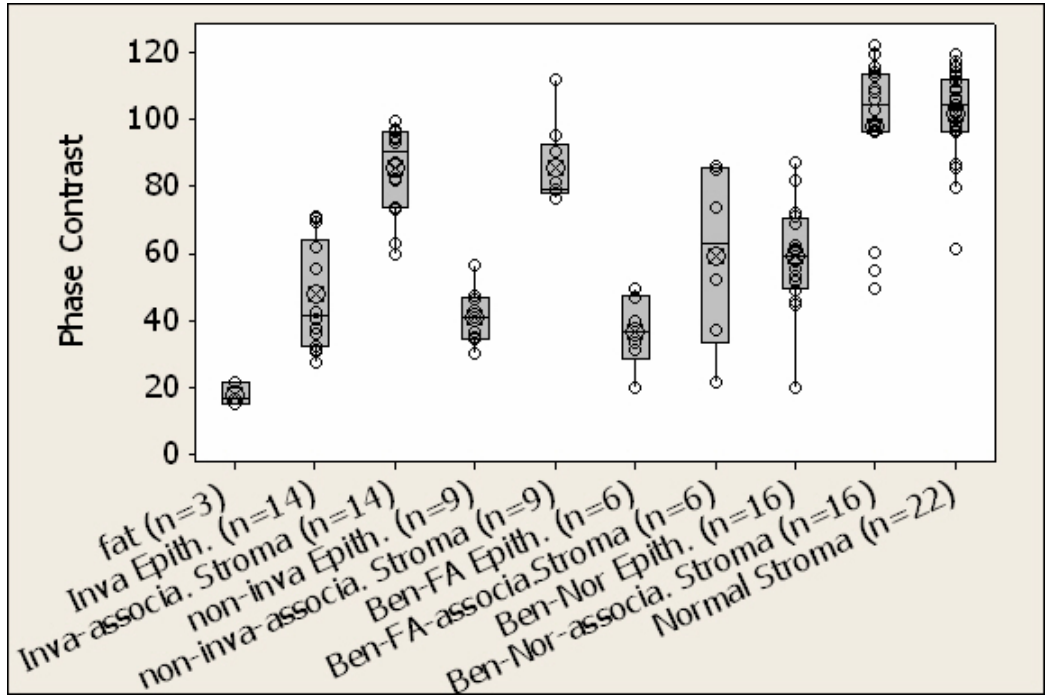
7.3.B.1 Statistical analysis based on case

In this analysis, the phase contrast value of each tissue type is analyzed based on the phase contrast values of all cases in this tissue type. As shown in Table 7.1, there were a total of 14 cases of invasive epithelium and associated stoma, 9 cases of non-invasive epithelium and associated stoma, 6 cases of fibroadenoma epithelium and associated stoma, 16 cases of normal epithelium and associated stoma, and 22 cases of non-associated stroma, and 3 cases of fat tissue. The average parameters are tabulated in Table 7.1, and shown as Box and whisker plots in the Figures 7.19.

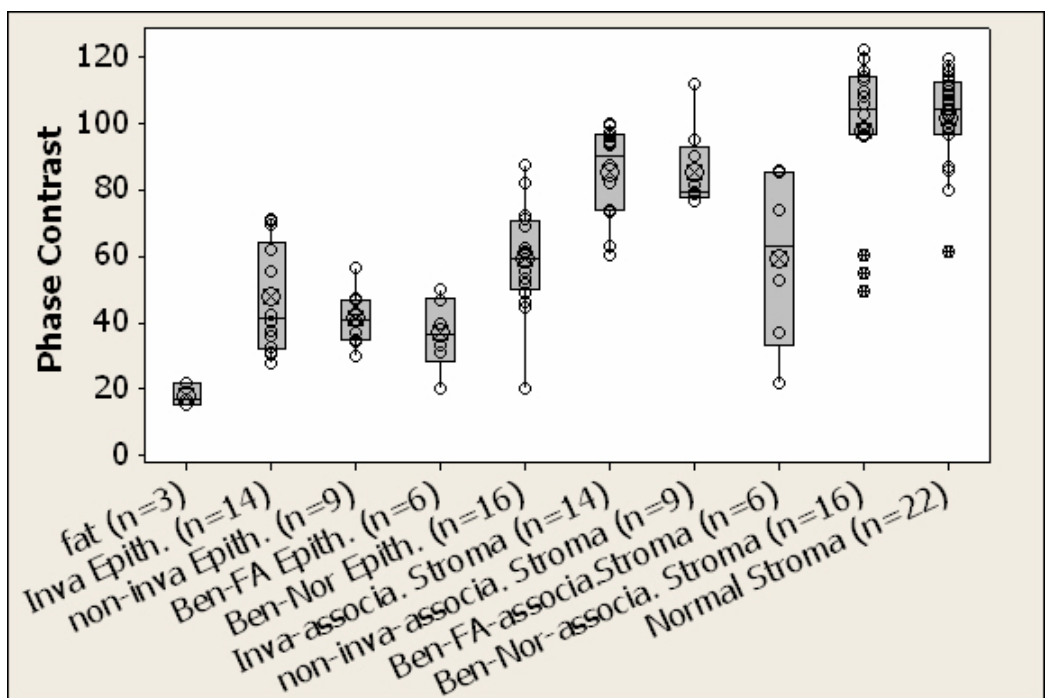
Tissue Type	Fat (n=3)	Invasive Cancer		Non-invasive Cancer		Benign Fibroadenoma		Benign Normal		Normal
		Epith. (n=14)	Stroma (n=14)	Epith. (n=9)	Stroma (n=9)	Epith. (n=6)	Stroma (n=6)	Epith. (n=16)	Stroma (n=16)	Stroma (n=22)
median	15	41.3	90.18	40.92	79.2	36.6	63.04	59.21	104.29	104.26
q1	0	32.55	73.64	34.73	78.94	31.04	37.02	49.01	96.3	96.73
min	0	27.51	59.99	30.12	76.62	20.06	21.52	19.92	49.6	61.35
max	16.84	70.97	99.62	56.41	111.79	49.71	85.98	87.4	122.15	119.44
q3	16.84	62	96.09	46.49	90.16	46.59	85.17	71.04	113.97	111.28
mean	10.61	47.7	85.33	41.09	85.29	36.77	59.29	58.95	97.8	101.58

Table 7.1 The variance parameters for Box and whisker plot of the phase contrast grey scale values of all cases for each tissue classification.

Figure 7.19 shows the summary data of phase contrast grey-scale values for all the cases in Box and whisker plot, where ‘o’ indicate all the data point, while ‘O’ with ‘x’ inside is the mean value for each group of data. Figure 7.19 (a) is grouped by epithelium with their associated stroma. It can be seen that the fat tissue has the smallest phase contrast value; all the epithelial tissues have smaller phase contrast values compared to their associated stroma tissue. It indicates that the stroma has higher scatter intensity than its associated epithelium tissue, and fat has the lowest scattering intensity compared with stroma and epithelium. Figure 7.19 (b) is grouped by epithelium, stroma and fat.



(a)



(b)

Figure 7.19. The Box and whisker plot of the gray scale values of all cases on the phase contrast images. (a) and (b) are using different grouping.

Across diagnostic categories, the phase contrast measures were lower in epithelium as compared to the associated stroma around that epithelium. In all epithelium tissues, normal epithelium had the highest scattering intensity. Measures for both the epithelium and stroma were comparable for invasive and non-invasive malignant tumors and generally higher than for benign tumors (fibroadenomas). The phase contrast of benign and normal stroma was higher than for tumor-associated stroma, indicating that the scatter of stroma could be diagnostically useful.

Tissue Type		Invasive Cancer		Non-invasive Cancer		Benign Fibroadenoma		Benign Normal		Normal	Fat (n=3)
		Epith. (n=14)	Stroma (n=14)	Epith. (n=9)	Stroma (n=9)	Epith. (n=6)	Stroma (n=6)	Epith. (n=16)	Stroma (n=16)	Stroma (n=22)	
Invasive Cancer	Epith. (n=14)	-	-	-	-	-	-	-	-	-	-
	Stroma (n=14)	10^{-5}	-	-	-	-	-	-	-	-	-
Non-invasive Cancer	Epith. (n=9)	0.3	$<10^{-7}$	-	-	-	-	-	-	-	-
	Stroma (n=9)	$<10^{-5}$	1	$<10^{-4}$	-	-	-	-	-	-	-
Benign Fibroadenoma	Epith. (n=6)	0.2	$<10^{-5}$	0.4	$<10^{-5}$	-	-	-	-	-	-
	Stroma (n=6)	0.4	0.009	0.2	0.02	0.04	-	-	-	-	-
Benign Normal	Epith. (n=16)	0.07	$<10^{-4}$	0.005	10^{-4}	0.006	1	-	-	-	-
	Stroma (n=16)	$<10^{-6}$	0.08	10^{-8}	0.1	0.003	0.01	10^{-8}	-	-	-
Normal	Stroma (n=22)	$<10^{-10}$	0.002	$<10^{-13}$	0.005	$<10^{-6}$	$<10^{-4}$	$<10^{-8}$	0.5	-	-
Fat (n=14)		$<10^{-4}$	$<10^{-6}$	$<10^{-4}$	$<10^{-7}$	0.007	0.01	$<10^{-7}$	$<10^{-9}$	$<10^{-12}$	-

Table 7.2 The p-values to determine if the values are significantly different from each tissue type, using a Student's t-test on the phase contrast values of all cases.

The Student's t-Test results for grey scale values of all cases are shown in Table 7.2, and from these p-values it is apparent that there are significant differences in phase contrast between epithelium and its associated stromal tissue, between epithelium and fat tissue, and between stromal tissue and fat tissue. In particular it is obvious that fat is

significantly different from every other tissue type, as should be expected, as indicated by the very small p-values.

When comparing the epithelial tissue and their associated stroma, the t-test between the benign normal epithelium and associated stroma, between invasive epithelium and associated stroma, between non-invasive epithelium and associated stroma and between fibroadenoma epithelium and associated stroma, all show significant differences with p values 10^{-8} , 10^{-5} , 10^{-4} , and 0.04. These indicate that in grey scale value there is more significant difference between benign normal epithelium and associated stroma, while the differences decrease between invasive and non-invasive malignant tissue, and the difference between the fibroadenoma epithelium and associated stroma is the smallest. This result indicates that the stroma in the abnormal tissue is affected by its associated epithelium. This alteration in the stroma appears not well documented, and may be an interesting observation to potentially exploit when looking at imaging cancers and fibroadenomas in vivo.

7.3.B.2 Statistical analysis based on ROI

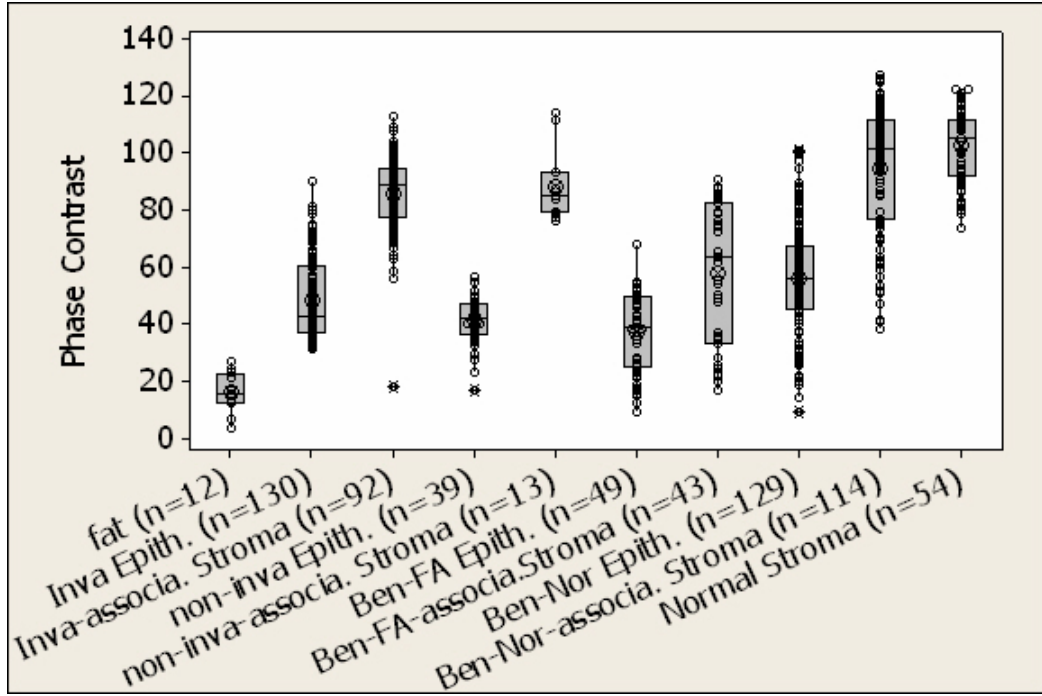
In this analysis, the phase contrast value of each tissue type is analyzed based on the phase contrast values of all ROIs in this tissue type. For each case in a certain tissue type, there are several ROIs. It is all these ROI values, but not the case values obtained from the weighted average of ROI values, will be analyzed directly. As shown in Table 7.3, there were a total of 130 ROIs of invasive epithelium, 92 ROIs of invasive associated stoma, 39 ROIs of non-invasive epithelium, 13 ROIs of non-invasive associated stoma, 49 ROIs of fibroadenoma epithelium, 43 ROIs of fibroadenoma associated stoma, 129

ROIs of normal epithelium, 114 ROIs of normal associated stoma, 54 ROIs of non-associated stroma, and 13 ROIs of fat tissue. The parameters for as Box and whisker plots are tabulated in Table 7.3, and shown as Box and whisker plots in Figure 7.20.

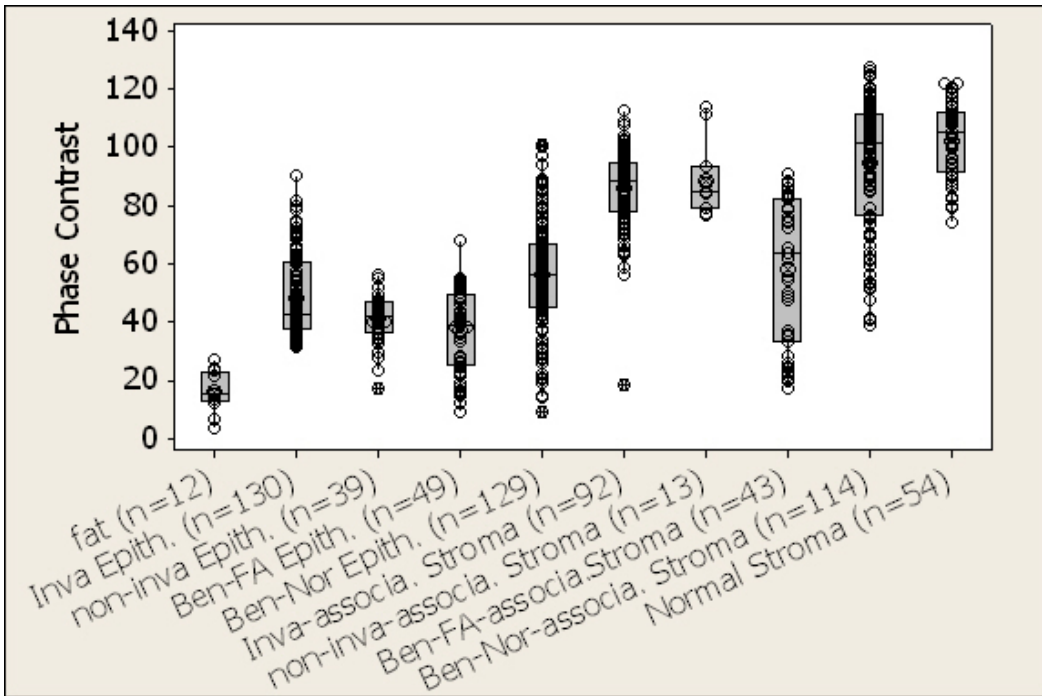
Tissue Type	Fat (n=12)	Invasive Cancer		Non-invasive Cancer		Benign Fibroadenoma		Benign Normal		Normal Stroma (n=54)
		Epith. (n=130)	Stroma (n=92)	Epith. (n=39)	Stroma (n=13)	Epith. (n=49)	Stroma (n=43)	Epith. (n=129)	Stroma (n=114)	
median	15.24	40	88.54	41.81	84.83	38.86	63.61	56.03	101.2	105.1
q1	12.15	32.65	77.45	36.1	79.11	25.44	33.18	46.35	76.9	92.04
min	3.37	12.16	18.21	16.76	76.38	9.06	16.83	8.99	38.5	73.94
max	27.18	90.32	112.98	56.29	114.12	67.69	90.78	100.9	127.4	122.26
q3	23.12	53.55	94.41	46.8	93.3	48.63	82.21	66.77	111.37	111.64
mean	16.08	48.06	85.85	41.19	88.25	36.69	57.82	56.2	94.62	102.39

Table 7.3 The variance parameters for Box and whisker plot of the phase contrast gray scale values of all ROIs for each tissue classification.

Figure 7.20 shows the summary data of phase contrast grey-scale values for all the ROIs in Box and whisker plot, where ‘o’ indicate all the data point, while ‘O’ with ‘x’ inside is the mean value for each group of data. Figure 7.20 (a) is grouped by epithelium with their associated stroma. We can get same result as what we got from Figure 7.19. The fat tissue has the smallest phase contrast value; all the epithelial tissues have smaller phase contrast values compared to their associated stroma tissue. It indicates that the stroma has higher scatter intensity than its associated epithelium tissue, and fat has the lowest scattering intensity compared with stroma and epithelium. Figure 7.20 (b) is grouped by epithelium, stroma and fat.



(a)



(b)

Figure 7.20. The Box and whisker plot of the gray scale values of all kinds of tissue on the phase contrast images. (a) and (b) are using different grouping.

Tissue Type		Invasive Cancer		Non-invasive Cancer		Benign Fibroadenoma		Benign Normal		Normal	Fat
		Epith.	Stroma	Epith.	Stroma	Epith.	Stroma	Epith.	Stroma	Stroma	
Invasive Cancer	Epith. (n=130)	-	-	-	-	-	-	-	-	-	-
	Stroma (n=92)	$<10^{-47}$	-	-	-	-	-	-	-	-	-
Non-invasive Cancer	Epith. (n=39)	0.0002	$<10^{-43}$	-	-	-	-	-	-	-	-
	Stroma (n=13)	$<10^{-8}$	0.5	$<10^{-7}$	-	-	-	-	-	-	-
Benign Fibroadenoma	Epith. (n=49)	$<10^{-5}$	$<10^{-34}$	0.07	$<10^{-11}$	-	-	-	-	-	-
	Stroma (n=43)	0.02	$<10^{-8}$	10^{-4}	$<10^{-6}$	$<10^{-5}$	-	-	-	-	-
Benign Normal	Epith. (n=16)	10^{-4}	$<10^{-29}$	$<10^{-10}$	$<10^{-7}$	$<10^{-10}$	0.7	-	-	-	-
	Stroma (n=114)	$<10^{-44}$	0.0008	$<10^{-46}$	0.12	$<10^{-40}$	$<10^{-11}$	$<10^{-32}$	-	-	-
Normal	Stroma (n=54)	$<10^{-46}$	$<10^{-10}$	$<10^{-45}$	0.001	$<10^{-42}$	$<10^{-14}$	$<10^{-40}$	0.005	-	-
Fat (n=12)		$<10^{-10}$	$<10^{-19}$	$<10^{-9}$	$<10^{-12}$	$<10^{-7}$	$<10^{-47}$	$<10^{-14}$	$<10^{-27}$	$<10^{-23}$	-

Table 7.4 The p-values to determine if the values are significantly different from each tissue type, using a Student's t-test on phase contrast values of all ROIs.

The Student's t-Test results for grey scale values of all ROIs are shown in Table 7.4, and from these p-values it is apparent that there are significant differences in phase contrast between epithelium and its associated stromal tissue, between epithelium and fat tissue, and between stromal tissue and fat tissue. In particular it is obvious that fat is significantly different from every other tissue type, as should be expected, as indicated by the very small p-values.

When comparing the normal stroma to all others stromas, the p-values between the normal stroma and benign normal associated stroma, non-invasive associated stroma, invasive associated stroma and fibroadenoma associated stroma, all show significant differences with p values 0.005, 0.001, 10^{-10} and 10^{-14} respectively. These indicate that in grey scale value there is more significant difference between normal stroma and epithelium (non-invasive, invasive and benign) associated stroma, especially in invasive

cancer and the fibroadenoma. This result indicates that the stroma is affected by its associated epithelium, especially in invasive cancer and fibroadenoma. This alteration in the stroma appears not well documented, and may be an interesting observation to potentially exploit when looking at imaging cancers and fibroadenomas in vivo.

7.4 Conclusion

The relative scattering intensity properties of totally 33 breast tissue sections, including 10 normal sections and 23 abnormal sections were studied by phase contrast images.

The results show that stroma has higher scattering intensity than their associated epithelium tissue, and fat has the lowest scattering intensity compared with stroma and epithelium. In all kinds of epithelial tissues, fibroadenoma epithelium has the lowest scattering intensity, and normal epithelium has the highest scattering intensity. In all stroma tissues, stroma associated with fibroadenoma epithelium has the lowest scattering intensity, and stroma associated with normal epithelium or not associated with any epithelium has the highest scattering intensity. The relatively low scattering intensity in fibroadenoma might be used as a way to differentiate fibroadenoma. The significant difference between normal stroma and abnormal epithelium associated stroma might be exploited in the intra-operative evaluation of margin involvement by tumor at the time of breast excision surgery.

Chapter 8: Conclusion remarks

A big advantage of NIR tomography in breast imaging is its potentiality to obtain the chromophore concentration information, such as total hemoglobin, oxygen saturation, water and the physical traits of the tissue, such as scatterer size and volume density. This thesis has studied the relationship between the sub-microscopic structures of breast tissue and its macroscopic scattering spectroscopy, and focused on exploring methods to obtain the sub-microscopic structures using macroscopic scattering spectroscopy obtained using our NIR Tomography system.

Mie theory estimation scattering spectra, was used to describe the scattering in breast tissue. Given the scatterer size distribution shape and the relative refractive index, the effective scatterer size and number density could be estimated by comparing the reduced scattering spectra with Mie theory. First, this method was applied retrospectively to normal whole breast spectra accumulated in ongoing clinical exams. The effective sizes ranged between 20 and 1400 nm, which are consistent with subcellular organelles and collagen matrix fibrils discussed previously. This estimation method was also applied to images from cancer regions, with results indicating that the effective scatterer sizes of ROI are pretty close to that of the background for both the cancer patients and benign patients; for the effective number density, there is a big difference between the ROI and background for the cancer patients, while for the benign patients, the value of ROI are relatively close to that of the background. The application of this method on the ongoing MRI-guided NIR studies indicated that the fibroglandular tissue had smaller effective scatterer size and larger effective number density than the adipose tissue.

In studying the relationship between the sub-microscopic structures of breast tissue and its macroscopic scattering spectroscopy, both electron microscopy (EM) and optical phase contrast microscopy were used to study the origin of scattering from tissue. Electron microscopy provides a direct way to quantify the size distribution of particles, and phase contrast microscopy can provide information about the relative scattering intensity on the tissue section.

EM studies were examined on high grade infiltrating ductal carcinoma, low grade infiltrating ductal carcinoma, fibroglandular tissue and adipose tissue. Results indicate that lipid-bound particle sizes appear to be distributed as a monotonic exponential function, with sub-micron structures dominating the distribution. The particle histograms were progressively decreasing in magnitude for these tissue types, and the average size of the particles increased, for these four tissues respectively. Given assumptions about the index of refraction change, then the shape of the scattering spectrum in the near infrared as measured through bulk tissue is consistent with what would be predicted by these particle size histograms. This study predicts that the average particle sizes are in the range of 110 to 230 nm, with normal epithelium being smaller in average size, and the cancer tissues having larger average size. Adipose tissues seemed to have the most uniform size distribution, with only a single exponential distribution. Collagen and stromal tissues were not studied extensively in this study, however subsequently were found to be the most dominant contribution to scattering in situ.

The relative scattering intensity properties of breast tissue sections (including 10 normal & 23 abnormal) were studied by phase contrast microscopy. The results show that stroma has higher scattering intensity than their associated epithelium tissue, and fat has

the lowest scattering intensity compared with stroma and epithelium. In all kinds of epithelial tissues, fibroadenoma epithelium has the lowest scattering intensity, and normal epithelium has the highest scattering intensity. In all stroma tissues, stroma associated with fibroadenoma epithelium has the lowest scattering intensity, and stroma associated with normal epithelium or not associated with any epithelium has the highest scattering intensity. The relatively low scattering intensity in fibroadenoma might be used as a way to differentiate fibroadenoma.

The studies in this thesis provide an interpretive approach to estimate average morphological scatter parameters of bulk tissue, through interpretation of diffuse scattering as coming from effective Mie scatterers.

References

1. Carney, P.A., Kasales, C. J., Tosteson, A. N. A., Weiss, J. E., Goodrich, M. E., Poplack, S. P., Wells, W. S., and Titus-Ernstoff, L., *Likelihood of additional work-up among women undergoing routine screening mammography: the impact of age, breast density, and hormone therapy use. Preventive Medicine*, 2004. **39**(48).
2. Poplack, S.P., Tosteson, A. N. A., Grove, M. R., Wells, W. A., and Carney, P. A., *Mammography in 53,803 Women from the New Hampshire Mammography Network. Radiology*, 2000. **217**: p. 832.
3. Dee, K.E., and Sickles, E. A., *Medical Audit of Diagnostic Mammography Examinations: Comparison with Screening Outcomes Obtained Concurrently*. *Am J Roentgenol*, 2001. **176**: p. 729.
4. Dehghani, H., Pogue, B. W., Poplack, S. P., and Paulsen, K. D., *Multiwavelength three dimensional near-infrared tomography of the breast: initial simulation, phantom, and clinical results. Applied Optics*, 2003. **42**: p. 135.
5. Durduran, T., Choe, R., Culver, J. P., Zubkov, L., Holboke, M. J., Giammarco, J., Chance, B., and Yodh, A. G., *Bulk optical properties of healthy female breast tissue. Phys. Med. Biol*, 2002. **47**: p. 2847.
6. Fantini, S., Walker, S. A., Franceschini, M. A., Kaschke, M., Schlag, P. M., and Moesta, K. T., *Assessment of the size, position, and optical properties of breast tumors in vivo by noninvasive optical methods. Applied Optics*, 1998. **37**: p. 1982.
7. Ntziachristos, V., and Chance, B., *Probing physiology and molecular function using optical imaging: applications to breast cancer. Breast Cancer Research*, 2001. **3**: p. 41.
8. Hillman, E.M.C., Hebden, J. C., Schweiger, M., Dehghani, H., Schmidt, F. E. W., Delpy, D. T. and Arridge, S. R., *Time resolved optical tomography of the human forearm. Phys. Med. Biol.*, 2001. **46**: p. 1117.
9. Hielscher, A.H., Scheel, A. K., Klose, A. D., Moa-Anderson, B., Backhaus, M., Netz, U., Muller, G. A., Burmester, G. R., and Beuthan, J., *Biomedical Topical Meetings*. 2004.
10. Schweiger, M., and Arridge, S. R., *Optical tomographic reconstruction in a complex head model using a priori region boundary information. Physics in Medicine and Biology*, 1999. **44**: p. 2703.
11. Boas, D.A., Chen, K., Grebert, D., and Franceschini, M. A., *Improving the diffuse optical imaging spatial resolution of the cerebral hemodynamic response to brain activation in humans. Opt. Lett.*, 2004. **29**: p. 1506.
12. Perelman, L.T., Wu, J., Itzkan, I., and Feld, M. S., *Photon migration in turbid media using path integrals. Phys. Rev. Lett*, 1994. **72**: p. 1341.
13. O'Leary, M.A., Boas, D. A., Chance, B., and Yodh, A. G., *Experimental images of heterogeneous turbid media by frequency-domain diffusing-photon tomography. Opt. Lett.*, 1995. **20**(5): p. 426.
14. Yodh, A.G., and Chance, B., *Spectroscopy and imaging with diffusing light. Phys. Today*, 1995. **48**: p. 34.
15. Arridge, S.R., and Hebden, J. C., *Optical imaging in medicine: II. Modelling and reconstruction. Phys. Med. Biol.*, 1997. **42**: p. 841.

16. Cerussi, A.E., Berger, A. J., Bevilacqua, F., Shah, N., Jakubowski, D., Butler, J., Holcombe, R. F., Tromberg, B. J., *Sources of absorption and scattering contrast for near-infrared optical mammography.[comment]*. Academic Radiology., 2001. **8**(3): p. 211-8.
17. Shah, N, C., A., Eker, C., Espinoza, J., Butler, J., Fishkin, J., Hornung, R., and Tromberg, B. J., *Noninvasive functional optical spectroscopy of human breast tissue*. Proc. Nat. Acad. Sci., 2001. **98**: p. 4420.
18. Pogue, B.W., Jiang, S., Dehghani, H., Kogel, C., Soho, S., Srinivasan, S., Song, X., Tosteson, T.D., Poplack, S., and Paulsen, K. D., *Characterization of Hemoglobin, Water and NIR Scattering in Breast Tissue: Analysis of inter-subject variability and menstrual cycle changes*. Journal of Biomedical Optics., 2004. **9**(3): p. 541-552.
19. Liu, H., Beauvoit, B., Kimura, M., and Chance, B., *Dependence of tissue optical properties on solute-induced changes in refractive index and osmolarity*. J. Biomed. Opt., 1996. **1**: p. 200-211.
20. Drezek, R., Dunn, A., and Richards-Kortum, R., *Light scattering from cells: finite-difference time-domain simulations and goniometric measurements*. Appl. Opt., 1999. **38**(16): p. 3651.
21. Chance, B., Luo, Q., Nioka, S., Alsop, D. C., and Detre, J. A., *Optical investigations of physiology: a study of intrinsic and extrinsic biomedical contrast*. Phil. Trans. R. Soc. Lond. B, 1997. **352**: p. 707-716.
22. Wang, X., Pogue, B. W., Jiang, S., Song, X., Paulsen, K. D., Kogel, C., Poplack, S. P., and Wells, W. A., *Approximation of Mie Scattering Parameters in Near-Infrared Tomography of Normal Breast Tissue In Vivo*. Journal of Biomedical Optics., 2005. **10**(5): p. 051704.
23. Wang, X., Pogue, B. W., Jiang, S., Dehghani, H., Song, X., Srinivasan, S., Brooksby, B. A., Paulsen, K. D., Kogel, C., Poplack, S. P., and Wells, W. A., *Image Reconstruction of Effective Mie Scattering Parameters of Breast Tissue In Vivo with Near-Infrared Tomography*. urnal of Biomedical Optics, 2006. **11**(4): p. 041106.
24. Pogue, B.W., *Frequency-domain optical spectroscopy and imaging of tissue and tissue-simulating media.* Ph.D. Thesis, 1996.
25. Srinivasan, R., and Singh, M., *Laser backscattering and transillumination imaging of human tissues and their equivalent phantoms*. IEEE Trans. Biomed. Eng., 2003. **50**(6): p. 724-730.
26. Poplack, S.P., Paulsen, K. D., Hartov, A., Meaney, P. M., Pogue, B. W., Tosteson, T. D., Grove, M. R., Soho, S. K., and Wells, W. A., *Electromagnetic Breast Imaging: Average Tissue Property Values in Women with Negative Clinical Findings*. Radiology, 2004. **231**: p. 571.
27. Jiang, H.B., *Frequency-domain fluorescent diffusion tomography: a finite-element-based algorithm and simulations*. Appl. Opt., 1998. **37**(22): p. 5337-5343.
28. McBride, T.O., Pogue, B. W., Jiang, S., Osterberg, U. L., and Paulsen, K. D., *A parallel-detection frequency-domain near-infrared tomography system for hemoglobin imaging of the breast in vivo*. Review of Scientific Instruments, 2001. **72**: p. 1817.

29. Pifferi, A., Swartling, J., Chikoidze, E., Toricelli, A., Taroni, P., Bassi, A., Andersson-Engels, S., and Cubeddu, R., *Spectroscopic time-resolved diffuse reflectance and transmittance measurements of the female breast at different interfiber distances*. *Journal of Biomedical Optics*, 2004. **9**: p. 1143.
30. Ntziachristos, V., Ma, X., Yodh, A. G., and Chance, B., *Multichannel photon counting instrument for spatially resolved near infrared spectroscopy*. *Review of Scientific Instruments*, 1999. **70**: p. 193.
31. Boyd, N.F., Byng, J. W., Jong, R. A., Fishell, E. K., Little, L. E., Miller, A. B., Lockwood, G. A., Tritchler, D. L., and Yaffe, M. J., *Quantitative Classification of Mammographic Densities and Breast Cancer Risk: Results From the Canadian National Breast Screening Study*. *Journal of the National Cancer Institute*, 1995. **87**: p. 670.
32. Boyd, N.F., Lockwood, G. A., Byng, J. W., Tritchler, D. L., and Yaffe, M. J., *Mammographic densities and breast cancer risk," Cancer Epidemiology Biomarkers and Prevention*. 1998. **7**: p. 1133.
33. Simick, M.K., Jong, R. A., Wilson, B. C., and Lilge, L., *Non-ionizing near-infrared radiation transillumination spectroscopy for breast tissue density and assessment of breast cancer risk*. *Journal of Biomedical Optics*, 2004. **9**: p. 794.
34. Tromberg, B.J., Shah, N., Lanning, R., Cerussi, A., Espinoza, J., Pham, T., Svaasand, L., and Butler, J., *Non-invasive in vivo characterization of breast tumors using photon migration spectroscopy*. *Neoplasia*, 2000. **2**(1-2): p. 26-40.
35. Thomsen, S., and Tatman, D., *Physiological and Pathological Factors of Human Breast Disease That Can Influence Optical Diagnosis*. *Annals of the New York Academy of Sciences*, 1998. **838**: p. 171.
36. Hasan, J., Byers, R., and Jayson, G. C., *Intra-tumoural microvessel density in human solid tumours*. *Br J Cancer*, 2002. **86**: p. 1566.
37. Rice, A., and Quinn, C. M., *Angiogenesis, thrombospondin, and ductal carcinoma in situ of the breast*. *J Clin Pathol*, 2002. **55**: p. 569.
38. Profio, A.E., and Navarro, G. A., *Scientific basis of breast diaphanography*. *Med. Phys.*, 1989. **16**: p. 60-65.
39. Okunieff, P., Hoeckel, M., Dunphy, E. P., Schlenger, K., Knoop, C., and Vaupel, P., *Oxygen tension distributions are sufficient to explain the local response of human breast tumors treated with radiation alone*. *Int. J. Radiation Oncology Biol. Phys.*, 1993. **26**: p. 631.
40. Tromberg, B.J., Coquoz, O., Fishkin, J. B., Pham, T., Anderson, E. R., Butler, J., Cahn, M., Gross, J. D., Venugopalan, V., Pham, D., *Non-invasive measurements of breast tissue optical properties using frequency-domain photon migration*. *Phil. Trans. R. Soc. Lond. B*, 1997. **352**: p. 661.
41. Pogue, B.W., Poplack, S. P., McBride, T. O., Wells, W. A., Osterman, K. S., Osterberg, U. L., and Paulsen, K. D., *Quantitative Hemoglobin Tomography with Diffuse Near-Infrared Spectroscopy: Pilot Results in the Breast*. *Radiology*, 2001. **218**: p. 261.
42. Pogue, B.W., Jiang, S., Srinivasan, S., Song, X., Dehghani, H., Paulsen, K. D., Tosteson, T. D., Kogel, C., Soho, S. K., and Poplack, S. P., *Biomedical Topical Meetings*, 2004.

43. Song, X., Pogue, B. W., Jiang, S., Doyley, M. M., Dehghani, H., Tosteson, T. D., and Paulsen, K. D., *Automated region detection based on the contrast-to-noise ratio in near-infrared tomography*. APPLIED OPTICS, 2004. **43**(5): p. 1053.
44. Jiang, H., *Subcellular sizing with polarized light spectroscopy*. *Opt. Commun.*, 2003. **226**(1-6): p. 279-283.
45. McBride, T.O., Pogue, B. W., Osterberg, U. L., and Paulsen, K. D., *Oxygen Transport to Tissue XXIV*, 2002. **85**.
46. Brooksby, B.A., Jiang, S., Dehghani, H., Kogel, C., Doyley, M., Weaver, J. B., Poplack, S. P., Pogue, B. W., and Paulsen, K. D., *MRI-NIR tomography of the breast*. *Rev. Sci. Instrum.*, 2004. **75**: p. 5262.
47. van Staveren, H.J., Moes, C. J. M., van Marle, J., Prahl, S. A., and van Gemert, M. J. C., *Light Scattering in Intralipid-10% in the wavelength range of 400-1100nm*. *Applied Optics*, 1991. **30**(31): p. 4507-4514.
48. Mourant, J.R., Fuselier, T., Boyer, J., Johnson, T. M., and Bigio, I. J., *Predictions and measurements of scattering and absorption over broad wavelength ranges in tissue phantoms*. *Applied Optics*, 1997. **36**(4): p. 949-957.
49. Srinivasan, S., Pogue, B. W., Jiang, S., Dehghani, H., Kogel, C., Soho, S., Chambers, J. G., Tosteson, T. D., Poplack, S. P., and Paulsen, K. D., *Interpreting hemoglobin and water concentration, oxygen saturation, and scattering measured by near-infrared tomography of normal breast in vivo*. *Proceedings of the National Academy of Sciences of the United States of America*, 2003. **100**(21): p. 12349.
50. Bevilacqua, F., Berger, A. J., Cerussi, A. E., Jakubowski, D., Tromberg, B. J., *Broadband Absorption Spectroscopy in Turbid Media by Combined Frequency-Domain and Steady-State Methods*. *Appl. Opt.*, 2000. **39**(34): p. 6498-6510.
51. Brooksby, B., Pogue, B. W., Jiang, S., Dehghani, H., Srinivasan, S., Kogel, C., Tosteson, T. D., Weaver, J., Poplack, S. P., and Paulsen, K. D., *Imaging breast adipose and fibroglandular tissue molecular signatures by using hybrid MRI-guided near-infrared spectral tomography*. *PNAS*, 2006. **103**(23): p. 8828.
52. McBride, T.O., Pogue, B. W., Jiang, S., Osterberg, U. L., Paulsen, K. D., and Poplack, S. P., *Multi-spectral near-infrared tomography: a case study in compensating for water and lipid content in hemoglobin imaging of the breast*. *Journal of Biomedical Optics*, 2001. **7**: p. 72.
53. Sastegar, S., Motamedi M., *A theoretical analysis of dynamic variation of temperature dependent optical properties in the response of laser irradiated tissue*. *Laser-tissue interaction*, 1990. **Proc. SPIE 1202**: p. 253-259.
54. Backman, V., Gopal, V., Kalashnikov, M., Badizadegan, K., Gurjar, R., Wax, A., Georgakoudi, I., Mueller, M., Boone, C. W., Dasari, R. R., and Feld, M. S., *Measuring cellular structure at submicrometer scale with light scattering spectroscopy*. *IEEE J. Sel. Top. Quantum Electron.*, 2001. **7**(6): p. 887-893.
55. Borhen, C.F.H., D.R., *Absorption and Scattering of Light by Small Particles*. 1998: John Wiley & Sons, Inc.
56. Bohren, C.F., and Huffman, D. R., *Absorption and Scattering of Light by Small Particles*. John Wiley & Sons, Inc., New York, 1998.
57. van de Hulst, H.C., *Light Scattering by Small Particles*. 1981: Dover, New York.

58. Perelman, L.T., Backman, V., Wallace, M., Zonios, G, Manoharan, R., Nusrat, A., Shields, S., Seiler, M., Lima, C., Hamano, T., Itzkan, I., Van Dam, J., Crawford, J. M., and Feld, M. S., *Observation of periodic fine structure in reflectance from biological tissue: a new technique for measuring nuclear size distribution. Phys. Rev. Lett.*, 1998. **80**(3): p. 627.
59. Bigio, I.J., Bown, S. G., Briggs, G., Kelley, C., Lakhani, S., Pickard, D., Ripley, P. M., Rose, I. G., and Saunders, C., *Diagnosis of breast cancer using elastic-scattering spectroscopy: preliminary clinical results. J. Biomed. Opt.*, 2000. **5**(2): p. 221-228.
60. Mourant, J.R., Johnson, T. M., and Freyer, J. P., *Characterizing mammalian cells and cell phantoms by polarized backscattering fiberoptic measurements. Appl. Opt.*, 2001. **40** (28): p. 5114-5123.
61. Wax, A., Yang, C., Backman, V., Kalashnikov, M., Dasari, R. R., and Feld, M.S., *Determination of particle size by using the angular distribution of backscattered light as measured with low-coherence interferometry. J. Opt. Soc. Am. A*, 2002. **19**(4): p. 737-744.
62. Wax, A., Yang, C., Backman, V., Badizadegan, K., Boone, C. W., Dasari, R. R., and Feld, M. S., *Cellular organization and substructure measured using angle-resolved low-coherence interferometry. Biophys. J.*, 2002. **82**: p. 2256-2264.
63. Backman, V., Gurjar, R. S., Perelman, L. T., and Gopal, V., *Imaging and measurement of cell structure and organization with submicron accuracy using light scattering spectroscopy. Optical Biopsy IV, Proc. SPIE*, 2002. **4613**: p. 101-110.
64. Mourant, J.R., Freyer, J. P., Hielscher, A. H., Eick, A. A., Shen, D., and Johnson, T. M., *Mechanisms of light scattering from biological cells relevant to noninvasive optical-tissue diagnostics. Appl. Opt.*, 1998. **37**(16): p. 3586-3593.
65. Hielscher, A.H., Mourant, J. R., and Bigio, I. J., *Influence of particle size and concentration on the diffuse backscattering of polarized light from tissue phantoms and biological cell suspensions. Appl. Opt.*, 1997. **36**(1): p. 125-135.
66. Wax, A., Yang, C. H., Muller, M. G., Nines, R., Boone, C. W., Steele, V. E., Stoner, G. D., Dasari, R. R., and Feld, M. S., *In situ detection of neoplastic transformation and chemopreventive effects in rat esophagus epithelium using angle-resolved low-coherence interferometry. Cancer Res.*, 2003. **63**: p. 3556-3559.
67. Jiang, H., Marquez, G., and Wang, L. V., *Determination of particle size distribution in concentrated suspensions: photon migration approach. OSA Trends Opt. Photonics Ser.*, 1998. **21**: p. 92.
68. Beauvoit, B., Evans, S.M., Jenkins, T.W., Miller, E.E., and Chance, B., *Correlation between the light scattering and the mitochondrial content of normal tissues and transplantable rodent tumors. Anal Biochem.*, 1995. **226**(1): p. 167-74.
69. Dunn, A., and Richards-Kortum, R., *Three-Dimensional Computation of Light Scattering From Cells. IEEE JOURNAL OF SELECTED TOPICS IN QUANTUM ELECTRONICS*, 1996. **2**(4): p. 898.

70. Pyhtila, J.W., Graf, R. N., and Wax, A., *Determining nuclear morphology using an improved angle-resolved low coherence interferometry system*. OPTICS EXPRESS, 2003. **11**(25): p. 3473.
71. Wilson, J.D., Bigelow, C. E., Calkins, D.J., and Foster, T. H., *Light Scattering from Intact Cells Reports Oxidative-Stress-Induced Mitochondrial Swelling*. Biophysical Journal, 2005. **88**: p. 2929-2938.
72. Graaff, R., Aarnoudse, J. G., Zijp, J.-R., Sloot, P.-M. A., de Mull, F. F. M., Greve, J., and Koelink, M. H., *Reduced light-scattering properties for mixtures of spherical particles: a simple approximation derived from Mie calculations*. Appl. Opt., 1992. **31**(10): p. 1370-1376.
73. Nilsson, A.M.K., Stureson, C., Liu, D. L., and Andersson-Engels, S., *Changes in spectral shape of tissue optical properties in conjunction with laser-induced thermotherapy*. Appl. Opt., 1998. **37**(7): p. 1256-1272.
74. Gelebart, B., Tinetti, E., Tualle, J.M., and Avriillier, S., *Phase function simulation in tissue phantoms: a fractal approach*. Pure Appl. Opt., 1996. **5**(4): p. 377-388.
75. Schmitt, J.M., and Kumar, G., *Optical scattering properties of soft tissue: a discrete particle model*. Appl. Opt., 1998. **37**(13): p. 2788-2797.
76. Wang, R.K., *Modelling optical properties of soft tissue by fractal distribution of scatterers*. J. Mod. Opt., 2000. **47**(1): p. 103-120.
77. Benz, E.B., Federman, M., Godleski, J.J., Bierbaum, B.E., Thornhill, T.S., and Spector, M., *Transmission electron microscopy of intracellular particles of polyethylene from joint replacement prostheses: size distribution and cellular response*. Biomaterials., 2001. **22**(21): p. 2835-42.
78. Gobel, G., Kuhn, J., and Fricke, J., *Dependent scattering effects in latex-sphere suspensions and scattering powders*. Waves in Random Media, 1995. **5**: p. 413-426.
79. Tinsley, S.G., and Bowman, A., J. Oil Colour Chem Ass., 1949. **23**: p. 348.
80. Hottel, H.C., Sarofim, A. F., Dalzell, W. H., and Vasalos, I. A., AIAA J., 1971: p. 910.
81. Roy, H.K., Liu, Y., Wali, R. K., Kim, Y. L., Kromine, A. K., Goldberg, M. J., and Backman, V., *Four-dimensional elastic light-scattering fingerprints as preneoplastic markers in the rat model of colon carcinogenesis*. Gastroenterology, 2004. **126**(4): p. 1071-1081.
82. Ntziachristos, V., Yodh, A. G., Schnall, M. D., and Chance, B., *MRI-guided diffuse optical spectroscopy of malignant and benign breast lesions*. Neoplasia, 2002. **4**(4): p. 347-354.
83. Blyschak, K., Simick, M., Jong, R., Lilge, L., *Classification of breast tissue density by Optical Transillumination Spectroscopy: optical and physiological effects governing predictive value*. Proceedings of SPIE - The International Society for Optical Engineering, 2003, 2003. **5260**: p. 568-579.
84. Ziv, E., Shepherd, J., Smith-Bindman, R., Kerlikowske, K., *Mammographic breast density and family history of breast cancer*. Journal of the National Cancer Institute., 2003. **95**(7): p. 556-8.
85. Jiang, S.D., Pogue, B. W., McBride, T. O., Doyley, M. M., Poplack, S. P., and Paulsen, K. D., *Near-infrared breast tomography calibration with optoelastic tissue simulating phantoms*. Journal of Imaging, 2003. **12**(4): p. 613-620.

86. Srinivasan, S., Pogue, B. W., Brooksby, B., Jiang, S., Dehghani, H., Kogel, C., Wells, W. A., Poplack, S. P., Paulsen, K. D., *Near-Infrared Characterization of Breast Tumors In-Vivo using Spectrally-Constrained Reconstruction*. TCRT (Technology in cancer research and treatment), 2005(Oct).
87. Saidi, I.S., Jacques, S. L., and Tittel, F. K., *Mie and Rayleigh modeling of visible light scattering in neonatal skin*. Appl. Opt., 1995. **34**(31): p. 7410-7418.
88. Beauvoit, B., Liu, H., Kang, K., Kaplan, P. D., Miwa, M., Chance, B., *Characterization of absorption and scattering properties for various yeast strains by time-resolved spectroscopy*. Cell Biophysics, 1993. **23**(1-3): p. 91-109.
89. Cubeddu, R., D'Andrea, C., Pifferi, A., Taroni, P., Torricelli, A., and Valentini, G., *Effects of the menstrual cycle on the red and near-infrared optical properties of the human breast*. Photochem. Photobiol., 2000. **72**(3): p. 383-391.
90. Srinivasan, S., Pogue, B. W., Jiang, S., Dehghani, H., and Paulsen, K. D., *Spectrally constrained chromophore and scattering near-infrared tomography provides quantitative and robust reconstruction*. Applied Optics, 2004. **44**(10): p. 1858-1869.
91. Brooksby, B., Jiang, S., Dehghani, H., Pogue, B. W., Paulsen, K. D., Weaver, J., Kogel, C., and Poplack, S. P., *Combining near infrared tomography and magnetic resonance imaging to study in vivo breast tissue: implementation of a Laplacian-type regularization to incorporate MR structure*. J. Biomed. Opt., 2005. **10**(5): p. 0515041-10.
92. Brooksby, B., Srinivasan, S., Jiang, S., Dehghani, H., Pogue, B. W., Paulsen, K. D., Weaver, J., Kogel, C., and Poplack, S. P., *Spectral-priors improve Near-Infrared diffuse tomography more than spatial-priors*. Optics Letters, 2005. **30**(15): p. 1968-1970.
93. Carpenter, C.M., Pogue, B. W., Jiang, S., Dehghani, H., Wang, X., Paulsen, K. D., Wells, W. A., Forero, J., Kogel, C., Weaver, J. B., Poplack, S. P., Kaufman, P. A., *Image-Guided Optical Spectroscopy provides Molecular-Specific Information In Vivo: MRI-Guided Spectroscopy of Breast Cancer Hemoglobin, Water & Scatterer Size*. Optics Letters, 2006. **Submitted**.
94. Barbour, R.L., Graber, H. L., Chang, J., Barbour, S. S., Koo, P. C., and Aronson, R., *MRI-guided optical tomography:prospects and computation for a new imaging method*. IEEE Comp. Sci. Eng., 1995. **2**: p. 63-77.
95. Borsic, A., Lionheart, W. R. B., and McLeod, C. N., *Generation of anisotropic-smoothness regularization filters for EIT*. IEEE transactions on medical imaging, 2002. **21**(6): p. 579-588.
96. Intes, X., Maloux, C., Guven, M., Yazici, T., and Chance, B., *Diffuse optical tomography with physiological and spatial a priori constraints*. Phys. Med. Biol., 2004. **49**(12): p. N155-N163.
97. Kaipio, J.P., Kolehmainen, V., Vauhkonen, M., Somersalo, E., *Inverse problems with structural prior information*. Inverse Problems, 1999. **15**(3): p. 713-729.
98. Kanmani, B., Vasu, R. M., *Diffuse optical tomography using intensity measurements and the a priori acquired regions of interest: theory and simulations*. Phil. Trans. R. Soc. Lond. B, 2005. **50**: p. 247-264.

99. Pogue, B.W., Paulsen, K. D., *High-resolution near-infrared tomographic imaging simulations of the rat cranium by use of a priori magnetic resonance imaging structural information*. Optics Letters, 1998. **23**: p. 1716.
100. Vauhkonen, M., Vadasz, D., Kaipio, J. P., Somersalo, E., and Karjalainen, P. A., *Tikhonov regularization and prior information in electrical impedance tomography*. IEEE transactions on medical imaging, 1998. **17**(2): p. 285-293.
101. Peters, V.G., Wyman, D. R., Patterson, M. S., Frank G. L., *Optical properties of normal and diseased breast tissue in the visible and near infrared*. Phys. Med. Biol., 1990. **35**: p. 1317-1334.
102. Jiang, S., Pogue, B.W., McBride, T.O., and Paulsen, K. D., *Quantitative Analysis of Near-Infrared Tomography: Sensitivity to the Tissue-Simulating Pre-Calibration Phantom*. J. Biomed. Opt., 2002. **8**(2): p. 308-315.
103. Drezek, R., Guillaud, M., Collier, T., Boiko, I., Malpica, A., Macaulay, C., Follen, M., Richards-Kortum, R., *Light scattering from cervical cells throughout neoplastic progression: influence of nuclear morphology, DNA content, and chromatin texture*. Journal of Biomedical Optics, 2003. **8**: p. 7-16.
104. Poplack, S.P., Paulsen, K. D., Hartov, A., Meaney, P. M., Pogue, B. W., Tosteson, T. D., Soho, S. K., and Wells, W. A., *Electromagnetic Breast Imaging - Pilot Results in Women with Abnormal Mammography*. Radiology, 2006. **in press**.
105. Bartek, M., Wang, X., Wells, W. A., Paulsen, K. D., Pogue, B. W., *Estimation of subcellular particle size histograms with electron microscopy for prediction of optical scattering in breast tissue*. Journal of Biomedical Optics, 2006. **11**(6): p. 064007.
106. Wells, W.A., Daghlian, C. P., Tosteson, T. D., Grove, M. R., Poplack, S. P., Knowlton-Soho, S., and Paulsen, K. D., *Analysis of the microvasculature and tissue type ratios in normal vs. benign and malignant breast tissue*. Analytical and Quantitative Cytology and Histology, 2004. **26**: p. 166-174.
107. Maier, J.S., Walker, S.A., Fantini, S., Franceschini M.A., and Gratton, E., *Possible Correlation between Blood-Glucose Concentration and the Reduced Scattering Coefficient of Tissues in the near-Infrared*. Optics Letters, 1994. **19**: p. 2062-2064.
108. Dunn, A., *Light Scattering Properties of Cells*. 1997, University of Texas, Austin: Austin, TX.
109. Srinivasan, S., Pogue, B. W., Jiang, S., Dehghani, H., Kogel, C., Soho, S., Gibson, J. J., Tosteson, T. D., Poplack, S. P., and Paulsen, K. D., *In Vivo Hemoglobin and Water Concentration, Oxygen Saturation, and Scattering Estimates from Near-Infrared Breast Tomography Using Spectral Reconstruction*. Academic Radiology, 2006. **in press**.
110. Beauvoit, B., Kitai, T., and Chance, B., *Contribution of the Mitochondrial Compartment to the Optical-Properties of the Rat-Liver - a Theoretical and Practical Approach*. Biophysical Journal, 1994. **67**: p. 2501.

Appendix – Programs used and created

List of Programs Created

```
fcn_musprime_MieA(A,n2,n1,wave1,dwave,wave2)
    % Get the musprime data from Mie theory. The refractive indexes
    are n2 and n1. The musprime spectra is in the range
    wave1:dwave:wave2 (nm). The average particle size is A (nm), with
    exponential decay histogram, number density is 1 (m-3).
```

```
fcn_musprime_MieAN(A,N,n2,n1,wave1,dwave,wave2)
    % Get the musprime data from Mie theory. The refractive indexes
    are n2 and n1. The musprime spectra is in the range
    wave1:dwave:wave2 (nm). The particle size is A (nm), number density
    is N (m-3).
```

```
fcn_musprime_MieA_table(A1,dA,A2,n2,n1,wave1,dwave,wave2)
    % Get the musprime data table from Mie theory. The refractive
    indexes are n2 and n1. The musprime spectra is in the range
    wave1:dwave:wave2 (nm). The average particle sizes are from A1 (nm)
    to A2 (nm), with step dA (nm). Number density is 1 (m-3).
```

```
[A_estimated,N_estimated]=ANestimation(A1,dA,A2,n2,n1,wave1,dwave,wave2,wave_nm)
    % Get the best estimated particle size A_estimated (nm) and
    number density N_estimated (m-3) from the experimental data by
    comparing it with simulation data from Mie theory. The refractive
    indexes are n2 and n1. The musprime spectra is in the range
    wave1:dwave:wave2 (nm). The simulation data to be compared with the
    experimental data includes a range for average particle sizes
    A1:dA:A2 (nm). In the comparison, the musprime spectra will be
    normalized at a certain wavelength wave_nm.
```

```
NPthetaSingle(A,polar,n1,n2,wave)
    % to get normalized phase function using Mie theory from a
    medium with exponential scatterer size distribution with single size
    at "A"(nm), and external refractive index "n1", internal refractive
    index "n2". Incident laser has wavelength 'wave' and polarization
    'polar'.
```

```
NPthetaEXP(A,polar,n2,n1 ,wave)
    % to get normalized phase function using Mie theory from a
    medium with exponential scatterer size distribution with average
    size at "A"(nm), and external refractive index "n1", internal
    refractive index "n2". Incident laser has wavelength 'wave' and
    polarization 'polar'.
```

```

APthetaEXP(A,n1,n2,polar,wave, angdevi)
    % to get averaged (over -angdevi to +angdevi degree) Ptheta data
    from Mie theory for a medium with exponential size distribution and
    average size "A", with external refractive index "n1", internal
    refractive index "n2", and using light with polarization "polar" and
    wavelength "wave".

APthetaSingle(A,n1,n2,polar,wave, angdevi)
    % to get averaged (over -angdevi to +angdevi degree) Ptheta data
    from Mie theory for a medium with single size "A", with external
    refractive index "n1", internal refractive index "n2", and using
    light with polarization "polar" and wavelength "wave".

[A_estimated,
error]=PthetaFitting(A0,dA,compAng,polar,wave,angdevi,n1,n2)
    % Compare the measured data with Mie theory at comparison angle
    'compAng' by the coefficients of polynomials got from polynomial
    fitting of the data. Use Newton-Raphson Method to update the scatter
    size iteratively to get the best estimated scatterer size in the
    medium. The initial guess for the average particle size is A0, the
    step size is dA. Suppose the experimental Ptheta data are averaged
    over angle (degree) -angdevi to +angdevi because of the experimental
    setup. The medium has a single particle size "A", with external
    refractive index "n1" and internal refractive index "n2". And the
    laser we use has polarization "polar" and wavelength "wave".

[A_estimated1, A_estimated2, A_estimated, devi_min1, devi_min2,
devi_min]=PthetaErrorPlotting(compAng)
    %Simulation study for scatterer size estimation from angular
    scattering data by error plotting. Get forward data from Mie theory
    first, add certain noise, get the derivative of the data, and then
    compare with original Mie theory by error plotting to get the
    estimated scatterer size. Both P1 and P2 polarizations are used, and
    their ratio are also used as the comparison data for estimation. The
    estimated average size using P1 data, P2 data and P1/P2 data are
    A_estimated1, A_estimated2 and A_estimated respectively; the minimum
    deviation are devi_min1, devi_min2, devi_min respectively. Comparison
    angle is 'compAng'

add_noise2(data1,data2,amp);
    % adds a normally distributed noise to data1 and writes it to data2.
    The amount of noise depends on value specified by amp.

```

List of Programs used

SphereSc(m,x,I,ang)
returns the scattered Light for a sphere, size x, refractive index relative to medium m at angle ang. Incident light has Stoke's Vector I.

```
% Written by and copyright
%      Dave Barnett
%      Optical Engineering Group
%      Dept. of Electrical and Electronic Engineering
%      Loughborough University
%      20th November 1996
```

[Cext, Cscat] = crosssection(m,a,wv)
it returns the extinction and scattering cross sections for a sphere, radius a, refractive index relative to medium m at wavelength wv.

```
% Written by and copyright
%      Dave Barnett
%      Optical Engineering Group
%      Dept. of Electrical and Electronic Engineering
%      Loughborough University
%      4th May 1999
```

[a,b]=ScatCoef(m,x,nmax)
it returns the two column vectors a and b containing the scattering coefficients for particles of size x and refractive index relative to medium m, from n=1 to n=nmax.

```
% Written by and copyright
%      Dave Barnett
%      Optical Engineering Group
%      Dept. of Electrical and Electronic Engineering
%      Loughborough University
%      20th November 1996
```

[p,t]=ALegendr(ang, nmax)
ALegendr the angular dependent Associated Legendre Polynomials.
it produces matrices p and t with rows n=1 to n=nmax for pi and tau functions respectively.

```
% Written by and copyright
%      Dave Barnett
%      Optical Engineering Group
%      Dept. of Electrical and Electronic Engineering
%      Loughborough University
%      20th November 1996
```

Programs created

1.

```
% Get the musprime data from Mie theory. The refractive indexes are
n2 and n1. The musprime spectra is in the range wavel:dwave:wave2
(nm). The average particle size is A (nm), with exponential decay
histogram, number density is 1 (m-3).
.
function f=fcn_musprime_MieA(A,n2,n1,wavel,dwave,wave2)
    format long

% build an exponential decay histogram with average particle size A
(nm)
a=0; average=0;
while average>(A*1.02) | average<(A*0.98)
    a=a+0.000001;
    integ=0;
    for j=1:A*0.01:A*5.01
        integ=a*A*0.01*exp(-a*j)+integ;
    end
    b=integ; average=0;
    for j=1:A*0.01:A*5.01
        average=j*A*0.01*a*exp(-a*j)/b+average;
    end
end

% musprime spectra calculating
I=[1;1;0;0];
i0=1;
for wave=wavel:dwave:wave2
    i1=1;
    i2=1;
    sum2=0;
    sum3=0;
    for j=1:A*0.1:A*5.01
        wv=2*pi*j/wave;
        sum=0;
        sum1=0;
        for ang=0:1:180

%% SphereSc(m,x,I,ang) returns the scattered Light for a sphere,
size x, refractive index relative to medium m at angle ang. Incident
light has Stoke's Vector I.
% Written by and copyright
%     Dave Barnett
%     Optical Engineering Group
%     Dept. of Electrical and Electronic Engineering
%     Loughborough University
%     20th November 1996
```

```

%%[[Cext, Cscat] = crosssection(m,a,wv) returns the extinction
and scattering cross sections for a sphere, radius a, refractive
index relative to medium m at wavelength wv.
% Written by and copyright
%      Dave Barnett
%      Optical Engineering Group
%      Dept. of Electrical and Electronic Engineering
%      Loughborough University
%      4th May 1999

        S=SphereSc(n1/n2,wv,I,ang*pi/180);
        x1(i1)=ang*pi/180;
        y1(i1)=S(1,1);
        sum=sum+y1(i1)*cos(x1(i1))*sin(x1(i1));
        sum1=sum1+y1(i1)*sin(x1(i1));
        i1=i1+1;
    end
    g1(i2)=sum/sum1;
    y2(i2)=Crosssection(n1/n2,j*1e-009,wave*1e-009);
    fn=(a*exp(-a*j)/b+a*exp(-a*(j+A*0.1))/b)/2;
    sum2=sum2+g1(i2)*y2(i2)*fn*A*0.1;
    sum3=sum3+y2(i2)*fn*A*0.1;
    i2=i2+1;
end
g(i0)=sum2/sum3;
musprime_MieA(i0)=1*sum3*(1-g(i0))/1000;
i0=i0+1;
end
f=musprime_MieA;
return

```

2.

```

% Get the musprime data from Mie theory. The refractive indexes are
n2 and n1. The musprimespectra is in the range wavel:dwave:wave2
(nm). The particle size is A (nm), number density is N (m-3).

function f=fcn_musprime_MieAN(A,N,n2,n1,wavel,dwave,wave2)
format long
musprime_MieAN=N*fcn_musprime_MieA(A,n2,n1,wavel,dwave,wave2);
f=musprime_MieAN;
return

```

3.

```
% Get the musprime data table from Mie theory. The refractive
indexes are n2 and n1. The musprime spectra is in the range
wavel:dwave:wave2 (nm). The average particle sizes are from A1 (nm)
to A2 (nm), with step dA (nm). Number density is 1 (m-3).

function f=fcn_musprime_MieA_table(A1,dA,A2,n2,n1,wavel,dwave,wave2)
format long

size_total=(A2-A1)/dA+1;
wave_total=(wave2-wavel)/dwave;
musprime_MieA_table=zeros(size_total,wave_total);

save musprime_MieA_table.mat musprime_MieA_table

i=1;
for A=A1:dA:A2
    musprime_MieA=fcn_musprime_MieA(A,n2,n1,wavel,dwave,wave2)
    musprime_MieA_table(i,:)=musprime_MieA;
    save musprime_MieA_table.mat musprime_MieA_table
    i=i+1;
end
return
```

4.

```
% Get the best estimated particle size A_estimated (nm) and number
density N_estimated (m-3) from the experimental data by comparing it
with simulation data from Mie theory. The refractive indexes are n2
and n1. The musprime spectra is in the range wavel:dwave:wave2 (nm).
The simulation data to be compared with the experimental data
includes a range for average particle sizes A1:dA:A2 (nm). In the
comparison, the musprime spectra will be normalized at a certain
wavelength wave_nm.

function
[A_estimated,N_estimated]=ANestimation(A1,dA,A2,n2,n1,wavel,dwave,wa
ve2,wave_nm)
format long

%loading the experimental data
load musprime_experi.txt

%fitting the experimental data using power law to the scattering
amplitude exp(a) and scattng power b.
data=musprime_experi;
x=data(:,1);
y=data(:,2)
Y=log(y);
```

```

p=polyfit(x,Y,1);
a=p(2);
b=-P(1);

%generating a good musprime data musprime_gener by power law using
the a and b got from the experimental data to represent the original
experimental data.
k=1;
for wave=wavel:dwave:wave2
    z=exp(a)*wave^(-b);
    musprime_gener(i)=z;
    k=k+1;
end

%to get the simulation data table from Mie theory for musprime (when
N=1) with average size A1:dA:A2 (nm),refractive index n2 and n1,in
the wavelength range wavel:dwave:wave2.
musprime_MieA_table=fcn_musprime_MieA_table(A1,dA,A2,n2,n1,wavel,dwa
ve,wave2);

load musprime_MieA_table.mat

i=1;
for A=A1:dA:A2
    musprime_MieA=musprime_MieA_table(i,:);

    %normalize both the experimental musprime data and simulation
musprime data at a certain wavelength 'wave_nm'
    wn=(wave_nm-wavel)/dwave+1;
    musprime_gener_nmlizd=musprime_gener/musprime_gener(wn);
    musprime_MieA_nmlizd=musprime_MieA/musprime_MieA(wn);

    %comparing the normalized experimental data and simulation data
using least square method
    wave_total=(wave2-wavel)/dwave+1;
    sum=0;
    for j=1:wave_total
        sum=sum+((musprime_MieA_nmlizd(j)-
musprime_gener_nmlizd(j))/musprime_MieA_nmlizd).^2;
    end
    devi(i)=sum;
end

% the least error shows the best fitting
[C,I]=min(devi);
A_estimated=A1+(I-1)*dA;

%Using the already known A_estimated, we can get the number density
by dividing the experimental musprime data at wavelength wave_nm by
the simulation data with A=A_estimated, N=1 at wave_nm.
N_estimated=musprime_gener(wn)/musprime_MieA_table(I,wn);

return

```

5.

```
% to get normalized phase function using Mie theory from a medium
with exponential scatterer size distribution with single size at
"A"(nm), and external refractive index "n1", internal refractive
index "n2". Incident laser has wavelength 'wave' and polarization
'polar'.
```

```
function f=NPthetaSingle(A,polar,n1,n2,wave)
format long

m=n2/n1;
I=[1;cos(2*polar*pi/180);sin(2*polar*pi/180);0];
i=1;
Astep=1;
theta=(0:Astep:180)*pi/180;
dtheta=Astep*pi/180;
for ang=0:Astep:180
    wv=2*pi*A/wave;
    S=SphereSc(m,wv,I,ang*pi/180);
    ptheta(i)=S(1,1);
    i=i+1;
end
ptheta_normalized=ptheta/(2*pi*sum(ptheta.*sin(theta)*dtheta));
f=ptheta_normalized;

return
```

6.

```
% to get normalized phase function using Mie theory from a medium
with exponential scatterer size distribution with average size at
"A"(nm), and external refractive index "n1", internal refractive
index "n2". Incident laser has wavelength 'wave' and polarization
'polar'.
```

```
function f=NPthetaEXP(A,polar,n2,n1 ,wave)
format long

m=n2/n1;

a=0;
average=0;
I=[1;cos(2*polar*pi/180);sin(2*polar*pi/180);0];
```

```

%           to make the size distribution function, with exponential
decrease shape and average size A

while average>(A*1.02) | average<(A*0.98)
    a=a+0.000001;
    integ=0;
    for j=A*0.01:A*0.01:A*5.01
        integ=a*A*0.01*exp(-a*j)+integ;
    end
    b=integ;
    average=0;
    for j=A*0.01:A*0.01:A*5.01
        average=j*A*0.01*a*exp(-a*j)/b+average;
    end
end
average;
a;
b;

%           [Cext, Cscat] = crosssection(m,a,wv) returns the extinction
%           and scattering cross sections for a sphere, radius a,
%           refractive index relative to medium m at wavelength wv
%           SphereSc(m,x,I,ang) returns the scattered Light for
%           a sphere, size x, refractive index relative to medium m
%           at angle ang.
%           Incident light has Stoke's Vector I.

Sstep=A*0.02;
i1=1;
for j=A*0.01:Sstep:A*5.01
    x=2*pi*j/wave;
    thegma(i1)=Crosssection(m,j*1e-009,wave*1e-009);
    fn(i1)=(a*exp(-a*j)/b+a*exp(-a*(j+Sstep))/b)*Sstep/2;
    i1=i1+1;
end
Astep=1;
theta=(0:Astep:180)*pi/180;
dtheta=Astep*pi/180;
i2=1;
for ang=0:Astep:180
    i1=1;
    for j=A*0.01:Sstep:A*5.01
        x=2*pi*j/wave;
        S=SphereSc(m,x,I,ang*pi/180);
        ptheta(i1)=S(1,1);
        i1=i1+1;
    end
    ptheta_total(i2)=sum(thegma.*ptheta.*fn)/sum(thegma.*fn);
    i2=i2+1;
end

ptheta_normalized=ptheta_total/(2*pi*sum(ptheta_total.*sin(theta)*dtheta));
f=ptheta_normalized;
% plot(theta,ptheta_normalized,'b-');
return

```

7.

% to get averaged (over -angdevi to +angdevi degree) Ptheta data from Mie theory for a medium with exponential size distribution and average size "A", with external refractive index "n1", internal refractive index "n2", and using light with polarization "polar" and wavelength "wave".

```
function f=APthetaEXP(A,n1,n2,polar,wave, angdevi)
format long
```

```
m=n2/n1;
```

```
% build an exponential decay histogram with average particle size A (nm)
```

```
average=0;
```

```
a=0;
```

```
I=[1;cos(2*polar*pi/180);sin(2*polar*pi/180);0];
```

```
while average>(A*1.02) | average<(A*0.98)
```

```
    a=a+0.000001;
```

```
    integ=0;
```

```
    for j=A*0.01:A*0.01:A*5.01
```

```
        integ=a*A*0.01*exp(-a*j)+integ;
```

```
    end
```

```
    b=integ;
```

```
    average=0;
```

```
    for j=A*0.01:A*0.01:A*5.01
```

```
        average=j*A*0.01*a*exp(-a*j)/b+average;
```

```
    end
```

```
end
```

```
average;
```

```
a;
```

```
b;
```

```
Sstep=A*0.02;
```

```
i1=1;
```

```
for j=A*0.01:Sstep:A*5.01
```

```
    x=2*pi*j/wave;
```

```
    thegma(i1)=Crosssection(m,j*1e-009,wave*1e-009);
```

```
    fn(i1)=(a*exp(-a*j)/b+a*exp(-a*(j+Sstep))/b)*Sstep/2;
```

```
    i1=i1+1;
```

```
end
```

```
Astep=1;
```

```
i2=1;
```

```
for ang=0:Astep:180
```

```
    i1=1;
```

```
    sum0=0;
```

```
    sum1=0;
```

```
for j=A*0.01:Sstep:A*5.01
```

```
    x=2*pi*j/wave;
```

```
    S=SphereSc(m,x,I,ang*pi/180);
```

```
    ptheta(i1)=S(1,1);
```

```

        i1=i1+1;
    end
    ptheta_total(i2)=sum(thegma.*ptheta.*fn)/sum(thegma.*fn);
    i2=i2+1;
end

theta=0:Astep:180;
ptheta_normalized=ptheta_total/sum(ptheta_total);
t=1;

% suppose the scattering angle is from 10 degree to 165 degree, with
% 1 degree step

for k=10:1:165
    sum2=0;
    for r=k-angdevi:1:k+angdevi
        sum2=sum2+ptheta_normalized(r);
    end
    Aptheta(t)=sum2/(2*angdevi+1);
    t=t+1;
end
theta=10:1:165;
f=Aptheta;
return
plot(theta,Aptheta,'b-')
plot(theta,abs(ptheta_normalized),'m-')
plot(theta,ptheta_total,'m-')
plot(theta,ptheta_normalized,'b-')

```

8.

% to get averaged (over -angdevi to +angdevi degree) Ptheta data from Mie theory for a medium with single size "A", with external refractive index "n1", internal refractive index "n2", and using light with polarization "polar" and wavelength "wave".

```

function f=APthetaSingle(A,n1,n2,polar,wave, angdevi)
format long
m=n2/n1;

I=[1;cos(2*polar*pi/180);sin(2*polar*pi/180);0];

i3=1;
i=1;
Astep=1;
for ang=0:Astep:180
    sum0=0;
    sum1=0;
    wv=2*pi*A/wave;
    S=SphereSc(m,wv,I,ang*pi/180);

```

```

        ptheta(i)=S(1,1);
        i=i+1;
    end
    ptheta_normalized=ptheta/sum(ptheta);
    t=1;

    % suppose the scattering angle is from 10 degree to 165 degree, with
    % 1 degree step

    for k=10:1:165
        sum2=0;
        for r=k-angdevi:1:k+angdevi
            sum2=sum2+ptheta_normalized(r);
        end
        Aptheta(t)=sum2/(2*angdevi+1);
        t=t+1;
    end
    APtheta=Aptheta/Aptheta(51);
    % plot(theta, Aptheta, 'b-');
    f=APtheta;
    % theta=0:Astep:180;
    % plot(theta, ptheta_normalized, 'b-');

    return

```

9.

Compare the measured data with Mie theory at comparison angle 'compAng' by the coefficients of polynomials got from polynomial fitting of the data. Use Newton-Raphson Method to update the scatter size iteratively to get the best estimated scatterer size in the medium. The initial guess for the average particle size is A0, the step size is dA. Suppose the experimental Ptheta data are averaged over angle (degree) -angdevi to +angdevi because of the experimental setup. The medium has a single particle size "A", with external refractive index "n1" and internal refractive index "n2". And the laser we use has polarization "polar" and wavelength "wave".

```

function [A_estimated,
error]=PthetaFitting(A0,dA,compAng,polar,wave,angdevi,n1,n2)
format long
load cylin.txt; (%loading the experimental data)
DATA=cylin;
x=DATA(:,1); y=DATA(:,2);
[C,I]=min(abs(x-compAng));
y=y/y(I); y=log10(y); p=polyfit(x,y,8);

% Only use the data from scattering angle 20 degree to 150 degree,
% with 1 degree step

A=A0;

```

```

theta=20:1:150;
yMIE1= APthetaSingle(A,n1,n2,polar,wave, angdevi);
pMIE1=polyfit(theta,yMIE1/yMIE1(compAng-9),8);
sum1=0;
for i=1:9
sum1=sum1+((p(i)-pMIE1(i))/pMIE1(i))^2;
end
devi1=(sum1/9)^0.5;
yMIE2=APthetaSingle(A+dA);
pMIE2=polyfit(theta,yMIE2/yMIE2(compAng-9),8);
sum2=0;
for i=1:9
sum2=sum2+((p(i)-pMIE2(i))/pMIE2(i))^2;
end
devi2=(sum2/9)^0.5;
j=1;
while devi1>0.005
t=(devi2-devi1)/dA;
A=A-devi1/t; A=abs(A);
yMIE1=APthetaSingle(A);
pMIE1=polyfit(theta,yMIE1/yMIE1(compAng-9),8);
sum1=0;
for i=1:9
sum1=sum1+((p(i)-pMIE1(i))/pMIE1(i))^2;
end
devi1=(sum1/9)^0.5;
yMIE2=APthetaSingle(A+dA);
pMIE2=polyfit(theta,yMIE2/yMIE2(compAng-9),8);
sum2=0;
for i=1:9
sum2=sum2+((p(i)-pMIE2(i))/pMIE2(i))^2;
end
devi2=(sum2/9)^0.5;
j=j+1
end
A_estimated=A; error=devi;
Return

```

10.

```

%Simulation study for scatterer size estimation from angular
scattering data by error plotting. Get forward data from Mie theory
first, add certain noise, get the derivative of the data, and then
compare with original Mie theory by error plotting to get the
estimated scatterer size. Both P1 and P2 polarizations are used, and
their ratio are also used as the comparison data for estimation. The
estimated average size using P1 data, P2 data and P1/P2 data are
A_estimated1, A_estimated2 and A_estimated respectively; the minimum
deviation are devi_min1, devi_min2, devi_min respectively. Comparison
angle is 'compAng'

```

```

function [A_estimated1, A_estimated2, A_estimated, devi_min1,
devi_min2, devi_min]=PthetaErrorPlotting(compAng)
format long
load NPthetaP116133.txt; (% the simulated data, with P1
polarization, n2=1.6,n1=1.33)
load NPthetaP216133.txt; (% the simulated data, with P2
polarization, n2=1.6,n1=1.33)

u=1;
for j=1:300
    yMIE1=NPthetaP116133(j,:);
    yMIE2=NPthetaP216133(j,:);
    t=1;

    % Only use the data from scattering angle 20 degree to 150 degree,
    with 1 degree step

    for k=21:151
        sum1=0;
        sum2=0;
        for r=k-0:k+0
            sum1=sum1+yMIE1(r);
            sum2=sum2+yMIE2(r);
        end
        AyMIE1(u,t)=sum1;
        AyMIE2(u,t)=sum2;
        t=t+1;
    end
    u=u+1;
end
AyMIE=AyMIE1./AyMIE2;

data11=AyMIE1(100,:);
save data11.txt data11 -ascii;
data12=ones(181,1);
save data12.txt data12 -ascii;
data21=AyMIE2(100,:);
save data21.txt data21 -ascii;
data22=ones(181,1);
save data22.txt data22 -ascii;
add_noise2('data11.txt','data12.txt',1);
add_noise2('data21.txt','data22.txt',1);
load data12.txt;
load data22.txt;

% Data will be first normalized at the comparison angle, and then be
taken log10(),and then diff(X) will be used to return the
differences calculated data along the scattering angle.

data12=data12/data12(compAng-19);
data22=data22/data22(compAng-19);
data=data12./data22;
    data12=log10(data12);
    data22=log10(data22);
    data=log10(data);
    theta=20:150;

```

```

    p1=diff(data12);
    p2=diff(data22);
    p=diff(data);
for j=1:300
    AyMIE1(j,:)=AyMIE1(j,:)/AyMIE1(j,compAng-19);
    AyMIE2(j,:)=AyMIE2(j,:)/AyMIE2(j,compAng-19);
end
AyMIE=AyMIE1./AyMIE2;

    AyMIE1=log10(AyMIE1);
    AyMIE2=log10(AyMIE2);
    AyMIE=log10(AyMIE);
    theta=20:150;
    pMIE1=ones(300,130);
    pMIE2=ones(300,130);
    pMIE=ones(300,130);
    for j=1:300
        Y1=AyMIE1(j,:);
        pMIE1(j,:)=diff(Y1);
        Y2=AyMIE2(j,:);
        pMIE2(j,:)=diff(Y2);
        Y=AyMIE(j,:);
        pMIE(j,:)=diff(Y);
    end
u=1;
for j=1:300
    sum1(u)=0;
    sum2(u)=0;
    sum(u)=0;

    for i=1:130
        sum1(u)=sum1(u)+((p1(i)-pMIE1(j,i))/pMIE1(j,i))^2;
        sum2(u)=sum2(u)+((p2(i)-pMIE2(j,i))/pMIE2(j,i))^2;
        sum(u)=sum(u)+((p(i)-pMIE(j,i))/pMIE(j,i))^2;
    end
    devi1(u)=(sum1(u)/130)^0.5;
    devi2(u)=(sum2(u)/130)^0.5;
    devi(u)=(sum(u)/130)^0.5;
    u=u+1;
end

[C1,I1]=min(devi1);[C2,I2]=min(devi2);[C,I]=min(devi);

j=1:300;
sizel=j(I1)*5; size2=j(I2)*5; size=j(I)*5;
devi_min1=C1; devi_min2=C2; devi_min=C;
A_estimated1=sizel; A_estimated2=size2; A_estimated=size;

figure
a=j*5;
plot(a,log10(devi1),'r^-')
hold on
plot(a,log10(devi2),'b*-')
hold on

```

```
plot(a,log10(devi),'go-')
return
```

11.

```
function add_noise2(data1,data2,amp);

% adds a normally distributed noise to data1 and writes it to data2.
The amount of noise depends on value specified by amp.

load (data1);
data1= load (data1);

n = randn(length(data1),1);
n = n./max(abs(n)); % make sure we go from -1 : 1
n2 = randn(length(data1),1);
n2 = n2./max(abs(n2)); % make sure we go from -1 : 1

data1(:,1) = log(data1(:,1));
data(:,1) = data1(:,1) + amp.*(data1(:,1)./100).*n;
data(:,1) = exp(data(:,1));
data1(:,1) = exp(data1(:,1));

fid = fopen(data2,'w');
for i = 1 : length(data)
    fprintf(fid,'%e %e\n', data(i,1));
end
fclose(fid);

plot(log(data1(:,1)),'k');
hold on
plot(log(data(:,1)),'r');

return
```

Programs Used

```
=====
1.

%%% CROSSSECTION  Scattering & Extinction Cross Sections
%      [Cext, Cscat] = crosssection(m,a,wv) returns the extinction
%      and scattering cross sections for a sphere, radius a,
%      refractive index relative to medium m at wavelength wv
%
%      If any of the parameters are vectors, return will a vector.

% Written by and copyright
%      Dave Barnett
%      Optical Engineering Group
%      Dept. of Electrical and Electronic Engineering
%      Loughborough University
%      4th May 1999

function [Cext, Cscat] = crosssection(m,a,wv)

wv = wv(:).';
a = a(:).';
m = m(:).';
x = 2*pi*a./wv;
if length(x)==1
    x = x*ones(size(m));
end
if length(m)==1
    m = m*ones(size(x));
end

nc = ceil(max(x)+4.05*(max(x)^(1/3))+2);
n=(1:nc).';

W = warning;
warning off
[a,b] = ScatCoef(m,x,nc);
% Check for invalid (NaN) results due to too many terms in
% relatively small particles.
invalid = find(any(isnan([a;b])));
while ~isempty(invalid)
    a(:,invalid) = 0;
    b(:,invalid) = 0;
    nc2 = ceil(max(x(invalid))+4.05*(max(x(invalid))^(1/3))+2);
    [A,B] = ScatCoef(m(invalid),x(invalid),nc2);
    a(1:nc2,invalid) = A;
    b(1:nc2,invalid) = B;
    invalid = find(any(isnan([a;b])));
    % remove invalidity of zero m or x
    % these _should_ return NaN!
    if length(x)>=max(invalid)
        invalid = invalid(x(invalid)~=0);
    else

```

```

        if x==0
            invalid = [];
        end
    end
    if length(m)>=max(invalid)
        invalid = invalid(m(invalid)~=0);
    else
        if m==0
            invalid = [];
        end
    end
end
warning(W);

Cext = ((wv.^2)/(2*pi)).*((2*n+1)'*real(a+b));
Cscat = ((wv.^2)/(2*pi)).*((2*n+1)'*(abs(a).^2+abs(b).^2));

```

```

=====
2.

```

```

% SphereSc  Stoke's vector of scattered light.
%   SphereSc(m,x,I,ang) returns the scattered Light for
%   a sphere, size x, refractive index relative to medium m
%   at angle ang.
%   Incident light has Stoke's Vector I.
%
%   If m and/or x are vectors, return will 3D, with m and/or x
%   parameters spanning third dimension.

```

```

% Written by and copyright
%   Dave Barnett
%   Optical Engineering Group
%   Dept. of Electrical and Electronic Engineering
%   Loughborough University
%   20th November 1996

```

```

%   Corrected 4th September 1997
%       i missing from calculation of S34

```

```

%   5th September 1997
%       calculation of E made more efficient.

```

```

%   Modified 14th December 1998
%       Generalised to receive vectors of m and x and return 3d
matrices.

```

```

%   30th December 1998
%       Changed to allow vector m and scalar x.

```

```

%   8th January 1999
%       Large ranges of x now computable - NaN check added to
scatcoefs

```

```

%      25th January 1999
%      Remove zero particle size or refractive index from
invalidity
%      criterion, to avoid infinite loop.

function S = SphereSc(m, x, I, ang)

if length(x)==1
    x = x*ones(size(m));
end
if length(m)==1
    m = m*ones(size(x));
end

nc = ceil(max(x)+4.05*(max(x)^(1/3))+2);
n=(1:nc).';
E = ((2*n+1)./(n.*(n+1)))*ones(1,length(x));
[p,t] = ALegendr(ang,nc);
W = warning;
warning off
[a,b] = ScatCoef(m,x,nc);
% Check for invalid (NaN) results due to too many terms in
% relatively small particles.
invalid = find(any(isnan([a;b])));
while ~isempty(invalid)
    a(:,invalid) = 0;
    b(:,invalid) = 0;
    nc2 = ceil(max(x(invalid))+4.05*(max(x(invalid))^(1/3))+2);
    [A,B] = ScatCoef(m(invalid),x(invalid),nc2);
    a(1:nc2,invalid) = A;
    b(1:nc2,invalid) = B;
    invalid = find(any(isnan([a;b])));
    % remove invalidity of zero m or x
    % these _should_ return NaN!
    if length(x)>=max(invalid)
        invalid = invalid(x(invalid)~=0);
    else
        if x==0
            invalid = [];
        end
    end
    if length(m)>=max(invalid)
        invalid = invalid(m(invalid)~=0);
    else
        if m==0
            invalid = [];
        end
    end
end
warning(W);

a = a.*E;
b = b.*E;
S1 = a.'*p + b.'*t;
S2 = a.'*t + b.'*p;

```

```

S11 = ((S2.*conj(S2))+(S1.*conj(S1)))/2;
S12 = ((S2.*conj(S2))-(S1.*conj(S1)))/2;
S33 = ((S1.*conj(S2))+(S2.*conj(S1)))/2;
S34 = i*((S1.*conj(S2))-(S2.*conj(S1)))/2;
S = zeros(4,length(ang),length(x));
S(1,(:,)) = permute(I(1)*S11 + I(2)*S12,[3 2 1]);
S(2,(:,)) = permute(I(1)*S12 + I(2)*S11,[3 2 1]);
S(3,(:,)) = permute(I(3)*S33 + I(4)*S34,[3 2 1]);
S(4,(:,)) = permute(-I(3)*S34 + I(4)*S33,[3 2 1]);

```

=====

3.

```

% ScatCoef Scattering coefficients
% [a,b]=ScatCoef(m,x,nmax)
% returns the two column vectors a and b containing
% the scattering coefficients for particles of size x
% and refractive index relative to medium m, from n=1
% to n=nmax.

% Written by and copyright
% Dave Barnett
% Optical Engineering Group
% Dept. of Electrical and Electronic Engineering
% Loughborough University
% 20th November 1996

% Corrected 4th September 1997
% m missing from calculation of dphim

% 5th September 1997
% computation method optimised by use of vector methods

% Modified 13th December 1998
% Generalised to receive vectors of rho and return
matrices.
% Corrected for complex m.

% 30th December 1998
% Changed to allow vector m and scalar x.

function [a,b] = ScatCoef(m,x,nmax)

m = m(:).';
x = x(:).';
if length(x)~=1
    x = x*ones(size(m));
end
if length(m)>1 & length(x)~=length(m)
    error('Dimensions of x & m must be the same or scalar')
end
N = ((1:nmax).')*ones(1,length(x));

```

```

% Ricatti-Bessel functions
phi = RB1(x, nmax);
phim = RB1(m.*x, nmax);
zeta = RB2(x, nmax);
xi = phi - i * zeta;

phin_1 = [sin(x);phi(1:(nmax-1),:)]';
phimn_1 = [sin(m.*x);phim(1:(nmax-1),:)]';
zetan_1 = [-cos(x);zeta(1:(nmax-1),:)]';

if length(m)>1
    m = ones(nmax,1)*m;
end
if length(x)>1
    x = ones(nmax,1)*x;
end

dphi = phin_1-N.*phi./x;
dphim = phimn_1-N.*phim./(m.*x);
dzeta = zetan_1-N.*zeta./x;
dxi = dphi - i * dzeta;
a = (m.*phim.*dphi - phi.*dphim) ./ (m.*phim.*dxi - xi.*dphim);
b = (phim.*dphi - m.*phi.*dphim) ./ (phim.*dxi - m.*xi.*dphim);

```

=====

4.

```

% ALegendr the angular dependent Associated Legendre Polynomials
% [p,t]=ALegendr(ang, nmax)
% produces matrices p and t with rows n=1 to n=nmax
% for pi and tau functions respectively.

```

```

% Written by and copyright
% Dave Barnett
% Optical Engineering Group
% Dept. of Electrical and Electronic Engineering
% Loughborough University
% 20th November 1996

```

```

function [p,t] = ALegendr(ang, nmax)
p(1,:) = ones(1,size(ang,2));
t(1,:) = cos(ang);
p(2,:) = 3*cos(ang);
t(2,:) = 2*cos(ang).*p(2,)-3;
for n=3:nmax
    p(n,:) = ((2*n-1)*cos(ang).*p(n-1,:) - n*p(n-2,:))/(n-1);
    t(n,:) = n*cos(ang).*p(n,:) - (n+1)*p(n-1,:);
end

```

=====